THESIS
3
2007

LIBRARY
Michigan State
University

This is to certify that the
dissertation entitled

The SEGUE Stellar Parameter Pipeline and The Alpha Elements of Stars in The Milky Way

presented by

Young Sun Lee

has been accepted towards fulfillment
of the requirements for the

Ph.D. degree in Astronomy and Astrophysics

Major Professor's Signature

8/21/08

Date

MSU is an affirmative-action, equal-opportunity employer

PLACE IN RETURN BOX to remove this checkout from your record.
TO AVOID FINES return on or before date due.
MAY BE RECALLED with earlier due date if requested.

DATE DUE	DATE DUE	DATE DUE

5/08 K /Proj/Acc&Pres/CIRC/DateDue.indd

THE SEGUE STELLAR PARAMETER PIPELINE AND THE ALPHA ELEMENTS OF STARS IN THE MILKY WAY

By

Young Sun Lee

A DISSERTATION

Submitted to
Michigan State University
in partial fulfillment of the requirements
for the degree of

DOCTOR OF PHILOSOPHY

Department of Physics and Astronomy

2008

ABSTRACT

THE SEGUE STELLAR PARAMETER PIPELINE AND THE ALPHA ELEMENTS OF STARS IN THE MILKY WAY

By

Young Sun Lee

I describe the development and implementation of the SEGUE (Sloan Extension for Galactic Exploration and Understanding) Stellar Parameter Pipeline (SSPP). The SSPP derives, using multiple techniques, radial velocities and stellar atmospheric parameters (effective temperature, $T_{\rm eff}$, surface gravity, log g, and metallicity, [Fe/H]) for AFGK type stars, based on medium-resolution spectroscopy and *ugriz* photometry obtained during the original Sloan Digital Sky Survey (SDSS-I) and its Galactic extension (SDSS-II/SEGUE). The SSPP also provides spectral classification for a wider range of stars, including stars with temperatures outside of the window where stellar parameters can not be estimated with the current approaches. Adding the average internal scatter from the multiple methods and the external uncertainty from the comparisons with the high-resolution analysis, quadratically, the typical uncertainties in the stellar parameters delivered by the SSPP are $\sigma(T_{\rm eff}) = 157$ K, $\sigma(\log\ g) = 0.29$ dex, and $\sigma([{\rm Fe/H}]) = 0.24$ dex, over the range 4500 K $\leq T_{\rm eff} \leq$ 7500 K.

Tests of the accuracy and precision of the SSPP, by comparing the stellar parameters for selected members of three globular clusters (M 13, M 15, and M 2) and two open clusters (NGC 2420 and M 67) to the literature values, are also presented. Spectroscopic and photometric data obtained during the SDSS-I and SDSS-II/SEGUE are used to determine atmospheric parameter and radial velocity estimates for stars in these clusters. Based on the scatter in the metallicities derived for the members of each cluster, I quantify the typical uncertainty of the SSPP values, $\sigma([{\rm Fe/H}]) = 0.13$

dex for stars in the range of $-0.3 \leq g - r \leq 1.3$ and $2.0 \leq \log g \leq 5.0$, at least over the metallicity interval spanned by the clusters studied ($-2.3 \leq$ [Fe/H] ≤ 0), and with signal-to-noise ratios greater than $\sim 10/1$. The surface gravities and effective temperatures derived by the SSPP are also compared with those estimated from the comparison of the color-magnitude diagrams with stellar evolution models; satisfactory agreement ($\sigma(T_{\rm eff}) < 200$ K and $\sigma(\log g) \leq 0.4$ dex) is found.

From the above considerations it is concluded that the SSPP is able to determine radial velocities and atmospheric parameters for stars (in the range 4500 K $\leq T_{\rm eff} \leq$ 7500 K) with sufficient accuracy and precision to enable detailed explorations of the chemical compositions and kinematics of the disk and halo populations of the Galaxy.

A method for determining the abundance ratio of the α-elements (O, Mg, Si, Ca, Ti) with respect to Fe (collectively parameterized as "[α/Fe]") is also explored. Results of a comparison with the ELODIE spectral library and from a noise injection experiment suggest that an accuracy in [α/Fe] of about 0.1 dex for spectra with $S/N \geq 20/1$ is achievable. This technique is used to estimate [α/Fe] for a total of 39,167 spectrophotometric and telluric calibration stars from the most recent public release (DR-6; Adelman-McCarthy et al. 2008), in order to study the α-abundance patterns in stars of the Galactic halo. Local space velocities (U, V, W) and orbital parameters (such as $Z_{\rm max}$, $R_{\rm apo}$, $R_{\rm peri}$, V_ϕ, and eccentricity) were calculated for this sample, and a total of 7590 potential halo stars were selected by applying cuts of $V_\phi \leq 80$ km s^{-1}, $Z_{\rm max} \geq 1$ kpc, and [Fe/H] ≤ -1.0. Furthermore, the sample was divided into two groups : a "dissipative component (or inner halo)" with stars having $40 \leq V_\phi \leq 80$ km s^{-1} and $R_{\rm apo} < 16$ kpc and an "accreted component (or outer halo)" with stars having $V_\phi < 40$ km s^{-1} or $R_{\rm apo} \geq 16$ kpc, or both. Results for the comparison of these two samples are presented as a first step toward understanding the assembly history of the halos of the Galaxy.

Copyright by
YOUNG SUN LEE
2008

Dedicated to my lovely wife, Ducksoon Noh

ACKNOWLEDGMENTS

It is a pleasure to thank the many people who helped make this thesis possible. Among them, especially, I would like to express my deep and sincere gratitude to my advisor, Dr. Timothy C. Beers, whose enthusiasm, inspiration, and encouragement greatly helped me get through the difficult times during my graduate study. Because of his support and encouragement, I was able to get involved with the Sloan Digital Sky Survey/Sloan Extension for Galactic Understanding and Exploration, and to learn how to collaborate with other great scientists who participated in the project to develop tools for reducing and handling the data. More importantly, I became a person capable of doing research. This is a priceless experience for my future career and research. I would also like to thank him for his patience and understandings in all the different situations I faced along the way. I appreciate his proofreading of my thesis as well. He was a truly great teacher for me and his influence, help, and support will remain in my mind forever. It must have been "meant-to-be" that I met him in Korea back in 2001.

I should also acknowledge Thirupathi Sivarani who taught me how to generate models of stellar atmosphere and synthetic spectra and provided for the initial start of developing the SEGUE Stellar Parameter Pipeline. Without her, I wouldn't have even started to think of constructing the pipeline. I also wish to express my warm and sincere thanks to Brian Yanny and Constance Rockosi who helped refine the SSPP with their valuable comments and suggestions. I would also like to thank my dissertation committee - Dr. Horace Smith, Dr. Stephen Zepf, Dr. Edward Brown, and Dr. Bernard Pope - for its useful comments on my thesis.

I am also indebted to my fellow graduate students for providing home-like atmosphere and for having a good time together. I am especially grateful to Brian

Marsteller, who is now in California, for our valuable research discussions, for teaching me how to observe using the 0.9 m telescope at Kitt Peak National Observatory and to reduce data, and for sharing a room with me at many meetings. I will surely miss the times we spent hanging out together at various conferences.

I should also thank Nathan DeLee for kindly providing solutions to the Linux problems that I encountered from time to time, and Christopher Waters for letting me use the LATEX class file, which made it much easier for me to write this thesis without hassling with the very tricky formatting guide line.

Finally, I owe my special thanks to my lovely wife, Ducksoon Noh, who trusted in me and depended on me. She came to this foreign soil with her very limited English, and we got married in a small chapel. During my last graduate study, her devoted support, dedication, and sacrifice made it possible for me to finish my thesis successfully. I would have loved to give her a big wonderful wedding with her parents present; however, we will remember and cherish our small but very beautiful wedding at the cozy and comfortable chapel with our friends forever.

TABLE OF CONTENTS

List of Tables ..... **xi**

List of Figures ..... **xiii**

1 Introduction **1**
1.1 The Milky Way Galaxy 1
1.1.1 Thin Disk 1
1.1.2 Thick Disk 3
1.1.3 Stellar Halo 4
1.1.4 Bulge 4
1.1.5 Dark Matter Halo 5
1.1.6 Formation of the Milky Way 5
1.2 Chapter Outline 7

2 Sloan Extension for Galactic Understanding and Exploration **9**

3 The SEGUE Stellar Parameter Pipeline (SSPP) **12**
3.1 Philosophy 12
3.2 Determination of Radial Velocities 15
3.2.1 The Adopted Radial Velocity Used by the SSPP 15
3.2.2 Checks on Radial Velocities – Zero Points and Scatter . . . 18
3.3 Calculation of Line Indices 20
3.3.1 Continuum Fit Techniques 21
3.3.2 Measurement of Line Indices 23
3.4 Methodology 24
3.4.1 Spectral Fitting With the `k24` and `ki13` Grids 24
3.4.2 Parameters Obtained from the Wilhelm et al. (1999) Procedures : `WBG` 28
3.4.3 The Neural Network Approaches : `ANNRR` and `ANNSR` 30
3.4.4 The χ^2 Minimization Technique Using the `NGS1` and `NGS2` Grids 34
3.4.5 Metallicity and Gravity Estimates from 3850–4250 Å : `CaIIK1` and `CaI1` 46
3.4.6 The Ca II K and Auto-Correlation Function Methods : `CaIIK2`, `CaIIK3`, and `ACF` 47
3.4.7 Calibration of a Ca II Triplet Estimator of Metallicity : `CaIIT` 50
3.4.8 Calibration of a Gravity Estimator Based on the Ca I (4227 Å) and Mg I b and MgH Features : `CaI2` and `MgH` 51
3.5 Empirical and Theoretical Predictions of $T_{\rm eff}$ and $g-r$ Color . 52
3.5.1 Predictions of $T_{\rm eff}$ 52
3.5.2 Predictions of $g-r$ Color 54

3.6 The Impact of Signal-to-Noise on Derived Atmospheric Parameters 56
3.7 Flags Raised During Execution of the SSPP 61
3.8 The SSPP Decision Tree for Final Parameter Estimation 66
3.8.1 Decisions on Effective Temperature Estimates 67
3.8.2 Decisions on Surface Gravity Estimates 67
3.8.3 Decisions on Metallicity Estimates 68
3.9 Validation of the Final SSPP Parameter Estimates 69
3.9.1 Validation from High-Resolution Spectroscopy 70
3.10 Assignment of Spectral Classifications for Early and Late-Type Stars 77
3.11 Distance Estimates 79
3.12 Empirical Uncertainties of Stellar Parameters of the SSPP . . . 80
3.13 Summary 81

4 Validation with Galactic Open and Globular clusters 84
4.1 Photometric and Spectroscopic Data 84
4.1.1 Photometric Data 87
4.1.2 Spectroscopic Data 89
4.2 Radial Velocities 94
4.3 Membership Selection from Spectroscopic Samples 94
4.3.1 Likely Member Star Selection for Globular Clusters 94
4.3.2 Likely Member Star Selection for Open Clusters 105
4.4 Determination of Overall Metallicities and Radial Velocities of the Clusters 106
4.4.1 Selection of True Members 107
4.4.2 Determination of Overall Estimates of Mean Cluster Metallicity and Radial Velocity 110
4.5 A Comparison of Derived Metallicities and Radial Velocities for True Cluster Members with Previous Studies 113
4.5.1 M 13 (NGC 6205) 113
4.5.2 M 15 (NGC 7078) 115
4.5.3 M 2 (NGC 7089) 116
4.5.4 NGC 2420 116
4.5.5 M 67 (NGC 2682) 117
4.6 A Comparison of Derived Metallicities and Surface Gravities for True Cluster Members with Color-Magnitude Diagrams 120
4.7 Summary 127

5 The [α/Fe] Abundance Patterns of Stars in the Galactic Halo 128
5.1 Introduction 128
5.2 Previous Studies 130
5.3 Determination of [α/Fe] 135
5.3.1 Methodology 135
5.3.2 Validation 137
5.4 Sample Selection 139
5.5 Computation of Kinematic and Orbital Parameters 142

5.6 Distributions of [α/Fe] 147
5.6.1 Distributions of V_ϕ and [Fe/H] with [α/Fe] cuts 148
5.6.2 Distributions of [α/Fe] with [Fe/H] cuts 150
5.6.3 Distributions of [α/Fe] with $R_{\rm apo}$ cuts 154
5.6.4 Distributions of [α/Fe] with V_ϕ cuts 156
5.7 Discussions and Implications 159
5.8 Summary and Conclusions 168

6 Conclusions and Future Work 173

A Line List for Line index Calculations 181

B Output Format of the SSPP 185

C Properties of Selected Cluster Members 193

References 243

LIST OF TABLES

3.1 Parameter Sensitivities to Radial Velocity Errors 13

3.2 Summary of High-Resolution Observations 16

3.3 Valid Ranges of $g - r$ and S/N for Individual Methods 25

3.4 Comparison of `NGS1` and `NGS2` Grids with Spectral Libraries and High-Resolution 44

3.5 Parameter Sensitivities to Signal-to-Noise 57

3.6 Brief Descriptions of SSPP Flags 61

3.7 Comparison of $T_{\rm eff}$ of Individual Methods with High-Resolution Analyses 70

3.8 Comparison of $\log g$ of Individual Methods with High-Resolution Analyses 73

3.9 Comparison of [Fe/H] of Individual Methods with High-Resolution Analyses 76

4.1 Properties of the Clusters 91

4.2 Derived Radial Velocities and Metallicities of the Clusters 111

4.3 Mean and 1 σ Values of Residuals in $T_{\rm eff}$ and $\log g$ 119

5.1 Variation of [α/Fe] with S/N 139

5.2 Results of K-S tests 151

A.1 Line Band and Sideband Widths and Output Format 181

B.1 Key to Each Column and Format of SSPP Parameter File 185

C.1 SSPP-Derieved Properties for Selected Member Stars of M 13 194

C.2 SSPP-Derived Properties for Selected Member Stars of M 15 214

C.3 SSPP-Derived Properties for Selected Member Stars of M 2 221

C.4 SSPP-Derived Properties for Selected Member Stars of NGC 2420 227

C.5 SSPP-Derived Properties for Selected Member Stars of M 67 238

LIST OF FIGURES

1.1 Side view of the Milky Way 2

3.1 Comparison plots of the radial velocity 17

3.2 Example of a fitted global continuum 21

3.3 Atmospheric parameter estimation with **ANNRR** 31

3.4 Atmospheric parameter estimation with **ANNSR** 33

3.5 Two examples of the results of the application of the **NGS1** grid 38

3.6 Comparison of parameters of **NGS1** grid with ELODIE library 40

3.7 Comparison of parameters of **NGS1** grid with MILES library 42

3.8 Comparison of parameters of **NGS1** grid with high resolution analysis . . 45

3.9 Comparison of $T_{\rm eff}$ of individual methods with high-resolution analysis . 72

3.10 Comparison of log g of individual methods with high-resolution analysis . 74

3.11 Comparison of [Fe/H] of individual methods with high-resolution analysis 78

4.1 Stars with available photometry in the field of M 13 85

4.2 Stars with available photometry in the field of M 15 86

4.3 Stars with available photometry in the field of M 2 88

4.4 Stars with available photometry in the field of NGC 2420 90

4.5 Stars with available photometry in the field of M 67 92

4.6 CMDs of the M 13 stars inside tidal radius and field region 95

4.7 CMDs of the M 15 stars inside tidal radius and field region 96

4.8 CMDs of the M 2 stars inside tidal radius and field region 97

4.9 CMDs of the NGC 2420 field region 98

4.10 CMDs of the M 67 field region 100

4.11 M 13 CMD based on the likely member stars 101

4.12 M 15 CMD based on the likely member stars 102

4.13 M 2 CMD based on the likely member stars 103

4.14 NGC 2420 CMD based on the likely member stars 104

4.15 M 67 CMD based on the likely member stars 106

4.16 Distributions of [Fe/H] and radial velocity for stars in M 13 region 107

4.17 Distributions of [Fe/H] and radial velocity for stars in M 15 region 108

4.18 Distributions of [Fe/H] and radial velocity for stars in of M 2 region . . . 110

4.19 Distributions of [Fe/H] and radial velocity for stars in NGC 2420 region . 112

4.20 Distributions of [Fe/H] and radial velocity for stars in M 67 region 114

4.21 Distributions of [Fe/H] as a function of $(g-r)_0$ and average S/N 118

4.22 Distributions of [Fe/H] as a function of estimated log g 121

4.23 Distributions of $T_{\rm eff}$ and log g for M 13 122

4.24 Distributions of $T_{\rm eff}$ and log g for M 15 123

4.25 Distributions of $T_{\rm eff}$ and log g for M 2 124

4.26 Distributions of $T_{\rm eff}$ and log g for NGC 2420 125

4.27 Distributions of $T_{\rm eff}$ and log g for M 67 126

5.1 Comparison of [α/Fe] from our estimates with the literature 138

5.2 Schematic diagram of U, V, and W velocities 141

5.3 Schematic diagram of cylindrical reference frame 143

5.4 Spatial distribution and a plot of [α/Fe] versus [Fe/H]. 144

5.5 Run of [α/Fe] over U, V, W, and V_ϕ 146

5.6 Distributions of [α/Fe] with $Z_{\rm max}$, $R_{\rm peri}$, $R_{\rm apo}$, and e 147

5.7 Distributions of V_ϕ and [Fe/H] with [α/Fe] cuts 149

5.8 Distributions of [α/Fe] and $R_{\rm peri}$ with [Fe/H] cuts 152

5.9 Distributions of [α/Fe] with $R_{\rm apo}$ 155

5.10 Distributions of [α/Fe], [Fe/H], and eccentricity with V_ϕ 157

5.11 Distributions of [α/Fe] with V_ϕ 158

5.12 Distributions of V_ϕ and [Fe/H] 160

5.13 Distributions of mean [α/Fe] 164

5.14 Distributions of [α/Fe] and $R_{\rm peri}$ with [Fe/H] 167

5.15 Distributions of [α/Fe] and $Z_{\rm max}$ with [Fe/H] 169

Images in this dissertation are presented in color.

CHAPTER 1: INTRODUCTION

1.1 THE MILKY WAY GALAXY

The Milky Way Galaxy is a spiral galaxy which resides in a relatively low over-density region of the Universe (the Local Group). Its total mass is estimated to be $\sim 10^{12} M_{\odot}$. Based on stellar ages, spatial distributions, kinematics, and chemical compositions (e.g., metallicity parameterized by [Fe/H][a]), stars in the Galaxy can be divided into several distinct populations, and structural components. The primary stellar components of the Galaxy are the disk systems, a stellar halo (or halos), and a central bulge. In addition to these, one can also infer the presence of a dark matter halo, whose properties are not well known at present. In this chapter, we briefly review each of these components. Figure 1.1 shows an edge-on schematic view of the major components of the Galaxy.

1.1.1 THIN DISK

The thin disk is not only the most luminous component of the Milky Way galaxy but it is the main site of active star formation in the Galaxy. It contains gas, dust, and open clusters, as well as both old and young stars, which are collectively known as Population I. Our Sun resides 8.5 kpc from the center of the Galaxy, and about 30

[a] $[Fe/H] = \log_{10}(N_{Fe}/N_H) - \log_{10}(N_{Fe}/N_H)_{\odot}$. N is the total number density of Fe or H atoms in a given volume in the star and the Sun (indicated by the $\odot$ subscript). "Metals" are understood to pertain to all elements heavier than He. The terms "metallicity" and [Fe/H] are used interchangeably throughout this thesis.

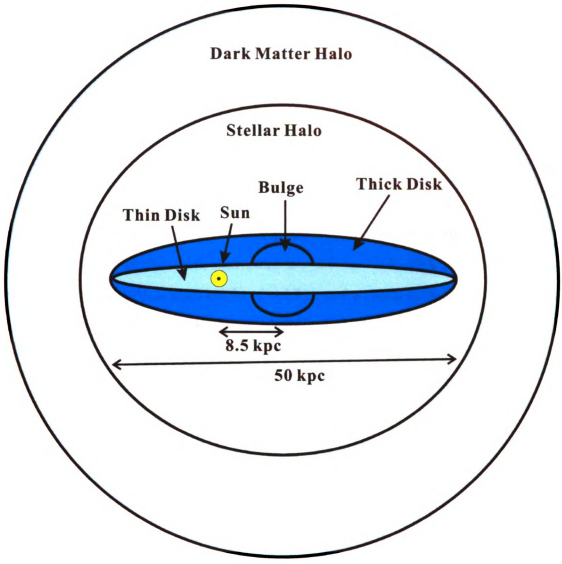


Figure 1.1 Schematic side view of the Milky Way.

pc from the Galactic plane. The radius of the luminous thin disk is about 25 kpc, including the gaseous disk. Most of the thin disk stars move around the Galactic center at a speed near 220 km s^{-1} (at the Sun's location) on circular orbits. Studies indicate that main sequence stars with spectral types G, K, or M, inhabit an old thin disk with a vertical scale height of about 300 pc (and a vertical velocity dispersion of $\sigma(W) \sim 20$ km s^{-1}), while young thin disk stars (spectral types O, B, and A) exhibit a scale height of 50 pc, and have a lower vertical velocity dispersion. The young thin

disk stars have metallicities ranging over [Fe/H] = −0.5 to +0.3. The old thin disk includes stars with metallicities over a similar range, but also somewhat lower. A recent study by Abadi et al. (2003) raised a possibility that some fraction of the old thin disk stars might have been accreted from a few satellite galaxies.

1.1.2 THICK DISK

The thick disk, identified by star counts more than 20 years ago (Gilmore & Reid 1983), is a kinematically and chemically distinct component of the Galaxy. The metallicity range of the thick disk stars is −2.0 to −0.5, with a peak at [Fe/H] $\sim$ −0.6. It has a vertical scale height of $\sim$ 1 kpc and a radial scale length of $\sim$ 3 kpc. The stellar mass of the thick disk is 10–20% of the thin disk stellar mass, and it is as about as old as the globular cluster 47 Tuc. The rotational velocity of the thick disk population is somewhat poorly known; some authors report a value $\sim$ 170 km s^{-1} (Norris 1986; Morrison, Flynn & Freeman 1990; Chiba & Beers 2000), while others (e.g., Wyse & Gilmore 1986; Gilmore, Wyse & Norris 2002) have derived $\sim$ 100 km s^{-1}. The vertical velocity dispersion of the thick disk stars is $\sigma(W) \sim 40$ km s^{-1}. There is also evidence (Chiba & Beers 2000) that the thick disk has a metal deficient tail, reaching as low as [Fe/H] = −2.0. This tail of the thick disk, whose origin still remains controversial, is referred to as the "metal-weak thick disk". The thick disk stars with [Fe/H] < −0.6 possess [α/Fe] = +0.4 (Bensby et al. 2000, and references therein), which indicates likely enrichments from core collapse supernovae. A decline of the α-abundance with respect to the Fe is also noticed for the metal rich stars of this component, implying Fe contributions from Type Ia supernovae. The thick disk might have formed from the pre-existing thin disk heated by interactions with dwarf galaxies or from the debris of disrupted dwarf galaxies involved in past encounters with the Galaxy.

1.1.3 Stellar Halo

The stellar halo includes the globular clusters (GCs) and field stars, with ages that are among the oldest objects in the universe (between 12 and 14 Gyr). The GCs are spherical conglomerations of stars, up to about 50 pc across, that contain 10^4 to 10^6 member stars. About 1% of the halo stars are contained in globular clusters. The stellar halo is roughly spherical or a slightly oblate spheroidal shape, extending to as large as 100 kpc. The main constituents of the stellar halo are old, low-metallicity stars with a mean [Fe/H] $= -1.6$. Its total mass is about $10^9 M_{\odot}$. Members of the halo population exhibit a negligible net rotation around the Galaxy, and high velocity dispersions (e.g., $\sigma(W) \sim 90$ km s^{-1}). The stellar density distribution in the halo can be described by a $r^{-3.5}$ form with a scale height of about 3 kpc. The typical [α/Fe] of the halo stars is [α/Fe] 0.3 to 0.4 dex, which suggests chemical enrichments from SNe II, probably at very early times.

Very recently, the stellar halo has been argued to comprise two distinct populations, a slowly rotating (0 to 50 km s^{-1}) inner halo population with a metallicity peak at [Fe/H] $= -1.6$, and a counter rotating (-40 to -70 km s^{-1}) outer halo population with a metallicity peak at [Fe/H] $= -2.2$. While the inner halo appears to dominate up to distance of 10$-$15 kpc, the outer halo dominates beyond 15$-$20 kpc (Carollo et al. 2007). The majority of the inner halo may have formed from dissipative collapsing gas clouds or proto-Galactic clumps, while the outer halo is suggested to have been accreted from the disruption of numerous dwarf satellites.

1.1.4 Bulge

The bulge of the Galaxy appears as box shape from our perspective, with a diameter of 2 kpc and a height of 400 pc. Due to the difficulty in decoupling the bulge population from stars of the inner disk, this region is not presently well studied. Its outer regions rotate at about 100 km s^{-1} and its total mass is around $10^{10} M_{\odot}$. The bulge is mainly

composed of old stars of the same age as the stellar halo, although the bulk of their metallicities are roughly solar. It appears that star formation in the bulge is still ongoing. The bulge populations exhibit a very broad metallicity distribution, with a peak of [Fe/H] ~ -0.3, which can be well described by a Simple closed box model (Sadler, Terndrup & Rich 1996, and references therein). High-resolution elemental analysis of several bulge stars indicates enhancement of [α/Fe] from SNe II (Rich & McWillian 2005, and references therein), implying very rapid star formation. The dominant old, metal-rich population of the bulge suggests an formation of the bulge by early, very intense star formation, likely from the gas ejected by halo star forming regions (Ferreras, Wyse, & Silk 2003). There is solid evidence for the existence of a bar connected to the bulge.

1.1.5 Dark Matter Halo

The dark matter halo is only detectable by its gravitational influence. Its existence was first inferred from studies of the Galactic rotation curve, which shows no sign of a decline out to a radius of 20 kpc, indicating a substantial amount of (unseen) matter must exist at least out to that radius, and probably much farther. Because this non-luminous matter has never been directly observed at any wavelength, it is known as *dark matter*, with no clear understanding of its nature. From an inventory of the mass of the other constituents of the Galaxy, the total mass of the dark matter in the Milky Way is ~ 10 times greater than the total mass of stars, and about 100 times greater than that of the gas and dust.

1.1.6 Formation of the Milky Way

Over the past fifty years, two major formation scenarios of the Milky Way galaxy have been suggested. The first was a rapid monolithic collapse model, proposed by Eggen, Lynden-Bell, & Sandage (1962). These authors made use of an observed

correlation between the metallicity of halo stars with their kinematics (in particular, their rotational velocity, or total angular momentum) to claim that a rapid collapsing protogalactic gas could have formed the stellar halo and continued (as it spun up) to form the disk. In this model, the collapse time is shorter than the Galactic revolution period ($\sim 2 \times 10^8$ yrs), but sufficiently long for massive stars to form in the metal deficient infalling gas so that the gas is able to be enriched with heavy elements. The series of star formation and collapse would lead to newly formed stars that exhibit different orbital eccentricities (changing from high eccentricity orbits for the low metallicity stars to low eccentricity orbits for the higher metallicity stars). and have higher metallicity as the collapse occurs. In this scenario, one would expect to find a metallicity gradient as a function of eccentricity in the resulting sample of stars.

The rapid collapse model was criticized by Searle & Zinn (1978). They gathered relatively accurate metallicity and horizontal-branch morphologies for about 50 globular clusters (GCs), based on the data available at that time, and searched for correlations in their properties with Galactocentric distance, $R_{\rm GC}$. They divided the GCs into inner and outer halo groups by separating them at a distance of $R_{\rm GC} \sim 8$ kpc. They found that not only did there exist no metallicity gradient with distance from the Galactic center for the outer halo GCs, but also that horizontal-branch morphologies between the inner and outer GCs is very different (which they attributed to age differences). These findings led them to conclude that the outer halo GCs formed through accretion of what they called "proto-Galactic fragments" over an extended period of time, up to several Gyrs.

Later, Zinn (1993) expanded the model further, and based on horizontal-branch morphology, distance, spatial distribution, rotational velocity, and velocity dispersion, he divided the GCs into two groups: "old" and "young", which were associated with a "dissipative" inner halo and an "accreted" outer halo.

The widely accepted ΛCDM (cold dark matter) structure formation paradigm (e.g., Navarro et al. 1997) favors the ideas envisioned by Searle & Zinn (1978). In this paradigm, all galaxies form from local over-densities in the primordial matter distribution, and grow hierarchically via mergers and the accretion of numerous smaller fragments over time. The manifest candidates for the building blocks are the dwarf spheroidal (dSph) and irregular (dIrr) galaxies we see today (actually, these might just be the survivors of the process). One of the predictions of the hierarchical structure formation approach is that one might expect to observe many more satellite galaxies surrounding existing large galaxies like the Milky Way than are in fact observed today. This is known as the "missing satellite problem". Although a number of faint dwarf galaxies have been recently discovered by the Sloan Digital Sky Survey (SDSS), the total number of the satellite galaxies around the Milky Way is still about four times smaller than modern predictions (Simon & Geha 2007).

1.2 Chapter Outline

Chapter 2 describes the Sloan Extension for Galactic Understanding and Exploration (SEGUE), which is one of the three surveys conducted during the first extension of SDSS, known as SDSS-II. The radial velocity and the methodology which are adopted in the SEGUE Stellar Parameter Pipeline (SSPP) are presented in Chapter 3. The stellar parameters derived by individual methods in the SSPP are compared with the results of high-resolution spectroscopic analysis in this chapter. In Chapter 4, the membership selection for two open clusters (M 67 and NGC 2420) and three globular clusters (M 15, M 13, and M 2) are presented, and the stellar parameters estimated from the SSPP are validated with the selected likely members of the clusters. Chapter 5 addresses a method for estimating [α/Fe] for SDSS/SEGUE stars, and validates the α-abundance determination by making comparisons with the ELODIE spectral library. The sample selection and the computation of the orbital parameters are

also described. The [α/Fe] patterns of Galactic halo stars, after dividing the stars into various sub-samples by several cuts (such as the rotational velocity, V_{ϕ}, around the Galactic center, the metallicity, the maximum distance, $Z_{\rm max}$, from the Galactic plane, and the apo-Galactic distance, $R_{\rm apo}$) are discussed. Finally, conclusions are provided in Chapter 6. Note that throughout the thesis, the term [α/Fe] is interchangeable with the α-abundance (e.g., high (low)-α is regarded as high (low) value of [α/Fe]).

Chapter 2: Sloan Extension for Galactic Understanding and Exploration

The Sloan Extension for Galactic Understanding and Exploration (SEGUE) is one of three surveys that are being executed as part of the current extension of the Sloan Digital Sky Survey (SDSS-II), which comprises the sub-surveys LEGACY, SUPERNOVA SURVEY, and SEGUE. LEGACY is a continuation of SDSS-I, in order to complete (in the northern Galactic cap) the imaging and spectroscopy which were not obtained due to weather and mechanical problems. SDSS-I (York et al. 2000) was designed to obtain five-color photometry over a quarter of the entire sky, and medium-resolution spectroscopy of 10^6 galaxies, 100,000 quasars, and several tens of thousands of stars, over the course of five years. SUPERNOVA SURVEY (Frieman et al. 2008) searches for supernovae in the redshift range $0.05 < z < 0.35$ by repeated scans of 300 deg^2 over an equatorial region.

The SEGUE program is designed, in part, to obtain *ugriz* imaging of some 3500 square degrees of sky outside of the original SDSS-I footprint (Fukugita et al. 1996; Gunn et al. 1998, 2006; York et al. 2000; Stoughton et al. 2002; Abazajian et al. 2003, 2004, 2005; Pier et al. 2003; Adelman-McCarthy et al. 2006, 2007, 2008). The regions of sky targeted are primarily at lower Galactic latitudes ($|b| < 35°$), in order to better sample the disk/halo interface of the Milky Way. As of Data Release 6 (DR-6, Adelman-McCarthy et al. 2008), about 85% of the planned additional imaging has

already been completed. SEGUE is also obtaining $R \simeq 2000$ spectroscopy, over the wavelength range 3800–9200 Å, for some 250,000 stars in 200 selected areas over the sky available from Apache Point, New Mexico. The spectroscopic candidates are selected on the basis of *ugriz* photometry to populate 14 target categories (see Table 2 in Adelman-McCarthy et al. 2008 for the target selection algorithms employed), chosen to explore the nature of the Galactic stellar populations at distances from 0.5 kpc to over 100 kpc from the Sun. Spectroscopic observations have been obtained for roughly 75% of the planned targets thus far, a total of about 190,000 spectra. The SEGUE data clearly require automated analysis tools in order to efficiently extract the maximum amount of useful astrophysical information for the targeted stars, in particular their stellar atmospheric parameters, over wide ranges of effective temperature ($T_{\rm eff}$), surface gravity ($\log g$), and metallicity ([Fe/H]).

The photometric data of SDSS-I and SEGUE are collected on moonless and cloudless nights of good seeing in five broad bands (u, g, r, i, z) with central wavelengths 3551, 4686, 6166, 7480, and 8932 Å (Fukugita et al. 1996), respectively, using an imaging array of 30 (6×5) 2048×2048 Tektronix CCDs (Gunn et al. 1998). The pixel size is 24 μm, corresponding to $0.396''$ on the sky. A series of software procedures, collectively known as the SDSS PHOTO pipeline (Lupton et al. 2001), processes and reduces the scanned images shortly after data are obtained. As part of these procedures, the instrumental fluxes and astrometric positions (Pier et al. 2003), as well as a determination of whether an object is likely to be stellar (i.e., a *point source*), or not (an *extended* source) are obtained. Afterwards, the photometric data are further calibrated by matching to brighter known standards observed with a smaller calibration telescope on Apache Point (Hogg et al. 2001; Smith et al. 2002; Tucker et al. 2006). The processed photometric data have been shown to exhibit 2% relative and absolute errors in g, r, and i, and 3%–5% errors in u and z for all stellar objects brighter than $g = 20$ (Stoughton et al. 2002; Abazajian et al. 2004, 2005;

Ivezić et al. 2004).

After gathering detailed information on objects from the photometric data, subsets of them are targeted during SEGUE for spectroscopy. A pair of plug-plates (referred to as the "bright" and "faint" plates) are obtained over the 3° field of the ARC 2.5m. A total of 640 optical fibers are employed to obtain $R = 2000$ spectra for approximately 600 program objects for each plug-plate (the remaining fibers are used for spectrophotometric and reddening calibration objects, and observations of the night sky). The exposure time depends on the observation conditions. For a bright plate, exposures are set to achieve a total $(S/N)^2 > 15/1$ from the two blue-side CCDs on the SDSS spectrographs; the exposure for a faint plate is set such that a total $(S/N)^2 > 50/1$ for all four (red and blue CCDs) on the SDSS spectrographs is achieved. In order to identify and remove cosmic ray hits, each plug-plate must have at least three exposures; the integration time for any single exposure is not longer than 30 minutes. For the purposes of targeting objects on these plug-plates, the boundary between the bright and faint plates is set at $r \sim 18.0$. The data thus obtained are processed through the SDSS spectroscopic pipeline software (SPECTRO2D and SPECTRO1D), which produces wavelength and flux-calibrated spectra, and also obtains estimates of radial velocities and line indices (Stoughton et al. 2002).

In the following, the colors ($u-g$, $g-r$, $r-i$, $i-z$, and $B-V$) and magnitudes (u, g, r, i, z, B, and V) without subscript "0" are understood to be de-reddened and corrected for absorption (using the dust maps of Schlegel et al. 1998), unless stated specifically otherwise.

Chapter 3: The SEGUE Stellar Parameter Pipeline (SSPP)

3.1 Philosophy

Numerous methods have been developed in the past in order to extract atmospheric-parameter estimates from medium-resolution stellar spectra in a fast, efficient, and automated fashion. These approaches include techniques for finding the minimum distance (parameterized in various ways) between observed spectra and grids of synthetic spectra (e.g., Allende Prieto et al. 2006), non-linear regression models (e.g., Re Fiorentin et al. 2007, and references therein), correlations between broadband colors and the strength of prominent metallic lines, such as the Ca II K line (Beers et al. 1999), auto-correlation analysis of a stellar spectrum (Beers et al. 1999, and references therein), obtaining fits of spectral lines (or summed line indices) as a function of broadband colors (Wilhelm et al. 1999), or the behavior of the Ca II triplet lines as a function of broadband color (Cenarro et al. 2001a, 2001b). However, each of these approaches exhibits optimal behavior over restricted temperature and metallicity ranges; outside of these regions they are often un-calibrated, suffer from saturation of the metallic lines used in their estimates at high metallicity or low temperatures, or lose efficacy due to the weakening of metallic species at low metallicity or high temperatures. The methods that make use of specific spectral features are susceptible to other problems, e.g., the presence of emission in the core of the Ca II K

line for chromospherically active stars, or poor telluric line subtraction in the region of the Ca II triplet. Because SDSS stellar spectra cover most of the entire optical wavelength range, one can apply several approaches, using different wavelength regions, in order to glean optimal information on stellar parameters. The combination of multiple techniques results in estimates of stellar parameters that are more robust over a much wider range of $T_{\rm eff}$, log g, and [Fe/H] than those that might be produced by individual methods. The SSPP implements this "multi-method" philosophy.

Table 3.1: Parameter Sensitivities to Radial Velocity Errors[b]

		RV	50 (km s^{-1})		100 (km s^{-1})		150 (km s^{-1})		200 (km s^{-1})	
	Name	Method	$<\Delta>$	σ	$<\Delta>$	σ	$<\Delta>$	σ	$<\Delta>$	σ
$T_{\rm eff}$										
	Ad	Adop	−0.6	18.8	−22.0	29.5	−48.3	44.4	−83.8	55.0
	T1	ki13	21.0	31.3	46.6	64.8	85.4	104.7	113.7	149.0
	T2	k24	1.4	8.8	−2.4	16.5	−4.7	30.6	−19.7	53.5
	T3	WBG	0.0	12.4	−1.5	6.1	−52.5	70.1	−81.0	106.0
	T4	ANNSR	−17.8	72.1	−131.6	100.2	−281.4	153.1	−458.3	232.9
	T5	ANNRR	−8.2	15.6	−45.2	39.4	−99.8	67.2	−164.0	95.4
	T6	NGS1	7.4	16.9	19.2	35.3	38.7	61.8	55.3	99.1
	T7	HA24	−4.6	10.9	−18.9	19.1	−41.1	29.0	−72.0	41.1
	T8	HD24	3.8	5.8	2.8	8.1	−0.9	10.1	−5.6	14.8
	T9	T_K	...	...	...	...	...	...	...	...
	T10	T_G	...	...	...	...	...	...	...	...
	T11	T_I	...	...	...	...	...	...	...	...
log g										
	Ad	Adop	0.037	0.052	0.071	0.091	0.077	0.135	0.008	0.207
	G1	ki13	0.034	0.099	0.066	0.148	0.127	0.224	0.122	0.379
	G2	k24	−0.019	0.050	−0.035	0.093	−0.025	0.162	−0.027	0.251

Table 3.1: Parameter Sensitivities to Radial Velocity Errors (continued)

	RV	50 (km s^{-1})		100 (km s^{-1})		150 (km s^{-1})		200 (km s^{-1})	
Name	Method	$<\Delta>$	σ	$<\Delta>$	σ	$<\Delta>$	σ	$<\Delta>$	σ
G3	WBG	−0.011	0.039	−0.044	0.198	−0.076	0.413	−0.081	0.620
G4	ANNSR	0.077	0.119	0.151	0.126	−0.236	0.463	−0.317	0.624
G5	ANNRR	0.092	0.068	0.116	0.139	0.046	0.229	−0.103	0.356
G6	NGS1	−0.034	0.054	−0.079	0.145	−0.156	0.293	−0.223	0.464
G7	NGS2	0.012	0.117	−0.001	0.259	−0.009	0.471	−0.131	0.632
G8	CaI1	0.057	0.118	0.143	0.173	0.241	0.249	0.331	0.331
G9	CaI2	−0.042	0.036	−0.116	0.091	−0.233	0.185	−0.385	0.294
G10	MgH	−0.001	0.011	−0.015	0.030	−0.037	0.057	−0.060	0.095
[Fe/H]									
Ad	Adop	−0.019	0.019	−0.096	0.047	−0.203	0.074	−0.353	0.116
M1	ki13	−0.012	0.034	−0.085	0.057	−0.209	0.090	−0.384	0.118
M2	k24	0.002	0.024	−0.057	0.046	−0.192	0.092	−0.404	0.145
M3	WBG	−0.046	0.057	−0.122	0.147	−0.256	0.411	−0.734	0.559
M4	ANNSR	−0.082	0.090	−0.171	0.161	−0.251	0.488	−0.526	0.524
M5	ANNRR	−0.027	0.027	−0.163	0.095	−0.364	0.196	−0.574	0.319
M6	NGS1	−0.008	0.021	−0.056	0.038	−0.157	0.061	−0.292	0.083
M7	NGS2	−0.044	0.033	−0.113	0.074	−0.261	0.136	−0.414	0.219
M8	CaKII1	0.010	0.054	0.029	0.082	0.023	0.144	−0.007	0.238
M9	CaKII2	0.000	0.000	0.014	0.034	0.000	0.095	0.003	0.051
M10	CaKII3	0.001	0.020	0.001	0.032	0.002	0.029	0.006	0.040
M11	ACF	0.005	0.013	0.012	0.021	0.021	0.025	0.030	0.026
M12	CaIIT	−0.000	0.000	0.013	0.071	0.022	0.088	0.062	0.120

[b]See Chapter 3.4 and 3.5 for descriptions of each method. $<\Delta>$ is the average of the differences between parameters obtained with, and without, the velocity shift; σ is the standard deviation of the differences. The T9, T10, and T11 estimates do not change with velocity errors because they are computed from the $g-r$ color.

3.2 Determination of Radial Velocities

3.2.1 The Adopted Radial Velocity Used by the SSPP

The *spZbest* fits file, which is generated from the SDSS spectroscopic reduction pipeline (Stoughton et al. 2002), provides two estimated radial velocities. One is an absorption (or emission)-line redshift computed from a cross-correlation procedure using templates that were obtained from SDSS commissioning spectra (Stoughton et al. 2002) – the **spectro1d** redshifts. Another estimate comes from performing a "best-match" procedure that compares the observed spectra with externally measured templates (in this case, the ELODIE library of high-resolution spectra, as described by Prugniel & Soubiran 2001), degraded to match the resolving power of SDSS spectra (Aldeman-McCarthy et al. 2008).

Previous experience with the analysis of SDSS stellar spectra suggested that the radial velocity estimated from the ELODIE template matches is often the best available estimate, in the sense that it is the most repeatable, based on spectra of "quality assurance" stars with multiple determinations. In addition, the **spectro1d** redshifts exhibit larger systematic offsets, as high as 12 km s^{-1} (Aldeman McCarthy et al. 2008). Hence, as a first choice, we adopt the radial velocity from the ELODIE template matches and set the radial velocity indicator flag to 'ELRV'. However, there are some cases where the velocities from the ELODIE template matches are not reported, because an adequate match to the (somewhat incomplete) ELODIE library could not be made with confidence. In such cases, we check the **spectro1d** redshifts; if a velocity is reported by this routine, we adopt it, and the radial velocity flag is set to 'BSRV'.

Table 3.2: Summary of High-Resolution Observations for SDSS and SEGUE Stars

Telescope	Instrument	Resolving power	Wavelength coverage (Å)	Number of stars
Keck - I	HIRES	45000	3800–10000	11
Keck - II	ESI	6000	3800–10000	25
HET	HRS	15000	4400–8000	110
Subaru	HDS	45000	3000–8000	9

If neither of the above two velocities are reported (which happens only rarely, and mainly for quite low S/N ($< 5/1$) spectra, then we obtain an independent estimate of the radial velocity based on our own IDL routines. The calculation of this radial velocity estimate is carried out by determining wavelength shifts for several strong absorption line features (Ca II K, Ca II H, Hδ, Ca I, Hγ, Hβ, Na I, Hα, and the Ca II triplet). After ignoring any likely spurious values (calculated velocity above +500 km s^{-1} or below -500 km s^{-1}) from the individual lines, we obtain a 3 σ-clipped average of the remaining radial velocities. If this computed average falls between -500 km s^{-1} and +500 km s^{-1}, we take the calculated radial velocity as the adopted radial velocity, and set the radial velocity flag to 'CALRV'. We have noticed that certain types of stars, in particular cool stars with large carbon enhancements, present a challenge for the radial velocity estimates adopted by the SSPP. We have developed new carbon-enhanced templates, based on synthetic spectra, which appear to return improved estimates. These will be implemented in the next version of the SDSS spectroscopic reduction pipeline, which we anticipate applying for the final SDSS-II data release, DR-7.

It should be noted that many of the techniques used for atmospheric parameter estimation in the SSPP work well even when the velocity determination for a given star

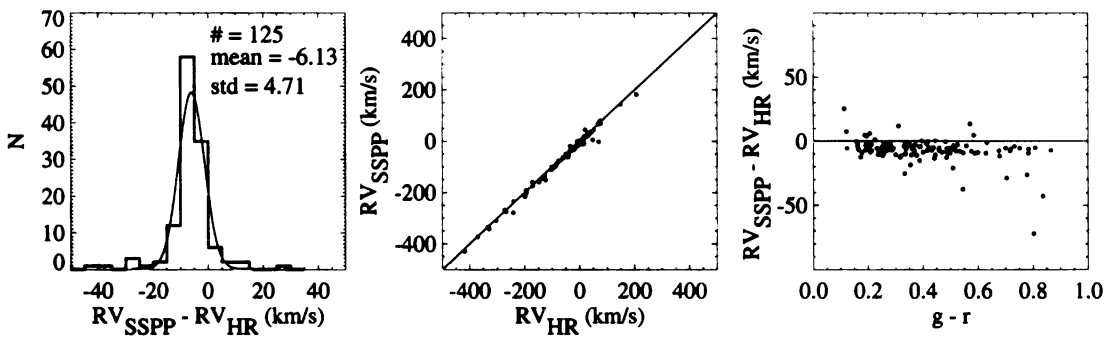


Figure 3.1 Comparison plots of the radial velocity adopted by the SSPP with that measured by high-resolution analyses (HR). An offset of -6.13 km s^{-1}, with $\sigma = 4.71$ km s^{-1}, is noted from the Gaussian fit to the residuals. This offset appears constant with $g - r$, as shown in the right-hand panel.

has errors of up to 100 km s^{-1} or more. Table 3.1, which summarizes an experiment on how the derived atmospheric parameters change as a result of systematically shifting the radial velocity estimate by 50, 100, 150, and 200 km s^{-1} relative to the original value, confirms this. We made use of 125 SDSS-I/SEGUE high-resolution calibration stars (obtained with the Hobby-Eberly Telescopy; HET, see Allende Prieto et al. 2008; hereafter Paper III), all of which have well-determined stellar parameters, thanks to their high quality ($S/N > 50/1$). See Chapter 3.4 and 3.5 for the naming convention and the description of each parameter estimation method. As can be seen in the table, most of the methods suffer zero-point shifts in log g and [Fe/H] less than 0.1 dex, with a scatter of below 0.2 dex, even for radial velocity shifts as high as 100 km s^{-1}. This level of scatter is on the order of the typical uncertainty ($\sim$ 0.2 to 0.3 dex) for these parameters obtained from our analysis of medium-resolution spectra in SDSS. The reason for the lack of significant scatter is that many of our methods compare with synthetic spectra over wide spectral ranges, rather than by a line-by-line comparison to weak individual lines, to determine the stellar parameters. Even for those techniques that employ line-index approaches, the SSPP employs relatively wide bandwidths, which mitigates against large variations due to radial velocity errors.

Thus, small shifts in a spectrum due to a poor radial velocity determination will not strongly influence our estimates of the stellar parameters.

If none of the above methods yields an acceptable estimate of radial velocity, or if the reported velocity is apparently spurious (greater than 1000 km s^{-1} or less than -1000 km s^{-1}), we simply ignore the spectrum of the star in our subsequent analysis, and set the radial velocity flag to 'NORV'.

3.2.2 Checks on Radial Velocities – Zero Points and Scatter

In order to check on the accuracy of the radial velocities adopted by the SSPP, we compare with over 150 high-resolution spectra of SDSS-I/SEGUE stars that have been obtained in order to calibrate and validate the stellar atmospheric parameters. Table 3.2 summarizes the available high-resolution data. We plan to continue enlarging this sample of validation/calibration stars in the near future.

The high-resolution spectra have been reduced and analyzed independently by two (C.A. and T.S.) of the authors in Paper III. A detailed description of the analyses can be found in Paper III. During the course of deriving the stellar parameter estimates from the high-resolution spectra, the radial velocities of stars are first measured. Note that C.A. only considered the HET spectra, while T.S. considered all available spectra. Thus, only the HET stars have radial velocities obtained by both analysts; for these stars we take an average of their independent determinations, which typically differ by no more than 1–2 km s^{-1}. A more detailed discussion is presented in Paper III.

Here we focus on the systematic errors of the adopted radial velocities. After rejecting problematic (e.g., $S/N < 20/1$) high-resolution spectra, or stars that appear to be spectroscopic binaries at high spectral resolution), 125 stars remain to compare with the adopted radial velocity results from the SSPP. Figure 3.1 shows the results of these comparisons. A consistent offset of -6.13 km s^{-1} (with a standard deviation

of 4.71 km s^{-1}) is computed from a Gaussian fit to the residuals; this offset appears constant over the color range $0.1 \leq g - r \leq 0.9$. An additional comparison with the radial-velocity distribution of selected member stars in the Galactic globular and open clusters reveals similar offsets (-8.68 km s^{-1} for M 15, -7.03 km s^{-1} for M 13, -7.47 km s^{-1} for M 67, and -8.26 km s^{-1} for NGC 2420; see Lee et al. 2008 for the membership selection criteria; hereafter Paper II). The origin of this velocity offset is as yet unclear; it may stem from the use of different algorithms in the fits to arc and sky lines (Adelman-McCarthy et al. 2008). It should be noted that an offset of +7.3 km s^{-1} is added to all DR-6 (Adelman-McCarthy et al. 2008) stellar radial velocities. This offset was computed by averaging the offsets of -6.8 km s^{-1} (M 15) and -8.6 km s^{-1} (M 13), and a -6.6 km s^{-1} offset for individual field stars, all obtained from preliminary results of an analysis of the clusters and the high-resolution spectroscopic analysis of SDSS-I/SEGUE stars that were carried out prior to DR-6 (Adelman-McCarthy et al. 2008). In Paper III, this offset is taken into account in the comparison of the radial velocity determinations. From the new high-resolution spectroscopic analysis of SDSS-I/SEGUE stars (Paper III) and the analysis of member stars of the clusters (Paper II), an average offset is -7.51 km s^{-1}. Therefore, in future data releases (e.g., DR-7), this very minor difference will likely be reflected in all adopted stellar radial velocities. However, in order to account for its presence and to be consistent with the DR-6 database, we apply an empirical +7.3 km s^{-1} shift to each adopted radial velocity obtained by the SSPP. After application of this velocity shift, the zero-point uncertainties in the corrected radial velocities determined by the SSPP (and the SDSS spectroscopic reduction pipeline it depends on) should be close to zero, with a random scatter on the order of 5 km s^{-1} or less. Note that the scatter in the determination of radial velocities, based on the average displacements of the "quality assurance" stars with multiple measurements varies from 5.0 km s^{-1} to 9.0 km s^{-1}, depending on spectral type, and exhibits a scatter of

2 km s^{-1} between observations obtained with the "faint" and "bright" spectroscopic plug-plates (Adelman-McCarthy et al. 2008).

3.3 Calculation of Line Indices

The initial step in calculation of line indices for SDSS spectra is to transform the wavelength scale of the original SDSS spectrum over to an air-based (rather than vacuum-based) wavelength scale, and to linearly rebin the spectrum to 1 Å bins in the blue (3800−6000 Å), and 1.5 Å bins in the red (6000−9000 Å). This slightly larger bin size is due to the degradation of the resolution in the red regions of the spectra. Then, based on the adopted radial velocity described above, the wavelength scale is shifted to a zero velocity rest frame.

The SSPP measures line indices of 82 atomic and molecular lines. Line-index calculations are performed in two modes; one uses a global continuum fit over the entire wavelength range (3850−9000 Å), while the other obtains local continuum estimates around the line bands of interest. The choice between which mode is used depends on the line depth and width of the feature under consideration. Local continua are employed for the determinations of stellar atmospheric parameters based on techniques that depend on individual line indices. Other techniques, such as the neural network, spectral matching, and auto-correlation methods, require wider wavelength ranges to be considered; for these the global continuum (or their own internal continuum routine) is used. We make use of the errors in the fluxes reported by the SDSS spectroscopic reduction pipeline to measure the uncertainty in the line indices. Details of the procedures used to obtain the continuum fits and line index measures (and their errors) are discussed below.

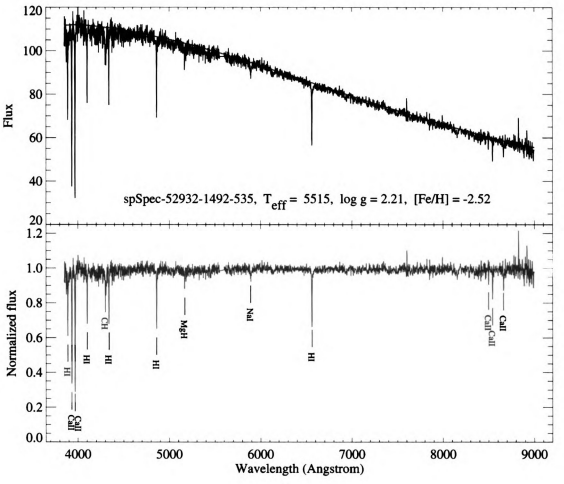


Figure 3.2 An example of a fitted global continuum for a metal-poor star. The derived parameters from the SSPP for this star are shown in the upper panel. The red line in the upper panel is the fitted continuum over the 3850−9000 Å wavelength range; the black line is the observed spectrum. The bottom panel shows the normalized flux, with strong metal and Balmer features labeled.

3.3.1 Continuum Fit Techniques

A. Global Continuum Fit

Determination of the appropriate continuum for a given spectrum is a delicate task, even more so when it must be automated, and obtained for stars having wide ranges of effective temperatures, as is the case for the present application.

In order to obtain a global continuum fit, the SSPP first divides the wavelength

range into two pieces: blue (3850−5800 Å) and red (5800−9000 Å). After removing the strong Balmer lines present in most spectra, the blue side is iteratively fit to a ninth-order polynomial, rejecting points that are more than 3 σ above the fitted function. The same procedure is applied to the red side, but using a fourth-order polynomial. Then, the two fitted pseudo-continua are spliced together, and the joined continuum is again fitted to a ninth-order polynomial. This is the final global pseudo-continuum used to calculate line indices.

The reason for dividing a spectrum into two regions is to avoid the continuum being placed at too high a level around the Ca II Triplet, due to the poor sky-line subtraction in this region in some cases. Fitting the entire range of a spectrum requires a high-order polynomial. As a result, the continuum on the red side of a spectrum will be artificially boosted due to the presence of poorly subtracted sky lines or noise spikes, if any. Use of a lower order polynomial fit to the red side avoids this potential problem.

The upper panel of Figure 3.2 shows an example of a fitted global continuum for a metal-poor giant, obtained by application of the procedure described above. The atmospheric parameters determined by the SSPP are also listed on the plot. The bottom panel is the normalized spectrum, obtained by division of the spectrum by the global continuum fit. Strong lines that play important roles in estimating the atmospheric parameters are labeled. It can be seen that a reasonable continuum estimate is obtained even in the region of the Ca II triplet, where residuals from poor sky subtraction can sometimes be problematic.

B. Local Continuum Fit

To compute a local continuum over the line band of interest, we first calculate a 5 σ-clipped average of the observed fluxes over the (blue and red) sidebands corresponding to each feature, as listed in Table A.1. Using these two points, a linear interpolation is

carried out over the region between the end point of the blue sideband and the starting point of the red sideband. This linearly interpolated flux is then connected piecewise with the fluxes of the red and blue sidebands, and a robust line fit is performed over the entire region of the blue sideband + line band + red sideband to derive the final local continuum estimate.

3.3.2 Measurement of Line Indices

Line indices (or equivalent widths) are calculated by integrating a continuum-normalized flux over the specified wavelength regions of each line band. Two different measurements of line indices, obtained from the two different continuum methods described above, are reported, even though the line-index based methods for stellar parameter estimates only make use of the local continuum-based indices. In order to avoid spurious values for the derived indices, if a given index measurement is greater than 100 Å, or is negative, we set the reported value to -9.999. No parameter estimates based on that particular line index are used.

Table A.1 lists the complete set of line indices made use of by the SSPP. Note that, unlike the case for most of the features in this table, the line indices listed in rows 74 (TiO1), 75 (TiO2), 76 (TiO3), 77 (TiO4), 78 (TiO5), 79 (CaH1), 80 (CaH2), 81 (CaH3), 82 (CaOH), and 83 (Hα), are calculated following the prescription given by the "Hammer" program (Covey et al. 2007). The line index for Ca I at 4227 Å, and the Mg I*b* and MgH features around 5170 Å, are computed following Morrison et al. (2003), so that they might be used to estimate $\log g$, as described in Chapter 3.4.

We follow the Cayrel (1988) procedure to compute an error for each line index measurement. The uncertainty (EW_{error}) in the index or measured equivalent width is:

$$EW_{error} = \frac{1.6 \times (resolution \times pixel\ size)^{1/2}}{SNR}, \tag{3.1}$$

where SNR is the signal-to-noise ratio in the local region of the spectrum, the *resolution* is taken to be $\sim$ 2.5 Å, and the *pixel size* is set to 1 Å for the blue region (3800−6000 Å), and 1.5 Å for the red region (6000−9000 Å), respectively. The noise spectrum provided by the SDSS spectroscopic reduction procedure is used to compute the local SNR.

3.4 METHODOLOGY

The SSPP employs a number of methods for estimation of effective temperature, surface gravity, and metallicity, based on SDSS spectroscopy and photometry. In this section the methods used by the SSPP are summarized. Since many of the methods implemented in the SSPP are already described by previously published papers, we will address those techniques briefly, and refer the reader to individual papers for detailed descriptions. The methods that are introduced here for the first time are explained in more detail. Note that some approaches derive all three atmospheric parameters simultaneously, while others are specific to an individual parameter. A given method is usually optimal over specific ranges of color, $g-r$, and S/N. Table 3.3 lists the ranges we have adopted in these observables for the SSPP. Details regarding the choice of the S/N cuts are presented in Chapter 3.6.

3.4.1 SPECTRAL FITTING WITH THE `k24` AND `ki13` GRIDS

These two methods are based on the identification of parameters for a model atmosphere that best matches the observed fluxes in a selected wavelength interval, as described in detail by Allende Prieto et al. (2006). Classical LTE line-blanketed model atmospheres are used to compute a discrete grid of fluxes; interpolation allows sub-grid resolution. The search is performed using the Nelder-Mead algorithm (Nelder & Mead 1965).

Table 3.3: Valid Ranges of $g - r$ and S/N for Individual Methods in the SSPP[c]

$T_{\rm eff}$			$\log g$			[Fe/H]			S/N	Reference
Name	Method	$g-r$	Name	Method	$g-r$	Name	Method	$g-r$		
T1	ki13	0.0 – 0.8	G1	ki13	0.0 – 0.8	M1	ki13	0.0 – 0.8	≥ 15	Chapter 3.4.1
T2	k24	0.0 – 0.8	G2	k24	0.0 – 0.8	M2	k24	0.0 – 0.8	≥ 15	Allende Prieto et al. (2006)
T3	WBG	−0.3 – 0.8	G3	WBG	−0.3 – 0.8	M3	WBG	−0.3 – 0.8	≥ 10	Wilhelm et al. (1999)
T4	ANNSR	−0.3 – 0.8	G4	ANNSR	−0.3 – 0.8	M4	ANNSR	−0.3 – 0.8	≥ 20	Chapter 3.4.3
T5	ANNRR	−0.3 – 1.2	G5	ANNRR	−0.3 – 1.2	M5	ANNRR	−0.3 – 1.2	≥ 10	Re Fiorentin et al. (2007)
T6	NGS1	−0.3 – 1.3	G6	NGS1	−0.3 – 1.3	M6	NGS1	−0.3 – 1.3	≥ 15	Chapter 3.4.4
...	.....	.....	G7	NGS2	0.0 – 1.3	M7	NGS2	0.0 – 1.3	≥ 20	Chapter 3.4.4
...	.....	.....	G8	CaI1	−0.3 – 0.8	M8	CaIIK1	−0.3 – 0.8	≥ 10	Chapter 3.4.5
...	.....	.....	...	.....	0.4 – 0.9	M9	CaIIK2	0.1 – 0.8	≥ 10	Beers et al. (1999)
...	.....	.....	...	.....	0.4 – 0.9	M10	CaIIK3	0.1 – 0.8	≥ 10	Chapter 3.4.6
...	.....	.....	...	.....	.....	M11	ACF	0.1 – 0.9	≥ 15	Beers et al. (1999)
...	.....	.....	...	.....	.....	M12	CaIIT	0.1 – 0.7	≥ 20	Cenarro et al. (2001a, b)
...	.....	.....	G9	CaI2	0.4 – 0.9	...	.....	.....	≥ 10	Morrison et al. (2003)
...	.....	.....	G10	MgH	0.4 – 0.9	...	.....	.....	≥ 10	Morrison et al. (2003)
T7	HA24	0.0 – 0.8	...	.....	.....	...	.....	.....	≥ 10	Chapter 3.5.1

Table 3.3: Valid Ranges of $g-r$ and S/N for Individual Methods (continued)

$T_{\rm eff}$			$\log g$			[Fe/H]			S/N	Reference
Name	Method	$g-r$	Name	Method	$g-r$	Name	Method	$g-r$		
T8	HD24	0.0 – 0.6	...	.....	.....	...	.....	.....	≥ 10	Chapter 3.5.1
T9	T_K	−0.3 – 1.3	...	.....	.....	...	.....	.....	N/A	Chapter 3.5.1
T10	T_G	−0.3 – 1.3	...	.....	.....	...	.....	.....	N/A	Chapter 3.5.1
T11	T_I	−0.3 – 1.3	...	.....	.....	...	.....	.....	N/A	Ivezić et al. (2008)

[c] HA24 and HD24 are the temperature estimates from the Hα and Hδ line indices in 24 Åwidths, respectively. The temperature estimated from Kurucz models is referred to as T_K; T_G is for the Girardi et al. (2004) isochrones. T_I is the temperature determined from equation 3.8. The S/N cut is not applied to these temperature estimates because they are computed based on the $g-r$ color. The ki13, k24, NGS1, and NGS2 are grid-matching based methods. WBG is the method from Wilhelm, Beers, & Gray (1999). ANNSR and ANNRR are the neural network approaches. CaIIK1 and CaI1 are determined from the 3850 – 4250 Å region. CaI2 and MgH are methods based on Morrison et al. (2003). CaIIK2 and CaIIK3 are the [Fe/H] estimates based on the Ca II K line. ACF is the Autocorrelation Function method, and CaIIT is based on the Ca II triplet line index. S/N is the average signal to noise ratio per pixel over the spectral region 4000–8000 Å. See Chapter 3.4 and 3.5 for detailed descriptions of individual methods and Chapter 3.6 for the S/N cuts. The nominal ('n') flag is raised for parameters which are based on spectra that satisfy at least some of the criteria listed above. However, for spectra with $5/1 \leq S/N < 10/1$, which would usually be rejected by strict application of the cuts above, the parameters are reported with the 'P' flag raised. No parameters are reported for spectra with $S/N < 5/1$, and the 'N' flag is raised.

The **k24** grid described by Allende Prieto et al. (2006) is used by the SSPP. It includes a predicted broadband color index $g-r$, as well as normalized spectral fluxes in the region 4400−5500 Å, at a resolving power of $R = 1000$. Kurucz (1993) model atmospheres and simplified continuum opacities are used to calculate synthetic spectra. The synthetic broadband photometry was derived from the spectral energy distributions provided by Kurucz (1993), using the passbands for point sources determined by Strauss & Gunn (2001), and an assumed (average) airmass of 1.3.

In addition to the **k24** grid, a second grid, referred to as **ki13**, is implemented in the SSPP. This second grid covers the same spectral window as the **k24**, but no photometry is considered. The use of only the normalized spectra de-couples the results based on this grid from reddening and photometric errors, although valuable information, mainly on the effective temperature, is sacrificed.

There are several other differences between the **k24** and **ki13** grids. The new grid (**ki13**) includes molecular line opacities, with the most relevant molecules in the range of interest being the CH G-band near 4300 Å, as well as the MgH band. In addition, the **ki13** grid takes advantage of a novel concept that allows for a significant increase in the speed of the calculation of model fluxes. The relevant opacities are not calculated for all depths in all models, but instead are obtained on a temperature and density grid, and later interpolated to the exact points in any given model atmosphere (Koesterke et al. 2008). The opacity grid includes 4 points per decade in density and steps of 125 K in temperature. With these choices, linear interpolation leads to errors in the normalized fluxes smaller than 1%.

Allende Prieto et al. (2006) made use of several libraries of observed spectra and atmospheric parameters to study systematic and random errors obtained from the **k24** analysis. Even at infinite signal-to-noise ratios, random errors appear significantly larger than systematic errors, and amount to 3% in $T_{\rm eff}$, 0.3 dex in $\log g$, and 0.2 dex in [Fe/H]. This is most likely the result of using over-simplified model fluxes

with a solar-scaled abundance pattern (including an enhancement of the α elements at low iron abundance), which is too limited to account for the chemical spread in real stars. The new `ki13` grid offers a significant improvement in random errors, which at high signal-to-noise amount to 2% in $T_{\rm eff}$, 0.2 dex in $\log g$, and 0.1 dex in [Fe/H], but a less robust behavior (due to the lack of color information) at low signal-to-noise ratios. Small systematic offsets in `ki13` detected from the analysis of the spectra in the ELODIE library (Prugniel & Soubiran 2001) are corrected using linear transformations.

As discussed in Allende Prieto et al. (2006), the `k24` approach performs best in the color range of roughly $0.0 \leq g - r \leq 0.8$; this range is also applied to the `ki13` grid. When it is run, the SSPP restricts the adopted parameters from these methods to fall in this color range. The SSPP refers to the $T_{\rm eff}$, $\log g$, and [Fe/H] estimated with the `ki13` grid as T1, G1, and M1, respectively, while the parameters estimated from the `k24` grid are referred to as T2, G2, and M2, respectively.

3.4.2 Parameters Obtained from the Wilhelm et al. (1999) Procedures : `WBG`

This method, which is referred to as `WBG` in this thesis, is based on the routines described by Wilhelm, Beers, & Gray (1999), to which we refer the interested reader. Extensions of this method, as used in the SSPP, are described below.

The procedures implemented in the SSPP are optimized for two separate temperature ranges, one for the warmer stars ($g - r \leq 0.25$), and one for the cooler stars, with redder colors than this limit. The stellar parameter determinations make use of comparisons to theoretical ugr colors and line parameters from synthetic spectra, both generated from ATLAS9 model atmospheres (Kurucz 1993). The synthetic spectra used in these procedures were generated using the spectral synthesis routine SPECTRUM (Gray & Corbally 1994).

For the hotter stars, the Balmer lines of the observed normalized spectra are fit with a Voigt profile to determine the Balmer-line equivalent widths and the $D_{0.2}$ (the line width at 20% below the local pseudo-continuum level) widths for Hδ, Hγ, and Hβ. The combination of Balmer-line equivalent widths, $D_{0.2}$, and $u-g$ and $g-r$ colors are used to establish initial $T_{\rm eff}$ and log g estimates, computed from functional trends in the theoretical model parameters. For stars cooler than $T_{\rm eff} \sim 8000$ K, the surface gravity is mainly determined by the $u-g$ color. For hotter stars the surface gravity is primarily determined by the $D_{0.2}$ parameter. A metallicity estimate is determined through the use of a combination of the equivalent width of the Ca II K line and a comparison to synthetic spectral regions that contain other (much weaker) metallic lines. Once an initial abundance is established, the procedure is iterated to convergence in all three stellar parameters.

For the cooler stars, only the $g-r$ color is used to establish an initial estimate of $T_{\rm eff}$. For these stars, log g is determined from the $u-g$ color for stars as cool as $T_{\rm eff} = 5750$ K. For stars cooler than this limit, the strength of MgH is compared to synthetic spectra of similar $T_{\rm eff}$ and [Fe/H] through the use of a band-strength indicator. The metal abundance is determined by the combination of the Ca II K line strength and a minimum χ^2 comparison to metallic-line regions in the spectra. The procedure is then iterated to convergence.

For stars with $S/N \geq 10/1$, the derived errors for the `WBG` approach are on the order of $\sigma(T_{\rm eff}) = 225$ K, $\sigma(\log\ g) = 0.25$ dex, and $\sigma([{\rm Fe/H}]) = 0.3$ dex. The color range of $g-r$ over which this approach is used for the SSPP is $-0.3 \leq g-r \leq 0.8$. The effective temperature, surface gravity, and [Fe/H] estimated from this technique are referred to as T3, G3, and M3, respectively.

3.4.3 The Neural Network Approaches : ANNRR and ANNSR

The SSPP implements flexible methods of regression that provide a global non-linear mapping between a set of inputs (the stellar spectrum $\mathbf{x}_i$) and a set of outputs (the stellar atmospheric parameters, $\mathbf{s} = \{T_{\rm eff}, \log\ g, [{\rm Fe/H}]\}$). These methods have been described in detail by Re Fiorentin et al. (2007), to which the interested reader is referred for more details.

For the present application, it should be noted that we have chosen not to include input photometry, although this certainly could be added if desired. Moreover, thanks to improved stellar models and data calibrations the models have been further developed in order to investigate the impact of noise and to extend the application of neural networks for low signal-to-noise spectra (P. Re Fiorentin et al., in preparation).

The procedures implemented in the SSPP use an initial Principal Component Analysis compression of the data, and are based on two different approaches – training the model on real (RR, e.g., SDSS spectra) or synthetic (SR) spectra to obtain atmospheric parameter estimates for the observed spectra. The method for training the model on the SDSS/SEGUE spectra is called **ANNRR**, while that for the synthetic spectra is referred to as **ANNSR**.

A. The ANNRR Approach

We build the models based on a set of 61,069 selected stars from the current SEGUE plug-plates, in directions of low reddening, for which have had atmospheric parameters estimated by a preliminary version of the SSPP.

The RR regression model (**ANNRR**) adopts a sample that is randomly split into two equal-sized sets, one for training and one for evaluation. Although not optimal, as one would ideally like to use a completely independent basis set for the training, this approach automates and – more importantly – generalizes the basis parameterizer. Indeed, the basis parameterizer may even comprise multiple algorithms, perhaps

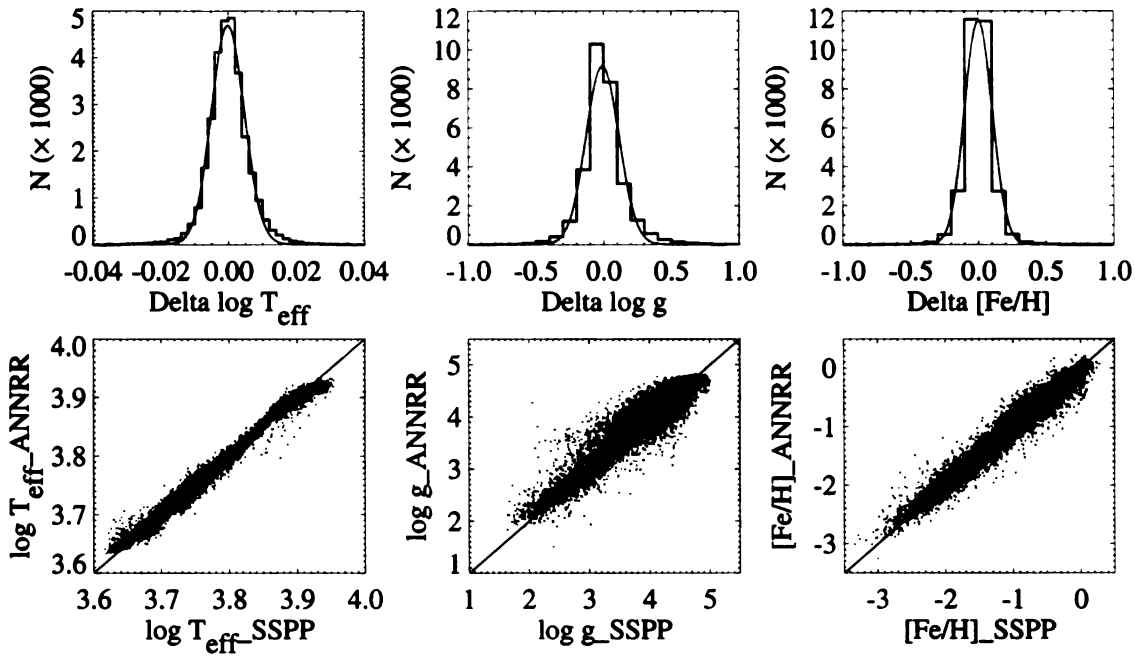


Figure 3.3 Atmospheric parameter estimation with **ANNRR**. We compare log $T_{\rm eff}$, log g, and [Fe/H] estimates from **ANNRR** with those from the SSPP. There are 30,000 stars compared for the **ANNRR** approach. Perfect correlation is shown with the solid red lines. The histograms of the discrepancies between the **ANNRR** approaches and the SSPP are shown in the first and third sets of panels, with a Gaussian fit shown as a red curve.

operating over different parameter ranges or used in a voting system to estimate atmospheric parameters. This is true in the present case, where the basis parameterizer comes from a preliminary version of the SSPP.

Figure 3.3 compares the stellar parameters obtained from the **ANNRR** approach with those from an earlier version of the SSPP adopted parameters, based on an evaluation set of some 30,000 SEGUE spectra. Overall we see good consistency, especially for stars with $T_{\rm eff} < 8000$ K (log $T_{\rm eff} = 3.90$). Above this effective temperature our models slightly underestimate log $T_{\rm eff}$ relative to the SSPP adopted values. Most regression models such as ours are designed to interpolate, rather than extrapolate. Extrapolation of the model to estimate atmospheric parameters that are not spanned by the training set is relatively unconstrained. Furthermore, the accuracy of the

RR model is limited by the accuracy of the target atmospheric parameters used in training, as well as their consistency across the parameter space. In this case, the SSPP estimates are combinations from several estimation models, each of which operates only over a limited parameter range. Thus, the transition we see above 8000 K may indicate a temperature region where one of the SSPP sub-models is dominating the SSPP estimates; such cases are not well generalized by our model. From this comparison, we find that the accuracies of our predictions (mean absolute errors) for each parameter are $\sigma(T_{\rm eff}) = 60$ K, $\sigma(\log g) = 0.11$ dex, and $\sigma([{\rm Fe/H}]) = 0.07$ dex, which are very low. This is partly due to the fact that the **ANNRR** method makes use of exactly the same type of data used in the training and application phases, thus eliminating the issue of discrepancies in the flux calibration or cosmic variance of the two samples.

B. The ANNSR Approach

Recently, an adequate noise model for SDSS spectra has been developed (see Chapter 3.6 for details). The SR regression model (**ANNSR**) adopts a sample of these noise-added synthetic spectra as the training set. This approach thus directly models the mapping between synthetic spectra and the atmospheric parameters, independent of any intermediate estimates. The **ANNSR** method is optimized to be able to deal separately with low S/N real spectra ($S/N < 35/1$, 22,196 stars) and high S/N real spectra ($S/N > 35/1$, 38,873 stars).

Figure 3.4 compares the atmospheric parameter estimates from the **ANNSR** with those from the SSPP for the 61,069 stars in the evaluation set. While the overall consistency between the two models is reasonably good, we notice discrepancies at the extreme parameter values, in particular for $T_{\rm eff}$ and log g.

Despite the fact that determinations of gravity and metallicity for low S/N spectra are underestimated, as measured by their mean accuracies with respect to the SSPP

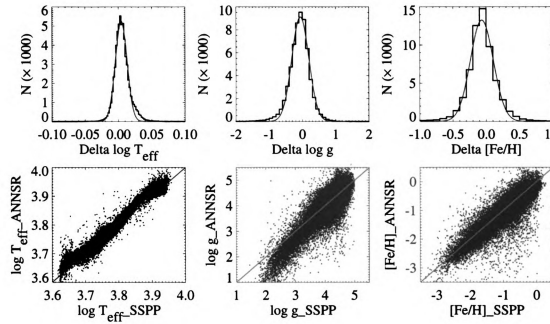


Figure 3.4 Atmospheric parameter estimation with **ANNSR**. We compare log $T_{\rm eff}$, log g, and [Fe/H] estimates from **ANNSR** with those from the SSPP. There are 61,069 stars compared for the **ANNSR** approach. Perfect correlation is shown with the solid red lines. The histograms of the discrepancies between the **ANNSR** approaches and the SSPP are shown in the first and third sets of panels, with a Gaussian fit shown as a red curve.

predictions, we can obtain estimates of $T_{\rm eff}$ with residuals of $\sim$ 125/129 K, log g with residuals of 0.21/0.28 dex, and [Fe/H] with residuals of 0.14/0.23 dex for the high/low S/N regimes, respectively. The reliability of the neural network approaches included in the SSPP is currently limited to $S/N \geq 10/1$.

The advantage of the **ANNSR** approach is that it is trained directly on synthetic spectra, dispensing with the need for a basis parameterizer. A very important aspect of this method is processing the synthetic and real data to appear as similar as possible; noise acts as a regularizer in the training phase. Inaccurate synthetic spectra (e.g., poor models or a poor flux calibration) degrade performance and/or give rise to systematic errors. However, there are inevitably problems with spectral mismatches, in the sense that the synthetic spectra do not reproduce all of the complexities of the

spectra of real stars. The absence of some molecular species in the linelists for the synthetic spectra may also be contributing to this problem, especially for cooler stars where they are expected to become more important.

Prior experience with the behavior of the neural network approach on the SDSS-I/SEGUE data indicated that the **ANNRR** performs well over a color range $-0.3 \leq g - r \leq 1.2$, so we restrict its application for the SSPP to this interval. The color range is restricted to $-0.3 \leq g - r \leq 0.8$ for the **ANNSR** estimates. The $T_{\rm eff}$, log g, and [Fe/H] obtained from the **ANNSR** approach are referred to as T4, G4, and M4, respectively; for the **ANNRR** approach, they are referred to as T5, G5, and M5, respectively.

3.4.4 The χ^2 Minimization Technique Using the NGS1 and NGS2 Grids

A. Grids of Synthetic Spectra

We have made use of Kurucz's NEWODF models (Castelli & Kurucz 2003), which employ solar relative abundances from Grevesse & Sauval (1998), to generate two sets of grids of synthetic spectra. The model atmospheres assume plane-parallel line-blanketed model structures in one-dimensional local thermodynamical equilibrium (LTE), and an enhancement of α-element abundances by +0.4 dex for stars with [Fe/H] ≤ -1.0 and +0.3, +0.2, and +0.1 for [Fe/H] $= -0.75$, -0.5, and -0.25, respectively. These new models include H_2O opacities, an improved set of TiO lines, and no convective overshoot (Castelli, Gratton, & Kurucz 1997).

For production of the synthetic spectra we employed the **turbospectrum** synthesis code (Alvarez & Plez 1998), with solar abundances from Asplund, Grevesse & Sauval (2005), which use the treatment of line broadening described by Barklem & O'Mara (1998). The sources of atomic lines used by **turbospectrum** mainly come from the VALD database (Kupka et al. 1999). Linelists for the molecular species CH, CN, OH,

TiO, and CaH are provided by B. Plez (see Plez & Cohen 2005, and Plez, private communication), while the lines of NH, MgH, and the C_2 molecules are adopted from the Kurucz line lists (see http://kurucz.harvard.edu/LINELISTS/LINESMOL/). The grid of the synthetic spectra has resolution of 0.01 Å or 0.005 Å, and spans from 3500 K $\leq T_{\rm eff} \leq$ 10,000 K in steps of 250 K, $0.0 \leq \log g \leq 5.0$ in steps of 0.25 dex, and $-4.0 \leq$ [Fe/H] $\leq +0.5$ in steps of 0.25 dex. The wavelength coverage is from 3000 Å to 10,000 Å. The micro-turbulence was assumed to be 2 km s^{-1}. These synthetic spectra are referred to as the `NGS1` grid. After their generation, these synthetic spectra were degraded to $R = 1000$, using a Gaussian convolution algorithm, then sampled into 1.67 Å per pixel for application of the `NGS1` grid spectral matching technique described below. There are two reasons for the degradation of the spectra to the lower resolution than that of the SDSS spectra. First, degrading the observed spectrum allows us to obtain higher S/N than the original; more reliable estimates of the parameters can thus be determined. Secondly, this grid is also used for application of the SSPP to non-SDSS spectra with lower resolution ($1000 \leq R \leq 2000$; e.g., Beers et al. 2007).

A second grid of model atmospheres was constructed from the Kurucz ATLAS9 models (Castelli & Kurucz 2003), which do not employ α-element enhancements for models with [Fe/H] ≤ -0.5. The `turbospectrum` synthesis code was again used to generate the synthetic spectra. The synthetic spectra have a resolution of 0.1 Å, and cover 4000 K $\leq T_{\rm eff} \leq$ 8000 K in steps of 250 K, $0.0 \leq \log g \leq 5.0$ in steps of 0.25 dex, and $-3.0 \leq$ [Fe/H] $\leq +0.5$ in steps of 0.25 dex. Ranges in [α/Fe] were introduced for spectral synthesis, over $-0.2 \leq$ [α/Fe] $\leq +0.8$, in steps of 0.2 dex for each value of $T_{\rm eff}$, log g, and [Fe/H]. The spectral range of this grid is 4500−5500 Å. The micro-turbulence was assumed to be 2 km s^{-1}. These synthetic spectra are referred to as the `NGS2` grid. This grid is smoothed to the resolution of the SDSS spectrographs ($R = 2000$); in contrast to the `NGS1` grid, this grid is not degraded to a

lower resolution. We retain the full resolution of this grid to enable the development of (future) methods for the determination of [α/Fe] for stars in the range 4000 K $\leq T_{\rm eff} \leq$ 8000 K (See Chapter 5.3). Since this is an independent grid, it is also possible to obtain another set of predicted stellar atmospheric parameters for the stars within this temperature range.

B. Pre-processing Observed Spectra for the χ^2 Minimization Technique

The observed SDSS spectra are processed as described in Chapter 3.3 above. The blue region of the spectrum contains most of the information required to constrain the stellar parameters, but for cooler stars, the observed signal-to-noise ratio peaks in the red region. As a compromise, and in order to speed up the analysis, we only consider the spectral range 4500$-$5500 Å. For the `NGS2` grid, we sample the spectrum into 1 Å bins; 1.67 Å bins are used for the `NGS1` grid, after degrading to $R = 1000$.

The spectrum under consideration is normalized after obtaining a pseudo-continuum over the 4500$-$5500 Å range. The continuum fit is carried out in a similar fashion to that described in §3, but iteratively rejecting the points which lie 1σ below and 4 σ above the fitted function, obtained from a ninth-order polynomial. The synthetic spectra used to match with the observed spectra are also normalized in the same fashion over the same wavelength range.

C. The Parameter Search Technique

Following the above steps, we next carry out a search for the best-fit model parameters, i.e., those that minimize the difference between the observed flux vector, O, and the synthetic flux vector, S, as functions of $T_{\rm eff}$, log g, and [Fe/H], using a reduced χ^2 criterion. That is,

$$\chi^2/DOF = \sum_{i=1}^{m+1} (O_i - S_i)^2/\sigma_i^2, \tag{3.2}$$

where σ_i is the error in flux in the ith pixel and DOF is the number of degrees of freedom.

To reduce the number of model spectra that must be considered in the calculation of the the reduced χ^2 values, we first obtain an approximate effective temperature based on a simple approach. This procedure, which we refer to as the Half Power Point (HPP) method (Wisotzki et al. 2000), obtains an estimate of the wavelength at which the total integrated flux over a spectrum is equal to half of the flux obtained over the entire wavelength region (in this case we use 3900−8000 Å). Since the flux distribution for a given stellar spectrum varies strongly with effective temperature, once we have determined the HPP wavelength, we are able to obtain a reasonably accurate estimate of effective temperature (or a broadband color such as $g - r$) by comparing with the HPP wavelengths obtained from a grid of synthetic spectra. The relation between effective temperature and HPP wavelength is established by fitting a polynomial:

$$T_{\rm eff} = (25.63 - 114.51 \cdot {\rm HPP} + 177.17 \cdot {\rm HPP}^2 - 93.55 \cdot {\rm HPP}^3) \times 10,000 \text{ K}, \quad (3.3)$$

where HPP $= \lambda/10{,}000$.

We initially select synthetic spectra over a broad range around this predicted effective temperature, within ±1500 K. For example, if the HPP predicted temperature of a star is 5000 K, we consider models between 3500 K and 6500 K. As long as the observed spectrum doesn't have a grossly incorrect spectrophotometric calibration, the estimated temperature will be well within this range. We then obtain the reduced χ^2 values between the observed and the selected synthetic spectra over a 4500−5500 Å wavelength window.

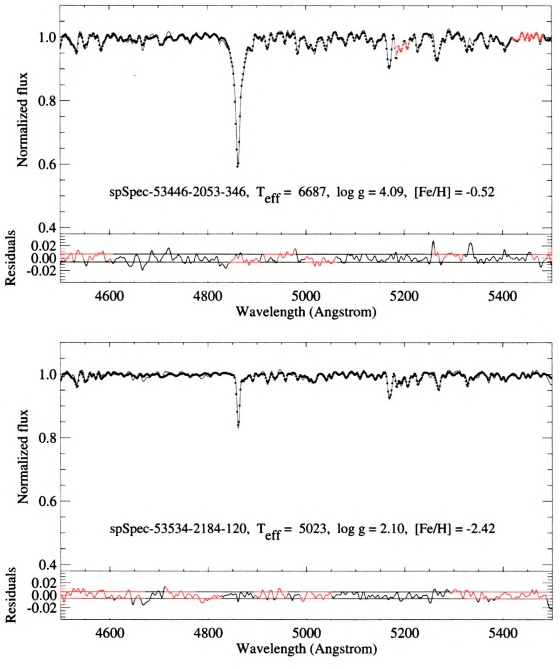


Figure 3.5 Two examples of the results of the application of the `NGS1` grid, for a warmer, metal-rich star (top panel), and for a cooler, metal-poor star (bottom panel). The black dots are the observed data points; the red lines are synthetic spectra generated with the atmospheric parameters adopted by the technique. The residuals between the observed and synthetic spectrum are also plotted at the bottom of each panel, with superposed red lines representing the one-sigma deviations of the residuals.

After trying out several function minimization techniques (e.g., Nelder & Mead 1965), we found that a simple biweight average of several dozen of the lowest reduced χ^2 values is sufficiently fast for computation in the IDL code used in the SSPP, and predicts the stellar parameters with the desired accuracy ($\leq$ 0.30 dex in [Fe/H]), thanks to the dense grid of the synthetic spectra employed. It also returns a robust estimate of the parameters for lower S/N ($< 20/1$) spectra.

Note, however, that whereas the values of reduced χ^2 respond sensitively to small changes in $T_{\rm eff}$ and [Fe/H], allowing for their optimal determinations, variations in the log g values do not strongly impact the reduced χ^2, due to a lack of gravity-sensitive lines in the spectral window we examine. This leads to potentially large errors in the estimated log g. This effect also appears in the function minimization techniques (e.g., Allende Prieto et al. 2006). We obtain a biweight average of the lowest 20 points of the reduced χ^2 values for the `NGS1` grid, and 50 points for the `NGS2` grid; the larger number of points included for the `NGS2` grid is to accommodate the addition of an α-abundance parameter.

Figure 3.5 shows two examples of synthetic spectra (red lines) with parameters set to those estimated by the procedure described above, over-plotted on the observed spectral data (black dots). The upper panel is for a warm, metal-rich main-sequence turn-off star; a cool metal-poor giant is shown in the bottom panel. The residuals between the observed and the synthetic spectrum are plotted at the bottom of each panel; superposed red lines show the standard deviation of the residuals to these fits.

D. Comparisons with Spectral Libraries and Analysis of High-Resolution SDSS-I/SEGUE Stars

In order to validate that the `NGS1` and `NGS2` grid approaches perform well in determining stellar parameter estimates, we compare the results from these techniques with literature values from two spectral libraries: ELODIE (Prugniel & Soubiran

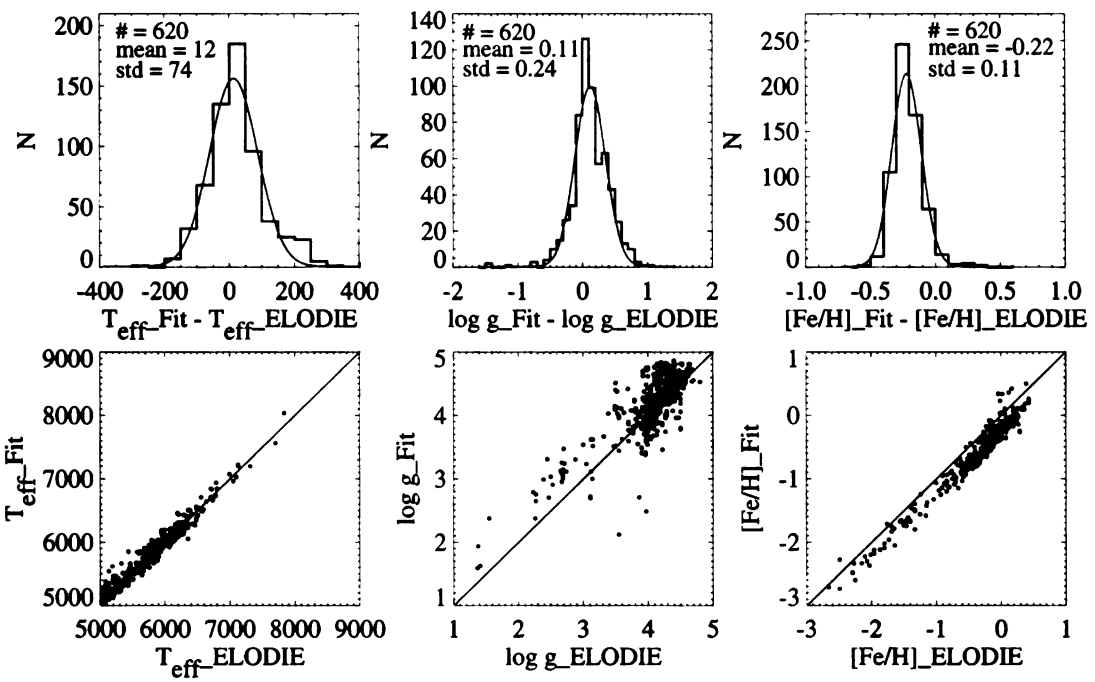


Figure 3.6 Comparison of parameters obtained from the NGS1 grid (Fit) with those from the ELODIE spectral library (ELODIE). The temperatures agree very well, while the surface gravity is over-estimated by +0.11 dex. The metallicity is under-estimated by −0.22 dex, but with a very small scatter, based on Gaussian fits to the residuals.

2001; Moultaka et al. 2004) and MILES (Sánchez-Blázquez et al. 2006), as well as with parameter estimates from an analysis of the SDSS-I/SEGUE stars with available high-resolution spectroscopy.

D.1 Validation from the ELODIE and MILES Spectral Libraries

The spectra in the ELODIE library were obtained with the ELODIE spectrograph at the Observatoire de Haute-Provence 1.93 m telescope, and cover the spectral region 4000−6800 Å. We employ 1969 spectra of 1390 stars with a resolving power R = 10,000, which are publicly available as part of the ELODIE 3 release (Moultaka et al. 2004). The spectra are first smoothed with a Gaussian kernel to match the SDSS resolution for the NGS2 grid and $R = 1000$ for the NGS1 grid, then are processed in the

same fashion as described in Chapter 3.4.4. Most of the spectra have quite high S/N ratios, and are accompanied with estimated stellar parameters from the literature. Each spectrum (and parameter estimate) has a quality flag ranging from 0 to 4, with 4 being best. In our comparison exercise, we only select stars with 4000 K $\leq T_{\rm eff} \leq$ 10,000 K with a quality flag ≥ 1 for the spectra and all of the parameters.

Our examination indicates that the `NGS1` grid approach works best in the range 5000 K $\leq T_{\rm eff} \leq$ 9000 K, and marginally well outside this range. Comparison plots between the literature values and the estimated parameters in this temperature range for 620 stars among the ELODIE spectral library are shown in Figure 3.6. A Gaussian fit to the residuals of each parameter reveals that the `NGS1` estimate of $T_{\rm eff}$ is very close to the ELODIE zero point (offset by only 12 K), with a scatter of only 74 K; the surface gravity is larger by 0.11 dex (σ = 0.24 dex); the metallicity is lower by 0.22 dex (σ = 0.11 dex), on average. For cooler stars, with 4000 K $\leq T_{\rm eff} \leq$ 5000 K, we find that $< \Delta(T_{\rm eff}) >$ and $< \Delta([{\rm Fe/H}]) >$ are 243 K (σ = 91 K) and 0.03 dex (σ = 0.17 dex), respectively, which are relatively small offsets and scatter, while the $< \Delta(\log g) >$ is 0.45 dex, with σ = 0.31 dex.

Because the spectra from the ELODIE library are of very high quality, one might wonder how the parameter estimates would compare for the lower S/N data included among the SDSS-I/SEGUE stars. In order to test this, we inject Gaussian noise into the ELODIE spectra to force them to S/N = 50/1, 25/1, 12.5/1, and 6.25/1 per pixel at 5000 Å, respectively, degrade them to R = 1000, and apply the same procedures as above for estimation of the stellar atmospheric parameters. These test spectra, and more detailed information on noise models can be found in ftp://hebe.as.utexas.edu/pub/callende/sdssim/. Table 3.4 lists the results of this exercise. Inspection of this table shows that, for $S/N \geq$ 12.5/1, the shifts and scatter in the determinations of the parameters remain acceptably small.

The MILES library includes 985 spectra obtained with the 2.5m INT and the

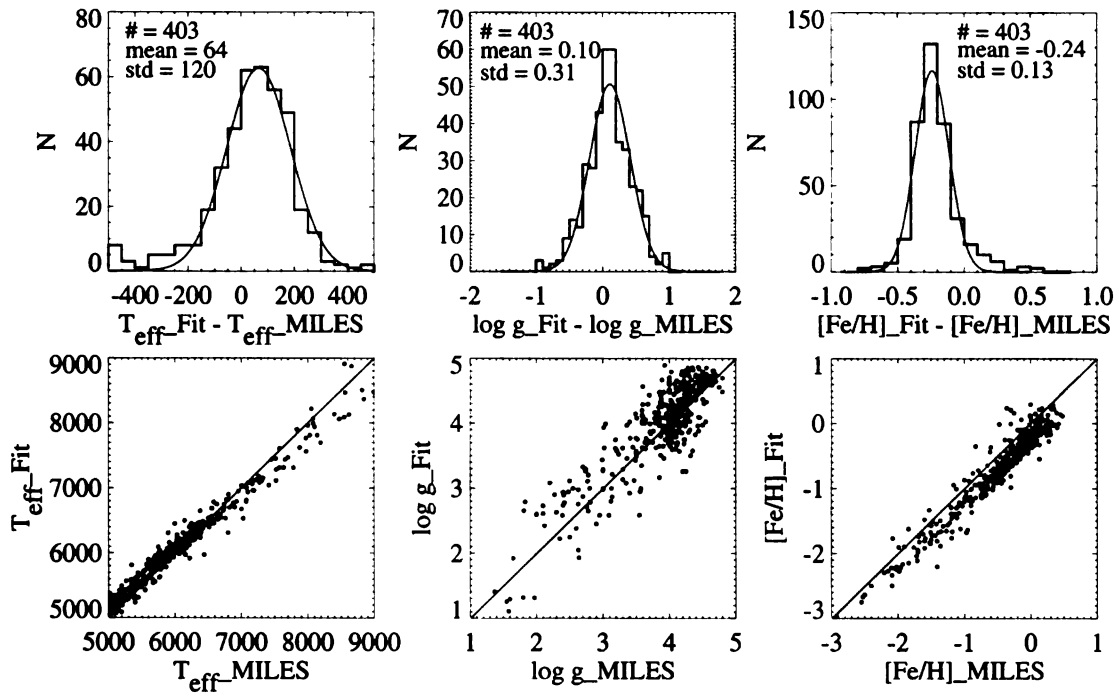


Figure 3.7 Comparison of parameters obtained from the `NGS1` grid (Fit) with those from the MILES spectral library (MILES). The temperature and surface gravity are over-estimated, by +64 K and +0.10 dex, respectively, while the metallicity is under-estimated by −0.24 dex, with a very small scatter, based on Gaussian fits to the residuals.

IDS spectrograph at La Palma. The wavelength coverage is 3530−7430 Å, and the resolution is $\sim$ 2.3 Å (Sánchez-Blázquez et al. 2006). We processed these spectra in the same manner as ELODIE to derive the stellar parameters from the `NGS1` and `NGS2` grids, but with no degradation of the spectra for the `NGS2` grid, since the resolution is similar to that of the SDSS spectra. After dropping the spectra with missing parameters, and outside the temperature range 5000 K $\leq T_{\rm eff} \leq$ 9000 K, 403 spectra remain. Figure 3.7 shows the comparison plots between the selected literature values and the parameters estimated from the `NGS1` procedure. It appears that the scatter of the temperature (σ = 120 K) and the gravity (σ = 0.31 dex) estimates are higher than those from the ELODIE spectral library comparison, while the metallicity estimate is in good agreement (σ = 0.17 dex), except for a small negative offset (−0.24 dex).

For the cooler stars, with 4000 K $\leq T_{\rm eff} \leq$ 5000 K, we obtain $< \Delta(T_{\rm eff}) > =$ 235 K with $\sigma =$ 130 K, $< \Delta([{\rm Fe/H}]) > = -0.10$ dex with $\sigma = 0.17$ dex, and $< \Delta(\log g) > = 0.45$ dex with $\sigma = 0.34$ dex.

Very similar behaviors were found for the comparison with the **NGS2** grid technique as for the **NGS1** grid technique, as listed in Table 3.4, which summarizes the offsets and scatter between the literature values and the estimated parameters for both synthetic grid approaches.

D.2 Validation from SDSS-I/SEGUE Stars with Available High-Resolution Spectra

As part of a long-term program to validate and improve estimates of stellar atmospheric parameters determined by the SSPP, over the past two years we have obtained higher resolution spectra for over 150 SDSS-I and SEGUE stars. The targets cover a wide range of temperature and metallicity, but somewhat less so in surface gravity. Existing "holes" in the parameter space will be given high priority for future high-resolution campaigns. The data have been independently reduced and analyzed by two authors (C.A. and T.S.) in Paper III; we refer to the analysis by C.A. as **HA1**, and to that by T.S. as **HA2**, For a detailed description of these analyses, the interested reader is referred to Paper III in this series. For simplicity of our present comparison, we adopt the values of stellar atmospheric parameters obtained by **HA1**, which consists of a homogeneous sample (observed with the same telescope and spectrograph) of stars used to derive the empirical error estimates for the atmospheric parameters determined by the SSPP.

Figure 3.8 shows a comparison between the parameters estimated from the **NGS1** grid approach and those determined from the **HA1** high-resolution analysis, over 5000 K $\leq T_{\rm eff} \leq$ 8000 K. As summarized in Table 3.4, the temperature and surface gravity estimates obtained from the **NGS1** result in offsets of +85 K ($\sigma =$ 164 K)

and +0.13 dex (σ = 0.30 dex), respectively, which are somewhat larger than for the two spectral libraries, However, the average metallicity offset (−0.24 dex) and scatter (0.16 dex) are very close to those obtained by comparison with the two libraries. A similar behavior can also be noticed for the NGS2 grid in Table 3.4.

Table 3.4: Comparison of Parameters from NGS1 and NGS2 Grids with ELODIE and MILES Libraries and High-Resolution Values[d]

				$T_{\rm eff}$		$\log g$		[Fe/H]	
Grid	Library	S/N	N	$<\Delta>$ (K)	σ (K)	$<\Delta>$ (dex)	σ (dex)	$<\Delta>$ (dex)	σ (dex)
NGS1									
	ELODIE	Full	620	+12	74	+0.11	0.24	−0.22	0.11
	ELODIE	50/1	617	+10	87	+0.09	0.25	−0.23	0.12
	ELODIE	25/1	617	+13	103	+0.09	0.28	−0.21	0.14
	ELODIE	12.5/1	601	+15	175	+0.13	0.37	−0.09	0.19
	ELODIE	6.25/1	541	+36	269	+0.25	0.50	+0.23	0.29
	MILES	Full	403	+64	120	+0.10	0.31	−0.24	0.13
	HR	Full	81	+85	164	+0.13	0.30	−0.24	0.16
NGS2									
	ELODIE	Full	615	...	...	+0.15	0.26	−0.22	0.13
	MILES	Full	385	...	...	+0.16	0.29	−0.24	0.15
	HR	Full	81	...	...	+0.17	0.29	−0.25	0.13

Considering the results from these three different comparisons for the NGS1 and NGS2 grids, a small systematic offset in our derived metallicity and gravity from these

[d]HR comes from the results of HA1 which is used, in Paper III, to determine empirical errors of the SSPP parameters.

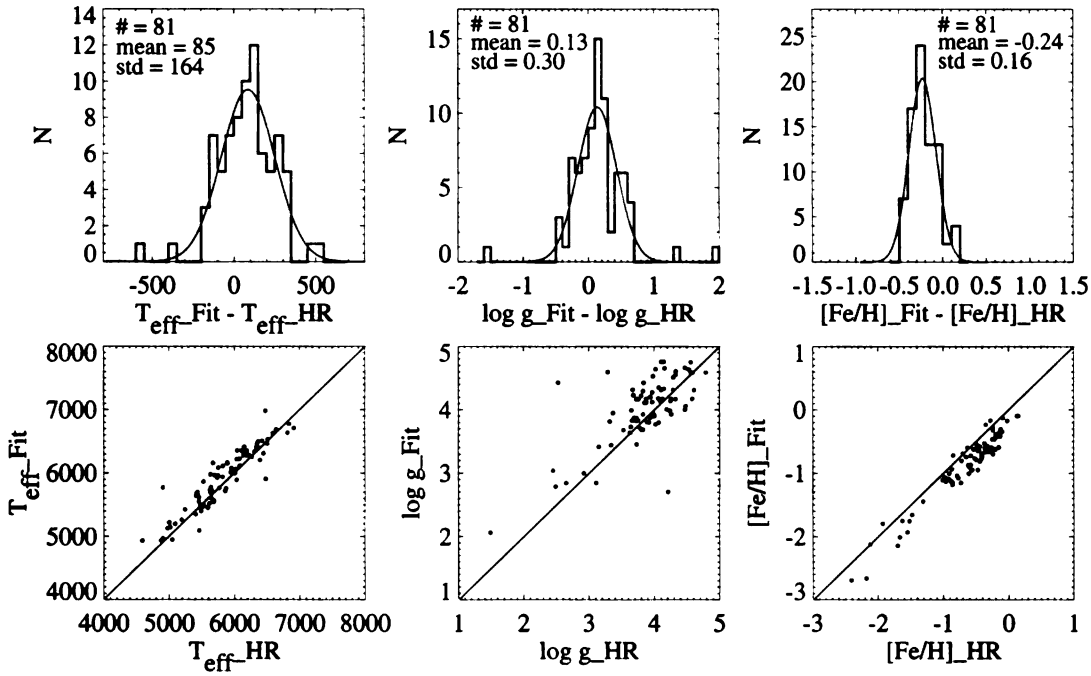


Figure 3.8 Comparison of parameters obtained from the **NGS1** grid (Fit) with one of the analyses of high-resolution spectroscopy of SDSS-I/SEGUE stars (HR). The parameters for the high-resolution data are the **HA1** results, which are used in Paper III to derive empirical errors of the SSPP parameters. The temperature exhibits a slightly higher offset than those from the comparisons with the ELODIE and MILES spectral libraries, but very similar offsets for the gravity and metallicity offsets.

two methods may exist. The slightly different offsets of the parameters between the two grids may come from the different resolutions employed. Therefore, we choose to adjust the offsets in log g by +0.11 dex and in [Fe/H] by −0.23 dex for the **NGS1** method, and +0.16 dex and −0.24 dex for the **NGS2** method, respectively, in order to place those two grids on the same abundance scale, on average, as the two external libraries and the high-resolution analysis results. The offsets represent averages of those from the ELODIE, MILES, and **HA1** comparisons.

The noise experiment summarized in Table 3.4, and another test (in Table 3.5, see Chapter 3.6 for details) indicate that a lower limit on S/N for obtaining useful parameter estimates from these two methods is, conservatively, $S/N \geq 15/1$ for the

NGS1 approach, and $S/N \geq 20/1$ for the NGS2 approach. The color ranges we adopt for these techniques are $-0.3 \leq g-r \leq 1.3$ for the NGS1 approach, and $0.0 \leq g-r \leq 1.3$ for the NGS2 approach. The $T_{\rm eff}$, log g, and [Fe/H] estimated from the NGS1 approach are designated as T6, G6, and M6, respectively, whereas the log g and [Fe/H] estimated from the NGS2 technique are referred to as G7 and M7, respectively. No independent estimate of $T_{\rm eff}$ is obtained from the NGS2 grid, as it is essentially degenerate with that determined from the NGS1 grid.

3.4.5 Metallicity and Gravity Estimates from 3850–4250 Å : CaIIK1 and CaI1

This method utilizes the NGS1 grid to estimate the metallicity and surface gravity, in a similar fashion as described in Chapter 3.4.4, but making use of a different wavelength window: 3850–4250 Å. Even though it covers a relatively short wavelength region, it is desirable for the determination of stellar parameters because it includes the Balmer lines as temperature indicators, the metallicity sensitive Ca II K and H lines, and the gravity sensitive Ca I (4226 Å) line. Comparisons with the results of the HA1 high-resolution analysis indicates an average zero-point offset in [Fe/H] of -0.06 dex, with a scatter of 0.25 dex, and an average zero-point offset in log g of $+0.05$ dex, and a scatter of 0.30 dex. The color range adopted for this approach is $-0.3 \leq g-r \leq 0.8$. The surface gravity and metallicity estimates obtained by this technique are referred to as G8 (CaI1) and M8 (CaIIK1), respectively.

3.4.6 The Ca II K and Auto-Correlation Function Methods : CaIIK2, CaIIK3, and ACF

A. Metallicity from CaIIK2 and CaIIK3

These methods are based on the procedures outlined by Beers et al. (1999), where the interested reader should look for more details. A brief summary follows.

The Ca II K method, which is designated as CaIIK2, makes use of a "band-switched" estimate of the pseudo-equivalent of the Ca II K line at 3933 Å, in combination with an estimate of a broadband color, to obtain a prediction of the [Fe/H] for a given star. The approach has been used for two decades during the course of the HK (Beers, Preston, & Shectman 1985, 1992) and the Hamburg/ESO objective prism surveys (Reimers & Wisotzki 1997; Christlieb 2003) for the determination of metallicities of stars with available medium-resolution (2–3 Å resolution, similar to the resolution of the SDSS spectra) follow-up spectroscopy. The original calibration is based on high-resolution abundance determinations (and $B-V$ colors) for a sample of $\sim$ 500 stars.

This method has been shown to perform well over a wide range of metallicities, in particular for stars with [Fe/H] < -1.0; external errors from the calibration indicate that it has an intrinsic error no greater than 0.15–0.20 dex in the color range $0.3 \leq B-V \leq 1.2$. Above [Fe/H] $= -1.0$, and in particular for cooler stars (below $T_{\rm eff} =$ 5000 K), the Ca II K line gradually begins to saturate. As a result, for cool, metal-rich stars, the method will generally return an estimate of [Fe/H] that is on the order of 0.5 dex too low. This is ameliorated somewhat by empirical corrections that are built into the program used to calculated this estimate, but it remains a source of concern. It is important to recognize that for stars with very low metallicities, and for warmer stars in particular, the Ca II K line is one of the few (in some cases only) metallic lines available in medium-resolution spectra. Hence, this estimator plays an

especially important role in such situations.

This method makes use of a broadband $B - V$ color, which we have to obtain by application of a transformation of the observed (or predicted, as discussed in Chapter 3.5.2) $g - r$ colors. In order to accomplish this task, we made use of several hundred stars with existing $B - V$ colors obtained during the course of the HK and Hamburg/ESO surveys that happened to fall in the SDSS footprint, and had available $g-r$ colors (note that only the fainter, non-saturated stars could be used). These stars covered a variety of metallicities, but in particular a large number of stars with [Fe/H] < -1.0 were included. An approximate transformation, suitable for low-metallicity stars, was obtained by Zhao & Newberg (2006); the transform $B - V = 0.187 + 0.916(g - r)$ was employed.

Comparison of the metallicities obtained from the `CaIIK2` method with those derived from the `HA1` high-resolution analysis, and for member stars of open and globular clusters with known [Fe/H], indicates that the [Fe/H] for stars with $g - r > 0.8$ are consistently underestimated (due to saturation of the Ca II K line).

As an alternative Ca II K-line approach, we have calibrated a new index, K24, which covers a broader region around the Ca II K line than the widest band considered for `CaIIK2`, and make use of the synthetic grids of predicted $g - r$ colors discussed above. Note that no "band switching" is used in this approach. A simplified neural network was designed to implement the prediction of [Fe/H] based on K24 and the synthetic $g - r$ color. As summarized in Table 3.9, this new calibration, which we refer to as `CaIIK3`, appears to exhibit similar (small) zero-point offsets and scatter as `CaIIK2` approach.

Due to concerns about the saturation of the Ca II K line for cooler stars, we consider only metallicities determined for stars using these two methods in the color range $0.1 \leq g - r \leq 0.8$. The parameters from these two approaches are referred to as M9 (`CaIIK2`) and M10 `CaIIK3`), respectively.

B. ACF

The auto-correlation function technique (ACF) was developed as an alternative method for metallicity estimation which should perform well at higher metallicities, where the Ca II K line-index techniques described above are limited by saturation. As described in Beers et al. (1999), and references therein, the method relies on an auto-correlation of a given stellar spectrum, which generates a correlation peak whose strength is proportional to the frequency and strength of weak metallic lines in a given spectrum. The more such lines exist, the stronger the signal.

The calibration from Beers et al. (2000) relied on a broadband $B - V$ color. Encouraged by our success with the re-calibration of the Ca II K approach to a (synthetic) native system $g - r$ color, we have designed a simple neural network that considers the auto-correlation function and the $g - r$ colors as inputs in order to predict [Fe/H].

The auto-correlation signal is expected to depend strongly on the signal-to-noise of a given spectrum, growing with decreasing S/N. In the low S/N limit ($\leq 10/1$), this function is responding to noise peaks rather than to the presence of metallic features. Our experiments with the sensitivity of abundance estimates on S/N (Chapter 3.6) reflects this expectation. As can be seen from Table 3.5, the ACF approach exhibits a reasonably small zero-point offset (+0.12 dex) and scatter (0.17 dex) at S/N levels as low as 15/1. We thus adopt this lower limit on S/N for determinations based on this method. The range of color adopted for application of this method is taken to be $0.1 \leq g - r \leq 0.9$. Blueward of this range, the auto-correlation signal becomes too weak to be useful. Note that this range extends slightly redder than the Ca II K line-index methods. The [Fe/H] estimate from the ACF approach is referred to as M11.

3.4.7 Calibration of a Ca II Triplet Estimator of Metallicity : CaIIT

The SDSS spectra extend to sufficiently red wavelengths to include the prominent Ca II triplet feature, which covers the spectral region 8400−8700 Å. These lines are known to be sensitive to both luminosity (surface gravity) as well as metallicity, so care must be exercised in their use as a metallicity indicator.

We have employed a line index that measures the integrated strength of these lines, corrected for the presence of the Paschen Series H lines, which also occur in this wavelength interval. The line index definition, and the calculation of the summed index, is as described by Cenarro et al. (2001a,b). In order to calibrate this index for use with SDSS spectra, we have taken the library of some 700 spectra (and their listed atmospheric parameters) given by Cenarro et al. (see http://www.ucm.es/info/Astrof/ellipt/CATRIPLET.html), rebinned the spectra to the SDSS spectral resolution, and calculated the corrected Ca II triplet index (which they refer to as CAT′. This index, along with their listed de-reddened value of the $B - V$ color, are used as inputs to an artificial neural network procedure in order to predict the estimated [Fe/H]. This procedure was able to reproduce the metallicity of the Cenarro et al. stars to within ±0.3 dex over the temperature range 4000 K to 8000 K, with some residual sensitivity to surface gravity. Clearly, the application of this approach would require a transform from $B - V$ to $g - r$, which we prefer to avoid.

Hence, we proceeded to test an approach that calibrated (with a simple neural network) the Cennaro et al. CAT′ index along with synthetic $g - r$ colors, both obtained from the synthetic spectra described above. This approach appears to work reasonably well, as demonstrated by inspection of the results shown in Table 3.9. The offsets and scatter obtained, relative to the high-resolution analyses, are quite competitive with other methods we have tested. However, it should be noted that the

predicted sensitivity of this method to S/N is, according to the summary in Table 3.5, apparently somewhat high; although the zero-point offsets remain small, the scatter appears large compared to other methods (0.3 to 0.5 dex, even at $S/N \geq 20/1$). The results in Table 3.5 are obtained from the application of noise models for SDSS spectra (see Chapter 3.6), and we suspect that these may be imperfect in the red regions, or at least over-aggressive, in the sense of injecting more noise than is typical for SDSS observations. We plan to investigate this behavior further in the near future.

The color range over which this estimate is employed by the SSPP is $0.1 \leq g-r \leq 0.7$. It may prove to be the case that we can set the red limit to larger values, once we understand the origin of the (apparently) large scatter obtained from the noise-injection test. For now, we set a conservative limit of $S/N \geq 20/1$ for application of this method. The [Fe/H] estimated from this method is referred to as M12 (`CaIIT`).

3.4.8 Calibration of a Gravity Estimator Based on the Ca I (4227 Å) and Mg I *b* and MgH Features : `CaI2` and `MgH`

Among the prominent metallic species in stellar spectra, the two that are most sensitive to surface gravity are the Ca I line at 4227 Å and the Mg I *b* and MgH features around 5170 Å. Both of these lines exhibit sensitivity to metallicity as well. We have adopted the line index measurements and quoted atmospheric estimates of [Fe/H] for the dwarfs and giants in the calibration sample of Morrison et al. (2003), which were measured at a similar spectral resolution to the SDSS (2.5–3.5 Å). Surface gravity estimates for the stars involved in this calibration were obtained from the compilation of Cayrel de Strobel (2001), while $B-V$ colors were obtained from the SIMBAD database.

These indices, along with their de-reddened $B-V$ colors and [Fe/H], are used as inputs to an artificial neural network procedure in order to predict the estimated

surface gravity log g. This procedure indicates that the prediction errors of the surface gravity, based on the Ca I and MgH indices are on the order of 0.35 dex and 0.30 dex, respectively. Small zero-point offsets, and similar levels of scatter, are indicated from the comparison with the high-resolution analyses in Table 3.9. Hence, we decided to proceed with these estimates (which require a color transform), rather than attempt a re-calibration to the synthetic spectra and colors.

As indicated by Morrison et al. (2003), these two methods are valid in the color range corresponding to $0.4 \leq g-r \leq 0.9$. The gravity estimated from Ca I is referred to G9 (`CaI2`), while that obtained from the MgH feature is referred to as G10 (`MgH`).

3.5 Empirical and Theoretical Predictions of $T_{\rm eff}$ and $g-r$ Color

3.5.1 Predictions of $T_{\rm eff}$

Effective temperatures predicted by the observed $g-r$ color, or through the strength of the Balmer lines, are sufficiently accurate to be considered as auxiliary estimators to those methods described in Chapter 3.4. We obtain two theoretical and three empirical temperature estimates during execution of the SSPP.

A. Theoretical $T_{\rm eff}$ Estimates : $\mathtt{T}_K$ and $\mathtt{T}_G$

Two theoretical temperature estimates are based on the `NGS1` grid of synthetic spectra generated using the Kurucz models described in Chapter 3.4, and by consideration of predicted colors from the Girardi et al. (2004) isochrones. For the temperatures based on Kurucz models ($\mathtt{T}_K$), we calculate an estimated $g-r$ color, adopting the SDSS filter and instrumental response functions (Strauss & Gunn 2001), then fit a fourth-order polynomial:

$$T_{\rm eff} = 7792.22 - 6586.18(g-r) - 4637.23(g-r)^2 - 1994.29(g-r)^3 - 386.24(g-r)^4 \quad (3.4)$$

In deriving the above relationship, we take into account stellar models with atmospheric parameters in the range $-2.0 \leq$ [Fe/H] ≤ -0.5 and $3.0 \leq \log g \leq 5.0$, where most SDSS-I/SEGUE stars are found. Stars at the extrema of these ranges will have less than ideal estimates of temperature, due to the sensitivity of $g-r$ color to either metallicity, surface gravity, or both. The effective temperature ($\mathtt{T}_K$) estimated from this relation is referred to as T9.

For the temperature estimates based on the Girardi et al. isochrones ($\mathtt{T}_G$), we assume that the stars are all older than 10 Gyrs, are moderately metal-poor (i.e., have metallicites in the range $-1.5 \leq$ [Fe/H] ≤ -0.5), and are subgiants or main-sequence stars, which is true for the great majority of the SDSS-I/SEGUE stars. The temperature relationship, based on a third-order polynomial, is:

$$T_{\rm eff} = 7590.26 - 6191.78(g-r) - 4270.92(g-r)^2 - 1225.12(g-r)^3 \quad (3.5)$$

This temperature estimate is referred to as T10.

B. Empirical $T_{\rm eff}$ Estimates : HA24, HD24, and $\mathtt{T}_I$

Two of the three empirical temperature estimates we employ are derived from the Balmer-line strengths, similar to the color estimates discussed above, but calibrated to the effective temperature estimates obtained from the methods discussed in §4. The temperatures estimated from the $HA24$ and $HD24$ indices, via the simple linear relationships below, are referred to as T7 (HA24) and T8 (HD24), respectively.

$$T_{\rm eff} = 4133 + 371 \cdot HA24 \tag{3.6}$$

$$T_{\rm eff} = 5449 + 206 \cdot HD24 \tag{3.7}$$

We restrict the regions over which the above relationships are applied to 1.0 Å $\leq$ $HA24 \leq$ 12.0 Å and 1.0 Å $\leq HD24 \leq$ 15.0 Å, respectively. If the $HA24$ index lies the validity range, we adopt $T_{\rm eff}$ estimate from $HA24$, and ignore the $HD24$ temperature estimate. If $HA24$ is out of range, we make use of the $HD24$ estimate of temperature.

The final empirical temperature estimate ($\mathtt{T}_I$) comes from the relationship between the effective temperature derived from a previous version of the SSPP and the observed $g-r$ color (Ivezić et al. 2008). The temperature estimated from the relationship below is referred to as T11:

$$\log\ T_{\rm eff} = 3.8820 - 0.3160(g-r) + 0.0488(g-r)^2 + 0.0283(g-r)^3. \tag{3.8}$$

It should be noted that $\mathtt{T}_K$, $\mathtt{T}_G$, and $\mathtt{T}_I$ are taken into account by the SSPP, provided that the color flag (see below) is not raised, and the expected temperature is beyond the region where the primary estimates derived from the techniques described in §4 apply. That is, they are used when the expected temperature is outside the range 4500 K $\leq T_{\rm eff} \leq$ 7500 K.

3.5.2 Predictions of $g-r$ Color

For a variety of reasons (e.g., nascent saturation, difficulties with de-blending of sources, high reddening, etc.), the SDSS PHOTO pipeline (Lupton et al. 2001) occasionally reports incorrect, or less-than-optimal, estimates of the broadband colors for a given target. Because several of the methods we employ in the SSPP require a good measurement of (at least) the $g-r$ color, it is useful to check if the reported $g-r$

color is commensurate with that predicted from the flux-calibrated spectrum of the source, or with the strength of spectral lines that correlate with effective temperature. This predicted color is used to raise a cautionary flag for stars with possibly incorrect reported colors, within some tolerance. We have developed three different methods to predict $g - r$ color in the SSPP, as described below.

A. Prediction of $g - r$ Color from the Half Power Point Method

The first technique, the Half Power Point (HPP) method (Wisotzki et al. 2000), has been described in Chapter 3.4 above, in connection with refining grid searches of parameter space. Here we obtain an empirical calibration of the $g - r$ color by fitting a functional relationship between the HPP wavelength of spectra for stars with well-measured SDSS colors, and located in regions of high Galactic latitude, where reddening is minimal. The best-fit relationship is:

$$g - r = -3.354 + 4.318 \cdot \mathrm{HPP} + 3.247 \cdot \mathrm{HPP}^2, \tag{3.9}$$

where HPP $= \lambda/10{,}000$. The expected error in prediction is about 0.08 magnitudes, over a broad range of color.

The predicted color obtained in this fashion is (obviously) also a way to identify stellar spectra with poor spectrophotometric flux calibrations. If the observed color reported by the SDSS PHOTO routine is believed to be correct, and there remains a difference with the color obtained from the above relationship, one might be justifiably concerned about the quality of the spectrophotometric correction that has been applied. Unresolved binaries, especially those involving a red and a blue member, can also be identified by looking for discrepancies between the observed and predicted $g - r$ colors.

B. Prediction of $g-r$ Color from the Hδ and Hα Lines

The strengths of the Balmer lines are also tightly correlated with $g-r$ color, over wide ranges of effective temperature. We have made use of the line indices for Hδ and Hα, as determined by the SSPP, to obtain the following relationships:

$$g - r = 0.469 - 0.058 \cdot HD24 \tag{3.10}$$

and

$$g - r = 0.818 - 0.092 \cdot HA24, \tag{3.11}$$

where $HD24$ and $HA24$ are the Hδ and Hα line indices calculated over a 24 Å band centered on these lines. Note that since the Hα line is stronger, at a given color, than the Hδ line, it can be used to determine predictions of colors for cooler stars. The Hα line is also located in a region of the spectrum where one expects generally fewer problems with contamination of the index from nearby metallic features.

3.6 The Impact of Signal-to-Noise on Derived Atmospheric Parameters

Only the very brightest stars in the SDSS-I/SEGUE sample were accessible for follow-up high-resolution spectroscopic observations as part of the SEGUE calibration effort (see Paper III). Thus, the high-resolution data by themselves provide no information on the accuracy of the parameter estimates from the SSPP for SEGUE spectra with lower signal-to-noise ratios (< about 30/1). To evaluate the accuracy and precision of the SSPP estimates of atmospheric parameters over a wide S/N range, we have developed a noise model for SEGUE data, applied it to the SDSS-I/SEGUE high-resolution calibration sample to create test spectra at many (more than 50) S/N

values, and compare with the outputs of the SSPP, as run on these noise-added spectra, with the SSPP parameters determined from the original SEGUE spectra, and from the analysis of the high-resolution data.

Table 3.5: Parameter Sensitivities to Signal-to-Noise[e]

	S/N	5		10		15		20		25	
	Name Method	$<\Delta>$	σ	$<\Delta>$	σ	$<\Delta>$	σ	$<\Delta>$	σ	$<\Delta>$	σ
$T_{\rm eff}$											
Ad	Adop	−32	175	0	103	7	74	1	57	1	49
T1	ki13	−0	316	−20	174	−8	119	−6	94	−5	72
T2	k24	−59	95	−39	74	−31	65	−24	54	−20	50
T3	WBG	4	12	4	9	4	8	4	8	4	8
T4	ANNSR	225	676	142	343	69	199	30	143	24	115
T5	ANNRR	−111	255	−13	154	19	106	24	78	27	62
T6	NGS1	−11	315	−15	166	−4	117	−3	92	−3	75
T7	HA24	199	510	58	238	40	167	25	123	18	101
T8	HD24	57	256	−29	155	−45	124	−52	97	−56	90
T9	T_K	...	...	...	...	...	...	...	...	...	...
T10	T_G	...	...	...	...	...	...	...	...	...	...
T11	T_I	...	...	...	...	...	...	...	...	...	...
log g											
Ad	Adop	−0.18	0.48	−0.11	0.28	−0.07	0.20	−0.06	0.16	−0.04	0.14
G1	ki13	−0.11	0.93	−0.07	0.50	−0.04	0.32	−0.04	0.27	−0.02	0.22
G2	k24	−0.20	0.62	−0.10	0.33	−0.07	0.26	−0.05	0.20	−0.04	0.17
G3	WBG	0.01	0.05	0.01	0.09	0.02	0.06	0.01	0.06	0.01	0.06
G4	ANNSR	−0.53	1.04	−0.32	0.66	−0.15	0.42	−0.10	0.31	−0.07	0.23
G5	ANNRR	−0.08	0.23	−0.03	0.19	−0.00	0.15	0.00	0.12	0.01	0.11
G6	NGS1	−0.07	0.94	−0.02	0.45	−0.02	0.31	−0.03	0.25	−0.02	0.20
G7	NGS2	−0.10	0.75	−0.05	0.40	−0.05	0.28	−0.05	0.22	−0.03	0.19

Table 3.5: Parameter Sensitivities to Signal-to-Noise (continued)

	S/N	5		10		15		20		25	
	Name Method	$<\Delta>$	σ	$<\Delta>$	σ	$<\Delta>$	σ	$<\Delta>$	σ	$<\Delta>$	σ
	G8 CaI1	−0.03	0.68	−0.01	0.42	−0.02	0.32	−0.03	0.23	−0.03	0.20
	G9 CaI2	−0.47	1.64	−0.05	0.75	−0.04	0.54	−0.03	0.42	−0.03	0.34
	G10 MgH	−0.01	0.40	−0.03	0.22	−0.03	0.15	−0.02	0.12	−0.01	0.10
[Fe/H]											
	Ad Adop	0.14	0.47	0.05	0.21	0.05	0.14	0.02	0.10	0.00	0.08
	M1 ki13	0.51	0.56	0.17	0.25	0.11	0.18	0.07	0.14	0.04	0.11
	M2 k24	−0.01	0.37	−0.03	0.20	−0.01	0.14	−0.02	0.11	−0.01	0.09
	M3 WBG	−0.27	0.40	−0.01	0.14	−0.01	0.07	0.01	0.05	0.01	0.05
	M4 ANNSR	0.20	0.86	−0.03	0.43	−0.02	0.31	−0.08	0.23	−0.12	0.16
	M5 ANNRR	−0.02	0.37	−0.01	0.17	0.00	0.11	−0.00	0.08	−0.00	0.07
	M6 NGS1	0.51	0.51	0.16	0.24	0.10	0.17	0.05	0.12	0.03	0.10
	M7 NGS2	0.53	0.58	0.24	0.26	0.22	0.19	0.14	0.14	0.09	0.11
	M8 CaKII1	0.21	0.51	0.06	0.32	0.04	0.22	0.02	0.15	0.01	0.13
	M9 CaKII2	−0.14	0.47	−0.03	0.19	0.01	0.11	0.02	0.07	0.02	0.06
	M10 CaKII3	−0.05	0.75	0.00	0.29	0.00	0.19	0.01	0.13	0.00	0.11
	M11 ACF	0.92	0.14	0.41	0.35	0.12	0.17	0.06	0.12	0.03	0.09
	M12 CaIIT	0.10	0.88	−0.04	0.82	−0.03	0.57	−0.03	0.48	−0.01	0.41

The noise characteristics of SDSS-I/SEGUE data are modeled down to a lower limit of signal-to-noise per pixel of 5/1. These estimates are based on the extracted, flux-calibrated, spectra and variance arrays from the SDSS/SEGUE spectroscopic reduction pipelines directly, not on the raw spectroscopic frames. Each SDSS-I/SEGUE

[e] $<\Delta>$ is the average of the differences between the noise-added spectra and the original spectra; σ is the standard deviation of the differences. The temperature estimates T9, T10, and T11 do not change with S/N, because they are computed from the $g-r$ color.

plug-plate has spectroscopic targets that span the entire magnitude range of the bright or faint plug-plates. The boundary between the faint and bright plug-plates is set to $r \sim 18.0$. Since all targets on a given plug-plate receive the same total exposure time, the relative contribution from the sky and object components of the noise changes over the magnitude range of the survey, with object noise dominant at high S/N and sky noise dominant at low S/N. The sky and stellar spectra have different spectral energy distributions, so in order to make a high S/N SEGUE spectrum and its variance array resemble lower S/N data, simply adding Poisson noise is not sufficient.

The noise model is constructed by measuring the ratio of sky-to-object flux for a large subset of all the SEGUE spectra, 85,000 in the case of the tests described here, and parameterizing the mean value of that ratio and the width of the scatter about the mean vs. S/N. This accounts for the increasing contribution from sky noise at lower S/N, and the range of final S/N for targets at any magnitude because of variable conditions, etc. Then, to make a spectrum of any desired final S/N, the model uses that relation to scale the input spectrum and variance. The model then enforces equality between that ratio of sky-to-object flux and the ratio of the variances of the sky and object flux, since both the flux and variances should be proportional to the total counts. This deals with differences in how the reduction pipeline flux calibrations are applied to the sky and objects fibers and their variances. The model then randomly draws a sky residual spectrum from the set of all sky fibers on all the SEGUE plug-plates and adds that zero-mean spectrum, now at the correct relative magnitude for the output S/N, to the noise-added data spectrum. We construct many (more than 50) realizations of each spectrum at each S/N value, each one with a different sky residual, and with the value used for the initial scaling of the input spectrum and its variance drawn as a Gaussian random deviate, described by the mean and scatter of the ratio of sky-to-object flux in the survey data.

The end result is a noise-added spectrum for which the signal-to-noise vs. wavelength is (as much as possible) indistinguishable from real data at similar a signal-to-noise ratio. Our test spectra have S/N values ranging from 2.5/1 to 55/1. We have tested the noise-added spectra by checking the accuracy of the radial velocities for the test spectra vs. S/N, and find good agreement with the accuracy as determined by comparing duplicate SEGUE observations that span the same range in S/N (C. Rockosi et al., in preparation). We have also measured the signal-to-noise ratio at important spectroscopic features as blue as Ca II K vs. the average signal-to-noise ratio for the test spectra, and found good agreement with the same measurement for real spectra at similar $g - r$ colors.

From a sample of 108 calibration stars with ~450 different realizations in each S/N bin, we selected a sub-sample of spectra with 40 different realizations per bin, and examined how the stellar parameters determined by the methods used by the SSPP depend on S/N (over the range $5/1 \leq S/N \leq 25/1$). Table 3.5 summarizes the results. The S/N ratio is calculated by averaging over the spectral region 4000−8000 Å. Since we have numerous realizations of each spectrum at the same approximate S/N, we calculated the average S/N, as well as the mean offset and scatter of the parameters (compared to the non noise-injected spectra) by, e.g., selecting spectra with S/N between 3/1 and 7/1 for $S/N \sim 5/1$. The same procedure is applied to the other S/N regimes.

The S/N cuts we have chosen for the individual methods used by the SSPP (listed in Table 3.3) are based on this experiment. The results for the temperature estimates T9, T10, and T11 are zeroed out in Table 3.5, because they are computed from the $g - r$ color alone.

3.7 Flags Raised During Execution of the SSPP

It is important that the SSPP be able to identify situations where the quoted atmospheric parameters may be in doubt, or simply to make the user aware of possible anomalies that might apply to a given star. We have designed a number of flags that serve this purpose.

Table 3.6: Brief Descriptions of SSPP Flags[f]

Position	Flag	Description	Category	Parameter
First				
	n	Appears normal	.....	Yes
	D	Likely white dwarf	Critical	No
	d	Likely sdO or sdB	Critical	No
	H	Hot star with $T_{\rm eff} > 10{,}000$ K	Critical	No
	h	Helium line detected, possibly very hot star	Critical	No
	l	Likely late type solar abundance star	Cautionary	Yes
	E	Emission lines in spectrum	Critical	No
	S	Sky spectrum	Critical	No
	V	No radial velocity information	Critical	No
	N	Very noisy spectrum	Cautionary	Yes
Second				
	n	Appears normal	.....	Yes
	C	The photometric $g - r$ color may be incorrect	Cautionary	Yes
Third				
	n	Appears normal	.....	Yes
	B	Unexpected Hα strength predicted from Hδ	Cautionary	Yes
Fourth				
	n	Appears normal	.....	Yes
	G	Strong G-band feature	Cautionary	Yes

Table 3.6: Brief Descriptions of SSPP Flags (continued)

Position	Flag	Description	Category	Parameter
	g	Mild G-band feature	Cautionary	Yes
Fifth				
	n	Appears normal	.....	Yes
	P	Parameters reported for $5.0 \leq S/N < 10.0$	Cautionary	Yes
	N	No parameters	Critical	No
RV				
	NORV	No radial velocity information	.....	No
	ELRV	Radial velocity from ELODIE template	.....	Yes
	BSRV	Radial velocity from `spectro1d`	.....	Yes
	RVCAL	Radial velocity calculated from SSPP	.....	Yes

There are two primary categories of flags – critical flags and cautionary flags. When a critical flag is raised, the SSPP is set to either ignore the determinations of atmospheric parameters for a given star, or it is forced (in the case of the color flag described below) to take steps that differ from normal processing in an attempt to rescue this information. Obviously, even when information is salvaged, the presence of a critical flag means the user must be aware that special steps have been taken, and the reported estimated parameters must be viewed with this knowledge in mind. The second category of flags are the cautionary flags, which are provided for user consideration, but are not necessarily cause for undue concern. Indeed, sometimes these flags are raised when all is in fact OK, but the flag has been raised due to a peculiarity in the spectrum that is relatively harmless, and which will not unduly influence determination of atmospheric parameters. The user should nevertheless be

[f]No parameters are reported when 'Critical' flags are raised.

aware of the existence of these flags.

The flags are combined into a single set of five letters, the meanings of which are summarized in Table 3.6, and described below in more detail. Five placeholders are used in order to accommodate cases where more than one sort of flag is raised.

The nominal condition for the five letter flag combination is 'nnnnn', which indicates that the SSPP is satisfied that a given stellar spectrum (and its reported $g-r$ colors and S/N) has passed all of the tests that have been performed, and the stellar parameters should be considered well determined.

The first letter in this combination is set to one of 10 different values: 'n', 'D', 'd', 'H', 'h', 'l', 'E', 'S', 'V', and 'N'. Their explanations follow:

- 'n': The letter 'n' indicates nominal.

- 'D': This flag is raised if a comparison of the breadth of the Hδ line at 20% below its continuum, $D_{0.2}$, and the line depth below the continuum, R_c, relative to their expected relationship for "normal stars", provided below, does not apply. The expected relationship is given by:

$$R_c = -0.009503 + 0.027740 \cdot D_{0.2} - 0.000590 \cdot D_{0.2}^2 + 0.000006 \cdot D_{0.2}^3 \quad (3.12)$$

  If $D_{0.2}$ is greater than 35.0 Å, and the predicted R_c from the above relationship is less than the measured value, then the star is most likely a white dwarf. This is a critical flag.

- 'd': This flag is raised if $D_{0.2}$ is less than 35.0 Å, and the predicted R_c from above is less than the measured value. In this case, the star is most likely a sdO or sdB star. This is a critical flag.

- 'H': This flag is raised when the estimated $T_{\rm eff}$ from the SSPP is greater than 10000 K, and is meant to indicate a hot star. This is a critical flag.

- 'h': This flag is raised if the estimated $T_{\rm eff}$ from the SSPP is greater than 8000 K, and either of the line indices of He I (at 4026.2 Å) or He I (at 4471.7 Å) is greater than 1.0 Å. This indicates that the star is likely to be a hot star. This is a critical flag.

- 'l': This flag is raised if the SSPP judges the star to have a high likelihood of being a late-type star (generally late K, M, or later spectral type), beyond the ability of the present pipeline to determine acceptable atmospheric parameter estimates. The condition used for raising the 'l' flag is that the Na line (5892.9 Å) index, as measured over a 24 Å band centered on this feature, is larger than 10 Å, and the $g - r$ color is greater than 0.8. This is a cautionary flag.

- 'E': This flag is raised if significant emission lines are detected in a spectrum. This is a critical flag.

- 'S': This flag is raised if the spectrum (according to the header information) is a night-sky spectrum. This is a critical flag.

- 'V': This flag is raised when an adequate radial velocity could not be found for a given spectrum. This is a critical flag.

- 'N': This flag is raised if the spectrum is considered noisy at the extremes of the wavelength range (e.g., around Ca II K and the Ca II triplet). This is a cautionary flag.

The flags that are used to fill out the remaining four positions of the five letter flag combination are 'C', 'B', 'G', 'g', 'P', and 'N', as described below. If none of these flags is raised, then the 'n' flag is raised in their place:

- 'C': This flag is raised if the SSPP is concerned that the reported $g - r$ color is incorrect. As mentioned above, we calculate three estimates of predicted $g - r$ colors, based on $HA24$, $HD24$, or the Half Power Point method. For each of these three predicted colors, we find the one which is closest to the reported $g-r$ color based on the photometry. If the difference between the reported color and the closest predicted color is larger than 0.2 magnitudes, the color flag ('C') is raised. The SSPP is set up to proceed with its calculations of atmospheric parameters using the predicted $g - r$ color. This flag is always found in the second position of the combination flag parameters. This is a cautionary flag.

- 'B': This flag is raised if the SSPP is concerned that there exists a strong mismatch between the strength of the *predicted* Hα line index $HA24$, based on the measured Hδ line index, $HD24$. For the great majority of "normal" stars, the predicted value of the Hα line index is found to be $HA24 = 2.737 + 0.775 \cdot HD24$. For stars with significant $HA24$ and $HD24$ measurements (which we take to mean that the values of these indices exceed zero by more than 2 σ, where σ is the error in the measured line index), if the difference between the predicted $HA24$ line index and the measured $HA24$ index is larger than 2.5 Å, then the 'B' flag is raised. This flag is always found in the third position of the combination flag parameters. This is a cautionary flag.

- 'G or g': This flag is raised if the SSPP suggests that the star may exhibit a strong ('G') or mild ('g') CH G-band (around 4300 Å), relative to expectation for "normal" stars. This flag is always found in the fourth position of the combination flag parameters. This is a cautionary flag.

- 'P or N': This flag is raised in order to indicate if a spectrum either does ('n'), which is innocuous, or does not ('P'), which may be of concern, pass through the S/N cuts listed in Table 3.3, but still has an average $S/N \geq 5/1$. If no

parameters are reported, or the average $S/N < 5/1$, the 'N' flag is raised. The flag 'P' is cautionary, while 'N' is a critical flag.

3.8 The SSPP Decision Tree for Final Parameter Estimation

The SSPP uses multiple methods in order to obtain estimates of the atmospheric parameters for each star over a very wide range in parameter space. Each technique has limitations as to its ability to estimate each parameter, arising from, e.g., the coverage of the grids of synthetic spectra, the methods used for spectral matching, and their sensitivity to the S/N of the spectrum, the range in parameter space over which the particular calibration used for a given method extends, etc.. Hence, it is necessary to specify a prescription for the inclusion or exclusion of a given technique for the estimation of a given atmospheric parameter. At present, this is accomplished by the assignment of a null (0, meaning the parameter estimate is dropped), or unity (1, meaning the parameter estimate is accepted) value to an indicator variable associated with each parameter estimated by a given technique, according to the $g - r$ and S/N criteria listed in Table 3.3, and the flags that are raised. In the future, we plan to devise an improved weighting scheme for the combinations of the parameter estimates, once the grid of high-resolution spectroscopic determinations of atmospheric parameters is more completely filled out.

The S/N of a given spectrum plays a crucial role in the final decision as to the estimate of a set of atmospheric parameters, and the techniques used (which differ in their sensitivity to S/N). Table 3.3 lists the ranges of S/N where each particular method is considered valid. All derived parameters that fall outside of the color and S/N ranges listed in this table, for a given technique, are set to $T_{\rm eff} = -9999$, $\log g = -9.999$, and [Fe/H] $= -9.999$, and have an indicator variable attached to a given

parameter set to zero by the SSPP. However, if the S/N of a spectrum is greater than 5/1, the parameters are saved (with the cautionary flag 'P' raised).

Recall that in cases where the color flag 'C' is raised, the predicted $g - r$ color determined by the procedures described above is used as an input (rather than the reported color) for the techniques that require this information.

3.8.1 Decisions on Effective Temperature Estimates

There are six primary temperature estimates determined by the SSPP, and an auxiliary set of five empirically and theoretically determined estimates. Note that a few of the primary techniques extend to temperatures below 4500 K and above 7500 K, although the accuracy obtained by these are lower than in the interval 4500 K $< T_{\rm eff} <$ 7500 K. Thus, for stars with temperatures outside of this interval, we also include the auxiliary temperature estimates (in fact, just those that lie within 3 σ of the mean of the full auxiliary set) in assembling the final average estimate of $T_{\rm eff}$. Averages are taken using the robust biweight procedure (See Beers, Flynn, & Gebhardt 1990, and references therein).

In cases where the color flag 'C' is raised, we ignore all temperatures that rely on the reported $g-r$ color, and only consider those based on spectroscopy alone (e.g., the spectral matching techniques and Balmer-line based temperature). A robust average of the accepted temperature estimates (those with indicator variables equal to 1) is taken for the final adopted temperature. An internal robust estimate of the scatter around this value is also obtained.

3.8.2 Decisions on Surface Gravity Estimates

There are ten methods used to estimate surface gravity by the SSPP. Application of the limits on $g-r$ and S/N eliminates a number of these estimates, and the biweight average of the accepted log g estimates (those with indicator variables equal to 1) is

taken for the final adopted surface gravity. An internal robust estimate of the scatter around this value is also calculated.

3.8.3 Decisions on Metallicity Estimates

Twelve different methods are employed to determine [Fe/H] in the present SSPP. As before, indicator variables of 1 or 0 are assigned to the result from each method, according to whether or not it satisfies the range of validity listed in Table 3.3.

Rather than simply averaging the (accepted) metallicity estimates for each star, we have introduced a routine to identify and remove likely outliers. This involves the calculation of correlation coefficients between the observed and the synthetic spectrum generated with the adopted temperature and gravity, and the individual estimates of the metallicity. Briefly, we start with the individual estimates of [Fe/H] (with indicator variables of 1), the adopted $T_{\rm eff}$, and log g, and use these parameters to generate a synthetic spectrum by interpolating the pre-existing grid of the synthetic spectra (specifically the `NGS1` grid). Then, we compute correlation coefficients between the observed and the generated synthetic spectrum in two different wavelength regions: 3850−4250 Å and 4500−5500 Å, where the Ca II K and H lines, as well as numerous metallic lines are present. We have avoided the region surrounding the CH G-band feature, as this molecular band can vary widely for stars with enhancements of carbon. Thus, for each estimator of [Fe/H] there are two values of the correlation coefficient determined. We then select the region with correlation coefficient closest to unity. This applies for all estimates of [Fe/H] from the individual methods. At the end of this process, we have N values of the correlation coefficient (maximum of $N = 12$) for the N estimates of [Fe/H] with indicator variables of 1. After this, we take a robust average of the N values, and reject the values that are less than 1 σ from the average. By application of this procedure, metallicity estimates that produce poor matches with the synthetic spectra are ignored, and are assigned indicator variables

of 0. The final adopted value of [Fe/H] is the biweight average of the remaining values of [Fe/H] (those with indicator variables of 1). This procedure is followed for all stars with adopted temperatures $T_{\rm eff} \geq 5000$ K. For stars with adopted temperatures below this value, we do not consider the region 3850−4250 Å for calculation of a correlation coefficient, because the Ca II K line is subject to saturation (and sometimes) the presence of line-core emission (due to an active chromosphere).

This procedure has been adopted after consideration of numerous alternative approaches for the final metallicity averaging. It appears to work (almost) as well as individual inspection by a trained spectroscopist, which would not be practical for the large numbers of spectra obtained by the SDSS.

3.9 Validation of the Final SSPP Parameter Estimates

We do not yet have at our disposal a completely satisfactory set of external spectral libraries, with suitable wavelength coverage and available atmospheric parameter estimates, that extends over the full range of parameter space explored by techniques employed by the SSPP. Hence, we are limited to comparison with the sets of parameters obtained from analysis of the high-resolution spectra for SDSS-I/SEGUE stars obtained to date, and with information available from the literature for stars in Galactic open and globular clusters that have been observed during the course of the SDSS. Since Paper III focuses on the global uncertainties in the derived parameters from the SSPP, in this thesis we concentrate on the comparison of individual methods with the results from the high-resolution analyses.

Table 3.7: Comparison of $T_{\rm eff}$ Estimates from Individual Methods with Those from Two High-Resolution Analyses[g]

	Name	Ad	T1	T2	T3	T4	T5	T6	T7	T8	T9	T10	T11
	Method	Adop	ki13	k24	WBG	ANNSR	ANNRR	NGS1	HA24	HD24	T_K	T_G	T_I
HA1	N	81	79	81	79	81	81	81	81	60	81	81	81
	$<\Delta>$	+194	+142	+312	+230	+300	+179	+85	+139	+163	+125	+45	+146
	σ	182	231	249	196	197	182	164	142	147	295	252	268
HA2	N	125	120	120	116	122	125	125	123	96	125	125	125
	$<\Delta>$	−32	−90	+46	−4	+36	−29	−140	−99	−74	−108	−178	−81
	σ	147	184	186	201	218	144	183	202	253	167	205	186
MEAN	N	125	120	120	116	122	125	125	123	95	125	125	125
	$<\Delta>$	+64	−2	+136	+94	+132	+56	−37	+8	+43	−39	−83	−2
	σ	126	171	219	195	218	135	174	162	187	208	209	193

3.9.1 Validation from High-Resolution Spectroscopy

Table 3.2 summarizes the high-resolution data for SDSS-I/SEGUE stars obtained to date. Although the stars in this table cover most of the range explored by the SSPP techniques, there remain gaps in this coverage that we hope to fill in the near future.

As noted above, these data have been reduced and analyzed independently by two (C.A. and T.S.) of the authors in Paper III, making use of different methodologies. Details are discussed in Paper III. Tables 3.7, 3.8, and 3.9 summarize the systematic offsets and scatters obtained for estimates of $T_{\rm eff}$, log g, and [Fe/H] from each of the techniques used by the SSPP, relative to high-resolution analyses carried

[g]'Ad' is the adopted estimate of $T_{\rm eff}$. HA1 indicates the analysis performed by C.A.; HA2 for T.S. MEAN is the average of the two analyses. 'N' is the number of stars compared. $<\Delta>$ is the mean zero-point offset from a Gaussian fit to the residuals of $T_{\rm eff}$ between the SSPP and the high-resolution analysis; σ is the standard deviation of the fit.

out individually and collectively. The differences in the numbers of stars considered independently arises because T.S. (results shown as **HA2** in the tables) analyzed all available spectra, while C.A. (results shown as **HA1** in the tables) performed analysis only for those stars observed with the Hobby-Eberly Telescope (HET). In the **HA2** analysis, two different approaches were employed. The first is a routine that optimizes the minimum distances between the observed and synthetic spectra over a grid. This method was employed for the HET and Keck-ESI spectra. The second is the traditional high-resolution analysis approach, using Fe I and Fe II lines to constrain $T_{\rm eff}$, log g, [Fe/H], and the microturbulence parameter. This approach was applied to the Keck-HIRES and Subaru-HDS data. More detailed explanations on the methods can be found in Paper III. The Keck-ESI, Keck-HIRES, and Subaru-HDS spectra with available parameters are defined as *OTHERS* in Paper III. In Paper III only the HET data analyzed by C.A. are used to derive the empirical random errors of the adopted parameters from the SSPP. However, in the present study, we consider all available parameter estimates from all methods considered in the SSPP. The rows labeled **MEAN** in Tables 3.7, 3.8, and 3.9 are the averaged results from **HA1** and **HA2** (for stars in common), supplemented with stars from **HA2** where **HA1** results were not obtained.

Figures 3.9, 3.10, and 3.11 provide comparisons of the estimates of atmospheric parameters for individual techniques used by the SSPP with those obtained from the high-resolution analysis (**HA1**), for $T_{\rm eff}$, log g, and [Fe/H], respectively.

Comparison of the estimated temperatures from the SSPP indicates, overall, very satisfactory results, although Table 3.7 reflects an interesting trend for $T_{\rm eff}$; estimates are mostly higher for the **HA1** residuals, and mostly lower for **HA2**. However, as can also be noted from this table, the final adopted value of effective temperature from the SSPP exhibits a very small offset (+64 K) compared to the **MEAN**, and a one-sigma scatter of 126 K, both of which are encouragingly small. It is clear from inspection

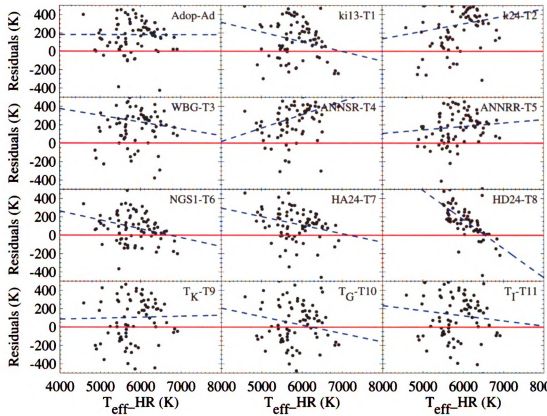


Figure 3.9 Comparison of effective temperatures estimated from individual methods with those from the HA1 high-resolution analysis of SDSS-I/SEGUE stars. 'HR' indicates the (HA1) high-resolution analysis results. Residuals are the differences between the individual estimates and the high-resolution results. The red solid line is the zero-point; the blue dashed line is a least squares fit to the residuals.

of Figure 3.9 that additional high-resolution observations are required of stars with both higher and lower temperatures than the present sample. The distribution of the final adopted temperatures indicates no significant trends in the temperature range 4500 K $\leq T_{\rm eff} \leq$ 7500 K, compared with the values from HA1, but there may exist a systematic offset of about 200 K.

Table 3.8 and Figure 3.10 for the surface gravity estimates reveal that the estimate G3 exhibits the highest offset, and largest scatter, relative to the high-resolution analyses, for reasons that are not presently clear. The residuals of the adopted values for surface gravity estimates from the SSPP are reasonably well distributed around

zero for the high-gravity regime. High-resolution spectra for additional stars with lower surface gravities are required in order to confirm whether the slopes in the regression fits to the residuals for individual methods are real, or simply influenced by a few low gravity stars. The mean offsets and one-sigma scatters in the final adopted estimate of log g from the comparison with **HA1** are +0.02 dex and 0.21 dex, respectively, and 0.00 and 0.23 dex for the **MEAN** comparisons. These are surprisingly good results for this difficult-to-estimate parameter.

Table 3.8: Comparison of log g Estimates from Individual Methods with Those from Two High-Resolution Analyses

	Name	Ad	G1	G2	G3	G4	G5	G6	G7	G8	G9	G10
	Method	**Adop**	**ki13**	**k24**	**WBG**	**ANNSR**	**ANNRR**	**NGS1**	**NGS2**	**CaI1**	**CaI2**	**MgH**
HA1	N	81	79	81	79	80	81	81	80	77	32	35
	$<\Delta>$	+0.02	+0.03	+0.06	−0.16	+0.01	+0.06	+0.06	+0.05	+0.05	+0.06	+0.04
	σ	0.21	0.34	0.33	0.69	0.25	0.22	0.30	0.29	0.30	0.30	0.26
HA2	N	125	120	120	116	118	123	122	120	117	47	51
	$<\Delta>$	−0.02	−0.05	+0.00	−0.19	+0.01	+0.01	−0.01	−0.04	+0.00	−0.03	+0.00
	σ	0.33	0.44	0.43	0.82	0.45	0.37	0.41	0.39	0.37	0.40	0.24
MEAN	N	125	120	120	116	118	123	122	120	117	47	51
	$<\Delta>$	+0.00	−0.01	+0.03	−0.19	+0.03	+0.02	+0.03	+0.01	+0.02	−0.00	+0.03
	σ	0.23	0.36	0.40	0.80	0.33	0.28	0.31	0.33	0.33	0.39	0.24

It can be seen from Table 3.9 and Figure 3.11 that, except for M12, which exhibits a somewhat larger zero-point offset in **HA2** and **MEAN**, but a small deviation from this zero point, all of the individual methods display satisfyingly small offsets with low scatter.

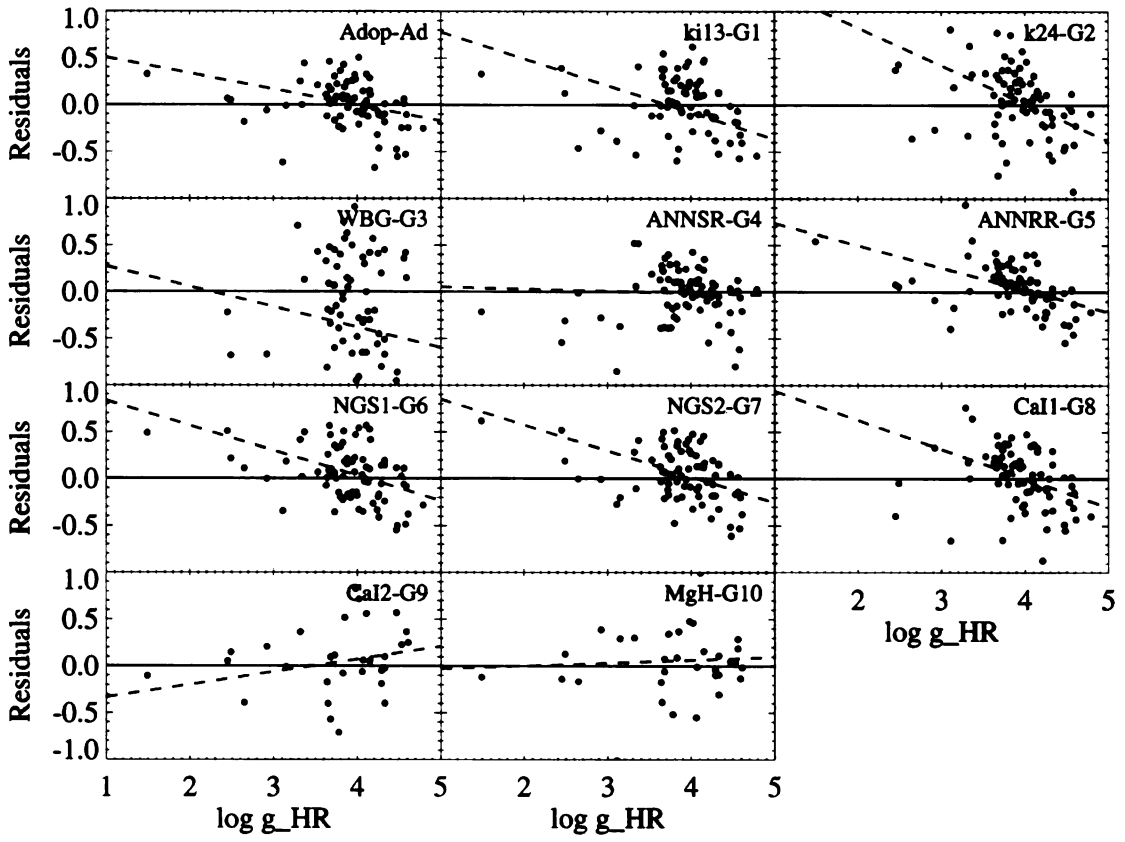


Figure 3.10 Same as Figure 3.9 but for the surface gravities, log g.

It is clear from inspection of Figure 3.11 that we could benefit from high-resolution analyses for more stars with intermediate metallicities, as well as for stars at the lowest metallicities. The mean offset (+0.02 dex) and one-sigma scatter (0.15 dex) of the residuals between the SSPP predictions of [Fe/H] and the high-resolution analysis (**HA1**) are quite encouraging, at least over the parameter space explored to date; the mean zero-point offset of +0.03 dex and scatter of 0.23 dex from **MEAN** is quite acceptable as well.

In summary, based on the sets of parameter comparisons with high-resolution analyses, in the effective temperature range of 4500 K $\leq T_{\rm eff} \leq$ 7500 K, if we take the results from **MEAN** as "ground truth", the SSPP is capable of producing estimates of the atmospheric parameters for SDSS-I/SEGUE stars to precisions of $\sigma(T_{\rm eff})$, $\sigma(\log g)$,

and σ([Fe/H]) of 141 K, 0.23 dex, and 0.23 dex, respectively, after adding systematic offsets quadratically. These uncertainties will be slightly reduced if we take into account the error contribution from the high-resolution analysis, as is done in Paper III. However, it should be kept in mind that the stars for which these comparisons are carried out are among the very brightest (high $S/N > 50/1$) observed with SDSS, and the overall precision of parameter determination will slightly decline with S/N, as shown in Table 3.5.

Table 3.9: Comparison of [Fe/H]Estimates from Individual Methods with Those from Two High-Resolution Analyses

	Name	Ad	M1	M2	M3	M4	M5	M6	M7	M8	M9	M10	M11	M12
	Method	Adop	ki13	k24	WBG	ANNSR	ANNRR	NGS1	NGS2	CaKII1	CaKII2	CaKII3	ACF	CaIIT
HA1	N	81	53	56	47	49	62	64	45	53	29	31	30	34
	$<\Delta>$	+0.02	+0.02	+0.02	+0.02	−0.02	−0.05	−0.02	−0.06	−0.00	+0.03	+0.06	+0.08	+0.06
	σ	0.15	0.14	0.14	0.19	0.13	0.16	0.14	0.12	0.24	0.24	0.20	0.19	0.22
HA2	N	125	80	82	63	70	102	97	73	84	46	56	43	52
	$<\Delta>$	+0.04	+0.06	+0.10	+0.03	−0.00	−0.01	+0.03	+0.02	−0.02	+0.07	+0.02	+0.09	+0.22
	σ	0.33	0.27	0.33	0.38	0.31	0.28	0.28	0.26	0.38	0.38	0.43	0.37	0.31
MEAN	N	125	80	82	63	70	102	97	73	84	46	56	43	52
	$<\Delta>$	+0.03	+0.05	+0.09	+0.01	−0.01	−0.03	+0.02	−0.01	−0.03	+0.03	−0.00	−0.00	+0.16
	σ	0.23	0.15	0.23	0.27	0.21	0.19	0.17	0.18	0.32	0.32	0.37	0.21	0.28

3.10 Assignment of Spectral Classifications for Early and Late-Type Stars

It is often useful to group stars into rough MK spectral classifications. It should be kept in mind, however, that for this, and any other exercise of assigning MK spectral types, that the MK system *does not apply* to stars other than Population I. That is, typing of metal-poor Population II stars is, *by definition*, not a strictly valid procedure. Nevertheless, the SSPP attempts to carry out this exercise using two approaches. The first is based on the spectral type listed in the ELODIE database for the best template match obtained for the determination of radial velocity (as described above), and applies to stars with spectral classes O to M.

For the coolest stars, measurement of accurate values of $T_{\rm eff}$, $\log g$, and [Fe/H] from spectra dominated by broad molecular features becomes extremely difficult (e.g., Woolf & Wallerstein 2006). As a result, the SSPP does not estimate atmospheric parameters for stars with $T_{\rm eff} < 4000$ K, but instead estimates the MK spectral type of each star using the "Hammer" spectral-typing software developed and described by Covey et al. (2007) [h]. The Hammer code measures 23 spectral indices, including atomic lines (H, Ca I, Ca II, Fe I, Mg I, Na I) and molecular bandheads (CN, G band, TiO, VO, CaH, FeH), as well as a select set of broadband color ratios. The best-fit spectral type of each target is assigned by comparison to the grid of indices measured from more than 1000 spectral-type standards derived from spectral libraries of comparable resolution and coverage (Allen & Strom 1995; Prugniel & Soubiran 2001; Hawley et al. 2002; Bagnulo et al. 2003; Le Borgne et al. 2003; Valdes et al. 2004; Sańchez-Blázquez et al. 2006).

Tests of the accuracy of the Hammer code with degraded ($S/N \sim 5/1$) STELIB (Le Borgne et al. 2003), MILES (Sánchez-Blázquez et al. 2006), and SDSS (Hawley

[h]The Hammer has been made available for community use: the IDL code can be downloaded from http://www.cfa.harvard.edu/ kcovey/

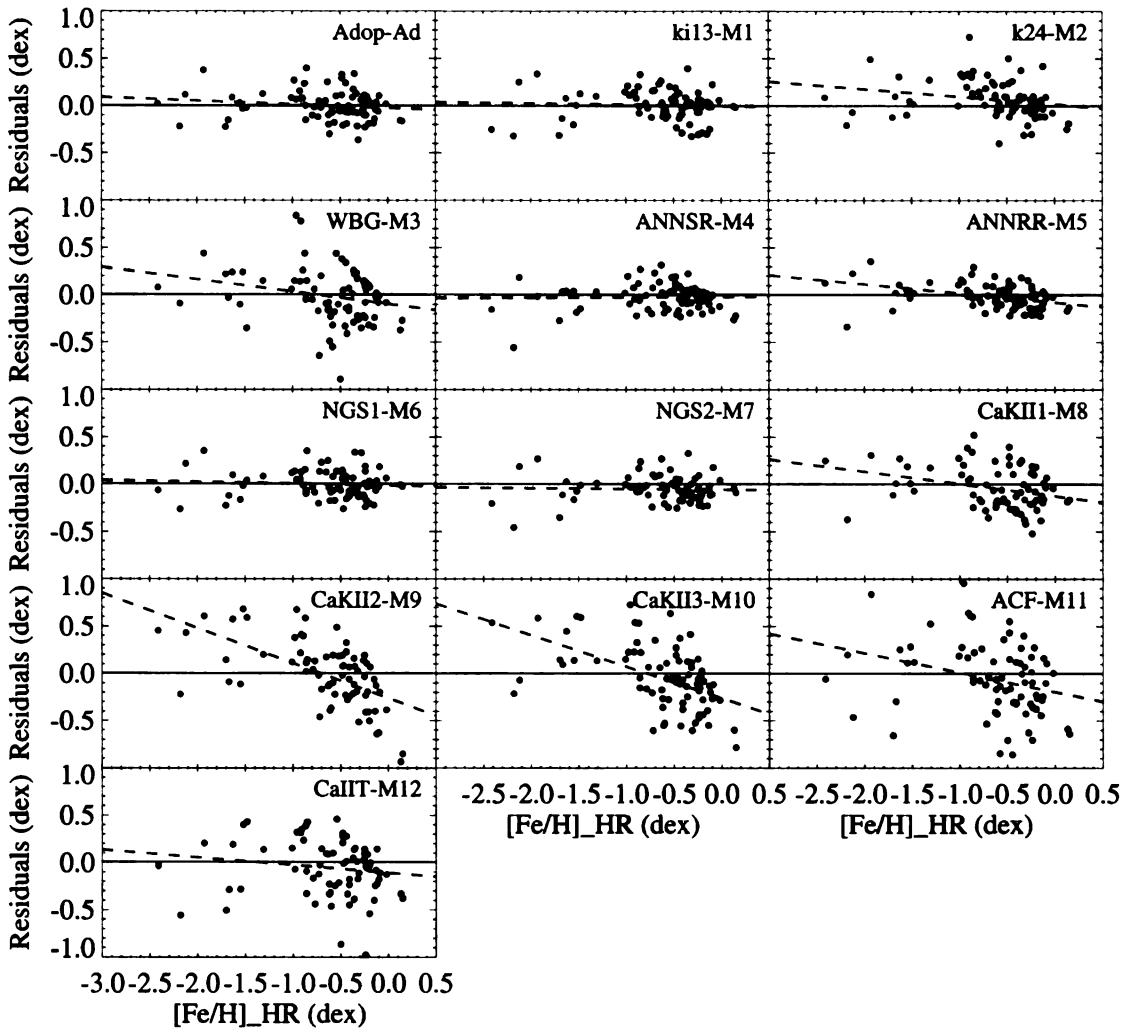


Figure 3.11 Same as Figure 3.9 but for the metallicities, [Fe/H].

et al. 2002) dwarf template spectra reveal that the Hammer code assigns spectral types accurate to within ±2 subtypes for K and M stars. The Hammer code also returns results for warmer stars, but as the set of indices used is optimized for cool stars, typical uncertainties are ±4 subtypes for A-G stars at $S/N \sim 5/1$; in this temperature regime, the SSPP atmospheric parameters are a more reliable indicator of $T_{\rm eff}$.

Given the science goals of, in particular, the SEGUE program, we emphasize two limitations to the accuracy of spectral types derived by the Hammer code:

- The Hammer code uses spectral indices derived from dwarf standards; spectral types assigned to giant stars will likely have larger, and systematic, uncertainties.

- The Hammer code was developed in the context of SDSS-I's high Galactic latitude spectroscopic program; the use of broadband color ratios in the indices will likely make the spectral types estimated by the Hammer code particularly sensitive to reddening. Spectral types derived in areas of high extinction (i.e., low-latitude SEGUE plug-plates) should be considered highly uncertain until verified with reddening-insensitive spectral indices.

3.11 Distance Estimates

A number of techniques are presently being explored by members of the SEGUE team in order to derive the best available estimates of distances for stars in the SDSS/SEGUE database. Many rely on the existence of either theoretical or empirical transformations of the substantial amount of photometric data that exists for Galactic clusters obtained with photometric systems other than *ugriz*. An et al. (2008) have recently reported accurate globular and open cluster fiducials for a set of 20 clusters observed by SDSS, making use of crowded-field photometric measurements. We expect to revise the distance estimates obtained by the SSPP, based on this work, in the near future.

For now, the SSPP assigns preliminary distance estimates for stars of different luminosity classifications based on the empirical fits of Beers et al. (2000) to the observed color-magnitude diagrams of Galactic clusters of different metallicities and with reasonably well-known distances (in the Johnson V, $B-V$ system). For convenience, we use the same transformations as mentioned above, based on the work of Zhao & Newberg (2006); $V = g - 0.561(g-r) - 0.004$, and $B - V = 0.187 +$

$0.916(g-r)$.

Beers et al. (2000) argue that their distances should be accurate to on the order of 10−20%; a typical value of 15% can be adopted for our distance estimates, although this needs to be confirmed with future work.

The SSPP does *not* make a stellar luminosity classification, but rather, it provides the atmospheric parameters from which the user can make an appropriate choice. Distance estimates are obtained for the following rough luminosity classes: Dwarf, Main-Sequence Turnoff, Giant, Asymptotic Giant Branch, and Field Horizontal-Branch. Note that distance estimates are obtained for all (feasible) cases where a star may fall into one or more of these classifications, but only one of the listed distances is likely to apply to a given star. The choice is left up to the user.

An alternative method for distance estimates in the SSPP is described by Allende Prieto et al. (2006), to which the interested reader is referred for a detailed description.

3.12 Empirical Uncertainties of Stellar Parameters of the SSPP

By directly comparing the stellar parameters obtained by the SSPP with the results of the high resolution analyses, The typical empirical errors of the stellar parameters delivered by the SSPP have been determined. Paper III describes in details the reduction of the data, comparison with spectral libraries, and other procedures of how to derive those quantities so that we refer to the paper for the detailed information. Therefore, this section will be a summary of Paper III.

We made use of the same sample (125 stars) which were used to compare the parameters from the individual methods with those of the two high resolution analyses. We divided the sample into two groups: HET (81 stars) and *OTHERS* (44 stars).

HET group consists of stars observed by Hobby-Eberly Telescope and *OTHERS* for others telescopes such as SUBARU, KECK-I and II. Table 3.2 summarizes the observation. The stars in HET sample were analyzed by the first author (C.A.) in the paper and the second author (T.S.) for the *OTHERS* sample.

By comparing S^4N (Allende Prieto et al. 2004) catalog as literature values with the results of the analysis of the HET sample, we estimated for the high resolution analysis the uncertainties of 90 K, 0.13 dex, and 0.05 dex $T_{\rm eff}$, log g, and [Fe/H], respectively. The comparison of the analysis of the HET sample with the SSPP returns the uncertainties of 158 K, 0.25 dex, and 0.12 dex $T_{\rm eff}$, log g, and [Fe/H], respectively. Therefore, considering the errors from the comparison with the S^4N catalog as bench-marking uncertainties, by quadratically subtracting the uncertainties from the S^4N catalog comparison from the SSPP results, we empirically determine the uncertainties in the stellar parameters estimated by the SSPP. The end results of the uncertainties are σ ($T_{\rm eff}$) = 130 K, σ (log g) = 0.21 dex, σ ([Fe/H]) = 0.11 dex.

3.13 SUMMARY

We have described the development and execution of the SEGUE Stellar Parameter Pipeline (SSPP), which makes use of multiple approaches in order to estimate the fundamental stellar atmospheric parameters (effective temperature, $T_{\rm eff}$, surface gravity, log g, and metallicity, parameterized by [Fe/H]) for stars with spectra and photometry obtained during the course of the original Sloan Digital Sky Survey (SDSS-I) and its current extension (SDSS-II/SEGUE).

The use of multiple approaches allows for an empirical determination of the internal errors for each derived parameter, based on the range of the reported values from each method. Among 128,000 spectra from 200 SEGUE plug-plates, typical internal errors for stars which have derived stellar parameters available, from the SSPP, in the range 4500 K $\leq T_{\rm eff} \leq$ 7500 K, are $\sigma(T_{\rm eff})$ = 70 K (s.e.m), σ(log g) = 0.18 (s.e.m),

and σ([Fe/H]) = 0.07 (s.e.m). Paper III points out that the internal scatter estimates obtained from averaging the multiple estimates of the parameters produced by the SSPP underestimate the external errors, owing to the fact that several methods in the SSPP use similar parameter indicators and atmospheric models.

The results of a comparison with an average of two different high-resolution spectroscopic analyses of over 100 SDSS-I/SEGUE stars suggests that the SSPP is able to determine $T_{\rm eff}$, log g, and [Fe/H] to precisions of 141 K, 0.23 dex, and 0.23 dex, respectively, after combining small systematic offsets quadratically for stars with 4500 K $\leq T_{\rm eff} \leq$ 7500 K. These errors differ slightly from those obtained by Paper III ($\sigma(T_{\rm eff})$ = 130 K, $\sigma(\log g)$ = 0.21 dex, and σ([Fe/H]) = 0.11 dex), even though they share a common set of high-resolution calibration observations. This arises because Paper III derived the external uncertainties of the SSPP only taking into account the stars observed with the HET (on the grounds of internal consistency). The sample referred to as *OTHERS* in Paper III exhibits somewhat larger scatter in its parameters, when compared with those determined by the SSPP. Observation of several hundred additional stars from SDSS-I/SEGUE with HET is now underway. Thus, in the future, we will be able to use a homogeneous sample gathered by HET in our tests. Also, additional high-resolution data for stars outside of our adopted temperature range will enable tests for both cooler ($T_{\rm eff} <$ 4500 K) and warmer ($T_{\rm eff} >$ 7500 K) stars.

Considering the average internal scatter from the multiple approaches and the external uncertainty from the comparisons with the high-resolution analysis together, the typical uncertainty in the stellar parameters delivered by the SSPP are $\sigma(T_{\rm eff})$ = 157 K, $\sigma(\log\ g)$ = 0.29 dex, and σ([Fe/H]) = 0.24 dex, over the temperature range 4500 K $\leq T_{\rm eff} \leq$ 7500 K.

However, it should be kept in mind that the errors stated above apply for the very highest S/N spectra obtained from SDSS ($S/N >$ 50/1), as only quite bright stars were targeted for high-resolution observations. The uncertainty of the parameter

estimates will be larger, with declining S/N, as shown in Table 3.5. In addition, outside of the quoted temperature range (4500 K $\leq T_{\rm eff} \leq$ 7500 K), we presently do not have sufficient high-resolution spectra to fully test the parameters obtained by the SSPP.

The results of a comparison to literature values of the overall [Fe/H] of selected member stars in a sample of Galactic open and globular clusters suggests that the metallicities estimated by the SSPP are within $\pm$ 0.1 dex of these values, for a wide range of colors ($-0.3 \leq g-r \leq 1.3$), down to a spectroscopic signal-to-noise of $S/N =$ 10/1. The following chapter discusses this analysis in great detail, and indicates that the valid range of the effective temperature for determining the stellar parameters by the SSPP is wider than that presently testable with the high-resolution analysis. Once we obtain high-resolution spectroscopy of hotter ($T_{\rm eff} >$ 7500 K) and cooler ($T_{\rm eff} <$ 4500 K) stars, we will be able to better confirm the color range where the SSPP is capable of estimating accurate parameters.

Approximate spectral types are assigned for stars, based on two methods, with differing limitations. A set of distance determinations for each star is also obtained, although future work will be required in order to identify the optimal method.

We conclude that the SSPP determines, with sufficient accuracy and precision, radial velocities and atmospheric parameter estimates, for stars in the effective temperature range from 4500 K to 7500 K, to enable detailed explorations of the chemical compositions and kinematics of the disk and halo populations of the Galaxy.

Chapter 4: Validation with Galactic Open and Globular clusters

4.1 Photometric and Spectroscopic Data

Galactic globular and open clusters are nearly ideal testbeds for validation of the stellar atmospheric parameters estimated by the SSPP. In most clusters, it is expected that their member stars were born simultaneously out of well-mixed, uniform-abundance gas at the same location in the Galaxy. Therefore, with the exception of effects due to post main-sequence evolution, primordial variations in carbon and nitrogen, or contamination from binary companions that have transferred material, the member stars should exhibit very similar elemental abundance patterns. Three of the clusters in our study, M 13, M 15, and M 2, have well known CN variations that extend to the main-sequence turnoffs (Smith & Briley 2006 for M 13; Cohen, Briley, & Stetson 2005 for M 15; Smith & Mateo 1990 for M 2). However, these abundance variations can be ignored when deriving metallicities from regions of the spectra that do not include CH, CN, or NH features, as is the case with most of our techniques (those that may be affected by the presence of such features are automatically de-selected in the determination of the adopted [Fe/H]).

True cluster members should exhibit small radial velocity differences with respect to their parent clusters. Furthermore, it is possible to examine theoretical predictions of temperatures and surface gravities for member stars that lie along the cluster

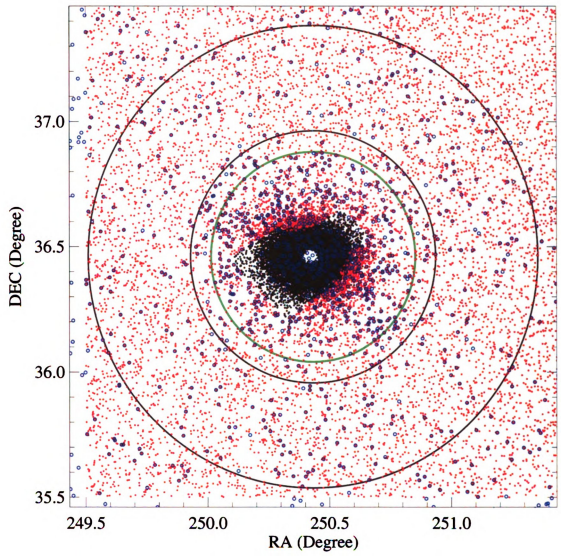


Figure 4.1 Stars with available photometry in the field of M 13. The red dots represent photometry from the SDSS PHOTO pipeline, while the black dots are from the crowded-field photometry analysis. Blue open circles indicate stars with available SDSS spectroscopy. The green circle is the tidal radius. The area inside this radius is regarded as the cluster region; the annulus between the two black circles is considered the field region.

main sequence (MS), red giant branch (RGB), or horizontal branch (HB) in color-magnitude diagrams (CMDs). As part of tests of the SEGUE star-selection algorithm (Adelman-McCarthy et al. 2008) and the SSPP, and during normal SEGUE operation, we have obtained *ugriz* photometry and medium-resolution ($R \sim 2000$) spec-

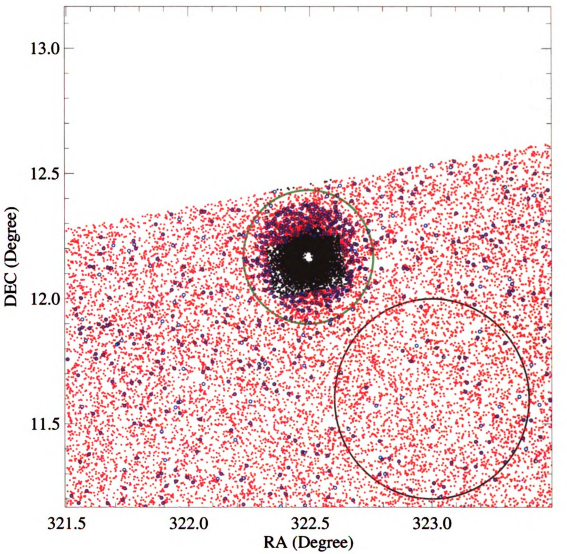


Figure 4.2 Same as Figure 4.1 but for M 15. Unlike M 13, the field region for M 15 is not annuli centered on the clusters, due to the proximity of these clusters to the edges of the scans. The region inside the black circle is taken for the field region. This is taken as the region where likely member stars are considered. See Chapter 4.3 for likely member selection.

troscopy for large numbers of stars along lines of sight toward the globular clusters M 13, M 15, and M 2 and the open clusters NGC 2420 and M 67. Below we discuss these photometric and spectroscopic data in more detail.

4.1.1 Photometric Data

The first-pass photometric data for each of the clusters used in the present study were secured by querying the DR-3 (Abazanjian et al. 2005), DR-5 (Adelman-McCarthy et al. 2007), and DR-6 (Adelman-McCarthy et al. 2008) releases from the SDSS Catalog Archive Server (CAS).

Figure 4.1 illustrates one of the primary challenges in working with data for clusters obtained with SDSS – the automated PHOTO pipeline (Lupton et al. 2001) was not designed to adequately deal with crowded fields such as the central regions of globular clusters. As a result, essentially all of the stars in this region (which are by definition the most likely ones to be cluster members) do not have reported apparent magnitudes in the SDSS CAS. To circumvent this limitation as much as possible, we have instead performed crowded field photometry for the center of the clusters, using the DAOPHOT/ALLFRAME suite of programs (Stetson 1987, Stetson 1994). A full description of the methods used and the photometric measurements obtained is provided by An et al. (2008). Briefly, DAOPHOT was run on each image, and the five images of each field (one for each filter) were then simultaneously run through ALLFRAME. HSTDAOGROW, which is a modified version of DAOGROW (Stetson 1990), was used to derive aperture corrections to the point-spread-function photometry for the SDSS aperture radius of $7.4''$. Finally, the DAOPHOT photometry was tied to the native 2.5-meter photometric system, using data in fields farther away from the clusters. This procedure also permits a check on the techniques used by the SDSS PHOTO pipeline in regions outside the cluster where the areal density of sources on the sky is sufficiently low.

After completing the above procedures, we finally combine the results from the PHOTO pipeline with those from the crowded-field photometry to obtain an almost complete catalog of *ugriz* photometry for stars in the region of each of our program clusters. All photometric data are corrected for extinction and reddening by appli-

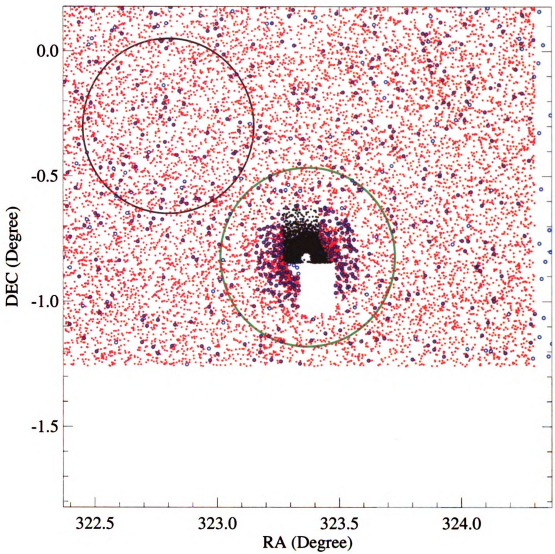


Figure 4.3 Same as Figure 4.1 but for M 2. Unlike M 13, the field region for M 2 is not annuli centered on the clusters, due to the proximity of these clusters to the edges of the scans. The region inside the black circle is taken for the field region. This is taken as the region where likely member stars are considered. See Chapter 4.3 for likely member selection.

cation of the Schlegel, Finkbeiner, & Davis (1998) maps. The average reddening ($E(B-V)$) for stars in the direction of these clusters is 0.017, 0.110, 0.045, 0.041, 0.032 for M 13, M 15, M 2, NGC 2420, and M 67, respectively. An et al. (2008) also adopt very similar values of the reddening. Comparing with the literature values

listed in Table 4.1, most of the average reddenings of the clusters agree within about 0.02 mags of our adopted values.

4.1.2 Spectroscopic Data

The spectroscopic data discussed in this section were obtained during the course of SEGUE tests and normal SEGUE observations.

An initial set of candidate member stars of the globular and open clusters studied in this thesis were selected on the basis of photometric and astrometric data (proper motions) from the literature. The central cores of the clusters were not targeted because the PHOTO pipeline does not resolve the very crowded fields into single star detections, and also due to limitations on the separations of the fibers during the spectroscopic follow-up stage. The primary method for selecting member candidates was performed by plotting a photometric CMD for a given cluster, and choosing stars from regions of this diagram that correspond to location on the MS turnoff or RGB of the cluster. An additional list of bright stars for M 15 and M 2 with previously available proper motions consistent with membership in the clusters was provided by Cudworth (1976 and private communication) and Cudworth & Rauscher (1987). Other stars in the fields of these clusters were used to fill spectroscopic fibers using the default SEGUE target selection algorithm (Adelman-McCarthy et al. 2008). While many of these additional targets turned out to be stars from the general field populations, a significant fraction turned out serendipitously to be members of the clusters.

For M 13, three specially designed plug-plates were obtained. Two of the three plug-plates followed the standard SEGUE target selection procedure (Adelman-McCarthy et al. 2008) of sampling stars with a variety of spectral types based on the SDSS imaging and PHOTO processing. An additional set of likely M 13 members, including several stars that were saturated in the SDSS image ($r < 14.5$) and with coordi-

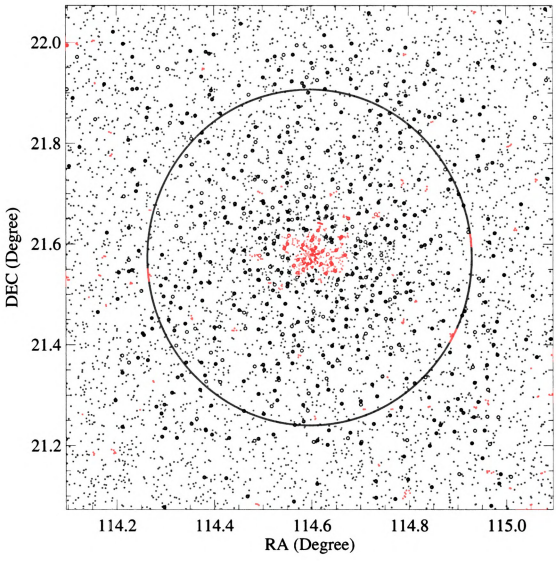


Figure 4.4 Same as Figure 4.1 but for NGC 2420. The green circle is $18'$ in radius; this is taken as the region where likely member stars are considered. See Chapter 4.3 for likely member selection.

nates from Cudworth & Monet (1979) and Cudworth (private communication), were added to the target list for the third plug-plate with high priority (bumping ordinary SEGUE targets), in order to obtain spectra of several likely giant-branch and horizontal-branch members.

In the case of NGC 2420, the stars chosen for spectroscopy were primarily tar-

geted from the SDSS photometry obtained by the PHOTO pipeline, using the normal SEGUE target selection algorithm. Additional stars with apparent magnitudes in the range $14.5 < g < 20.5$ that fell within 0.5 degrees from the center of NGC 2420 were also targeted for spectroscopy. However, due to crowding, if two objects were within $55''$ of one another, then only one received a fiber. Thus, not every star in the central region of NGC 2420 was targeted. There were about 480 objects selected in this way, including a number of non-cluster members that are located in the NGC 2420 field.

Table 4.1: Properties of the Clusters[i]

	M 13 (NGC 6205)	M 15 (NGC 7078)	M 2 (NGC 7089)	NGC 2420	M 67 (NGC 2682)
RA (J2000)	16:41:41.5	21:29:58.3	21:33:29.3	07:38:23	08:51:18
DEC (J2000)	+36:27:37	+12:10:01	−00:49:23	+21:34:24	+11:48:00
(l, b)	(59.0, +40.9)	(65.0, −27.3)	(58.4, −35.8)	(198.1, +19.6)	(215.7, +31.9)
[Fe/H]	−1.54	−2.26	−1.62	−0.44	+0.02
m - M	14.48	15.37	15.49	12.54	9.97
V_r(km s^{-1})	−245.6	−107.0	−5.3	75.5	32.9
$E(B-V)$	0.02	0.10	0.06	0.03	0.06
r_t	25.18′	21.50′	21.45′	5′	25′

For M 67, the initial targets came from the SDSS imaging data processed by the PHOTO pipeline. However, for this cluster, many candidate members with positions,

[i]The parameter r_t is the tidal radius in arc minutes for M 13, M 15, and M 2 and the apparent diameter in arc minutes for NGC 2420 and M 67 from Dias et al. (2002). The listed distance modulus, m−M, is corrected for extinction. The parameters for the globular clusters, M 13, M 15, and M 2 are from Harris (1996); those for the open clusters NGC 2420 and M 67 are from WEBDA (http://www.univie.ac.at/webda/). The radial velocity (V_r) listed for NGC 2420 and M 67 is the average of the literature values (see Chapter 4.5). The [Fe/H] of NGC 2420 and M 67 is based on the high-resolution spectroscopy described by Gratton (2000).

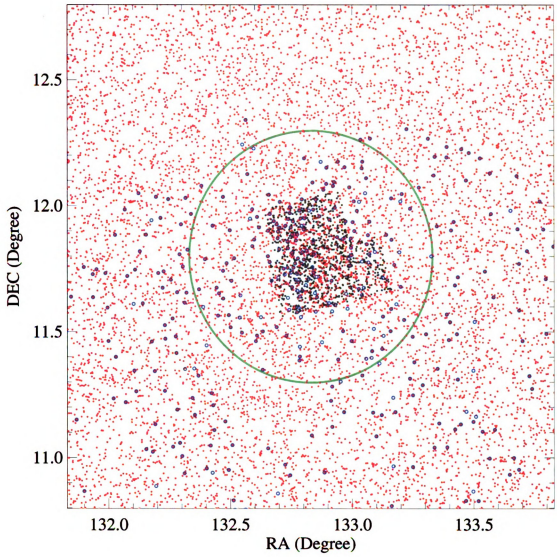


Figure 4.5 Same as Figure 4.1 but for M 67. The green circle is $30'$ in radius; this is taken as the region where likely member stars are considered. See Chapter 4.3 for likely member selection.

magnitudes, and colors from the WEBDA (http://www.univie.ac.at/webda/) catalogs were added to the target lists. The bright targets (with $r < 14$) saturate the SDSS imaging camera, so these were added from the literature (Sanders 1989; Fan et al. 1996). Such bright stars present difficulties for regular SDSS spectroscopic observations (such as scattering light onto adjacent fibers), so there were exposed for

shorter than normal integration times. About 200 very bright stars between about $12 < g < 14$ were targeted.

Note that in each cluster field some stars with no pre-existing *ugriz* photometry from the PHOTO pipeline were also targeted from the catalogs in the literature. For those stars, we obtained *ugriz* photometry from the DAOPHOT procedure.

In total, we obtained SDSS spectroscopy for 1920, 1280, 1280, 1280, and 640 targets, including sky spectra and calibration object spectra, in the fields of M 13, M 15, M 2, NGC 2420, and M 67 respectively. Therefore, the total number of selected member stars will vary from cluster to cluster. The particular clusters that were chosen was essentially set by their presence (or not) in the SDSS-I/SEGUE footprint, since the usual observing process requires that photometry be available prior to spectroscopic targeting. Some otherwise problematic clusters were included as a result. For example, M 2 presents a special challenge for separation of its likely members from the general field population, as its radial velocity is close to zero, where it overlaps strongly with several Galactic stellar populations. In addition, this cluster is the most distant among the sample under investigation; as a result, the spectra obtained are generally of lower S/N than the rest of our sample. However, M 2 is located in the equatorial stripe ($-1.27^\circ < \delta < 1.27^\circ$), which was scanned multiple times during SDSS-I and SDSS-II; hence we have very accurate photometry to employ. For the remaining sample of clusters with available photometry, we attempted to cover as wide a metallicity range as possible for spectroscopic study. The reduced spectra were processed through the SSPP in order to estimate $T_{\rm eff}$, log g, and [Fe/H], among other quantities. Table 4.1 summarizes the global properties of the clusters under consideration in this study, taken from the compilation of Harris (1996) for the globular clusters and from the literature, and WEDBA or Gratton (2000) for the open clusters.

4.2 Radial Velocities

There are two estimated radial velocities provided from the SDSS spectroscopic pipeline. One is an absorption-line redshift obtained by cross-correlating the spectra with templates that were acquired from SDSS commissioning spectra (Stoughton et al. 2002). Another comes from matching the spectra with ELODIE template spectra (Prugniel & Soubiran 2001). In most cases the velocity based on the ELODIE template matches appears to be the best available estimate, as spectra of "quality assurance" stars with multiple measurements show the most repeatable values for this estimator. We adopt this velocity in most of our analysis. A more detailed description of the determination of the best available radial velocity, and of the zero-point offsets in the radial velocities, can be found in Chapter 3.

4.3 Membership Selection from Spectroscopic Samples

Owing to an insufficient number of stars with available spectroscopy for each cluster, it is not possible to obtain a well-defined Color Magnitude Diagram (CMD) based solely on spectroscopically observed stars. Thus, we make use of photometric data in the field of each cluster, and describe below how we obtain a relatively clean CMD for individual clusters, and select likely member stars from the spectroscopic data.

4.3.1 Likely Member Star Selection for Globular Clusters

One of the primary issues that one needs to address when creating a CMD for a star cluster, or for selecting likely member stars, is the removal of contamination from field stars. In order to approximately isolate the likely cluster members from the field stars along the line of sight, we have made use of the CMD mask algorithm

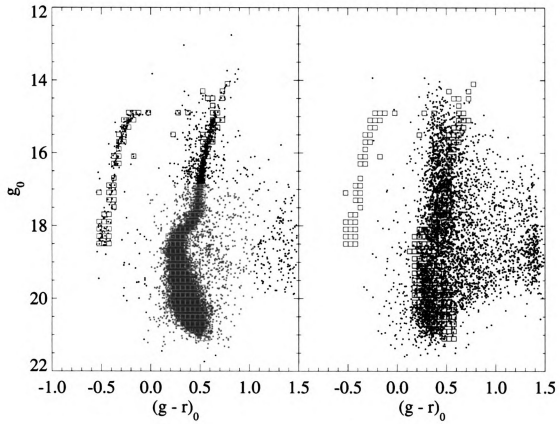


Figure 4.6 Color-Magnitude Diagrams of the M 13 stars inside the tidal radius (left panel), and inside the field region (right panel), shown as black dots. The selected sub-grids from the CMD mask algorithm are shown as red squares in the left panel and green squares in the right panel. These selected sub-grids are used in the analysis.

described by Grillmair et al. (1995). We illustrate the basic idea by application of this algorithm to the M 13 field shown in Figure 4.1. We first select all stars inside the estimated tidal radius ($25.2'$; Harris 1996), shown as the innermost green circle in Figure 4.1. This is regarded as the cluster region. The red dots represent stars with available photometry from the SDSS PHOTO pipeline (Lupton et al. 2001); the black dots are stars with photometry obtained from DAOPHOT. The blue open circles indicate stars with available spectroscopy. We then choose an annulus outside the cluster region, indicated on the figure as the region between the two black circles, as the field or background region.

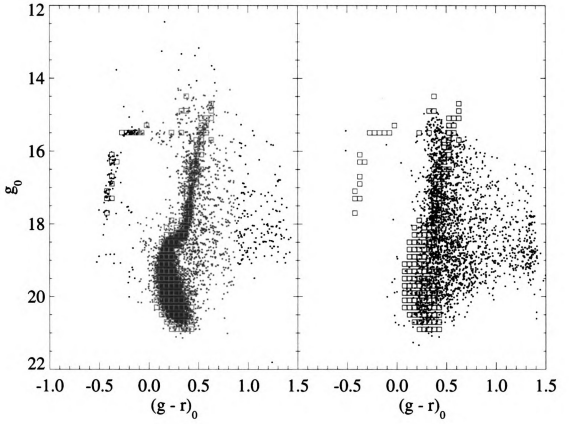


Figure 4.7 Same as Figure 4.6 but for M 15.

We next obtain CMDs of each region, spanning $-1.0 \leq (g-r)_0 \leq 1.5$ and $12 \leq g_0 \leq 22$, and then subdivide these diagrams such that the size of each sub-grid is 0.2 mag wide in g_0 and 0.05 mag wide in $(g-r)_0$ color. The total number of sub-grids for the CMDs in each region is thus 2500 (50×50). Figure 4.6 shows the resulting CMDs of the cluster (left panel) and field (right panel) regions, over-plotted with squares representing the selected sub-grids, obtained as described below.

We first calculate the signal-to-noise (s/n) in each preliminary sub-grid by application of equation 4.1 over the entire CMD region shown in Figure 4.6. Here we assume that the field stars outside the tidal radius are uniformly distributed throughout the annulus area.

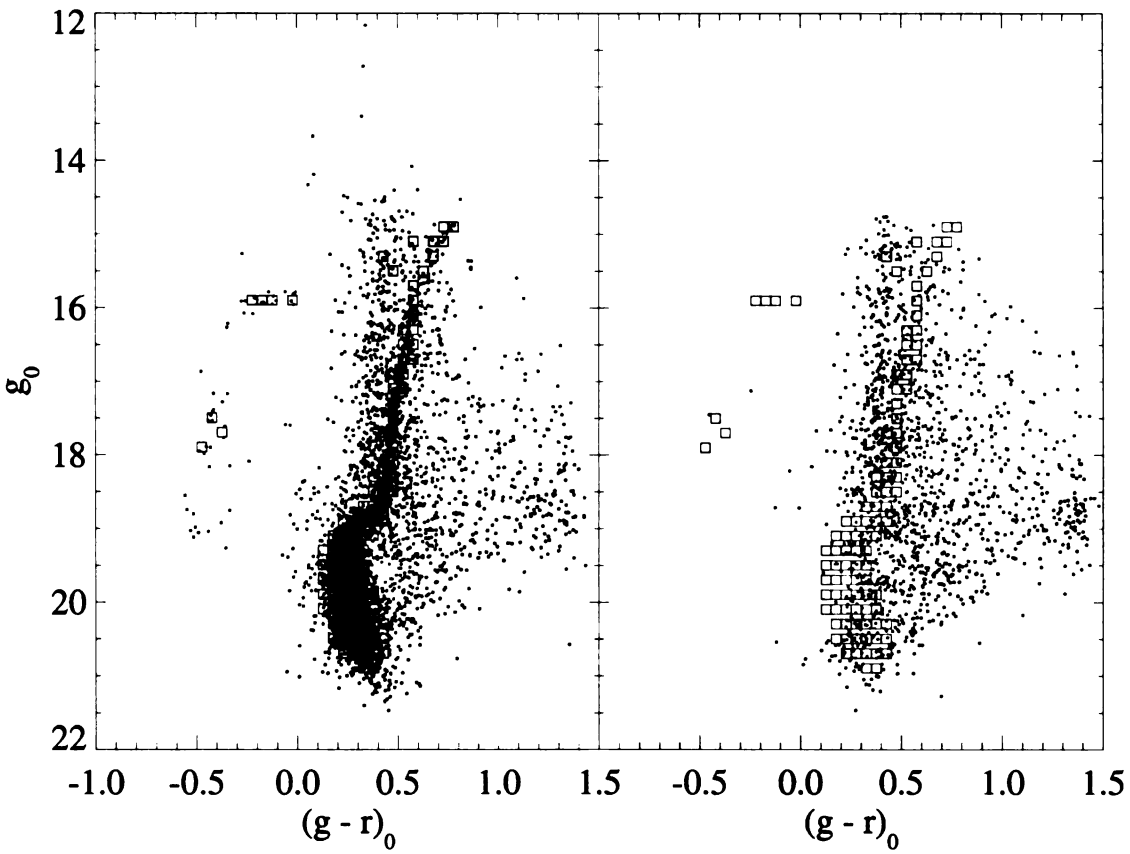


Figure 4.8 Same as Figure 4.6 but for M 2.

$$s/n(i,j) = \frac{n_c(i,j) - g n_f(i,j)}{\sqrt{n_c(i,j) + g^2 n_f(i,j)}}. \tag{4.1}$$

In the above, n_c and n_f refer to the number of stars in each sub-grid with color index i and magnitude index j, counted within the cluster region and field region, respectively. The parameter g represents the ratio of the cluster area to the field area.

The following procedures are applied in order to find the optimal range of colors and magnitudes that correspond to the likely members of each cluster. First, we sort the elements of $s/n(i,j)$ in descending order, so that we obtain a one-dimensional array of $s/n(i,j)$ with index l; the array element with the highest $s/n(i,j)$ corresponds to $l = 1$. The next step is to obtain star counts in gradually larger regions of the

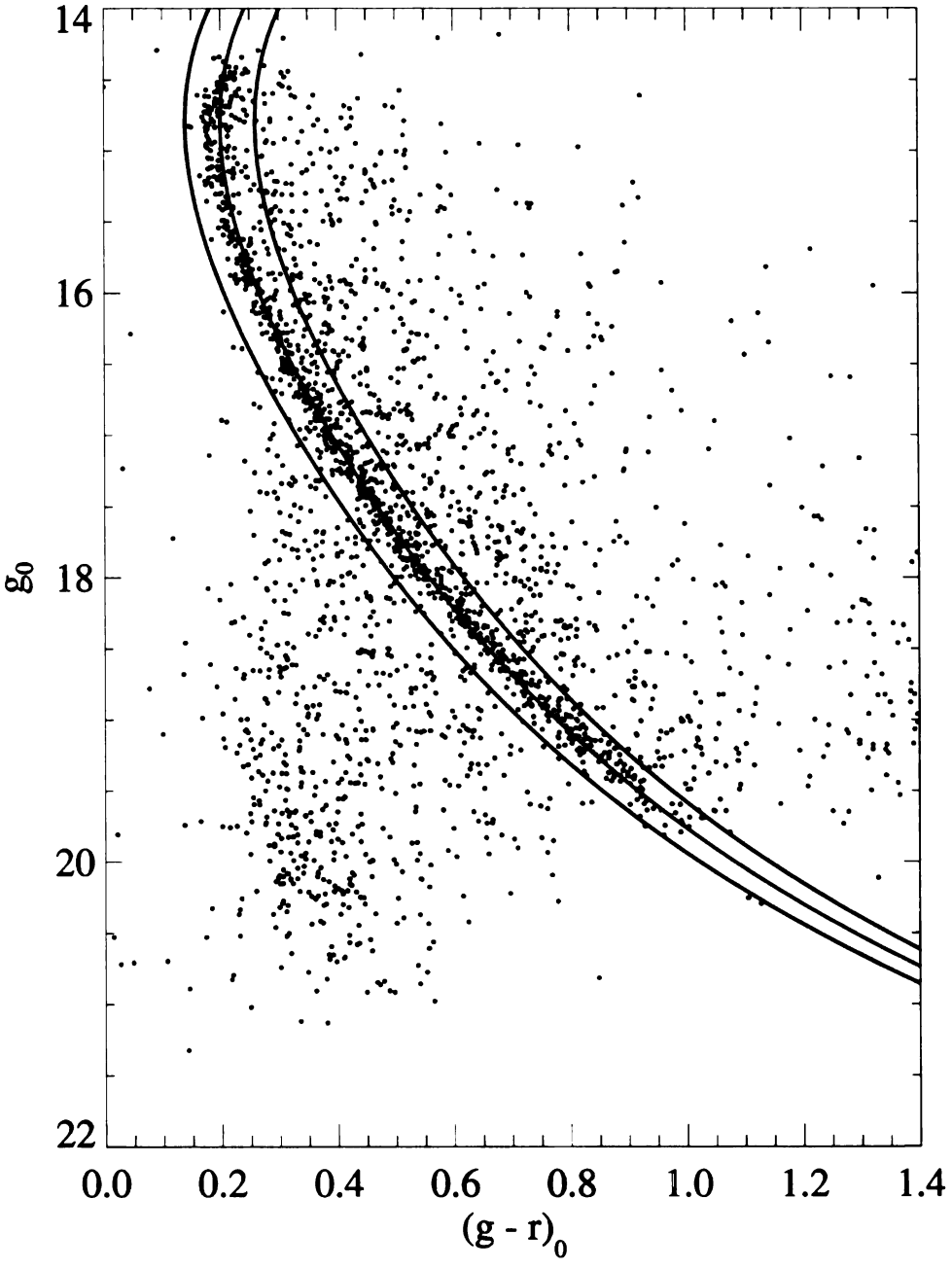


Figure 4.9 Color-Magnitude Diagrams of the NGC 2420 field. The red line is the fiducial obtained by application of a robust fourth-order polynomial fit. The stars inside the blue lines, determined by offsets from the adopted fiducial of ± 0.06 mags in $(g-r)_0$, are regarded as likely member stars from the photometric sample.

CMDs. The accumulated area is represented as $a_k = ka_l$, where $a_l = 0.01$ mag^2, which is the same for all sub-grids, and is the area of a single sub-grid in the CMD

array, and the k is the number of sub-grids to combine. Finally, the cumulative signal-to-noise ratio, $S/N(a_k)$, as a function of a_k, is calculated from:

$$S/N(a_k) = \frac{N_c(a_k) - gN_f(a_k)}{\sqrt{N_c(a_k) + g^2 N_f(a_k)}} \tag{4.2}$$

where

$$N_c(a_k) = \sum_{l=1}^{k} n_c(l), \quad N_f(a_k) = \sum_{l=1}^{k} n_f(l) \tag{4.3}$$

The parameter $n_c(l)$ denotes the number of stars within the cluster region having ordered color-magnitude index l; $n_f(l)$ represents the same quantity for the field region. Based on the maximum value of $S/N(a_k)$, a threshold value of s/n is picked in order to select high-contrast surface-density areas (i.e, high s/n) between the cluster and field regions. These are considered to be the sub-grids that contain likely cluster members. After removing single-star events in areas of the CMDs where the field-star density is low, all stars in sub-grids with $s/n(i,j)$ greater than the threshold value of s/n are selected. These stars are considered as the photometrically likely member stars for a given cluster.

The red squares shown in the left panel of Figure 4.6 are the sub-grids with s/n greater than the threshold value; the corresponding sub-grids in the field region are shown as green squares in the right panel of this figure. Figure 4.11 depicts the CMD of the selected likely members of M 13 from the photometry data, shown as black dots. The same procedures are performed to differentiate the likely member stars of M 15 and M 2, based on photometry alone. Figures 4.2 and 4.3 show fields in the the vicinity of M 15 and M 2, respectively. Due to the lack of photometry data (the available scans do not allow for full regions, centered on the cluster, to be

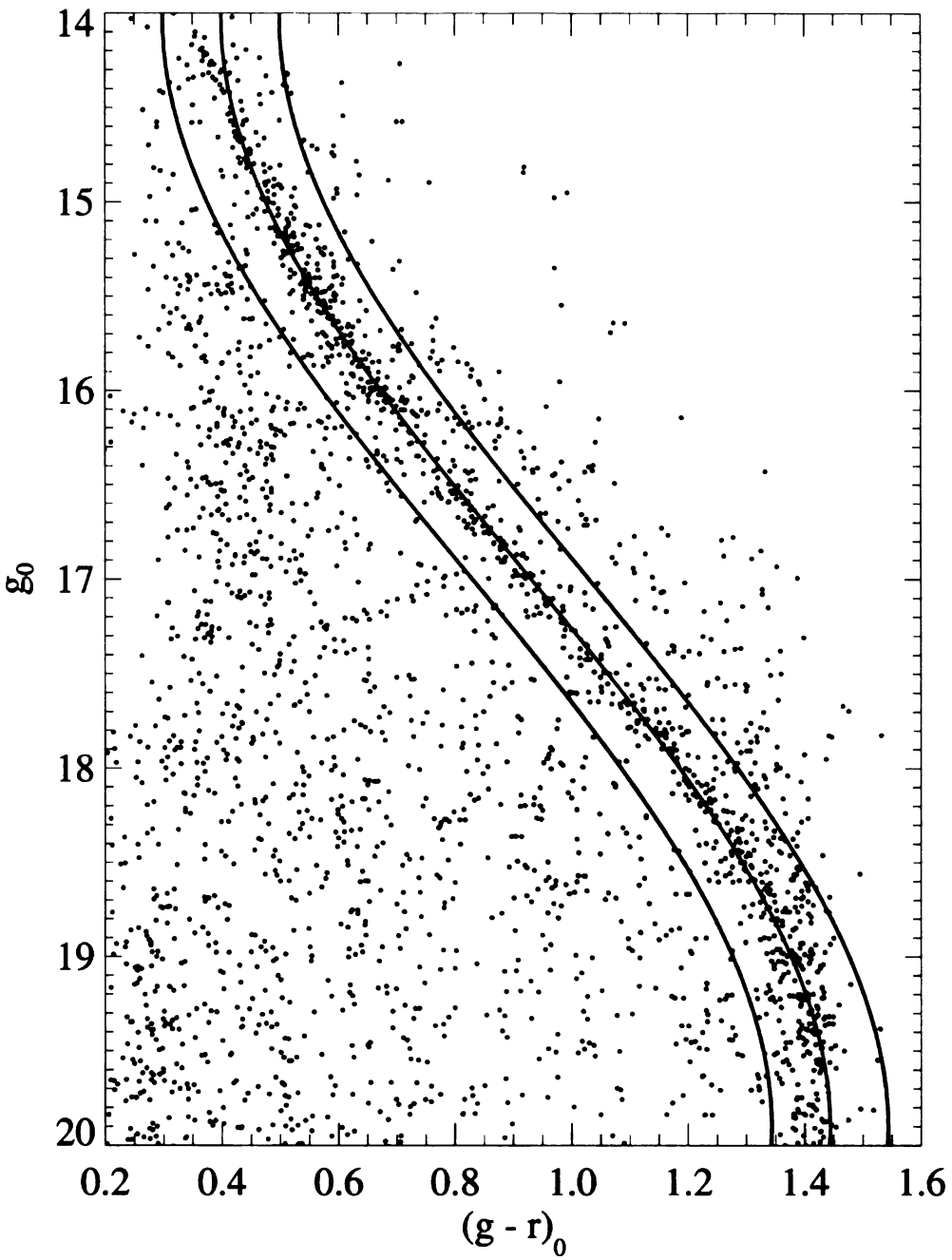


Figure 4.10 Color-Magnitude Diagrams of the M 67 field. The red line is the fiducial obtained by application of a robust fourth-order polynomial fit. The stars inside the blue lines, determined by offsets from the adopted fiducial of $\pm$ 0.10 mags in $(g-r)_0$, are regarded as likely member stars from the photometric sample.

examined), the field regions (black circles in the figure) are offset from the clusters. Furthermore, the cluster region for M 15 is a bit smaller than the tidal radius for this

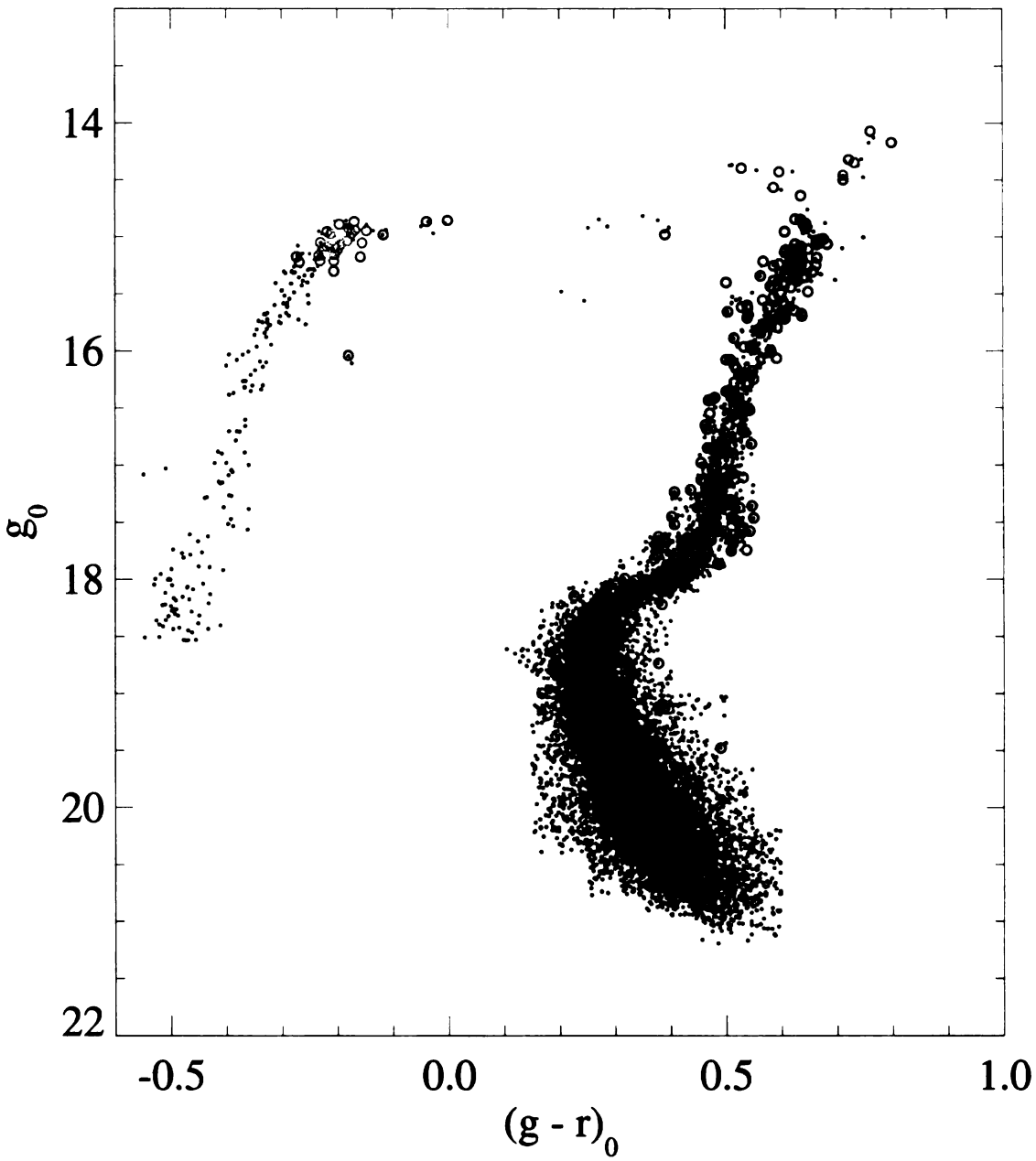


Figure 4.11 The M 13 Color-Magnitude Diagram based on the likely member stars (black dots) selected from the photometric sample. The likely members identified from the spectroscopic sample are indicated with red open circles.

cluster. Choosing a smaller region for M 15 doesn't affect our analysis, since the full tidal radius of M 15 is considered as we select likely members from the spectroscopic sample. Figures 4.7 and 4.8 show the CMDS of the cluster and field regions for M 15

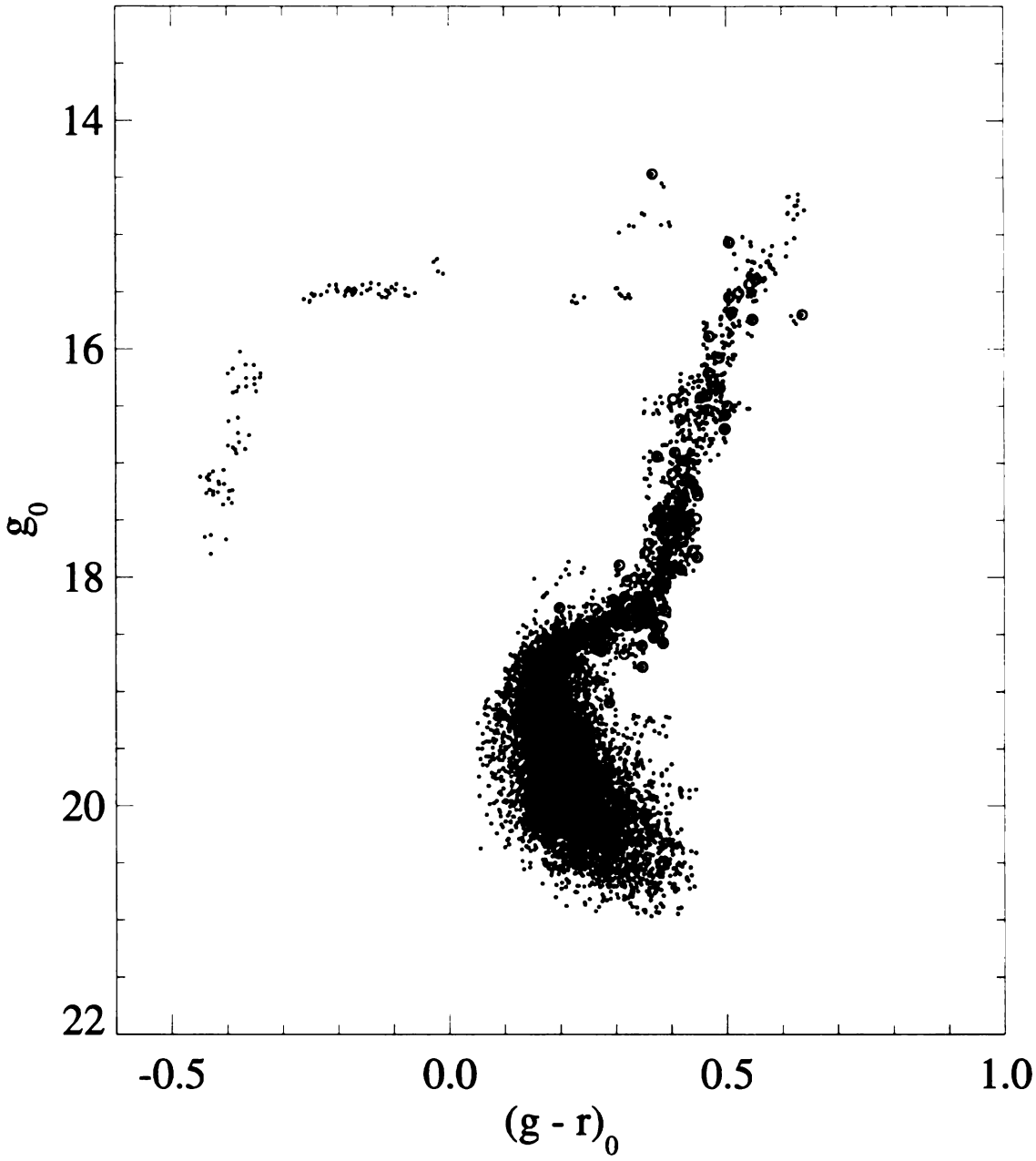


Figure 4.12 Same as Figure 4.11 but for M 15.

and M 2, respectively, with the sub-grids determined.

We now proceed to select the stars that are likely members of the globular clusters from the available spectroscopic sample. This step begins by selection of the stars within the cluster tidal radii that pass the photometric criterion for membership,

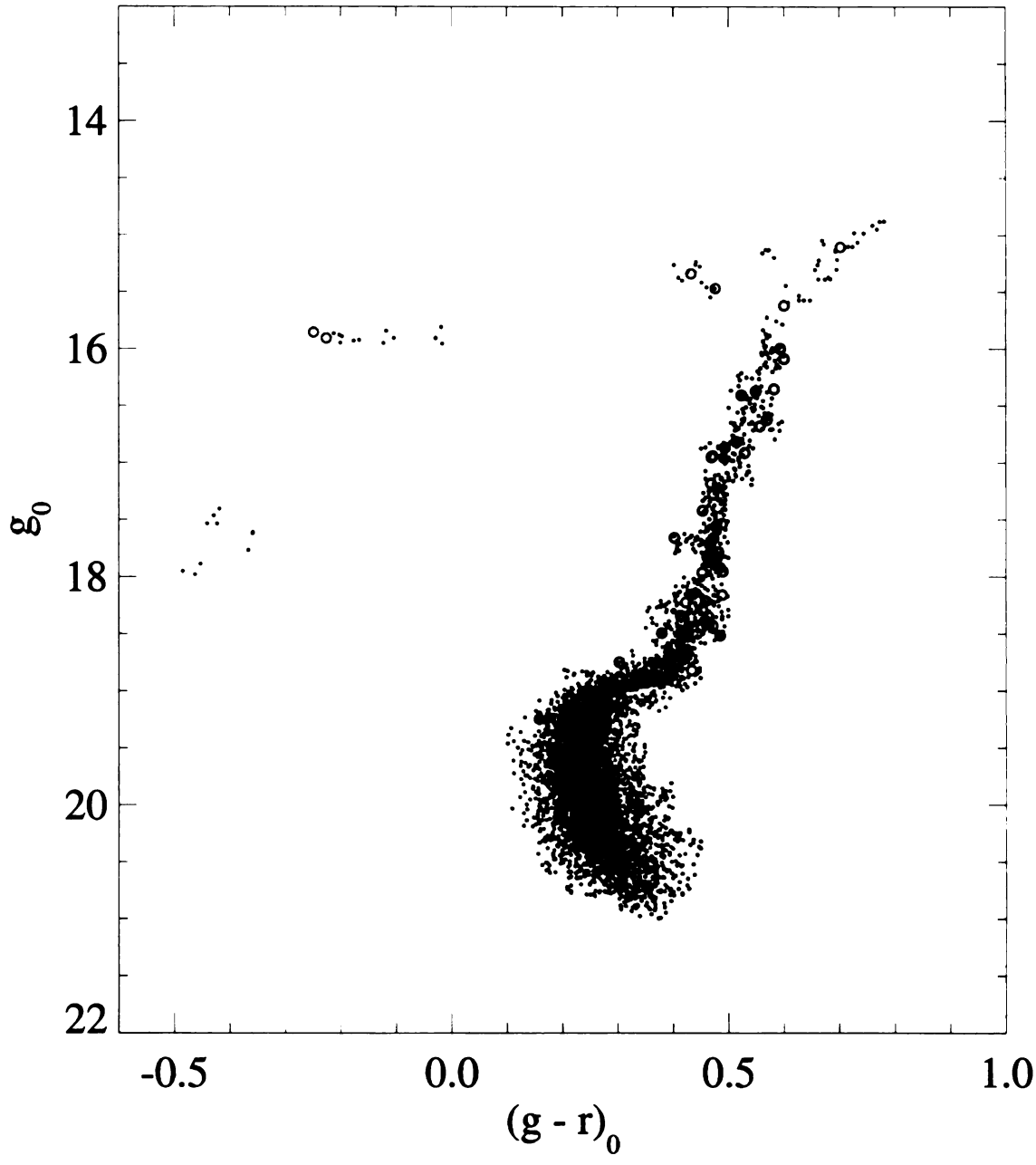


Figure 4.13 Same as Figure 4.11 but for M 2.

based on their location on the cluster CMDs according to the algorithm described above.

Figure 4.11 displays the cleaned CMD of M 13, overplotted with the likely members from the spectroscopic sample (shown as red circles). The same procedures are

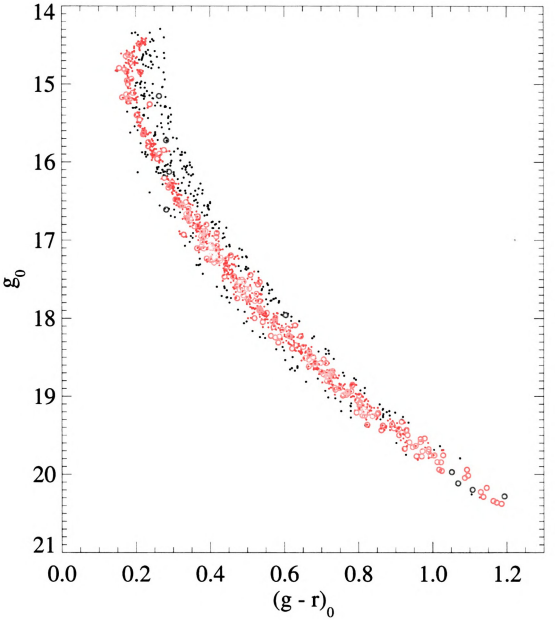


Figure 4.14 Same as Figure 4.11 but for NGC 2420.

carried out to identify likely member stars of M 15 and M 2 from their spectroscopic data. Figures 4.12 and 4.13 are the cleaned CMDs of M 15 and M 2, respectively, with the likely members indicated by the red open circles. At this stage of the analysis there are 458 likely members for M 13, 164 for M 15, and 105 for M 2 identified.

Additional cuts, based on the derived metallicity estimates and RVs, in order to select "true member stars", are described in Chapter 4.4.

4.3.2 Likely Member Star Selection for Open Clusters

Since the fields of nearby open clusters are not as crowded as those of globular clusters, the signal-to-noise ratio between the cluster region and the background region is not sufficiently high to select likely cluster members by means of the CMD mask algorithm (see Figure 4.4 and 4.5). As an alternative, we first obtain a fiducial line for an open cluster (including its main sequence and sub-giant branch, if it exists) by use of an robust polynomial fitting procedure. As an example, Figure 4.9 displays the CMD of the NGC 2420 field inside a radius of 0.3 degrees from the center of the cluster. According to the open cluster catalog of Dias et al. (2002), the apparent diameter of this cluster is only $5^{'}$ on the sky, but we prefer to adopt a $18^{'}$ radius, in order to include as many member stars as possible. The red line is the fiducial line derived from the robust polynomial fit. The blue lines are the upper and lower limits (fiducial ± 0.06 dex in $(g-r)_0$), determined by eye. Stars from the spectroscopic sample that fall within the $18^{'}$ radius and inside the blue limit lines in Figure 4.9 are identified.

A similar procedure is applied to M 67, except that a $30^{'}$ (apparent diameter of $25^{'}$; Dias et al. 2002) radius and fiducial $\pm$ 0.10 mag in $(g-r)_0$ is used. Figure 4.14 and 4.15 depict the selected likely member stars as red circles (from the spectroscopic data) and black dots (from the photometry data). Based on this selection method, there are 238 and 65 (66) for NGC 2420 and M 67, respectively. The first listed number for M 67 indicates the stars with available estimates of [Fe/H] from the SSPP, while the quantity in parentheses represents the number of stars with available radial velocities (RVs). Additional cuts, based on the derived metallicity estimates and RVs, in order to select "true member stars", are described below.

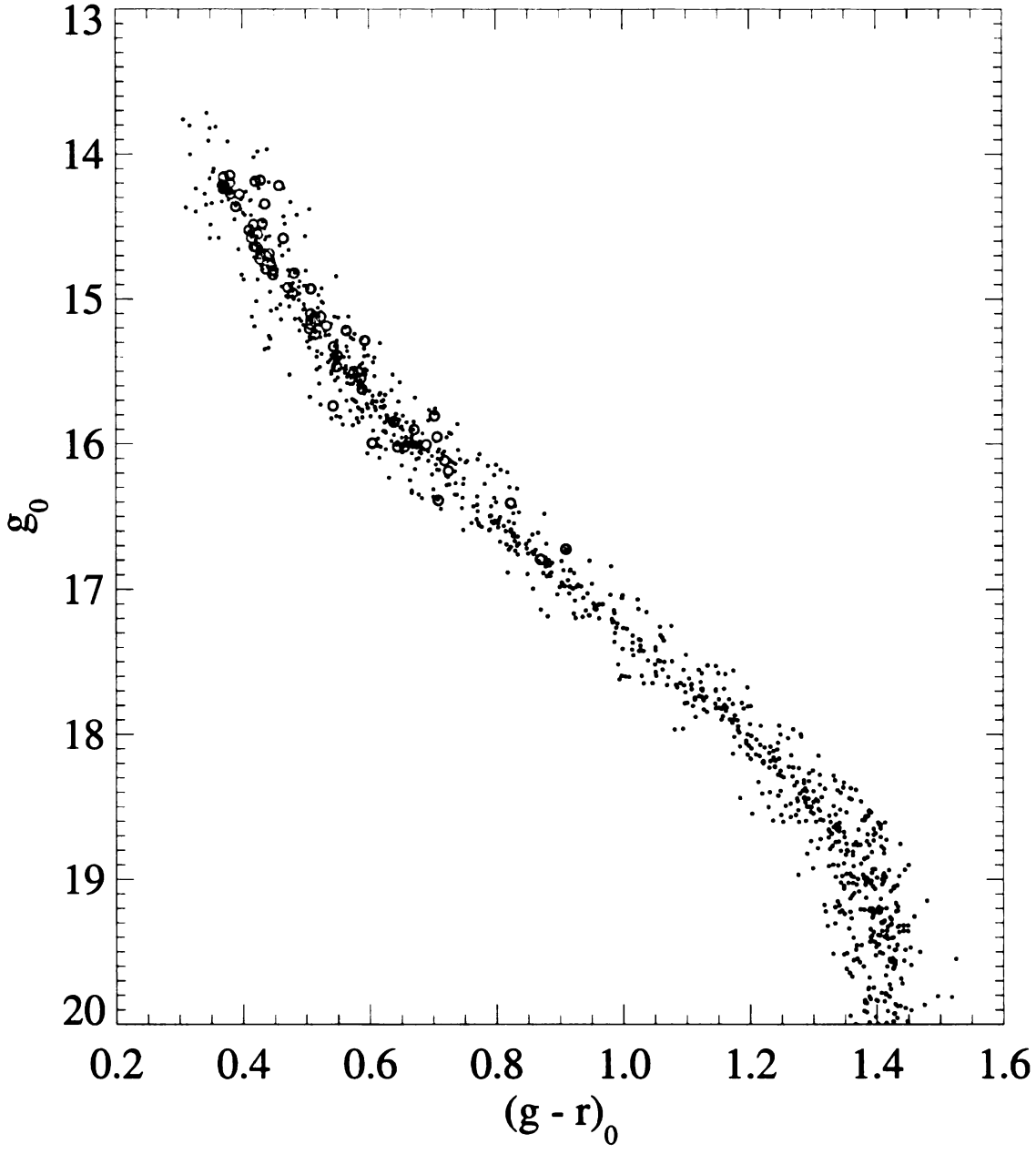


Figure 4.15 Same as Figure 4.11 but for M 67.

4.4 Determination of Overall Metallicities and Radial Velocities of the Clusters

In order to investigate the accuracy of our derived metallicities and RVs, we now consider the global distribution of these parameters obtained from the current version

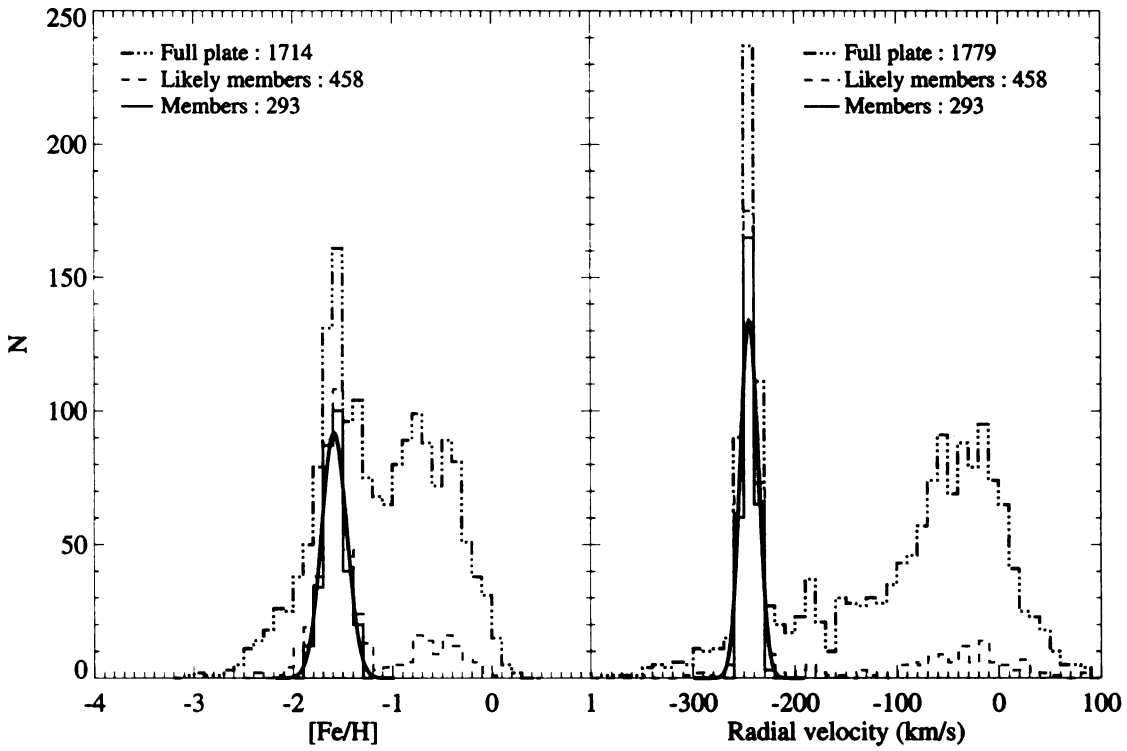


Figure 4.16 Distributions of [Fe/H] and radial velocity for stars in the direction of M 13. Gaussian fits (blue solid curves) to the distribution of the selected true members, shown in the green histograms, are over-plotted.

of the SSPP for the likely cluster members. In this section, we describe a method to isolate "true member stars" from the selected likely member stars from the spectroscopic samples described above. We then use these subsamples to determine our best estimates of the overall metallicities and RVs of the clusters considered in this study.

4.4.1 Selection of True Members

We establish the criteria for carrying out metallicity and RV cuts as follows.

The left panel of Figure 4.16 illustrates the [Fe/H] distribution for three different subsamples of stars in the region of the globular cluster M 13. The first, shown as the black dot-dashed line, represents the distribution of derived metallicities for the 1714 stars with available estimates of [Fe/H] along the line of sight to this cluster. Note

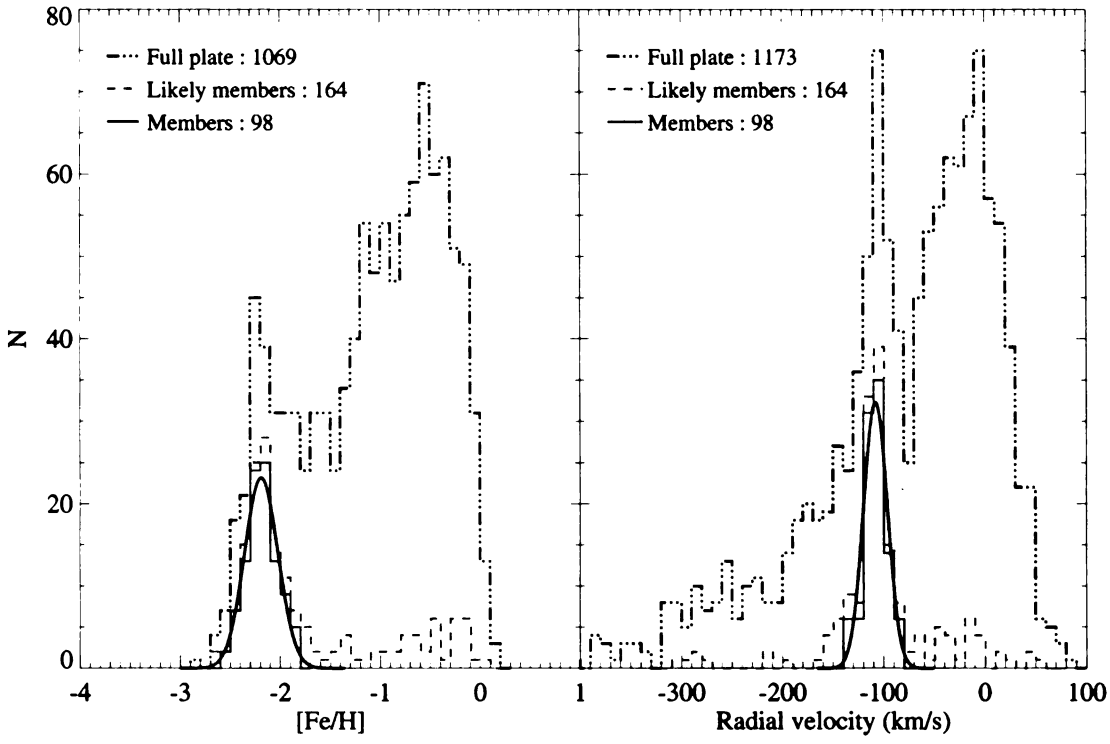


Figure 4.17 Same as Figure 4.16 but for M 15.

that this distribution includes numerous stars that cannot be considered members of the cluster, as they cover a much wider range of [Fe/H] than might be expected if they were drawn exclusively from the cluster member population. The dot-dashed line in the right panel of Figure 4.16 shows the RV distribution of these same stars.

The red dashed line in the left panel of Figure 4.16 is the distribution of [Fe/H] for the 458 likely members selected from the spectroscopic sample as described in §3. We obtain a Gaussian fit to the *highest peak* of the distribution of these stars (red dashed line in Figure 4.16), and obtain an estimate of the mean (<[Fe/H]>) and standard deviation (σ) for this distribution. Similar fits are obtained for the distribution of RVs for the likely members shown in the right panel of Figure 4.16. On the basis of these fits, we now trim likely outliers by application of a 2-σ clipping procedure, for example:

$$< [\mathrm{Fe/H}] > -2\sigma_{[\mathrm{Fe/H}]} \leq [\mathrm{Fe/H}]_\star \leq < [\mathrm{Fe/H}] > +2\sigma_{[\mathrm{Fe/H}]} \quad (4.4)$$

$$< \mathrm{RV} > -2\sigma_{\mathrm{RV}} \leq \mathrm{RV}_\star \leq < \mathrm{RV} > +2\sigma_{\mathrm{RV}} \quad (4.5)$$

In the above, $[\mathrm{Fe/H}]_\star$ and $\mathrm{RV}_\star$ correspond to the values of these parameters for each star under consideration. The stars surviving both of these clips are considered *true cluster members* for the purpose of this study. Note that at no point have we considered the external "known" values of [Fe/H] and RV for the clusters as a whole.

The same procedure is performed for stars in M 15, M 2, NGC 2420, and M 67. Based on the application of these membership cuts, we now have a total of 293 stars identified as true members of M 13, 98 stars as true members of M 15, 76 stars as true members of M 2, 163 stars as true members of NGC 2420, and 52 stars as true members of M 67. The distribution of [Fe/H] and RV for the surviving members (*true cluster members*) of M 13 are shown as green histograms in the left and right panels of Figure 4.16, respectively. Similar plots for M 15, M 2, NGC 2420, and M 67 are shown in Figures 4.17, 4.18, 4.19, and 4.20, respectively. M 2 is the most distant object among the clusters considered in this study, and the signal-to-noise ratio of the spectra obtained for its members are generally lower than for stars in the other clusters of our sample. This results in a smaller number of stars with reliable [Fe/H] estimated than for the other globular clusters. Tables C.1−C.5 list the observed and derived quantities for all of the individual stars considered as true member stars in the analysis of each cluster. The columns are as defined in the table notes for Table C.1.

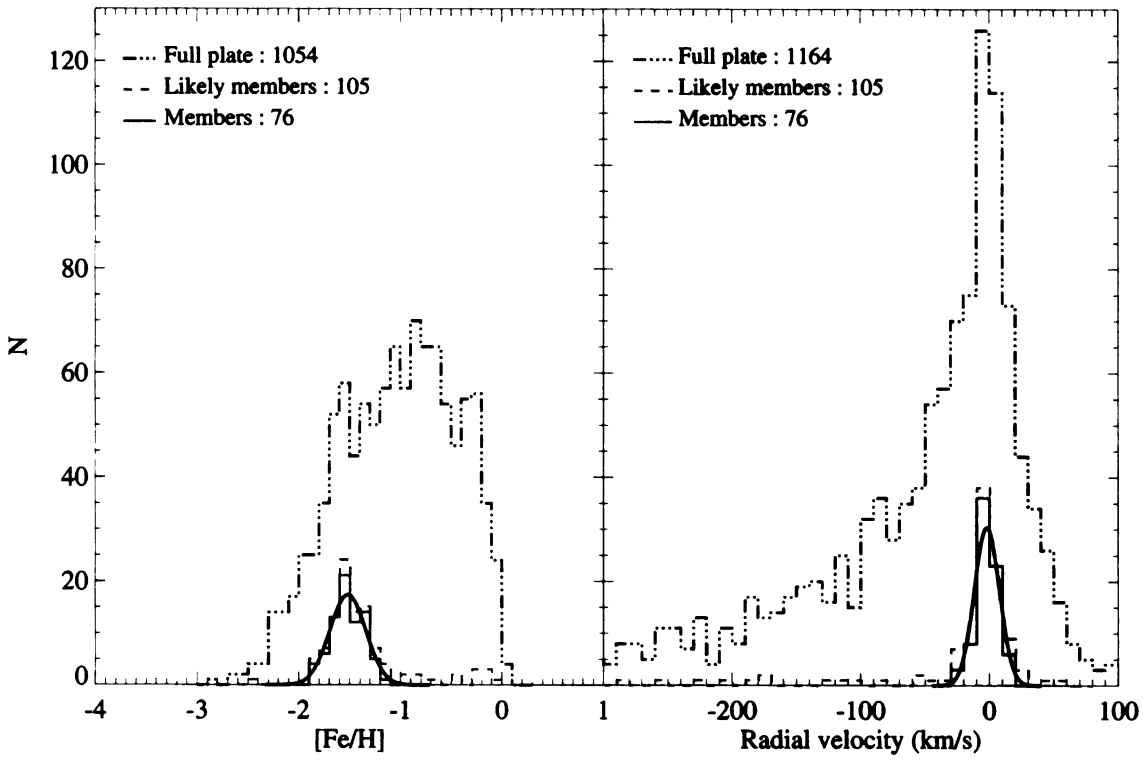


Figure 4.18 Same as Figure 4.16 but for M 2.

4.4.2 Determination of Overall Estimates of Mean Cluster Metallicity and Radial Velocity

We now obtain final estimates of the cluster metallicities and radial velocities, based on Gaussian fits to the surviving true member stars for each cluster, as shown by the blue curves in Figures 4.16–4.20. The parameters in the top half in Table 4.2 summarize these determinations. The mean and 1 σ spread of the metallicities of the true member stars are listed in columns (2) and (3), respectively; columns (4) and (5) are for the radial velocities. Column (6) lists the total number of selected true member stars associated with each cluster, based on our analysis. External estimates of the metallicities and radial velocities for the globular clusters, adopted from the Harris (1996) compilation, are listed in columns (7) and (8). The radial velocities for the open clusters are averages of literature values. See Chapter 4.5 for the details.

Column (9) lists metallicity estimates for these clusters obtained from high-resolution spectroscopy of a limited number of brighter stars by Kraft & Ivans (2003) for M 15 and M 13, Ivans (private communication) for M 2, and Gratton (2000) for NGC 2420 and M 67.

Table 4.2: Derived Radial Velocities and Metallicities of the Clusters[j]

Cut	Cluster	<[Fe/H]>	σ ([Fe/H])	<RV>	σ (RV)	N_{tot}	$[Fe/H]_H$	RV_H	$[Fe/H]_{HR}$
			dex	km s^{-1}	km s^{-1}			km s^{-1}	
	(1)	(2)	(3)	(4)	(5)	(6)	(7)	(8)	(9)
[Fe/H] & RV									
	M 13	−1.59	0.13	−244.8	8.8	293	−1.54	−245.6	−1.63
	M 15	−2.19	0.17	−108.2	11.7	98	−2.26	−107.0	−2.42
	M 2	−1.52	0.18	−2.1	9.8	76	−1.62	−5.3	−1.56
	NGC 2420	−0.38	0.10	+75.1	5.9	163	...	+75.5	−0.44
	M 67	−0.08	0.07	+34.9	4.1	52	...	+32.9	+0.02
RV									
	M 13	−1.59	0.13	−244.8	8.9	319	−1.54	−245.6	−1.63
	M 15	−2.19	0.18	−108.4	12.2	110	−2.26	−107.0	−2.42
	M 2	−1.51	0.18	−1.8	10.3	82	−1.62	− 5.3	−1.56
	NGC 2420	−0.38	0.11	+75.1	6.0	171	...	+ 75.5	−0.44
	M 67	−0.08	0.07	+34.8	5.8	56	...	+ 32.9	+0.02

[j] $[Fe/H]_H$ and RV_H for the globular clusters M 13, M 15, and M 2 are from Harris (1996). Values of $[Fe/H]_{HR}$, which are based on high-resolution spectroscopy, are from Kraft & Ivans (2003; M 13 and M 15), from Ivans (private communication; M 2), and from Gratton (2000; NGC 2420 and M 67). RV_H for the open clusters is computed by taking averages of the literature values. See Chapter 4.5 for details. The column labeled N_{tot} lists the total number of true members assigned to each cluster. The parameters in the upper portion of the table are derived with both [Fe/H] and RV cuts imposed; only the RV cuts are imposed for the lower portion.

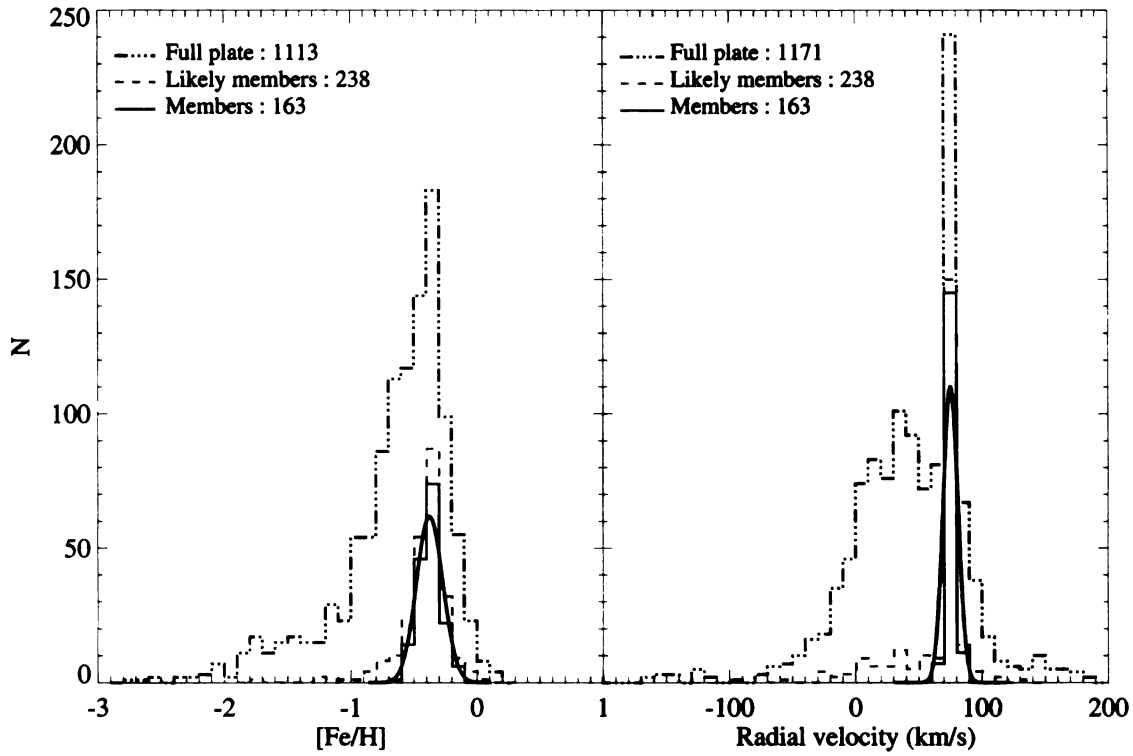


Figure 4.19 Same as Figure 4.16 but for NGC 2420.

We have checked to see if there is any change of the mean and scatter of our derived metallicity and the radial velocity for the clusters if we only impose radial velocity cuts (and not metallicity cuts) to the membership selection. As seen in the lower half of Table 4.2, little change in these quantities occurs. The total number of the true members identified is not much different either. Thus, cluster membership could have been made by consideration of the radial velocity, tidal radius, and CMD alone.

In order to check for trends in our metallicity determinations as a function of color or quality of the the spectra, the distribution of [Fe/H] for the true member stars of each cluster, as a function of $(g-r)_0$ (left panel) and $<S/N>$, the average signal-to-noise ratio per pixel for spectra of member stars over the 4000−8000 Å region (right panel), is shown in Figure 4.21. The red line is the literature value listed in Table 4.2; the green dashed line applies to our our derived mean estimates. Although, as

expected, the scatter becomes larger with declining $<S/N>$, it is clear that there exist no significant trends on [Fe/H] with color or $<S/N>$; the SSPP determinations appear quite robust.

The distribution of the SSPP-derived estimates of metallicity as a function of estimated log g, shown in Figure 4.22, also confirms that the [Fe/H] estimated by the SSPP is reliable over a wide range of luminosity classes; no significant trends are found with respect to the estimated surface gravity estimates.

4.5 A Comparison of Derived Metallicities and Radial Velocities for True Cluster Members with Previous Studies

In this section we present a more detailed comparison of our derived metallicity and radial velocity of each cluster with various values reported in the literature.

4.5.1 M 13 (NGC 6205)

The three spectroscopic plug-plate observations of this cluster provide the largest number (293) of true members selected among the clusters in this study. Our estimate of the mean abundance, $<$[Fe/H]$> = -1.59$, is very close to the Harris (1996) estimate ([Fe/H] $= -1.54$). However, the recent study of Kraft & Ivans (2003) reported a revised cluster abundance for this cluster, derived from high-resolution spectroscopy of 28 giants. Their value indicates a metallicity for M 13 (based on Fe II lines) that is a bit lower than that given by Harris, [Fe/H] $= -1.60$, but only 0.01 dex different than the value we obtained from the SSPP. An alternative [Fe/H] (from Fe I lines) reported by these authors indicates a slightly lower value, [Fe/H] $= -1.63$. Sneden et al. (2004) obtained [Fe/H] $= -1.62$ (from Fe I lines) and [Fe/H] $= -1.55$ (from Fe II lines), based on a sample of stars observed with the KECK/HIRES spectrograph

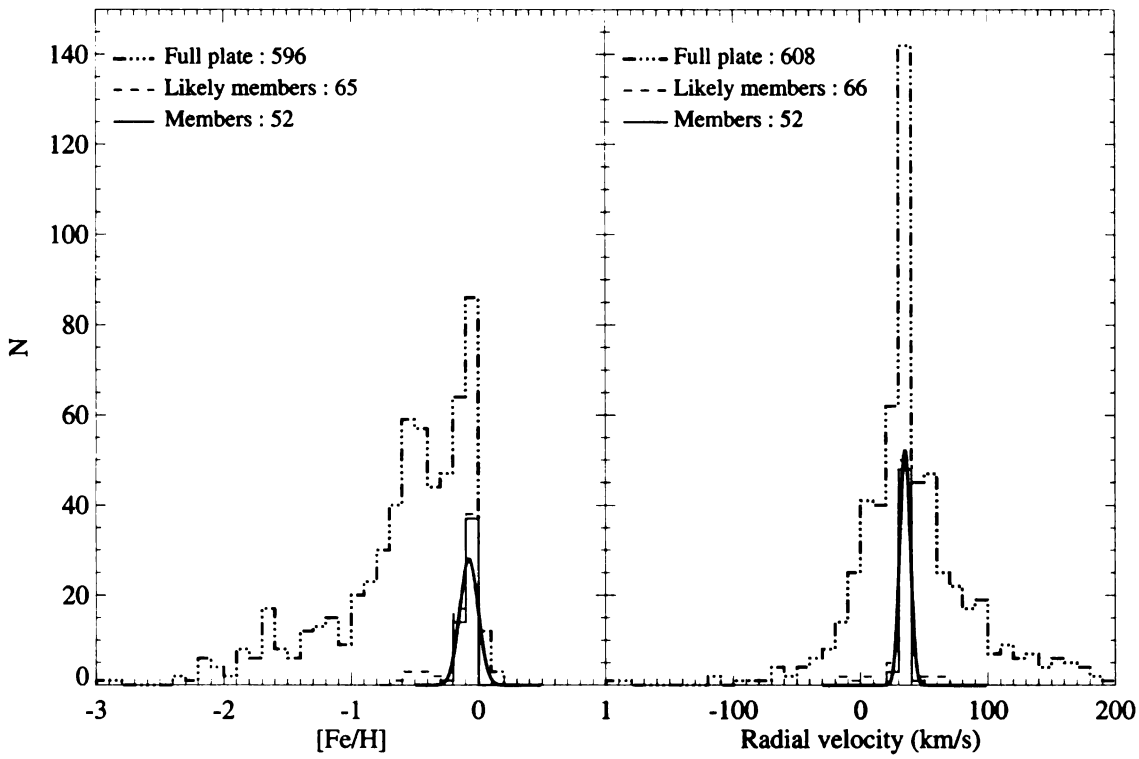


Figure 4.20 Same as Figure 4.16 but for M 67.

($R \sim 45,000$). Cohen & Meléndez (2005) reported higher values for the metallicity of this cluster, [Fe/H] $= -1.50$, based on a high-resolution ($R = 35{,}000$) analysis of a sample of 25 stars, extending from the giant branch to near the main-sequence turnoff. Pritzl et al. (2005) determined [Fe/H] $= -1.57$ from a compilation of high-resolution data in the literature. Very recently, Kirby et al. (2008) obtained medium-resolution ($R \sim 6000$) spectroscopy for 69 giants in this cluster, over the wavelength range 6300–9100 Å. They report an average of [Fe/H] $= -1.66$, which is slightly lower than our estimate. Considering the range of [Fe/H] obtained from previous studies, it is clear that the SSPP determination of overall [Fe/H] for M 13 is in excellent agreement. Our derived spread in the metallicities of the M 13 true member stars (0.13 dex) is also satisfyingly low, especially considering the wide range of temperatures and gravities for true members that are considered here.

Our estimate of the mean radial velocity, <RV> $= -244.8$ km s^{-1}, with a standard

deviation of 8.8 km s^{-1}, is in good agreement with that given by Harris (−245.6 km s^{-1}). It is important to note that, as mentioned in Paper I, we have already added +7.3 km s^{-1} to all DR-6 (Adelman-McCarthy et al. 2008) stellar radial velocities, in order to correct a recognized systematic offset.

4.5.2 M 15 (NGC 7078)

There are a total of 98 stars selected by our procedures as true members of this cluster. Our derived overall abundance of M 15, <[Fe/H]> = −2.19, is close to the value listed by Harris ([Fe/H] = −2.26). Sneden et al. (1997) reported [Fe/H] = −2.40, based on high-resolution spectra for 18 bright giants, in good agreement with the value of [Fe/H] = −2.37 obtained by Sneden et al. (2000), from observations of giants at the tip of the RGB. Kraft & Ivans (2003) obtained [Fe/H] = −2.42 (from Fe II lines) and [Fe/H] = −2.50 (from Fe I lines) for this cluster, based on high-resolution spectroscopy of nine giants. A value of [Fe/H] = −2.38 was reported by Pritzl et al. (2005) from a compilation of high quality data in the literature. Otsuki et al. (2006) reported [Fe/H] = −2.29 from an analysis of high-resolution spectra obtained for six giants in this cluster. Most recently, Kirby et al. (2008) calculated [Fe/H] = −2.42 from medium-resolution spectra of 44 giants. Since most of the high-resolution analyses indicate [Fe/H] $\sim$ −2.40 for M 15, this might indicate that the SSPP overestimates [Fe/H] by about 0.2 dex at low metallicities. A forthcoming study of the cluster M 92 (based on SDSS-II data that has only been recently obtained) will seek to confirm this tendency. The spread in the metallicities of true member stars in M 15 reported by the SSPP is quite low (0.17 dex).

Our estimate of the mean radial velocity, <RV> = −108.2 km s^{-1}, with a standard deviation of 11.7 km s^{-1}, agrees very well with that of Harris (−107.0 km s^{-1}).

4.5.3 M 2 (NGC 7089)

Only a limited number of true member stars (76) are selected by our procedures for this distant cluster, as the spectra obtained by SDSS for this cluster are generally of lower quality than for other clusters in our study. The faintness of M 2 is also a reason it has not received a great deal of attention by studies at high spectral resolution. Our derived average metallicity, <[Fe/H]> = −1.52, is slightly higher than the Harris (1996) value ([Fe/H] = −1.62), but in very good agreement with the value obtained by Ivans (private communication), [Fe/H] = −1.56. The estimated spread in our derived metallicities, 0.18 dex, is quite small, but larger than the spreads obtained for M 13 and M 15, as expected due to the inclusion of stars in our analysis with low S/N ($\sim$ 10/1).

Our estimate of the mean radial velocity, <RV> = −2.1 km s^{-1}, with a standard deviation of 9.8 km s^{-1}, is a bit higher (by about 3.2 km s^{-1}) than that provided by Harris (−5.3 km s^{-1}). Although still small, this is the largest offset in radial velocity among the clusters we consider in this study. However, it should be recalled that the mean metallicity of M 2 is quite close to that expected for members of the field halo population ([Fe/H] $\sim$ −1.6), and its (near zero) radial velocity is buried in the peak of foreground disk stars, which increases the likelihood that non-cluster stars could have crept into our true member sample.

4.5.4 NGC 2420

There are 163 true member stars selected for this open cluster. The mean metallicity of the selected true member stars reported by the SSPP is <[Fe/H]> = −0.38, which is only slightly higher than the value determined by Gratton (2000) from high-resolution spectroscopy of a single member star ([Fe/H] = −0.44). Friel & Janes (1993) reported [Fe/H] = −0.42 for nine member stars, based on medium- and low-resolution spectroscopic data. Friel et al. (2002) determined [Fe/H] = −0.38 ± 0.07,

based on medium-resolution spectra of 20 member stars. The most recent study, by Anthony-Twarog et al. (2006), indicated [Fe/H] = -0.37 ± 0.05 dex, derived from intermediate-band $vbyCaH\beta$ photometry. These values agree excellently with our own metallicity estimate for this cluster. The derived spread in the metallicities of the true member stars is also very low (0.10 dex).

Concerning the radial velocity for this cluster, Friel et al. (1989) derived 80.0 $\pm$ 6 km s^{-1} from 6 stars. Scott et al. (1995) reported 67.0 km s^{-1} from 19 member stars. Friel (1993) reported 84.0 km s^{-1}. Rastorguev et al. (1999) reported a value of 71.1 km s^{-1}. The literature value of radial velocity for NGC 2420, listed in Table 4.2, is an average of these four values (+75.5 km s^{-1}). This average is in excellent agreement with our derived estimate of +75.1 km s^{-1}, with a standard deviation of 5.9 km s^{-1}.

4.5.5 M 67 (NGC 2682)

Only one plug-plate (640 spectra) has been obtained for this open cluster. This, and the expected large amount of contamination from disk stars, resulted in a relatively small number (52) of true members being identified by our procedures. The SSPP-derived mean metallicity is <[Fe/H]>= -0.08, with a small spread (0.07 dex). This is lower by 0.1 dex than that of Gratton (2000), [Fe/H] = +0.02, derived from a high-resolution study of a single member star. Shetrone & Sandquist (2000) determined [Fe/H] = -0.05 for 10 blue stragglers and turnoff stars, based on high-resolution ($R \sim 30,000$) spectroscopy. A value of [Fe/H] = $+0.02 \pm 0.03$ dex was determined by Yong et al. (2005) from a high-resolution ($R \sim 28,000$) spectroscopic analysis of three member stars. Randich et al. (2006) analyzed 10 member stars of this cluster, based on high-resolution ($R \sim 45,000$) spectroscopy, and derived [Fe/H] = $+0.03 \pm 0.01$ dex. Friel & Boesgaard (1992) computed [Fe/H] = $+0.02 \pm 0.12$ dex for three F dwarfs observed at medium spectral resolution. From a medium-

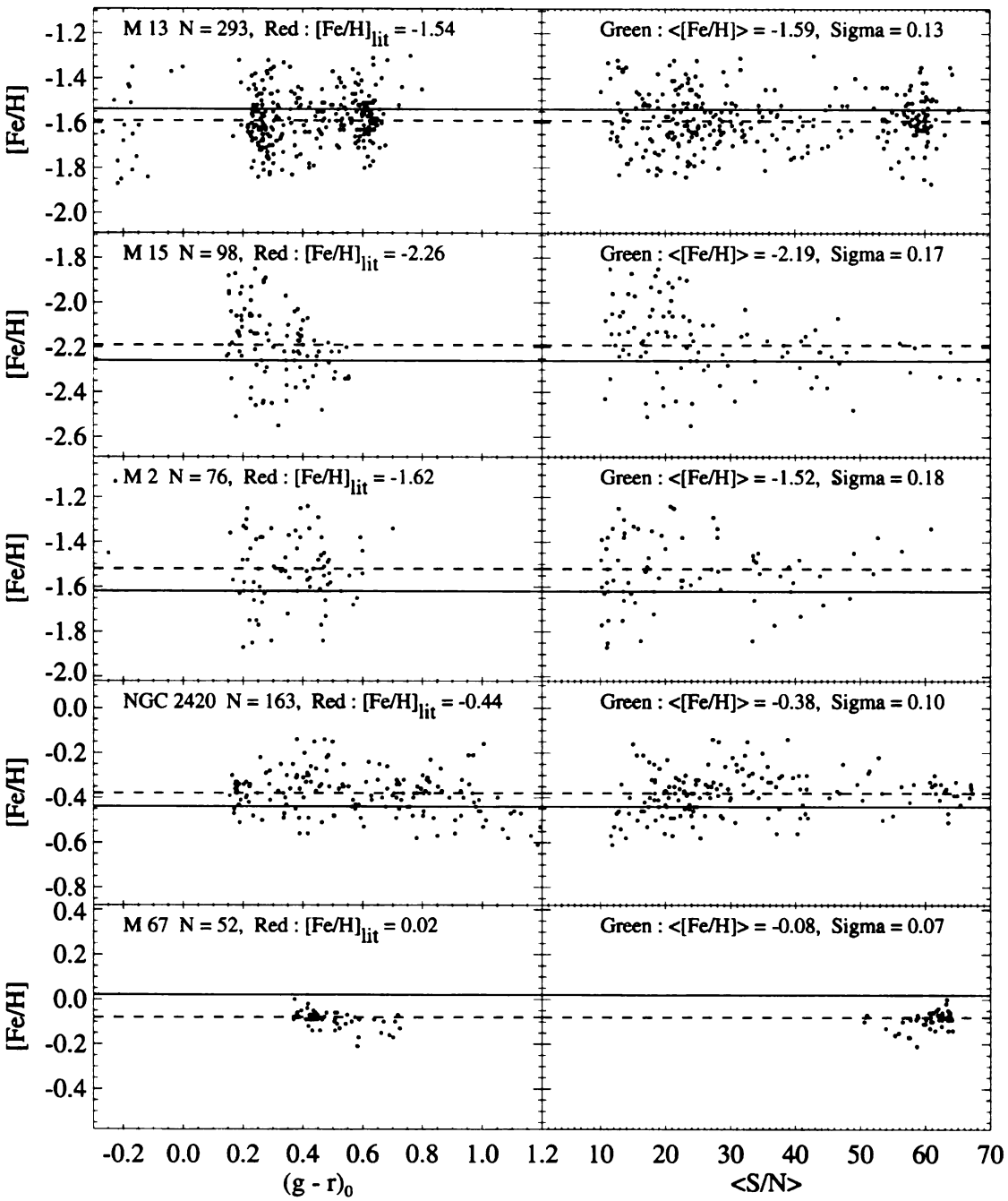


Figure 4.21 Distributions of [Fe/H] as a function of $(g-r)_0$ (left panels) and average ratio of signal to noise (right panels) for selected true member stars of M 13, M 15, M 2, NGC 2420, and M 67. The overall mean [Fe/H] determined in this study for each cluster is shown with the green dashed line; the red solid line represents the adopted literature value in each panel. No obvious trends exist as a function of either color or signal-to-noise.

resolution spectroscopic study of of 25 members, Friel et al. (2002) estimated [Fe/H] $= -0.15 \pm 0.05$ dex. Other catalogs of open clusters (e.g., Twarog et al. 1997; Chen et al. 2003) report a solar metallicity for this cluster. All of these literature values agree (within our observed scatter of 0.1 dex) with our metallicity estimate, which suggests that the metallicity estimated by the current version of the SSPP is reliable for stars with abundances near the solar value. Note that this is a marked improvement with respect to previous versions of the SSPP, which tended to underestimate [Fe/H] for solar-metallicity stars by up to 0.5 dex.

Table 4.3: Mean and 1 σ Values of Residuals in $T_{\rm eff}$ and $\log g$ Between SSPP and Model Fits[k]

		$T_{\rm eff}$		$\log g$	
Cluster	N	$<\Delta>$ (K)	σ (K)	$<\Delta>$ (dex)	σ (dex)
M 13	293	+165	194	−0.29	0.40
M 15	98	−13	134	−0.25	0.31
M 2	76	+31	114	−0.22	0.35
NGC 2420	163	+71	193	−0.14	0.46
M 67	52	−31	58	+0.15	0.07

For the radial velocity of M 67, Girard et al. (1989) reported 33.6 $\pm$ 0.72 km s^{-1}, based on a reanalysis of the compilation of a large set of member stars with radial velocity measurements (Mathieu et al. 1986). Scott et al. (1995) determined 32 km s^{-1} from 26 member stars. Values of 32 $\pm$ 11 km s^{-1} from 4 stars, 33 km s^{-1}, and 33.6 km s^{-1} were estimated by Friel et al. (1989), Friel & Janes (1993), and Rastorguev

[k]These values are 5 σ-clipped averages and standard deviations. N is the total number of the selected member stars.

et al. (1999), respectively. Yong et al. (2005) obtained a very similar value, of 33.3 km s^{-1}, from three member stars. Taking an average of all these measurements, we obtain 32.9 km s^{-1}, as listed in Table 4.2. This value agrees with our derived mean radial velocity of +34.9 km s^{-1} within the standard deviation of our measurements, 4.0 km s^{-1}.

As discussed above, taking into account only the scatter in the metallicities and radial velocities calculated from the members of each cluster, we are able to derive estimates of the typical external uncertainties for the SSPP estimates of these quantities, σ([Fe/H]) $\sim$ 0.13 dex, and σ(RV) $\sim$ 8.0 km s^{-1}. The scatter in the radial velocity is also noted to increase with decreasing [Fe/H]. This is the expected behavior, since the metallic lines of a metal-poor star are weaker than those of a metal-rich star of the same effective temperature, making it more difficult to identify strong features to anchor the determination of radial velocity. A similar behavior can be found for [Fe/H], that is, larger errors with declining metallicity, from inspection of Table 4.2.

4.6 A Comparison of Derived Metallicities and Surface Gravities for True Cluster Members with Color-Magnitude Diagrams

In the previous section, we considered the accuracy with which the SSPP obtains estimates of metallicity and radial velocity. We now consider the accuracy with which the SSPP obtains estimates of effective temperatures, $T_{\rm eff}$, and surface gravities, log g. One excellent "global" test of these estimates is to examine the locations of the true member stars on the observed CMD (based on the totality of likely photometric member data) for each cluster. One can also compare with corresponding theoretical CMDs.

Figures 4.23–4.27 show plots of the SSPP-estimated temperatures and gravities

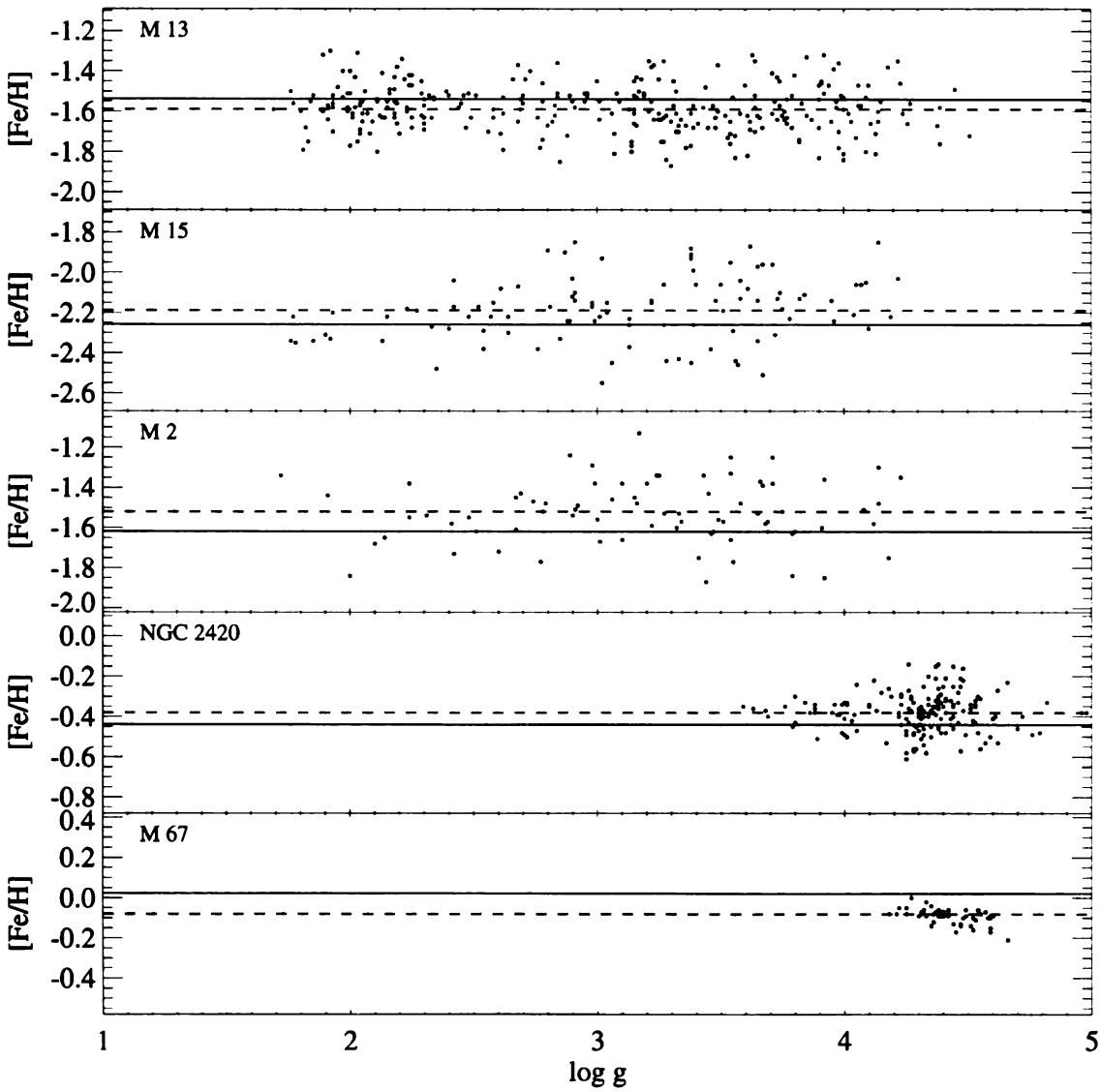


Figure 4.22 Distributions of [Fe/H] as a function of estimated log g for the selected true member stars of M 13, M 15, M 2, NGC 2420, and M 67. The overall mean [Fe/H] determined in this study for each cluster is shown with the green dashed line; the red solid line represents the adopted literature value in each panel. No obvious trends exist as a function of surface gravity.

for true member stars superposed on the photometrically cleaned CMDs for each of our clusters. Note that in order to obtain the theoretical temperature scales (shown along the top of the left-hand panels in each figure), we make use of a linear relation between $(g-r)_0$ color and $T_{\rm eff}$ by performing a least square fit in this plane to the

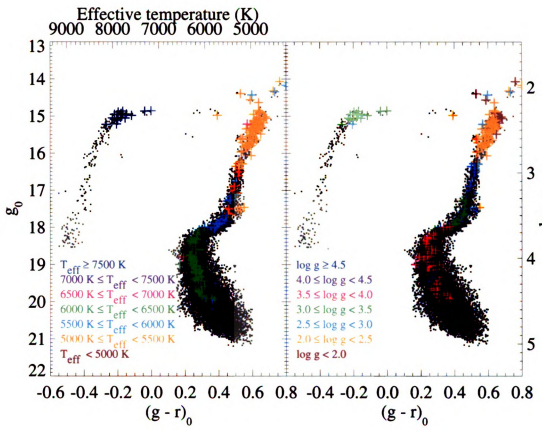


Figure 4.23 Distributions of effective temperature (left panel) and surface gravity (right panel) of the selected true member stars superposed on the CMD for M 13. Each color represents a temperature range of width 500 K, and a surface gravity range of 0.5 dex, respectively. The temperature scales on the top of the left-hand panel come from a linear relation between $(g-r)_0$ color and $T_{\rm eff}$ obtained by performing a least square fit to the theoretical models of Girardi et al. (2004). A similar procedure is applied for transforming the g_0 magnitude to a theoretical log g scale shown on the ordinate in the right-hand panel.

theoretical models of Girardi et al. (2004). We choose the isochrones from this study that have the closest [Fe/H] to the derived metallicity of each cluster, and adopt an age of 13.5 Gyr for the globular clusters, 2.2 Gyr for NGC 2420, and 4.3 Gyr for M 67 (adopting the ages from WEBDA for the open clusters). A similar procedure is applied for transforming the g_0 magnitude to a theoretical log g scale (shown along the far right axis in the right-hand panels of each figure). Distance moduli from the Harris (1996) compilation for the globular clusters and WEBDA for the open clusters

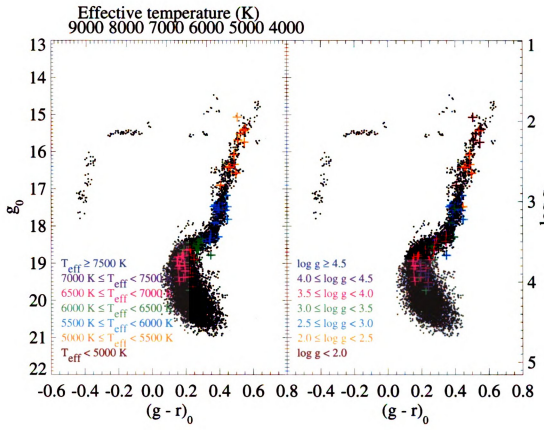


Figure 4.24 Same as Figure 4.23 but for M 15.

(also listed in Table 4.1) are used in order to compute apparent magnitudes.

In these figures, we plot the SSPP-estimated parameters for true member stars in different colors, corresponding to different ranges of temperature and surface gravity (as shown in the legend for each plot). Each color represents a range of 500 K in $T_{\rm eff}$ and 0.5 dex in log g, respectively. The effective temperature estimated by the SSPP appears in excellent agreement for most of the true member stars, with only a few exceptions. Such stars could either be outright errors in the SSPP predictions, or could just be foreground/background stars that survived the various membership cuts we have applied. Inspection of the figures also reveals the presence of a few stars close to the main-sequence TO in M 13, M 15, and M 2 that appear to have slightly higher or lower SSPP-estimated log g than expected from the theoretical scale. The surface

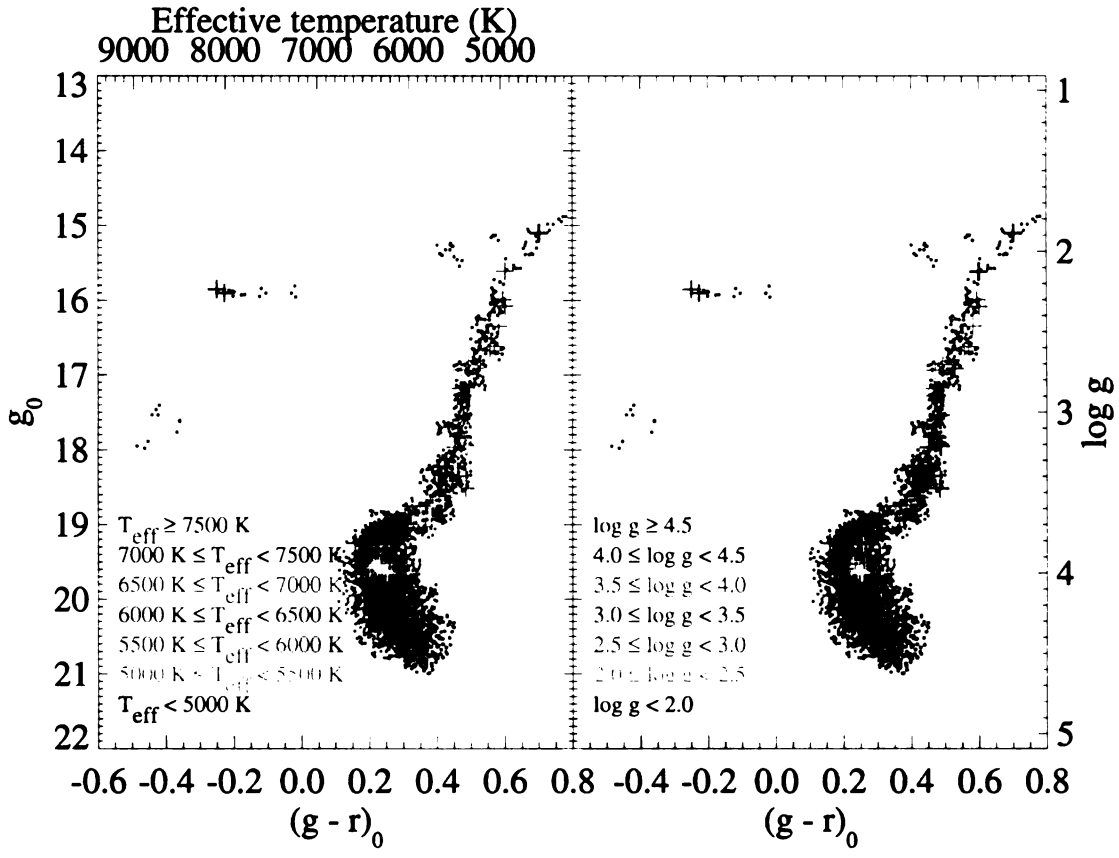


Figure 4.25 Same as Figure 4.23 but for M 2.

gravities of stars along the RGB appear to be very well estimated. Such behavior is perhaps to be expected, since the stars close to the TO region are at the low end of the S/N range that we accept for SSPP parameter determinations ($\sim$ 10/1), and thus are subject to greater errors in the determination of their atmospheric parameters. The RGB stars are among the brightest stars in the globular clusters, and hence are likely to have the best-determined estimates.

Careful inspection of Figure 4.26 for NGC 2420 indicates that gravity estimates for most of the main-sequence stars are well estimated from the SSPP, with the exception of the faintest stars. These stars have only low S/N ($\sim$ 10/1) spectra available, resulting in higher uncertainties in determinations of their surface gravities. It should also be recalled that surface gravity is a difficult parameter to estimate, especially

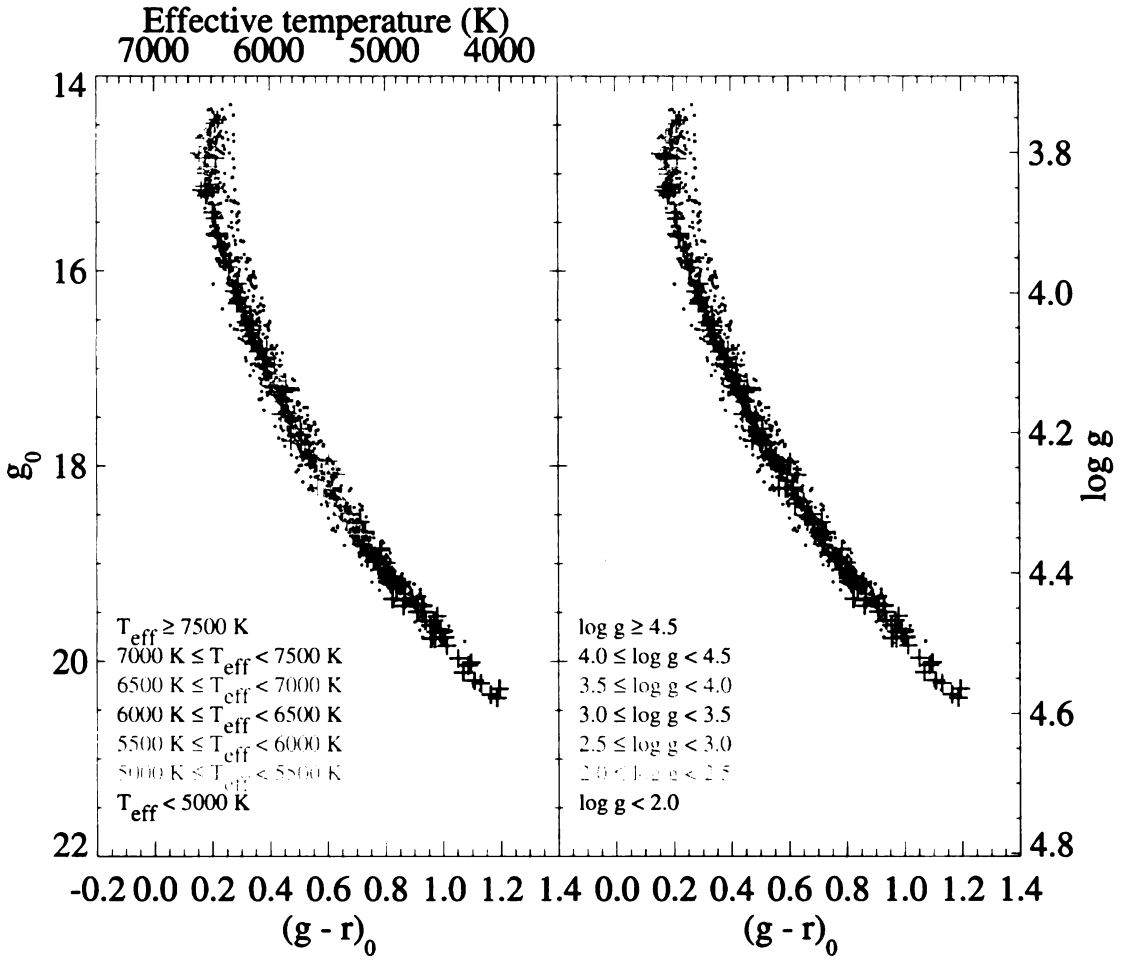


Figure 4.26 Same as Figure 4.23 but for NGC 2420.

from spectra of the resolving power obtained by the SDSS. Overall, we are pleased to see as good a behavior in the estimates of this parameter as that demonstrated in Figures 4.23–4.27.

In addition, using the derived relations between $(g-r)_0$ and $T_{\rm eff}$, and g_0 and log g from the isochrones, we predicted $T_{\rm eff}$ and log g from the observed $(g-r)_0$ and g_0, respectively. Table 4.3 lists the averages and standard deviations of the residuals of the effective temperatures and surface gravities between the SSPP estimates and the calculated values. Even though we have employed a simple relationship between $(g-r)_0$ with $T_{\rm eff}$, we see good agreement between the SSPP estimates and the

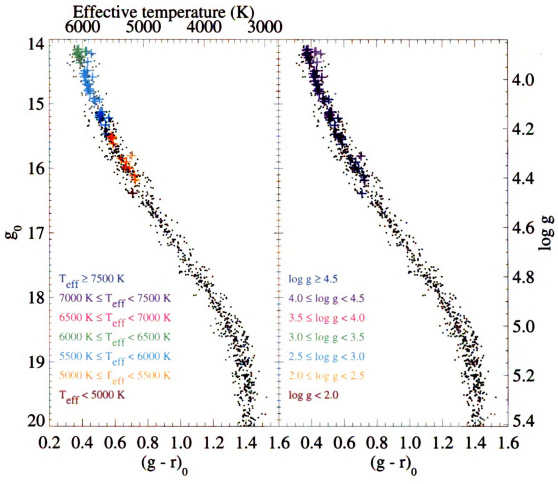


Figure 4.27 Same as Figure 4.23 but for M 67.

theoretical values in $T_{\rm eff}$. Although, as expected, there is a rather large offset and scatter in the gravity, indicating a more complex function is needed (or the isochrones themselves are in doubt), the scatters are still within the bin sizes (0.5 dex) for this parameter used in Figures 4.23–4.27. The relatively larger zero-point offsets in $T_{\rm eff}$ for M 13 and NGC 2420 is caused by the linear relation having to cover a large range of $(g-r)_0$: -0.4 to 0.8 for M 13 and 0.1 to 1.2 for NGC 2420.

4.7 SUMMARY

Based on photometric and spectroscopic data reported in SDSS-I and SDSS-II/SEGUE, we have examined estimates of stellar atmospheric parameters and heliocentric radial velocities obtained by the SEGUE Stellar Parameter Pipeline (SSPP) for selected true members of three Galactic globular clusters, M 13, M 15, and M 2, and two open clusters, NGC 2420 and M 67, and compared them with those obtained by external estimates for each cluster as a whole.

From the derived scatters in the metallicities and radial velocities obtained for the selected true members of each cluster, we quantify the typical external uncertainties of the SSPP-determined values, $\sigma([\mathrm{Fe/H}]) = 0.13$ dex, and $\sigma(\mathrm{RV}) \sim 8.0$ km s^{-1}, respectively. These uncertainties apply for stars in the range of $-0.3 \leq g-r \leq 1.3$ and $2.0 \leq \log g \leq 5.0$, at least over the metallicity interval spanned by the clusters studied ($-2.3 \leq [\mathrm{Fe/H}] \leq 0.0$). Therefore, the metallicities and radial velocities obtained by the SSPP appear sufficiently accurate to be used for studies of the kinematics and chemistry of the metal-poor and near-solar metallicity stellar populations in the Galaxy. We have also confirmed that T_{eff} and $\log g$ are sufficiently well determined by the SSPP to distinguish between different luminosity classes, through a comparison with theoretical predictions.

CHAPTER 5: THE [α/Fe] ABUNDANCE PATTERNS OF STARS IN THE GALACTIC HALO

5.1 INTRODUCTION

The currently favored hierarchical structure formation model (e.g., White & Rees 1978) suggests that galaxies like the Milky Way grow by means of mergers and accretion of numerous smaller fragments (often referred to as "mini-haloes"), dark matter dominated systems that collapsed around defects imprinted on the universe as it emerged from the Big Bang. It is believed that primordial gas falls into these systems as it cools, and star formation commences. Although it is not established with certainty, the preponderance of evidence suggests that the first stellar systems formed in this manner should bear a resemblance to low luminosity dwarf spheroidal (dSph) galaxies.

It follows from the above that the early dwarf-like galaxies would each have their own star formation and chemical enrichment history *before* they are assimilated into their host galaxy. Thus, there may exist differences in the observed elemental abundances of stars that originated in dwarf galaxies of different masses, and had different star-formation rates and histories. In addition, as pointed out by Gilmore & Wyse (1998), because the orbits of the accreted stars from a given dwarf galaxy (stripped due to the tidal effects from the parent galaxy) are not altered much over time, captured stars from the dwarf galaxy will preserve distinct kinematics which can persist

for a long period of time. Therefore, a detailed elemental abundance analysis of stars in a galaxy (especially its halo), along with their kinematics, can provide clues to the accretion history of a giant galaxy like the Milky Way.

The chemical elements O, Mg, Si, Ca, and Ti are often referred to as the "α" elements, since they share a common formation mechanism, the capture of an α-particle (nucleus of a He atom), are produced by massive stars ($> 8\ M_{\odot}$) during their explosions as a core collapse supernovae (Timmes, Woosley, & Weaver 1995). This so-called Type II Supernova (SNe II) explosion occurs only a few million years after the formation of a massive star, due to the short main-sequence lifetimes of such stars. Iron (Fe) is also produced in these events, but much more Fe is generated during a Type Ia supernova (SNe Ia), over a much longer timescale, on the order of 0.1 to a few Gyr (Matteucci & Recchi 2001). Type Ia supernovae are thermonuclear explosions that take place in a binary system when material in the envelope of a binary companion star is transferred onto the surface of a white dwarf (mostly made of Carbon and Oxygen), to the point that its mass approaches the Chandrasekhar limit ($1.4\ M_{\odot}$). Nucleosynthesis occurs during these explosions and a large fraction of the iron-peak elements (Ni, Co, etc.) are produced (Nomoto, Thielemann, & Wheeler 1984).

Thus, the ratio of the abundance of the α-elements to that of iron, which is expressed as "[α/Fe]" (the mean of [O/Fe], [Mg/Fe], [Si/Fe], [Ca/Fe], and [Ti/Fe] in most cases), has often been used as an indicator of not only the star formation and chemical enrichment history of the Galaxy and its known satellite galaxies, but also to search for distinctive chemical signatures of accreted stars from dwarf galaxies. While a typical halo star exhibits [α/Fe] $\sim$ 0.3 to 0.4 dex, indicating enhancement from SNe II, many stars in dSphs exhibit relatively lower [α/Fe] compared to Galactic halo stars with the same metallicity (Shetrone et al. 2001, 2003; Fulbright 2002; Tolstoy et al. 2003; Geisler et al. 2005). It is thought that the low α-abundances in these

systems is due to the slower star formation rates (therefore, more contribution of Fe from SNe Ia) in the dSphs than occurred for the bulk of the halo of the Milky Way (Unavane et al. 1996). However, it should be kept in mind that observations are only now being obtained for the lowest luminosity dSphs (many of which were discovered from SDSS imaging), and it may indeed be the case that the [α/Fe] in these galaxies is more similar to those of the Galactic halo.

Stars on extreme retrograde orbits, or stars that exhibit distinct orbital parameters (e.g., large apo-Galactic distance or large distance from the Galactic plane), which differ from the majority of halo stars, have been proposed to originate in previously stripped dwarf galaxies. For example, a few halo stars that do not exhibit typical halo α-enhancements have been found (Carney et al. 1997; King 1997) and interestingly, these stars have large apo-Galactic distance ($R_{\rm apo}$) or are on counter-rotating orbits. One possible explanation for these α-poor stars with peculiar orbits is that these stars might have come from smaller galaxies with low star formation rates, which were self-enriched with Fe from the contribution of SNe Ia before they torn apart. For this reason, some studies (e.g., Stephens & Boesgaard 2002) specifically targeted stars with distinct orbital parameters to compare their elemental abundances with those of typical halo stars, in order to investigate this possible accretion signature among the stars in the Galactic halo. In the following section, we summarize some of major efforts to search for such accretion signatures, focusing on the α-abundance analysis.

5.2 Previous Studies

Nissen & Schuster (1997) performed an elemental abundance analysis of 13 halo and 16 disk stars, with atmospheric parameters in the range $5400 \leq T_{\rm eff} \leq 6500$ K, $4.0 \leq \log g \leq 4.6$, and $-1.3 \leq$ [Fe/H] ≤ -0.5. Some of them were of similar metallicity, even though they belonged to different stellar populations. After they derived their

orbital parameters, such as the maximum distance ($R_{\rm apo}$) from the Galactic center and the maximum distance ($Z_{\rm max}$) from the Galactic plane, they divided their sample into two groups by cutting on the Galactic rotational velocity (V_ϕ) – halo stars with $V_\phi \leq 50$ km s^{-1} and disk stars with $V_\phi \geq 150$ km s^{-1}. They found that 8 of their halo stars had significantly lower [α/Fe] ratios than those of the disk stars with the same metallicity, and that these stars have the largest values of $Z_{\rm max}$ and $R_{\rm apo}$ among their sample. They concluded that the low α-stars may have come from external systems such as the dwarf satellites of the Milky Way, and further argued that the α-poor stars may belong to an accreted outer halo population while the α-rich stars may belong to an inner halo, which formed from the dissipative collapse of a proto-galactic gas cloud (i.e., similar to the model of Eggen, Lynden-Bell, & Sandage 1962).

However, just one year later, Gilmore & Wyse (1998) argued that these stars could not possibly have been accreted from systems that are similar to the presently observed dSphs, because most of the stars in the sample of Nissen & Schuster (1997) have low $R_{\rm peri}$ (< 1 kpc). They reasoned that low mass dSphs would be tidally disrupted before they obtained such small $R_{\rm peri}$ orbits. They claimed that the stars in the Nissen & Schuster (1997) sample might have formed in sufficiently dense "transient star-forming regions", which could survive from close encounters with the Galactic center and self-enrich to relatively high metallicities.

Fullbright (2002) studied the elemental abundances and kinematic properties of 73 stars in the metallicity range $-2.0 <$ [Fe/H] < -1.0. He noted, after dividing his sample into three velocity bins, that the α-abundances in this metallicity range decline with increasing Galactic rest-frame velocities. He also compared the abundance pattern of the field halo stars with the dSph giant stars studied by Shetrone et al. (2001), and noticed different abundance patterns between them. From the disagreement in the chemical abundance patterns between the two, he suggested that the α-poor stars may not have been accreted from the dSph galaxies like those in the

sample of Shetrone et al. (2001).

Stephens & Boesgaard (2002) measured elemental abundances for metal-poor halo dwarfs selected based on their kinematics (those with $R_{\rm apo}$ larger than 16 kpc, $Z_{\rm max}$ greater than 5 kpc, and V velocity less than –400 km s^{-1}). The stars chosen by these criteria represent the outer halo, and the extreme retrograde stars, respectively. Their analysis indicated that the α-abundance increases as the metallicity decreases (on average), stars with [Fe/H] < -2.0 have higher values of [α/Fe] than more metal-rich halo stars ($\sim$ 0.3 dex), and that metal-rich halo stars ([Fe/H] ≥ -1.0) exhibit lower [α/Fe] values than typical halo stars. They further divided their sample into two subsets on apo-Galactic distance – a presumed inner halo with $R_{\rm apo} < 16$ kpc, and an outer halo with $R_{\rm apo} > 16$ kpc. They concluded that the inner-halo stars possess higher [α/Fe] than the outer halo stars of the same metallicity. Following the reasoning of Gilmore & Wyse (1998), and since most of their halo stars have apo-Galactic distances large enough to reach to the orbits of debris from dwarf satellites (and have peri-Galactic distances of $\sim$ 7 kpc), they inferred from a kinematical point of view that their sample might have come from disrupted dwarf galaxies. They conjectured that their halo stars could perhaps have formed around 1 Gyr after the initial burst of star formation in a distant halo region. Based on this argument, they concluded that late accretion of objects similar to the present-day dwarf satellites was rare in the history of the formation of the Milky Way.

An analysis of the α-and Fe abundances for about 150 field metal-poor subdwarfs and subgiants in the solar neighborhood was performed by Gratton et al. (2003). After computing the orbital parameters for their sample, they grouped them into three subsets, which they referred to as a "dissipative collapse component", an "accretion component", and a "thin disk" component. Their first group had Galactic rotational velocities greater than 40 km s^{-1} and apo-Galactic distances less than 15 kpc. This population included both halo and thick-disk stars, which possibly formed from a

dissipative collapsing proto-Galactic system. Their second group consisted of stars with orbits consistent with minimal or retrograde rotation about the Galaxy. These stars, they argued, could have presumably been accreted from other systems. Their third component, the thin-disk stars, had $(Z_{\rm max}{}^2+4e^2)^{1/2} < 0.35$, where e is the orbital eccentricity.

Their analysis indicated that, although both the dissipative and the accretion component share the same metallicity range, the dissipative component exhibits higher α-abundances, with a smaller scatter than that of the accretion component, which agrees with the result of Nissen & Schuster (1997). This higher α-abundance implies that the dissipative component experienced a higher star formation than that of the accretion component, and the smaller scatter indicates that the stars in the dissipative component formed out of a well-mixed interstellar medium (ISM). A much larger scatter in α-abundances at a given [Fe/H] was noticed for the stars of the accretion component. They pointed out that the accretion component stars probably formed in a slow star formation environment with a different chemical history, leading to the lower average values of [α/Fe] at the same metallicity. They also found that in their sample the α-abundances correlated better with the peri-Galactic distances than with apo-Galactic distances.

Venn et al. (2004) compiled an extensive set of Galactic stars with chemical abundances measured from the literature, and compared them with those measured for the dSphs around the Milky Way. First, these authors separated their Galactic sample into thin, thick disk, and halo components, using a Bayesian classification criterion based on Gaussian velocity ellipsoids. In addition, extremely retrograde stars with $V < -420$ km s^{-1} were selected. Their analysis indicated that the Galactic halo stars had abundance ratios in the range $0.0 <$ [α/Fe] < 0.4, with a plateau at 0.4 dex at low metallicity, while the counter-rotating stars exhibited [α/Fe] = 0.2, on average. The [α/Fe] distribution of the low mass dwarf galaxies generally doesn't

follow that of the halo stars, although the extreme counter-rotating stars exhibits values that are somewhat close to those of the dwarf spheroidals. Based on this, they pointed out that there might exist the possibility of early merging of both low mass dwarf galaxies and higher mass galaxies.

In their recent review paper, Geisler et al. (2007) gathered all existing Galactic stars with detailed elemental abundances measured to date, and compared the [α/Fe] distribution, as a function of [Fe/H], of the Galactic stars with that of 13 dSphs around the Milky Way galaxy. Their comparison revealed that while 12 of the dSphs exhibited very similar abundance patterns to one another, these were rather different from stars in the halo of the Galaxy. The [α/Fe] of the dSphs is slightly lower than that of the Galaxy at [Fe/H] < -2.0, but substantially lower at [Fe/H] $= -1.0$. However, the Sagittarius (Sgr) galaxy, a massive dSph, proved a bit of an exception. The Sgr galaxy has some stars with α-abundances similar to the halo at intermediate metallicity ([Fe/H] ~ -1.0). From this comparison, they concluded that it is unlikely that a significant fraction of the more metal-rich halo stars came from disrupted low-mass dSphs. However, they also suggested that at least some of the metal-poor halo stars may have come from typical dSphs. A portion of the intermediate metallicity and metal-rich halo stars may have come from massive dwarf galaxies like Sgr.

Summarizing the previous studies, although the abundance patterns (focusing on [α/Fe]) of the stars in the Galactic halo are not similar to those of the stars in most of the present-day dSph galaxies, the Galactic halo stars with low metallicity ([Fe/H] $<$ -2.0) do appear to overlap, at least somewhat, with those of the dwarf galaxy stars, especially those with lower metallicity. Therefore, some of the metal-poor ([Fe/H] $<$ -2.0) halo stars could have come from the low mass dwarf galaxies very early in the history of the Galaxy, or even at later times, depending on the accretion timescale. There is also the possibility that some fraction of the halo stars (in particular the metal-rich ones) might have been accreted from massive dwarf galaxies like Sgr in

very early times, before SNe Ia kicked in to contribute Fe to the ISM in the massive dwarf galaxies. This picture may well agree with numerical simulations (Robertson et al. 2005; Font et al. 2006a, 2006b) which claim that the bulk of the Galactic halo formed through the accretions of a few massive dwarf galaxies ($5 \times 10^{10} M_{\odot}$) as much as 10 Gyr ago.

In our present study, which focuses on the α-abundance for very large samples of stars in the Galactic halo, several of the issues raise by previous work can be confronted. It should be kept in mind that, although the accuracy of the α-abundance estimates for our halo sample is definitely somewhat lower than that of the stars in other studies (due to the much lower resolution of the SDSS spectra from which they are measured), we have a significantly larger sample size than any previous studies, so the uncertainty of individual α-abundance measurements can be statistically compensated for on average.

5.3 Determination of [α/Fe]

5.3.1 Methodology

As described in Chapter 2, we have obtained large numbers of stellar spectra through the SDSS-I and SEGUE surveys. Hence, we need tools for determining a parameter such as [α/Fe] in a fast and automated fashion, as done with the SSPP. One of the best ways to achieve this goal is to make use of a pre-existing grid of synthetic spectra. With the pre-existing grid there is no need to generate a synthetic spectrum iteratively while attempting to estimate a parameter that fits an observed spectrum.

Thus, in order to estimate [α/Fe], we have generated a grid of synthetic spectra, using Kurucz NEWODF models (Castelli & Kurucz 2003) and the TURBOSPECTRUM synthesis code (Alvarez & Plez 1998). More detailed descriptions of the Kurucz NEWODF models and the source of the linelists used to synthesize the spectra

can be found in Chapter 3.4.4. The grid spans 4000 K $\leq$ $T_{\rm eff}$ $\leq$ 8000 K in steps of 250 K, 1.0 $\leq$ log g $\leq$ 5.0 in steps of 0.2 dex, $-3.0 \leq$ [Fe/H] ≤ 0.2 in steps of 0.2 dex, and $-0.1 \leq [\alpha/\mathrm{Fe}] \leq 0.6$ dex, in steps of 0.1 dex. In generating the synthetic spectra, we increased, by the same amount, the abundances for all α-elements (O, Mg, Si, Ca, Ti). The resolution of the generated synthetic spectra is 0.1 Å, and a micro-turbulence of 2 km s^{-1} was assumed. Each spectrum covers the wavelength range 4500–5500 Å. The reason for choosing this wavelength range is that it contains a large set of metallic lines, but avoids the CH G band (4300 Å), which is often a strong feature in metal-poor stars. Most importantly, this region of the wavelength possesses strong Mg I, Mg I*b*, and MgH lines, which are sensitive features for estimation of the α-abundance.

After their creation, the synthetic spectra were degraded to the SDSS resolution ($R = 2000$) and processed in the same manner as described in Chapter 3.4.4 for the `NGS2` grid to obtain the normalized spectra. Our target spectra were also normalized in the same fashion.

The parameter search technique is the same as for the `NGS2` grid, which is described in Chapter 3.4.4. However, for the application of the α-abundance determination, we employ the stellar parameters derived by the SSPP as initial starting guesses. This choice is made because we are dealing with a lot of synthetic spectra ($\sim$ 50,000), and calculating the reduced χ^2 values for the entire synthetic spectra for each observed spectrum would require a large amount of computing time.

We select the synthetic spectra that are within $\pm$ 1000 K of the SSPP $T_{\rm eff}$, $\pm$1.5 dex of the SSPP log g, and $\pm$ 1.5 dex of the SSPP [Fe/H], and compute the reduced χ^2 values for the selected synthetic spectra against an observed spectrum. After this calculation, using the IDL multi-dimensional optimization routine AMOEBA, we search for the best matching synthetic spectrum. Because this routine is susceptible to becoming stuck in a local minimum for lower S/N spectra, we determine another

set of the parameters by taking an average of 20 points near the minimum reduced χ^2 values. The final estimate of [α/Fe] is the average of the two sets of determinations.

5.3.2 VALIDATION

Once a tool to determine a physical quantity is developed, one has to calibrate and validate it with external measurements. For the purpose of this comparison, we again introduce the ELODIE spectral library (Moultaka et al. 2004) as an external source. First, we performed a literature search for previously measured α-element abundances for the stars in the library, using the VizieR[1] database, and found 414 stars with the required information. As mentioned above, due to the nature of the wavelength range selected for determining [α/Fe], Mg will have the most weight in the α-abundance estimate. Therefore, we also gave more weight to previously measured Mg abundances, rather than taking the average of all available α-element measurements for a given star.

The chosen spectra from the library were processed exactly in the same way as the synthetic spectra, after degrading them to $R = 2000$, and the [α/Fe] abundance for the selected individual stars was estimated. Figure 5.1 shows the results of the comparison. The subscript "Lit" indicates the value from the literature and "Fit" from our determination. The red crosses in the bottom left figure denote our determinations. A Gaussian fit to the residuals between our values and those from the literature indicate that there is little systematic offset, and further indicates a very small scatter (standard deviation of 0.04 dex). No trends in the estimated α-abundance as a function of [Fe/H] are noted for stars with [Fe/H] < -0.5 in the figure.

Since the spectra in the ELODIE library have very high S/N ($> 100/1$), while the SDSS spectra cover a wide range of S/N, we also have to check how the S/N of a spectrum impacts our determination of the α-abundance. We have used the

[1]http://webviz.u-strasbg.fr/viz-bin/VizieR

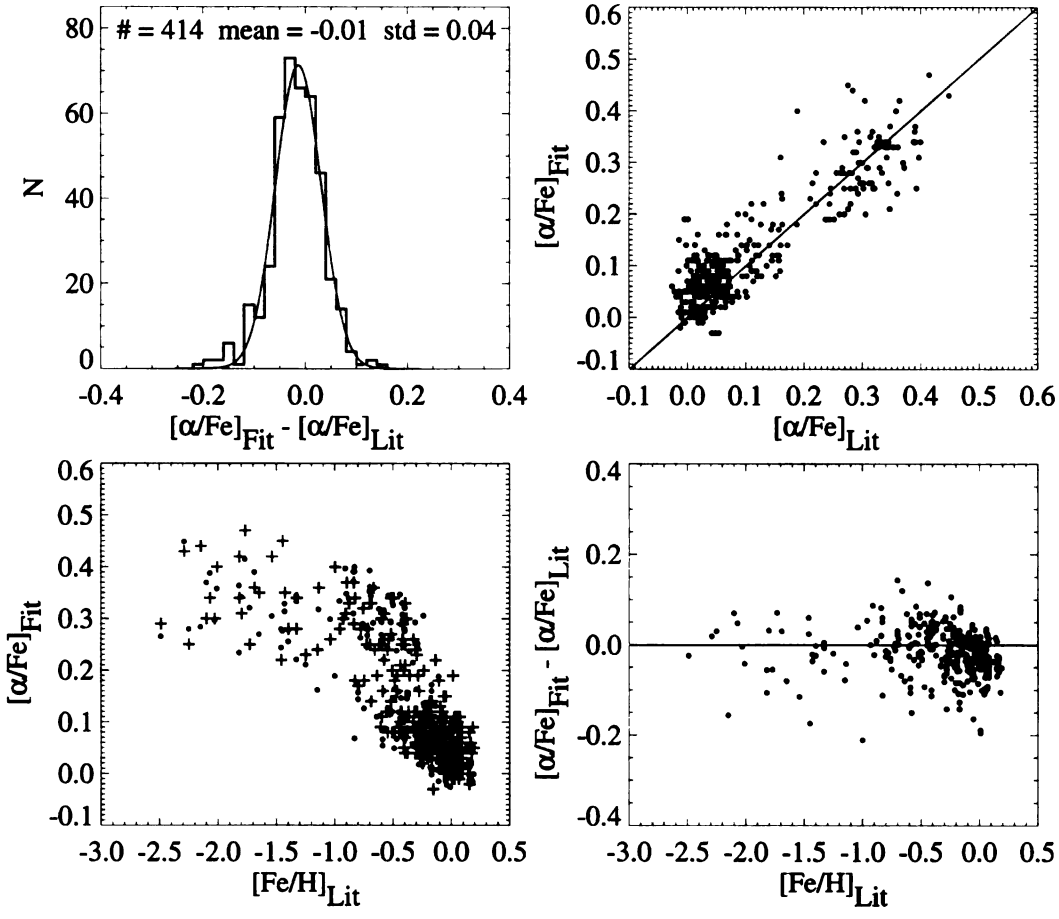


Figure 5.1 Comparison of [α/Fe] from our estimates (Fit) with those from the literature (Lit). The red crosses in the bottom left panel are our determinations.

already existing noise-added high resolution calibration stars presented in detail in Chapter 3.6. In this experiment, and likewise for the SSPP noise test, we attempt to quantify the mean standard deviation of the α-abundance obtained from the noise added spectra by comparing with the α-abundance estimated from the spectra before noise injection. Table 5.1 reflects the Gaussian means and standard deviations from the noise experiment. As can be seen in the table, although no significant offset and a small standard deviation (< 0.1 dex) are found down to $S/N \sim 15/1$, in our analysis of the α-determinations we only consider stars with $S/N \geq 20$. At $S/N = 20/1$, it

is expected that the typical maximum uncertainty in [α/Fe] will be < 0.1 dex, after quadratically adding the offsets and standard deviations at $S/N = 20/1$ and for the original ELODIE S/N.

Table 5.1: Variation of [α/Fe] with S/N

S/N	Mean	Sigma
5.0	0.029	0.202
10.0	−0.014	0.128
14.9	−0.022	0.092
19.9	−0.016	0.075
24.9	−0.013	0.065
29.9	−0.010	0.057
35.0	−0.008	0.052
40.0	−0.006	0.047
45.1	−0.005	0.044
50.2	−0.005	0.041

5.4 Sample Selection

Our program stars are the spectrophotometric and reddening standards from Data Release 6 (DR-6; Adelman-McCarthy et al. 2008). In a typical SDSS spectroscopic observation, together with other original targets, spectra of 16 calibration stars per plug-plate are obtained (the calibration stars are further divided into two subsets, the spectrophometric and telluric calibration stars).

The spectrophotometric calibration stars are used during the course of SDSS pipeline reductions to remove the effects on the flux distribution of the SDSS spectra

arising from the wavelength response of the telescope, the spectrographs, and the Earth's atmosphere. Normally, there are three conditions imposed to select stars for the spectrophotometric calibration: (1) the spectra of the stars should not be rich in absorption lines produced by metallic species, (2) the stars are bright enough to achieve high $S/N(> 20/1)$ in their spectra, and (3) their spectra can be well-synthesized to match stars of known flux distributions. Stars with [Fe/H] ~ -2.0, near the main-sequence turnoff of the halo, satisfy these requirements. The ranges of color and apparent magnitude used for selecting such stars are $0.6 < u - g < 1.2$, $0 < g - r < 0.6$, and $15.5 < g < 17.0$, respectively. In order to find possible spectrophotometric calibration stars even in a low density region, such as the Galactic pole, rather wide color ranges are chosen. Stars as blue as possible are selected because they are the mostly likely candidates for [Fe/H] ~ -2.0.

The telluric calibration stars are used during the SDSS pipeline for subtracting features due to night sky emission and absorption lines from the observed spectra. The same color ranges are used to select these stars, however, their apparent magnitudes are fainter ($17.0 < g < 18.5$) than the spectrophotometric calibration stars, resulting in lower S/N than the former. The typical range of S/N for these stars is 20/1 to 30/1.

From the selection criteria (especially for the spectrophotometric calibration stars), a bias is introduced by the effort to identify metal-poor stars. However, it is almost impossible to distinguish more metal deficient stars among stars with [Fe/H] < -2.0, because the sensitivity of the broad color bands to the metallicity is not sufficiently high to discriminate the lowest metallicity stars ([Fe/H] < -2.5). Therefore, it is believed that the metallicity distribution of the calibration stars mimics the true shape of the low metallicity tail of the metallicity distribution function (MDF) for stars outside the disk populations. This does not apply to stars with [Fe/H] > -2.0. Since proper motion is not used to select the calibration stars, no kinematic bias is

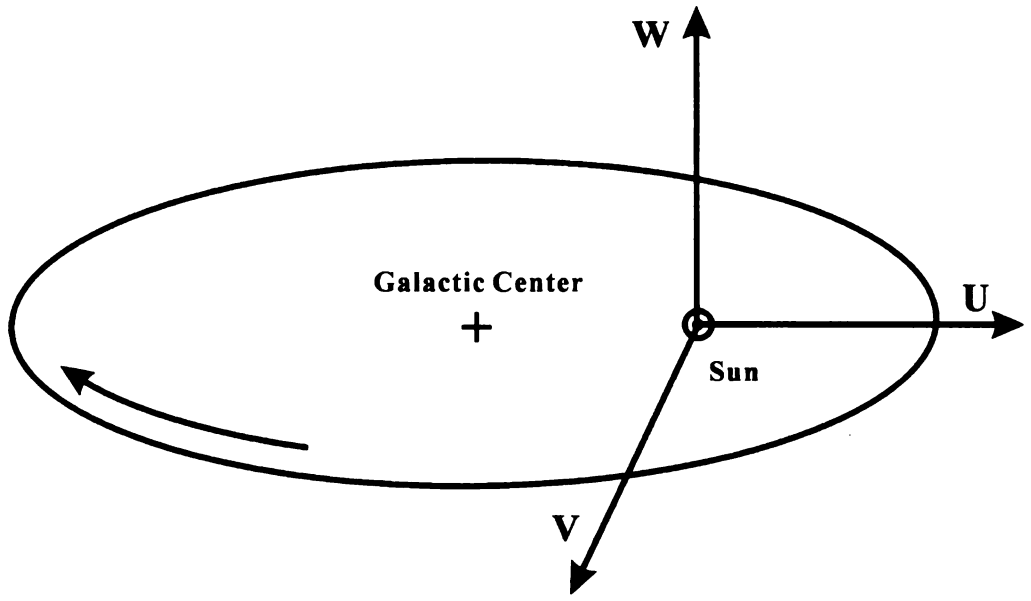


Figure 5.2 Schematic diagram of the U, V, and W Galactic velocity components.

introduced.

A total of 39,167 calibration stars are selected and processed by the SSPP in order to derive the stellar atmosphere parameters. During the execution of the SSPP, distances to each star are estimated by assigning each star to luminosity classes of "dwarf', "subgiant", or "giant", using the derived gravity of each star and by comparing its observed apparent magnitude with its calculated absolute magnitude from calibrated open and globular cluster sequences (see Beers et al. 2000). The accuracy of the distance estimated in this way is expected to be between 10 % and 20 %. The radial velocity of a star is also determined from the SSPP. Once the stellar parameters of the program stars are derived by the SSPP, the α-abundances of our objects are estimated. As mentioned above, we choose to only retain α-estimates for the stars with $S/N > 20/1$ for further analysis.

5.5 Computation of Kinematic and Orbital Parameters

We impose three additional cuts on our sample to derive the most accurate estimates of their kinematics and orbital parameters. First, stars which are in the range 5000 K $< T_{\rm eff} <$ 6800 K are selected, a range that corresponds to the region where the SSPP is best able to derive the atmospheric parameters. Secondly, stars with distances d $<$ 4 kpc from the Sun are chosen, in order to confine the kinematical and orbital analyses to a local volume. This distance cut also reduce the uncertainties in the transverse velocity which are computed from the proper motion and the distance. The typical error in the derived transverse velocities at d = 1 kpc is 22 km s^{-1}, under the assumption that the errors in the proper motion is 3.5 mas/yr and the distance error is 15%. Similarly, transverse velocity errors of 37 and 46 km s^{-1} are calculated at d = 2 kpc and d = 4 kpc, respectively. The final cut is $6 < R < 12$ kpc, where R is the Galactocentric distance projected onto the Galactic plane. The total number of stars surviving these cuts is 18,769.

The proper motions for our sample stars are gathered from the re-calibrated USNO-B catalog, with typical errors of 3 to 4 mas/yr (Munn et al. 2004). Along with the distance estimates and radial velocities, the proper motions enable us to calculate the three dimensional space motions, which are represented by the U, V, W velocities. The zero point of these velocities is the Local Standard of Rest (LSR), which is defined as a frame in which the average space motions of the stars in the Solar neighborhood are zero. The direction toward the Galactic anti-center is positive for the U velocity component, positive toward the Galactic rotation direction for the V velocity component, and positive toward the Galactic north pole for the W velocity component. Figure 5.2 shows a schematic diagram of this kinematic coordinate system. The values of $(U_\odot, V_\odot, W_\odot) = (-9, 12, 7)$ km s^{-1} (Mihalas & Binney 1981)

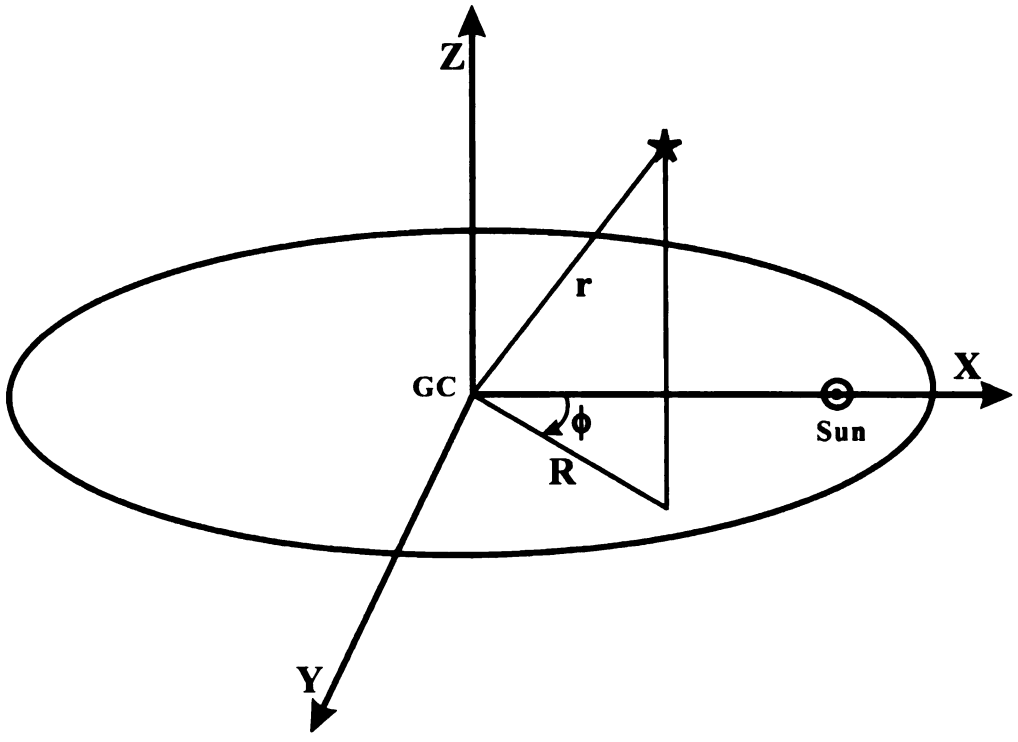


Figure 5.3 Schematic diagram of the Galacto-centric cylindrical reference frame. GC stands for the Galactic Center.

for the Sun's peculiar motions with respect to the LSR is corrected for during the computation of the full space motions of the stars.

By adopting an analytic Stäckel-type gravitational potential (which assumes the Galaxy possesses a flattened, oblate disk and a nearly spherical massive halo) and by integrating orbital paths of the stars, we calculate V_ϕ, the rotational component of a star's motion about the Galactic center in a cylindrical coordinate system, as illustrated in Figure 5.3 (assuming the rotational velocity of the LSR is 220 km s^{-1} (Kerr & Lynden-Bell 1986), $R_{\rm peri}$, the closest distance of a stellar orbit from the Galactic center, $R_{\rm apo}$, the farthest distance of a stellar orbit from the Galactic center, $Z_{\rm max}$, the maximum distance of a stellar orbit above or below the Galactic plane, and the orbital eccentricity (e).

A total sample of 17,450 stars with $S/N \geq 20$ spectra and suitably estimated

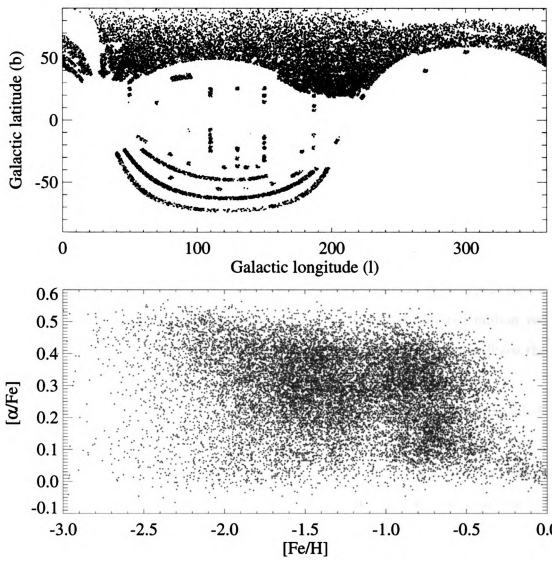


Figure 5.4 Spatial distribution of the sample (17450 stars) in a Galactic coordinate system (top) and a plot (bottom) of [α/Fe] as a function of [Fe/H].

parameters was assembled. The top panel of Figure 5.4 displays the spatial distribution of this final sample in Galactic longitude (l) and latitude (b). The lower panel shows the [α/Fe] distribution with respect to [Fe/H]. At lower metallicities, one can notice the existence of a plateau with [α/Fe] $\sim$ 0.4 dex, which is a typical value for halo stars below [Fe/H] $= -1.0$. Above [Fe/H] $= -1.0$, the α-abundance decreases with metallicity and reaches the solar value at [Fe/H] $= 0$, as found in other studies

(Fuhrmann 1998, 2004; Prochaska et al. 2000; Feltzing, Bensby, & Lundstrom 2003; Bensby et al. 2005). The plateau with the high-α value indicates that the halo stars have been chemically enriched from Type II supernovae, apparently including the metal-poor ([Fe/H] < -0.5) thick disk stars. The lower half of the downturn feature also consists of metal-rich thick disk stars with lower α-abundance, as indicated by Feltzing, Bensby, & Lundstrom (2004). These lower α-abundances are presumably caused by a greater Fe contribution from Type Ia supernovae. This implies that whatever is the astrophysical origin of the thick disk, its progenitor had to have a period of star formation long enough for SNe Ia to explode and pollute the ISM with Fe. Studies (e.g., Matteucci & Greggio 1986; Smecker-Hane & Wyse 1992) indicate that the duration of the star formation can be from several hundred million years to 2 Gyrs. There are not many thin disk stars in our sample, but we still see them ([Fe/H] > -0.3) with [α/Fe] < 0.1 in the figure.

The [α/Fe] patterns with respect to the U, V, W, and V_ϕ velocities are depicted in Figure 5.5. Note the mixed population of thin and thick disk stars with low-α (< 0.2 dex) around $V_\phi \sim 200$ km s^{-1}, and a population with higher α-values with slightly lower V_ϕ (around 180 km s^{-1}). Below $V_\phi < 100$ km s^{-1}, which is going into the halo-dominated regime, we see stars with high-α, but also a significant number of stars with low-α. It is interesting to see that there are not many low -α stars between 80 km s^{-1} and 170 km s^{-1} in V_ϕ velocity. While Chiba & Beers (2000) reported $V_\phi \sim 170$ km s^{-1}, Gilmore, Wyse, & Norris (2002) derived $V_\phi \sim 100$ km s^{-1} for the thick-disk population. If the value of 100 km s^{-1} by Gilmore, Wyse, & Norris (2002) represents the thick-disk population, the region showing the smaller number of stars with low-α is the thick disk regime. Furthermore, if the thick disk formed from debris of mergers with satellite systems, as envisioned e.g., by Abadi et al. (2003), the satellites should have been massive enough so that they would not be disrupted until they arrived in the disk plane. It is believed that massive dwarf galaxies (not

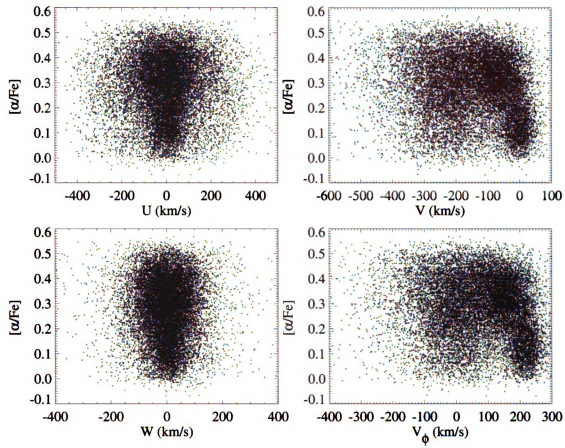


Figure 5.5 Run of [α/Fe] over U, V, W, and V_ϕ.

the present dwarf galaxies, which are of lower mass) experienced an early era of rapid star formation, which produced high values of α by SNe II from dying high mass stars. Relatively few low-α stars might be produced as a result. This may account, at least in part, for the region devoid of stars near 100 km s^{-1} in the figure.

Plots of [α/Fe] with various orbital parameters, such as $Z_{\rm max}$, $R_{\rm apo}$, $R_{\rm peri}$, and eccentricity are shown in Figure 5.6. Not much trend of [α/Fe] with respect to the orbital parameters is noticed, but after excluding the thin- and metal-rich thick disk stars, we see that as $R_{\rm peri}$ decreases, the spread of [α/Fe] becomes larger; a similar behavior applies as the eccentricity increases.

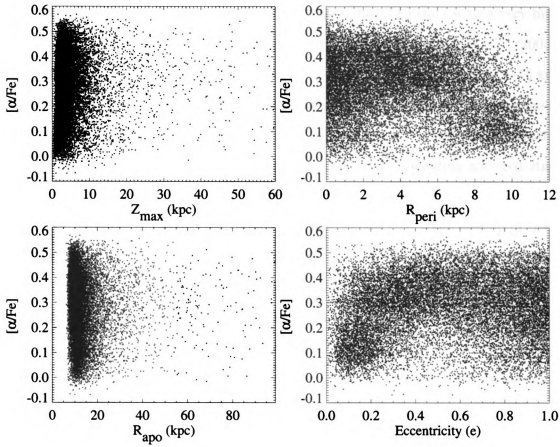


Figure 5.6 Distributions of [α/Fe] with respect to $Z_{\rm max}$, $R_{\rm peri}$, $R_{\rm apo}$, and eccentricity (e)

5.6 Distributions of [α/Fe]

In order to investigate the α-abundance patterns for stars in the Galactic halo, we first have to set the selection criteria for halo stars. We impose three criteria on the parameters V_ϕ, $Z_{\rm max}$, and [Fe/H]. First, we select stars with $V_\phi \leq 80$ km s^{-1}, which is more than 2 σ (2 $\times$ 39 km s^{-1}) away from the typical thick-disk velocity ellipsoid centered on V_ϕ = 180 km s^{-1} (Soubiran et al. 2003). In addition, by cutting the sample with [Fe/H] ≤ -1.0, we are able to eliminate most of metal-poor disk stars. Finally, we choose stars with $Z_{\rm max} \geq 1$ kpc, so that potential thin and thick disk stars that slip through the above cuts can be excluded. Applying these conditions

to the total sample of 17,450 stars allows us to assemble 7580 stars with a very high probability of halo membership. Following the scheme of Gratton et al. (2003), throughout this study we will refer to stars with $V_\phi \geq 40$ km s^{-1} and $R_{\rm apo} < 16$ kpc as a "dissipative" component, which is the dominant population in the inner halo, and with $V_\phi < 40$ km s^{-1} or $R_{\rm apo} \geq 16$ kpc (or both) as an "accreted" component, which presumably makes up most of the outer halo stars, including accreted stars from disrupted dwarf galaxies. We also refer to these components as the inner halo, and outer halo, respectively, even though it is understood that some overlap of these components surely exists. The dividing line of 40 km s^{-1} and 16 kpc will also provide an adequate number of stars for both groups. Mostly, the observed properties of the distribution of [α/Fe] of the accreted and dissipative components made with various cuts on several parameters such as V_ϕ, $R_{\rm apo}$, [Fe/H], etc., will be discussed in this section. Detailed discussions and implications of the patterns found in this section are deferred to the following section.

5.6.1 Distributions of V_ϕ and [Fe/H] with [α/Fe] cuts

Figure 5.7 shows histograms of V_ϕ (left) and [Fe/H] (right) with various bins of [α/Fe] for the accreted (or outer halo; red line) and dissipative (or inner halo; black line) components divided at $R_{\rm apo} = 16$ kpc. The black vertical line is the division between prograde and retrograde motion around the Galactic center. The cuts on [α/Fe] for each histogram are shown in the top of each right-hand panel. $N_{\rm tot}$ is the total number of stars in each [α/Fe] bin. It is clear from inspection of the left-hand panels that while the dissipative component ($R_{\rm apo} < 16$ kpc) are more concentrated on zero or slightly positive rotation velocity, the accreted components are somewhat shifted to counter-rotational velocities, with a long tail of negative velocities for all α-cuts, confirming Carollo et al. (2007)'s claim that the outer halo population exhibits a net retrograde rotation between –40 and –70 km s^{-1}, while the inner halo population

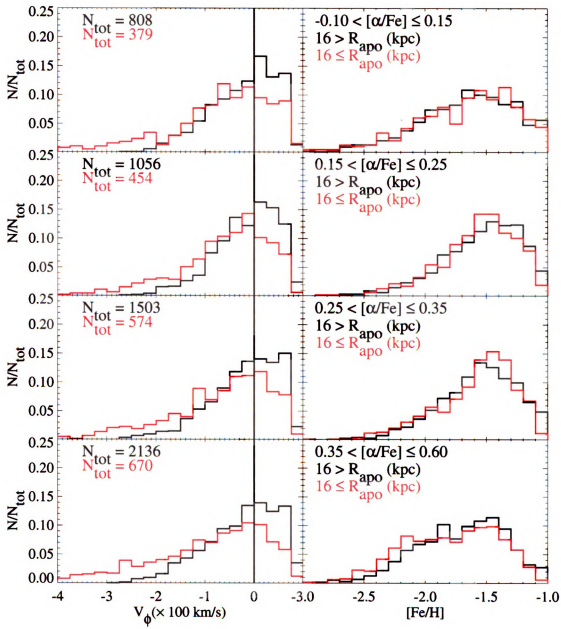


Figure 5.7 Distributions of V_ϕ (left) and [Fe/H] (right) with different bins of [α/Fe] for the accreted (red line) and dissipative (black line) components, divided at $R_{\rm apo} = 16$ kpc.

consists of stars on net prograde orbits between 0 and 50 km s^{-1}. It is also interesting to note that there is a greater fraction of extremely retrograde ($V_\phi < -250$ km s^{-1}) stars included for the outer halo stars than for the inner halo stars, giving more

weight to the net retrograde property of the outer halo. The distribution of [Fe/H] provides another intriguing feature – more stars are seen below [Fe/H] = –1.8 for the outer halo in the range –0.1 < [α/Fe] < 0.15 and 0.35 < [α/Fe] < 0.6. Carollo et al. (2007) demonstrated that the peak of the metallicity distribution function (MDF) of the outer halo population occurs at [Fe/H] = –2.2, which is close to what is seen here. This may imply that the low-metallicity stars in the outer halo may split into distinct populations with varying levels of α-enhancement, preferentially low and high α-abundance, hinting they would form in environments which had gone through different chemical enrichment history. There may be a similar weak feature among the inner halo stars as well, although it is not as apparent as that for the outer halo stars.

5.6.2 Distributions of [α/Fe] with [Fe/H] cuts

In order to further examine the features found in Figure 5.7, after breaking up the sample into the dissipative component with $V_\phi \geq 40$ km s^{-1} and $R_{\rm apo} < 16$ kpc, and the accreted component with $V_\phi < 40$ km s^{-1} and $R_{\rm apo} \geq 16$ kpc, we constructed histograms of [α/Fe] and $R_{\rm peri}$ for various metallicity regimes, as shown in Figure 5.8. The metallicity cuts used to make the histograms is listed in the top legend of each right-hand panel. The distribution in black applies to the dissipative component, while the accreted component is shown in red. The prominent pattern that can be noticed in the left hand panels of the figure is that as the cut on [Fe/H] decreases, the fractional number of stars with intermediate α-abundance ($\sim$ 0.25 dex) is reduced, whereas that of the low (below 0.2 dex) and high(above 0.3 dex)-α stars is increasing, implying a bifurcation of the population in a given metallicity range. It appears that this pattern occurs for the inner halo stars, too, although the outer halo stars have a more conspicuous feature at the low metallicity end. It is clear from the peaks of the α-abundance distribution in the first two top left-hand panels that the outer halo stars

have, on average, lower [α/Fe] with a larger scatter than the inner halo stars for the range [Fe/H] > −1.8, confirming the claims of previous studies (e.g., Nissen & Schuster 1997; Gratton et al. 2003) that the stars with exotic kinematics (e.g., retrograde motion) have lower mean values of α-abundance at a given metallicity. Below [Fe/H] = −1.8, the difference in mean [α/Fe] values between the two components disappears, owing to the much larger scatter in the [α/Fe] distribution.

In the histograms of the right-hand panels shown in Figure 5.8, it can be seen that most of the inner halo stars with [Fe/H] > −2.2 are clustered at $R_{\rm peri}$ less than 3 kpc, with a small spread. Below this metallicity, the fraction of high $R_{\rm peri}$ stars increases; the scatter in $R_{\rm peri}$ becomes larger as well. A more salient feature in the distribution of $R_{\rm peri}$ can be seen for the outer halo stars in the histograms, which exhibit a much flatter distribution as [Fe/H] decreases. Since it is thought that if stars possess a common set of kinematics they are likely to share a common origin, the presence of multiple (and different) features in the kinematics within one group in the narrow range of the metallicity may indicate a mixture of diverse populations. A more detailed discussion on this point is presented below.

Table 5.2: Results of Kolmogorov-Smirnoff (K-S) tests

[Fe/H]	Inner	Outer	Inner + Outer	Inner vs Outer
−1.4 ∼ −1.0	1.000000	1.000000	1.000000	0.000012
−1.8 ∼ −1.4	0.228898	0.015397	0.030933	0.000144
−2.2 ∼ −1.8	0.026533	0.000000	0.000000	0.309947
−2.5 ∼ −2.2	0.000366	0.000000	0.000000	0.543394
−3.0 ∼ −2.5	0.060502	0.000246	0.000271	0.562488

One of the best ways of testing whether a distribution of one sample differs from

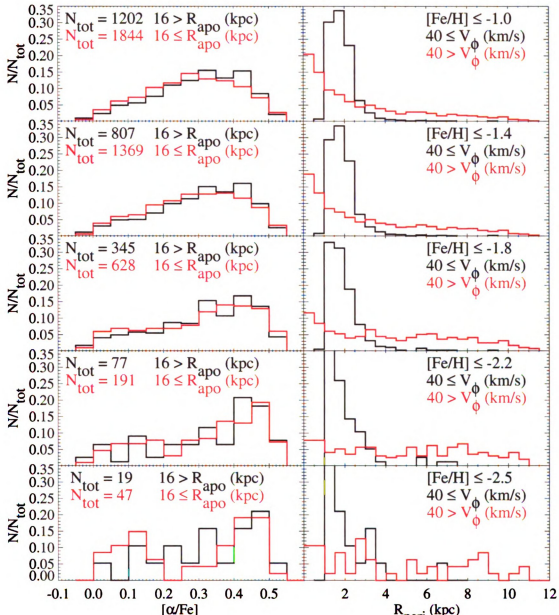


Figure 5.8 Distributions of [α/Fe] (left) and $R_{\rm peri}$ (right) with different bins of [Fe/H] for the inner (black) and outer (red) halo. Note that the inner and outer halo should satisfy both $R_{\rm apo}$ and V_ϕ cuts.

that of another is to use a Kolmogorov-Smirnoff (K-S) test. Therefore, in order to examine if there exist different populations in our data, we performed a K-S test, with a null hypothesis that the distribution of [α/Fe] shown in the lower panels for

the individual cuts on metallicity could be drawn from the distribution of the same parent population as that shown in the upper panels. In this test, we obtained for $-1.8 < [Fe/H] \leq -1.4$, one-sided probabilities of 0.228898, 0.015397, and 0.030933 for the inner, outer, and the inner and outer combined cases, respectively. For $-2.2 < [Fe/H] \leq -1.8$, one-sided probabilities of 0.026533 for the inner, and less than 0.000001 for both the outer and inner and outer combined data set were calculated. For $-2.5 < [Fe/H] \leq -2.2$, one-sided probabilities of 0.000366 and below 0.000001 for both the outer and the inner and outer combined stars. For $-3.0 < [Fe/H] \leq -2.5$, one-sided probabilities of 0.060502, 0.000246, and 0.000271 were derived for the inner, the outer, and the inner and outer together, respectively. The second, third, and fourth column in Table 5.2 summarize the test results. As listed in the table, the null hypothesis is strongly rejected for most cases, in particular below [Fe/H] = −1.8, confirming the existence of multiple populations in our data. Thus, it can be inferred that the stars in individual metallicity bins were born from an ISM that had been polluted by different processes.

We also carried out a K-S test between the inner and outer halo populations under the hypothesis that the distribution of [α/Fe] shown in black (inner halo) for each metallicity bin could be reproduced from the distribution of the same parent population as that shown in the red (outer halo). The fifth column in Table 5.2 shows the results of this test. It is very interesting to see that the null hypothesis is only rejected for the metallicity range $-1.8 <[\ Fe/H] \leq -1.0$, but not for lower metallicities. Hence, the inner and outer halo stars with [Fe/H] > −1.8 formed in environments that experienced different enrichment histories. A plausible interpretation for the cases with [Fe/H] < −1.8, which are not highly rejected, is that no matter whether those stars were accreted from smaller subsystems or formed in dissipatively collapsing proto-galactic clouds, it may be the case that the chemical enrichment history in the regions where they were born may be the same at very low metallicity.

5.6.3 DISTRIBUTIONS OF [α/Fe] WITH R_{apo} CUTS

Inspection of the right-hand panels of Figure 5.9, which display the distributions of [α/Fe] separated by various cuts on R_{apo}, clearly reveals that there are a greater fraction of low -α stars for the accreted component than found for the dissipative component as the apo-Galactic distance increases. The apo-Galactic distance range for each plot is listed in the top of each left-hand panel. This agrees with the results from Stephens & Boesgaard (2002), who claimed that the average value of [α/Fe] for the stars with $R_{apo} > 16$ kpc at the same metallicity is slightly lower than that of the lower orbit stars with $R_{apo} < 16$ kpc. The inner halo stars seem to exhibit similar properties, but is not completely clear. The relative number of the high-α stars with $R_{apo} > 16$ kpc, however, is reduced significantly, and the low-α stars are relatively increased. This figure (the third right-hand panel) also indicates that there are some fraction of low [α/Fe] stars even among the prograde stars having R_{apo} as large as twice the Sun's orbit. These kinematically peculiar prograde stars may form in localized star-forming regions at large Galactic distances, which had prolonged star formation until the onset of SNe Ia. Considering their large apo-Galactic distances, an external origin cannot be ruled out.

The left-hand panels of Figure 5.9 show [α/Fe] as a function of [Fe/H]. The mean value of [α/Fe] at a given metallicity was calculated by averaging the α-abundance in a bin of 0.5 dex in metallicity. The mean α-abundances, with error bars indicating the standard error of mean (s.e.m) for both the inner (blue diamond) and the outer (green triangle) are over-plotted in the figure. An odd feature in Figure 5.9 is that, as exhibited in the left-hand panels of the figure, below [Fe/H] = –2.0 the mean value of the α-abundance for the accreted component at a given metallicity is substantially lower than that of the dissipative component, although the uncertainty could be higher due to the small number of stars in that regime. The discrepancy becomes higher as the apo-Galactic distance becomes larger. It appears that is also the case for

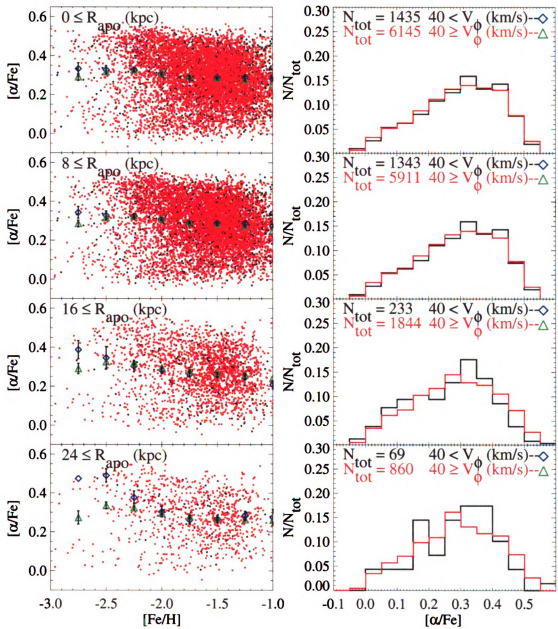


Figure 5.9 Distributions of [α/Fe] (right) and plots of [α/Fe] versus [Fe/H] (right) with various cuts on $R_{\rm apo}$. The blue diamonds denote mean values of [α/Fe] of the inner halo stars at a given metallicity and the outer halo stars for the green triangles.

the range [Fe/H] > –1.5, but we don't clearly see the same behavior in the range –2.0 < [Fe/H] < –1.5. The larger discrepancy in mean α-abundance may be attributed to a more clear separation between the inner and outer halo stars at high $R_{\rm apo}$ at low

metallicity, but smaller differences due to overlapping populations at low $R_{\rm apo}$.

Another interesting fact is that there may be trends in α-abundance with metallicity, provided that the low-α stars are removed, as found in Figure 20 and 21 in the paper by Stephens & Boesgaard (2002). This will be discussed in more detail below.

5.6.4 Distributions of [α/Fe] with V_ϕ cuts

Now we make use of V_ϕ as a cut to examine how [α/Fe] (left panels), [Fe/H] (middle panels), and eccentricity (right panels) are distributed over this variable. Figure 5.10 displays the results. The range of V_ϕ used to cut the sample is listed in the top of each middle panel. Just as before, the sample is divided into the inner and outer halo stars by cutting on the $R_{\rm apo}$ distance at 16 kpc. The first thing noticed in this figure is that as the V_ϕ cut declines, the fraction of the number of low metallicity stars increases for the outer halo stars, as found by Carollo et al. (2007). The same effect, but somewhat smaller, is exhibited by the inner halo stars, presumably due to overlapping populations. The distribution of [α/Fe] for the outer halo stars is shifted to lower α down to $V_\phi \sim$ –200 km s^{-1}, compared to that of the inner halo stars. Below V_ϕ = –200 km s^{-1}, the distribution is again shifted to high-α for the accreted component, but still, some low -α stars exist. It is very interesting to note the somewhat larger fraction of the low-α stars among the accreted sample with even moderate rotation velocity, as shown in red in the top left panel. This is already seen in the third right-hand panel of Figure 5.9.

From the distribution of the eccentricity, it can be inferred that without separating the sample into two groups, the inner halo component with stars having $V_\phi >$ –50 km s^{-1} is oblate, since it has lots of stars with high eccentricities, while the outer halo component with stars having $V_\phi <$ –50 km s^{-1} has a slightly spherical shape, with lower eccentricity, as also identified by Carollo et al. (2007).

The left-hand panels of Figure 5.11, which show [α/Fe] versus [Fe/H] for various

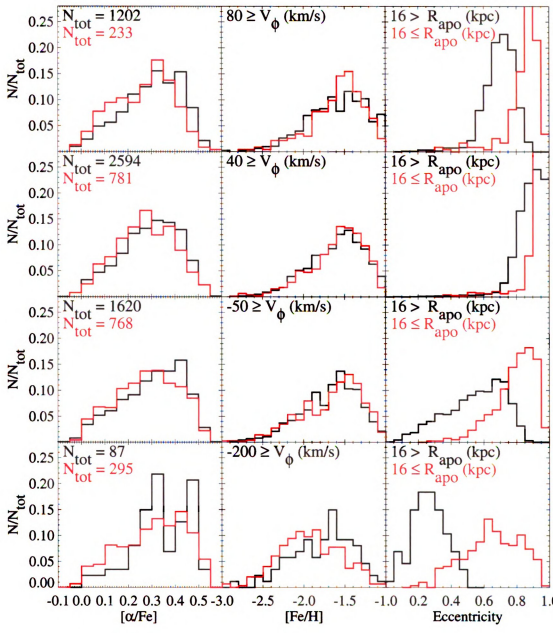


Figure 5.10 Distributions of [α/Fe] (left), [Fe/H] (middle), and eccentricity (right) for the stars selected by various cuts on V_ϕ.

cuts on V_ϕ, exhibit somewhat different results from those found from Figure 5.9. Note that each histogram is cumulative in V_ϕ, as indicated in the top of each panel. The mean values of[α/Fe] were calculated with the same way as in Figure 5.9. and the symbols represent the same groups (blue diamond - inner halo, green triangle -

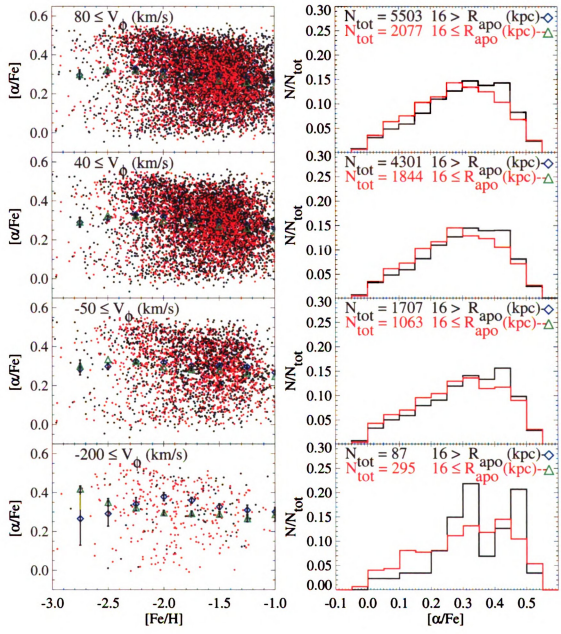


Figure 5.11 Fractional histograms of [α/Fe] (right) and plots of [α/Fe] versus [Fe/H] (right) for the stars selected by various cuts on V_ϕ.

outer halo). In this figure, down to [Fe/H] = –2.25, the accreted stars display lower α values on average for all rotation velocity cuts, as seen by other studies (Nissen & Schuster 1997; Gratton et al 2003; Stephens & Boesgaard 2002). Below [Fe/H] = –2.25, although not many stars are involved, the dissipative component exhibits lower

(or at the same level) α-enhancement on average, which is directly opposite to what was found in Figure 5.9. Furthermore, the discrepancy in the mean α values becomes larger with lower V_ϕ. This may be because of the sample selection. We may regard the stars with V_ϕ < -200 km s^{-1} as outer halo stars, no matter what the $R_{\rm apo}$ they have. This behavior may also suggest that V_ϕ is a better parameter to distinguish the low metallicity outer halo stars from the inner halo stars. Yet, since we separated the sample into two groups for V_ϕ 200 km s^{-1}, we may see this kind of behavior. There may be a weak trend of [α/Fe] with respect to [Fe/H] for both the inner and outer halo, at least down to [Fe/H] = –2.0. However, below this metallicity, it is hard to tell due to the downturn of [α/Fe]. Larger numbers of low metallicity stars are clearly required. The histograms of [α/Fe] in the right-hand panels of the figure reveals the same results seen in Figure 5.9; the overall mean value of [α/Fe] is lower for the stars with higher $R_{\rm apo}$ than those with lower $R_{\rm apo}$ over all ranges of V_ϕ.

5.7 Discussions and Implications

What do the patterns and behaviors identified in the previous section imply? We first consider the inner halo stars. Since a typical halo star has [α/Fe] = 0.3 to 0.4, even taking into account the uncertainty in estimating [α/Fe] from our technique, the fact that most of the inner halo stars with [Fe/H] > –1.8 are concentrated at high-α in Figure 5.8 indicates that the more metal-rich inner halo is well described by a canonical Galactic chemical model (Tinsley 1979). In this simple model, second generation stars were born in a low metallicity gas cloud with a standard initial mass function (IMF), and are expected to have α-enhancements on the order of 0.4 dex, the standard SN II ratio. Another possible interpretation is that, as Font et al. (2006a) demonstrated in their simulations of hierarchical formations of stellar halos within the context of a standard ΛCMD universe, the inner halo could have been built up from dwarf galaxies with high levels of α-elements, with a significant contribution

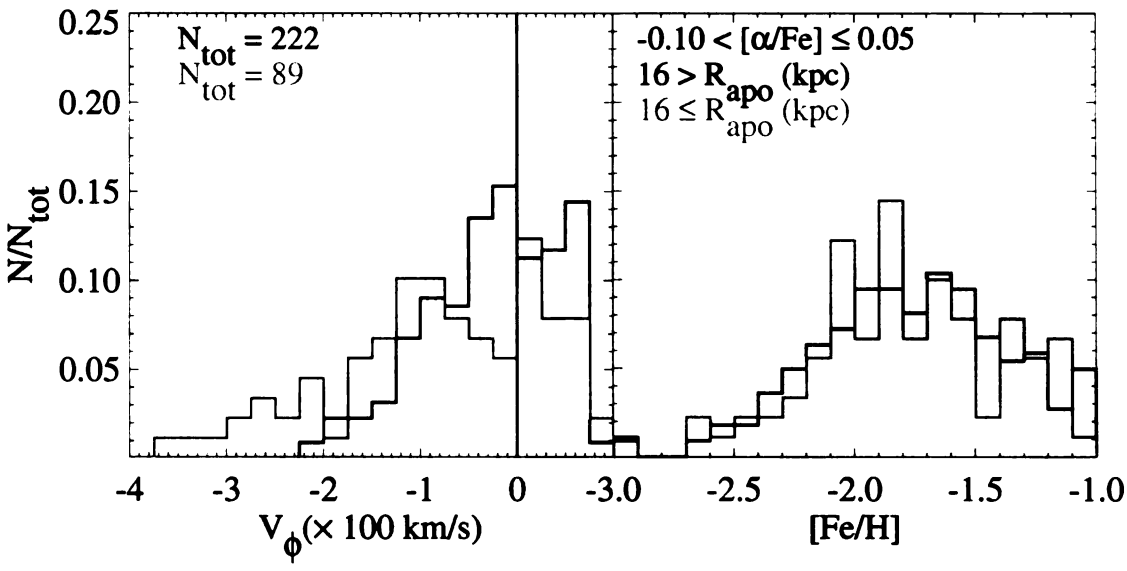


Figure 5.12 Distributions of V_ϕ (left) and [Fe/H] (right) for stars with [α/Fe] < 0.05

from a few high mass systems very early in the process, before contributions from Type Ia SNe could lower the ratio of [α/Fe].

In contrast, the dissipative component with [Fe/H] < –1.8 is not well explained by only SNe II enrichment, due to the apparent bifurcation of the α distribution into both high and low -α stars. One might naively think that the low-α stars with [Fe/H] < –1.8 might have formed in another environment, such as the low mass dwarf galaxies, and were accreted later on. The hierarchical galaxy formation (e.g., Font et al. 2006a, 2006b) also suggests that the accretion of the low-α, low metallicity stars is possible at later epochs of halo formation. The histograms of the right-hand panels of Figure 5.8 might support this conjecture. Even though in the histograms most of the inner halo stars with [Fe/H] > –2.2 are clustered at $R_{\rm peri}$ less than 3 kpc, with a small spread, there are some stars with high values of $R_{\rm peri}$ and [Fe/H] < –2.2, which might have been accreted. However, taking into account the prograde motion of these stars, and the likely inside-out formation of the halo, late accretion of the inner region of the halo is not expected to have occurred.

One possible origin for the low-α inner halo stars is that, as Gilmore & Wyse

(1998) suggested for the metal-rich, low-α halo sample of Nissen & Schuster (1997), those stars might have formed in fragmented star-forming regions of the proto-galactic cloud which had a persistent star formation period of more than a few Gyr, so that they were self-enriched by SNe Ia. In this case, the regions where those stars were born should be a low mass (or low density) environment; otherwise, the stars would have higher metallicity due to rapid star formation. At present, this explanation seems at least plausible.

Others (e.g., McWilliam 1998; Ryan et al. 1996) have reasoned that low metallicity stars formed in an early Galaxy which was chemically contaminated by stochastic star formation. Hence, stars with [Fe/H] < -1.8 might have formed from gas clouds polluted by a single, or only a few SNe (Audouze & Silk 1995; Tsuijimoto et al. 1999), which might account for the larger scatter we see in our data at the very low metallicity end. This is, however, in conflict with the findings of Arnone et al. (2005), who detected a very small cosmic scatter in Mg abundance for stars in the metallicity range $-3.0 <$ [Fe/H] < -2.2, pointing toward a well mixed, homogeneous ISM. It seems that our data are likely to be more consistent with inhomogeneous chemical evolution models (e.g., Ishimaru & Wanajo 1999; Argast et al. 2000), at least in the range [Fe/H] < -1.8.

As Carollo et al. (2007) asserted that the outer halo formed through assembly of smaller subsystems, assuming that *all* outer halo stars were accreted from external systems, the low-α outer halo stars might have formed in low mass dwarf galaxies and accreted early in the history of the Galaxy, similar to the conclusions of other studies (Gratton et al. 2003; Venn et al. 2004; Geisler et al. 2007). Geisler et al. (2007) reported that there is marginal overlap between the stars in dSphs and the halo stars at the very low metallicity end, but more metal-poor stars with [Fe/H] $<$ -2.4 in dSphs are need to be observed at high spectral resolution in order to confirm this. This picture agrees with the recent simulations of the stellar halo formation

models by Font et al. (2006a, 2006b) and Johnston et al. (2008) who claimed that the stars accreted from the surviving satellites possess low-α abundance.

Font et al. (2006b) suggested that one may be able to track down the debris (e.g., cold tidal streams) of dwarf galaxies disrupted by recent interaction with their parent galaxy by selecting stars with $[\alpha/\mathrm{Fe}] < 0.05$. If we apply this cut to our halo sample and look at the distribution of V_ϕ as plotted in Figure 5.12, it can be noticed that a larger portion of the stars exhibit retrograde motion for both the inner and outer halo. The MDF is also shifted to lower metallicity compared to the first right-hand panel of Figure 5.7. This MDF shift to lower metallicity and low α-abundance implicate that the progenitors of the low-α stars selected were not that massive, and the accretion happened recently. This is due to the fact that if the progenitors of the low-α stars were massive and the epoch of the accretion was early, the overall metallicity should have been shifted to higher metallicity with high α-abundance. On the other hand, if the mass of the progenitors was low and the epoch of the accretion was early, then although we might expect stars of low metallicity, the overall α-abundance would be high. This interpretation is well described in the recent paper by Johnston et al. (2008), especially their Table 1. These authors found from their models of eleven stellar halos, simulated within the context of a standard ΛCMD, that the distribution of $[\alpha/\mathrm{Fe}]$ of stellar halo stars is a good indicator of the epoch of halo accretion, thanks to the few Gyr time interval between the onset of SNe II and SNe Ia, while the [Fe/H] distribution of the stars is sensitive to the mass of accreted dwarf galaxies. Based on this scheme, we may be able to roughly estimate the epoch of the accretion and the dominant mass scales involved.

Where did the high-α outer halo stars with $[\mathrm{Fe/H}] < -1.8$ seen in the figure come from? One could argue that the progenitors of the high-α outer halo stars should have been massive enough to produce the typical halo level of the α-enhancement ($\sim$ 0.3 dex or more) from SNe II. This would exclude the current low mass dwarf

galaxies around the Milky Way as progenitors of the accreted stars, because most of the stars observed in the dSphs do not exhibit such high-α enhancements (Shetrone et al. 2001, 2003; Fulbright 2002; Tolstoy et al. 2003; Geisler et al. 2005). So, it remains possible that they might have been accreted very early from massive dwarf galaxies such as Sgr, as pointed out by Geisler et al. (2007), who found good agreement in [α/Fe] between the Sgr stars and the halo stars in the metallicity range $-1.6 <$ [Fe/H] < -1.0. This may account at least for the high-α stars for [Fe/H] > -1.8 in the figure. For the low metallicity end, more metal-poor stars in Sgr are needed to confirm that. Font et al. (2006a, 2006b) also suggested that the high-α, low metallicity outer halo stars formed in a few massive systems and were accreted very early before significant Fe contribution from SNe Ia could take place.

Another credible explanation, although contrary to the above argument, could be that the high-α outer halo stars with [Fe/H] < -1.8 formed in very low mass dwarf galaxies in which the ISM was not so well mixed after the first burst of star formation. It is known that only a few SNe II are sufficient to enrich the ISM of small parcels of gas to that of the typical halo α-abundance level. The recent study by Recchi et al. (2008) revealed that a differential galactic wind may cause the global metallicity of a galaxy to be reduced by preferentially pushing away the metallic elements. Such a wind might therefore generate the high-α and low metallicity environment required to explain these stars. This might suggest that the presently observed ultra faint dwarf galaxies (e.g., Belokorov et al. 2006; Zucker et al. 2006; Belokurov et al. 2007), recently found from the SDSS photometry, might be good candidates. In these very low mass dwarf galaxies, the galactic winds would be very effective to push out the ISM, due to their weak internal gravity. The recent discovery (Kirby et al. 2008) of stars with [Fe/H] < -3.0 in these low luminosity dwarfs provides an additional clue. These authors argued that the low luminosity dwarf galaxies might be the building blocks of the Galactic halo, since the MDFs of these galaxies have very similar low

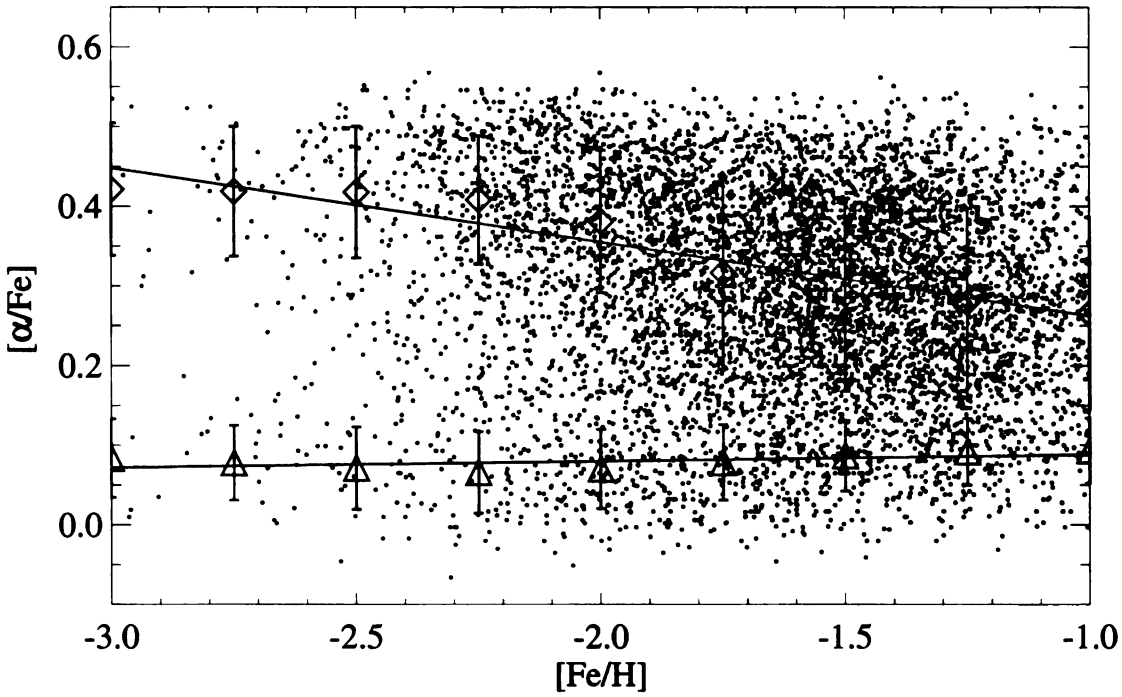


Figure 5.13 Distributions of mean [α/Fe] at a given metallicity for two separate samples. The blue diamonds with error bars are mean values of [α/Fe] in a bin of 0.5 dex in metallicity, obtained from the sample after removing the stars with [α/Fe] < 0.25 for [Fe/H] < -1.8. The green triangles with error bars are mean values of [α/Fe] in a bin of 0.5 dex in metallicity from the stars with [α/Fe] < 0.15. The cut of [Fe/H] $= -1.8$ is chosen because the bifurcation starts showing in Figure 5.8 at this metallicity. The red lines are linear fits to the average values of the α-abundance for each group.

metallicity tails as the MDF of the halo, as also suggested by Carollo et al. (2007). Once the α-abundance of the stars in the low luminous dwarf galaxies is measured, this connection would become clearer. This picture is also in line with the inhomogeneous chemical evolution model. It could be the case that the stars with [Fe/H] < -2.2 for both the accreted and the dissipative components formed from an ISM which had experienced stochastic star formation, while above this limit stars more likely formed in well mixed and homogeneous star forming regions.

It is very intriguing to compare Figure 5.9 and 5.11 with Figure 9 in Font et al. (2006a) and Figure 9 in Font et al. (2006b), who simulated various types of stellar halos formed solely by accretions from dwarf satellite galaxies in a ΛCMD

cosmology. In their models, while the stellar halos generally exhibit a gradient of α-abundance against [Fe/H] (increasing α with decreasing metallicity), the surviving satellites exhibit around the solar α-abundance, which closely follow the abundance patterns of the present-day dSphs and the Milky Way halo. In order to illustrate this with our data, Figure 5.13 shows [α/Fe] versus [Fe/H], after separating the entire sample of halo stars into two sub-samples. One group consists of stars with [α/Fe] $>$ 0.25 for [Fe/H] = –1.8, which is the point where the bifurcation begins to show in Figure 5.8. The blue diamonds with error bars in Figure 5.13 are the mean values of [α/Fe] in a bin of 0.5 dex in metallicity for this group. The red line is the linear fit to the average values of the α-abundance. The other group is composed of stars with [α/Fe] $<$ 0.15, and the green triangles in the figure are the mean values of α-abundance for this group. This figure exhibits a very similar behavior to the stellar halos formed by Font et al. (2006a, 2006b), including the low-α stars as well, under the assumption that all low-α stars were accreted from low mass dwarf galaxies. This similarity suggests that at least some of the low-α stars in our sample may have come such a process. These papers claimed that the low-α stars were accreted from dwarf galaxies about 5 to 6 Gyr ago, rather late in the Galaxy formation process, after SNe Ia went off to pollute the ISM with Fe.

Interestingly, Stephens & Boesgaard (2002) also identified a gradient of the α-abundance with respect to [Fe/H] in their sample with abnormal kinematics (e.g., Figure 20 and 21 in their paper). They reported a slope of –0.15, assuming a linear relation. From our data, we derive a slope of –0.093 from a linear fit to the average values of [α/Fe]. The slight difference between the two values may be caused by the cut-off in [Fe/H] = –1.0 in our data.

From the above statements and looking at the α-abundance distribution for [Fe/H] $<$ –1.8 in Figure 5.8, we can conclude that there is no significant fraction of stars that may have been accreted from the small systems similar to the low mass dSphs we

observe today around the Milky Way, since we there is a much larger fraction of the stars (from both the inner and outer halo populations) clustered at high α-abundance, which is not the case for the low mass dSphs. This agrees with other previous studies (Shetrone et al. 2001, 2003; Fulbright 2002; Venn et al. 2004; Geisler et al. 2007). However, there remains the possibility for early accretion from massive satellites, which are responsible for the low metallicity, low-α stars. The ultra low luminous dwarf galaxies are also possible sources for the low metallicity, low-α halo stars.

In Figure 5.14 we plot [α/Fe] as a function of $R_{\rm peri}$ (right), in hopes of exploring the origin of the bifurcation at the very low metallicity end. Note that the distributions are cumulative on [Fe/H] as denoted in the top of each panel, unlike the panels of Figure 5.8. The behavior of the bifurcation in the α-abundance is more apparent in this figure. Gilmore & Wyse (1998) argued that the low mass dwarf galaxies like the ones we see today around the Galaxy cannot be the source of the low-α halo stars with low $R_{\rm peri}$ values, because they are not massive enough to hold the stars with their internal gravity, and member stars would be tidally dissolved into the halo before they obtain orbits with such small $R_{\rm peri}$distances. Generally, it is known that a small system interacting with a larger system will lose most of its mass if its internal average density is less than about three times the mean density of the larger system (e.g., Johnston, Hernquist, & Bolte 1996). This was the argument they put forward to dispute the claims of Nissen & Shuster (1997) that the metal-rich ($-1.4 <$ [Fe/H] < -0.8) and low-α halo sample they studied could have been a population accreted from the low mass galaxies like the dwarf Sphs.

By extending their argument to lower metallicity and looking at the [α/Fe] distribution of the very low metallicity sample, as a function of $R_{\rm peri}$, we may check if this logic also holds for our low-α, low metallicity stars. As can be seen in the figure, the majority of the presumably accreted stars with [Fe/H] ≤ -2.2 have $R_{\rm peri} > 2$ kpc, which is about twice the distance than for the sample of Nissen & Schuster (1997).

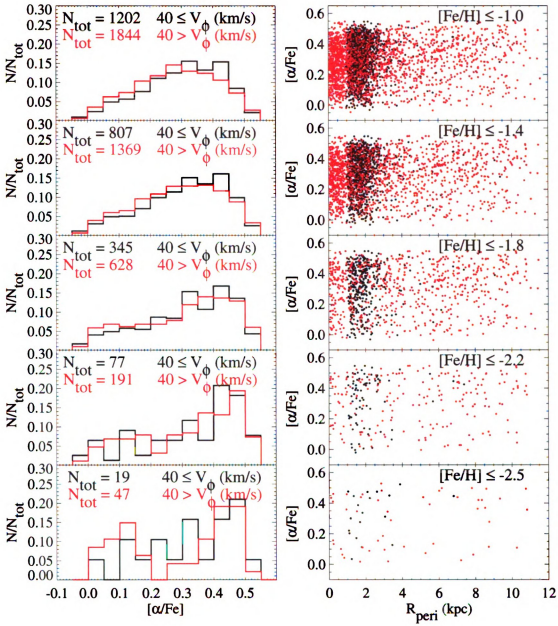


Figure 5.14 Distributions of [α/Fe] (left) and $R_{\rm peri}$ (right) with various cuts on [Fe/H]. As in Figure 5.8 the dissipative (black) and the accreted (red) components are shown.

Therefore, some of the counter-rotating stars with low-α might come from low mass dwarf satellites, as Stephens & Boesgaard (2002) claimed for their halo stars with abnormal kinematics. It is probable that while the high-α stars with $R_{\rm peri} < 2$ kpc originated from high mass dwarf galaxies, the high-α stars with $R_{\rm peri} > 2$ kpc might

have formed in very low mass dwarf galaxies where ISM mixing was not efficient. These issues will only become clearer once the α-abundance is measured for the stars in the low luminosity dwarf galaxies, and for the low metallicity stars in the Sgr galaxy.

With the exception of a few stars having $R_{\rm peri} > 3$ kpc, most of the low metallicity inner halo stars have $1.0 < R_{\rm peri} < 3.0$ kpc. This is partly due to the rotation velocity cut (40 km s^{-1} $< V_\phi <$ 80 km s^{-1}), but they still represent the typical value of the inner halo. Most of them are found with [α/Fe] > 0.25, so that they may have formed in a homogeneous ISM enriched by SNe II. Considering all of the evidence, it may be the most reasonable interpretation that the low α-inner halo stars formed in fragmented, localized star-forming regions of proto-Galactic clouds that experienced periods of persistent star formation.

Figure 5.15 is a very similar plot as Figure 5.14, but for $Z_{\rm max}$. The fact that most of low-α and low metallicity stars with prograde orbits are located within $Z_{\rm max} < 5$ provides more evidence for the fragmented proto-Galactic cloud origin, rather than the accretion origin. Some stars with $Z_{\rm max} < 2$ kpc might be members of the metal weak thick disk, which are located at the very low metallicity tail of the metallicity distribution function.

5.8 Summary and Conclusions

We have developed a method for estimating the α-abundance, parameterized as [α/Fe], and have compared our results with the ELODIE spectral library, after searching the literature for α-abundance measurements available for the stars in the library. A Gaussian fit to the residuals between the estimated and the literature values shows a very small scatter (1 $\sigma = 0.04$ dex) with negligible offset (–0.01 dex). Furthermore, we tested the abundance variation as a function of signal to noise (S/N); results of that test indicated that the standard deviation of our determinations is less than 0.1

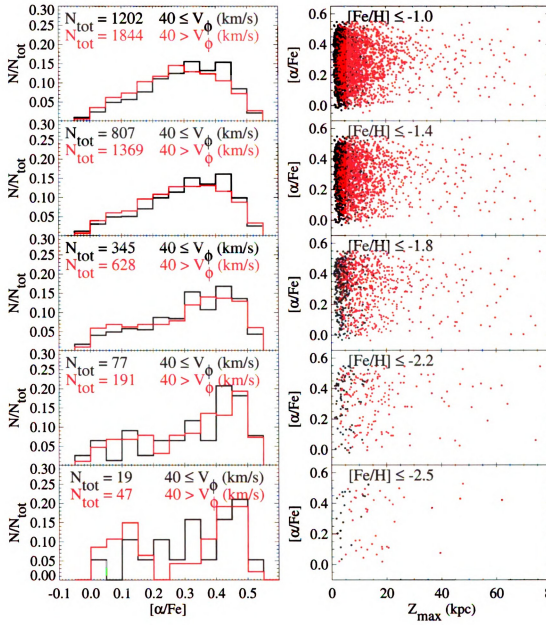


Figure 5.15 Distributions of [α/Fe] (left) and $Z_{\rm max}$ (right) with different bins of [Fe/H].

dex with a very small offset (–0.022 dex) for stars with spectra having S/N as low as 15. We chose to adopt a more conservative cut of $S/N \geq 20$ for the present analysis.

A total of 39,167 spectrophotometric and telluric calibration stars from the SDSS DR-6 (Adelman-McCarthy et al. 2008) was assembled in order to study the α-

abundance pattern in stars of the Galactic halo. Using the stellar parameters, heliocentric radial velocity, proper motions, and distance estimates, we derived local space velocities (U, V, W) and orbital parameters such as $Z_{\rm max}$, $R_{\rm apo}$, $R_{\rm peri}$, V_ϕ, and eccentricity. After calculation of these parameters, we selected samples of likely halo stars by imposing cuts of $V_\phi \leq 80$ km s^{-1}, $Z_{\rm max} \geq 1$ kpc, and [Fe/H] ≤ -1.0. A total sample of 7590 stars survived these additional cuts. The sample was divided into two groups, a dissipative component (or inner halo) with stars having $40 \leq V_\phi \leq 80$ km s^{-1} and $R_{\rm apo} < 16$ kpc, and an accreted component (or outer halo) with stars having $V_\phi < 40$ km s^{-1} or $R_{\rm apo} \geq 16$ kpc, or both. We examined α-abundance distributions of these components with various cuts on the metallicity and the kinematic parameters. Our major findings can be summarized as follows:

- The distribution of V_ϕ for the accreted component is shifted toward the counter-rotating direction for all [α/Fe] bins (Figure 5.7). There are larger fractions of stars with low metallicity ([Fe/H] < -1.8) for $-0.1 <$ [α/Fe] < 0.15 and $0.35 <$ [α/Fe] < 0.6 among the outer halo stars. This behavior may imply that the low metallicity outer halo stars may comprise multiple populations with different levels of α-enhancement; preferentially low and high-α. These two properties agree with the findings by Carollo et al. (2007), both kinematically and chemically.

- The distribution of [α/Fe] in each [Fe/H] cut reveals that as the metallicity of outer halo stars decreases, the fraction of stars with intermediate α-abundance (~ 0.25) decreases, while that of the low (below 0.2)- and high (above 0.3)-α stars increases, as shown in Figure 5.8. This implies bifurcation of the population in a given metallicity range. This may also apply to the inner halo stars. The outer halo stars have lower [α/Fe], on average, than the inner halo stars for the range [Fe/H] > -2.2.

- The low-α inner halo stars with peculiar kinematics (high $R_{\rm peri}$ or high $R_{\rm apo}$) may possibly have formed in low mass gas clouds fragmented from proto-Galactic halo clouds, while the high-α inner halo stars are well described by canonical halo formation models. Or it can be understood, within the context of hierarchical galaxy formation models, that a few very massive systems could build up the halo with a high level of the α-abundance like in our inner halo stars. The existence of both low and high-α stars at the very low metallicity end in the inner halo suggests a stochastic star formation process in the halo, which is consistent with the inhomogeneous chemical evolution model. This is also the case for the outer halo population, as shown by application of a K-S test (Table 5.2).

- It is not clear where the high-α stars with very low metallicity ([Fe/H] < -2.5) in the outer halo came from. However, one possible solution is that these stars may have their origin due to the accretion of objects similar to the very low mass dwarf galaxies which have been discovered recently from SDSS. Those galaxies would have been expected to have very inhomogeneous ISM, enriched by only a few SNe II.

- It is plausible, by comparing with models of stellar halo formation from Font et al. (2006a, 2006b), that some fraction of the low -α stars with low metallicity ([Fe/H] < -2.0) might have once been members of low mass dwarf galaxies like the ones we see at present. However, it is not likely that metal-rich ([Fe/H] $>$ -1.8) outer halo stars could have been accreted from low mass dwarf galaxies, because their α-abundance, on average, are much higher than that of the typical stars in dSphs. They might have been accreted from massive systems at during early epochs of halo formation. It seems unlikely that a large fraction of halo stars have been accreted from low mass dwarf galaxies like those around the Milky Way at present.

- Assuming all low-α stars ([α/Fe] < 0.15) were captured from other small systems, and excluding them in the averaging the α-abundance in each bin of metallicity, there may exist a relation between [α/Fe] and [Fe/H] (Figure 5.13) as found by Stephens & Boesgaard (2002). A slope of -0.093 is derived by a linear fit to the mean values of [α/Fe].

- The mean value of [α/Fe] for stars on prograde orbits is slightly higher than that of the counter-rotating stars at a given $R_{\rm apo}$ distance, providing evidence for the extra-galactic origin for the counter-rotating stars. The discrepancy becomes larger as the metallicity decreases and $R_{\rm apo}$ increases.

- For metallicities above [Fe/H] = –2.25, the accreted stars display lower α values, on average, for all rotation velocity cuts (Figure 5.11). Below [Fe/H] = –2.25, although not many stars are involved, the dissipative component exhibits lower (or at the same level) α-enhancement, on average. The discrepancy in the mean α values becomes larger with lower V_ϕ, providing more supporting evidence for the accretion of these stars from very low mass dwarf galaxies.

From these findings, we can conclude that there is no significant fraction of halo stars that may have been accreted, especially at very late time, from small systems like the low mass dSphs we observe today around the Milky Way. There exists the possibility for early accretion from massive satellites, which are responsible for intermediate metallicity, low-α halo stars. The ultra low luminous dwarf galaxies discovered recently may be possible sources for the very low metallicity, very high-α halo stars.

CHAPTER 6: CONCLUSIONS AND FUTURE WORK

We have presented the development and execution of the SEGUE Stellar Parameter Pipeline (SSPP), which makes use of multiple approaches in order to estimate the fundamental stellar atmospheric parameters (effective temperature, $T_{\rm eff}$, surface gravity, log g, and metallicity, parameterized by [Fe/H]) for stars with spectra and photometry obtained during the course of the original Sloan Digital Sky Survey (SDSS-I) and its first extension (SDSS-II/SEGUE).

The use of multiple methods provides an empirical determination of the internal errors for each derived parameter, based on the range of the reported values from each method. Among 128,000 spectra from 200 SEGUE plug-plates, all of which have derived stellar parameters available from the SSPP, typical internal errors, in the range 4500 K $\leq T_{\rm eff} \leq$ 7500 K, are $\sigma(T_{\rm eff}) = 70$ K (s.e.m), $\sigma(\log\ g) = 0.18$ (s.e.m), and $\sigma([{\rm Fe/H}]) = 0.07$ (s.e.m). However, Allende Prieto et al. (2008; Paper III) point out that the internal scatter estimates obtained from averaging the multiple estimates of the parameters produced by the SSPP underestimate the external errors, because several methods in the SSPP make use of similar wavelength regions and atmospheric models.

A comparison with the averaged results of two different high-resolution analyses of over 100 SDSS-I/SEGUE stars indicates that the SSPP is able to determine $T_{\rm eff}$, log g, and [Fe/H] to precisions of 141 K, 0.23 dex, and 0.23 dex, respectively, after combining small systematic offsets quadratically for stars with 4500 K $\leq T_{\rm eff} \leq$

7500 K. These errors are slightly different from those obtained by Paper III ($\sigma(T_{\rm eff})$ = 130 K, $\sigma(\log g)$ = 0.21 dex, and σ([Fe/H]) = 0.11 dex), although they share a common set of high-resolution calibration observations. The reason for this is that Paper III derived the external uncertainties of the SSPP only considering the stars observed with the HET (on the grounds of internal consistency). The sample referred to as *OTHERS* in Paper III exhibits somewhat larger scatter in its parameters, when compared with those determined by the SSPP.

Taking into account the average internal scatter from the multiple approaches and the external uncertainty from the comparisons with the high-resolution analysis together, the typical uncertainty in the stellar parameters determined by the SSPP are $\sigma(T_{\rm eff})$ = 157 K, $\sigma(\log\ g)$ = 0.29 dex, and σ([Fe/H]) = 0.24 dex, over the temperature range 4500 K $\leq T_{\rm eff} \leq$ 7500 K.

Observation of several hundred additional stars from SDSS-I/SEGUE with HET, which is now underway, will provide a more homogeneous sample for our tests. In addition, additional high-resolution data for stars outside of our adopted temperature range will help test the uncertainties in the stellar parameters for both cooler ($T_{\rm eff}$ < 4500 K) and warmer ($T_{\rm eff}$ > 7500 K) stars. These data, and a much more extensive set of high-resolution observations of stars over the full parameter range, are planned to be taken over the next several years. Once obtained, we plan to use the new observations to make use of a method for applying zero-point corrections and inverse variance weighting for obtaining an optimal estimate of stellar parameters over the entire parameter space.

Using photometric and spectroscopic data reported in SDSS-I and SDSS-II/SEGUE, we have examined estimates of stellar atmospheric parameters and heliocentric radial velocities obtained by the SEGUE Stellar Parameter Pipeline (SSPP) for selected true members of three Galactic globular clusters, M 13, M 15, and M 2, and two open clusters, NGC 2420 and M 67, and compared them with those obtained by external

estimates for each cluster as a whole.

From the estimated scatters in the metallicities and radial velocities calculated for the selected true members of each cluster, we quantify the typical external uncertainties of the SSPP-determined values, $\sigma([\mathrm{Fe/H}]) = 0.13$, down to a spectroscopic signal-to-noise limit of $S/N = 10/1$, and $\sigma(\mathrm{RV}) \sim 8.0$ km s^{-1}, respectively. These uncertainties apply for stars in the range of $-0.3 \leq g - r \leq 1.3$ and $2.0 \leq \log g \leq 5.0$, at least over the metallicity interval spanned by the clusters studied ($-2.3 \leq [\mathrm{Fe/H}] \leq 0.0$). We have also confirmed that T_{eff} and $\log\, g$ are sufficiently well determined by the SSPP to distinguish between different luminosity classes, through a comparison with theoretical predictions.

From the above considerations of the uncertainties achieved from the comparisons with the high resolution analyses and the selected true member stars of the globular and open clusters, we conclude that the SSPP determines, with sufficient accuracy and precision, radial velocities and atmospheric parameter estimates, for stars in the effective temperature range from 4500 K to 7500 K, to enable detailed explorations of the chemical compositions and kinematics of the disk and halo populations of the Galaxy.

The SSPP also obtains approximate spectral types for stars, based on two methods, with differing limitations. A set of distance determinations for each star is obtained as well, although future work will be required in order to identify the optimal method. An et al. (2008) have developed a set of cluster fiducials in the "natural system" of SDSS, *ugriz*, based on crowded field photometric analysis of SDSS observations. Once available, we plan to implement distance estimates from these fiducials into the SSPP.

We have developed a method for estimating the α-abundances, parameterized as $[\alpha/\mathrm{Fe}]$, and compared with the ELODIE spectral library, after searching the literature for the α-abundance measurements available for the stars in the library. A Gaussian

fit to the residuals between the estimated and the literature values shows a very small scatter (1 σ = 0.04 dex) with negligible offset (–0.01 dex). Furthermore, we tested the abundance variation as a function of signal to noise (S/N); results of that test indicated that the standard deviation is less than 0.1 dex with a very small offset (–0.022 dex) for stars with spectra down to S/N = 15. We chose to adopt a more conservative cut of $S/N \geq 20$ for the present analysis.

A total of 39,167 spectrophotometric and telluric calibration stars from the SDSS DR-6 (Adelman-McCarthy et al. 2008) was assembled in order to study the α-abundance pattern in stars of the Galactic halo. Using the stellar parameters, heliocentric radial velocity, proper motions, and distance estimates, we derived local space velocities (U, V, W) and orbital parameters such as $Z_{\rm max}$, $R_{\rm apo}$, $R_{\rm peri}$, V_ϕ, and eccentricity. After calculation of these parameters, we selected samples of likely halo stars by imposing cuts of $V_\phi \leq 80$ km s^{-1}, $Z_{\rm max} \geq 1$ kpc, and [Fe/H] $\leq$ –1.0. A total sample 7590 stars survived these additional cuts. The sample was divided into two groups, a dissipative component (or inner halo) with stars having $40 \leq V_\phi \leq 80$ km s^{-1} and $R_{\rm apo} < 16$ kpc, and an accreted component (or outer halo) with stars having $V_\phi < 40$ km s^{-1} or $R_{\rm apo} \geq 16$ kpc, or both. We examined α-abundance distributions of these components with various cuts on the metallicity and the kinematic parameters.

Based on this analysis, our primary conclusions are the following:

- The distribution of V_ϕ for the accreted component is shifted toward the counter-rotating direction for all [α/Fe] bins (Figure 5.7). There are larger fractions of stars with low metallicity ([Fe/H] < -1.8) for –0.1 $<$ [α/Fe] $<$ 0.15 and 0.35 $<$ [α/Fe] $<$ 0.6 among the outer halo stars. This behavior may imply that the low metallicity outer halo stars may comprise multiple populations with different levels of α-enhancement; preferentially low- and high-α. These two properties agree with the findings by Carollo et al. (2007), both kinematically

and chemically.

- The distribution of [α/Fe] in each [Fe/H] cut reveals that as the metallicity of outer halo stars decreases, the fraction of stars with intermediate α-abundance ($\sim$ 0.25) decreases, while that of the low (below 0.2)- and high (above 0.3)-α stars increases, as shown in Figure 5.8. This implies bifurcation of the population in a given metallicity range. This may also apply to the inner halo stars. The outer halo stars have lower [α/Fe], on average, than the inner halo stars stars for the range [Fe/H] $>$ –2.2.

- The low-α inner halo stars with peculiar kinematics (high $R_{\rm peri}$ or high $R_{\rm apo}$) may possibly have formed in low mass gas clouds fragmented from proto-Galactic halo clouds, while the high-α inner halo stars are well described by canonical halo formation models. Or it can be understood, within the context of hierarchical galaxy formation models, that a few very massive systems could build up the halo with a high level of the α-abundance like in our inner halo stars. The existence of both low and high-α stars at the very low metallicity end in the inner halo suggests a stochastic star formation process in the halo, which is consistent with the inhomogeneous chemical evolution model. This is also the case for the outer halo population, as shown by application of a K-S test (Table 5.2).

- It is not clear where the high-α stars with very low metallicity ([Fe/H] $<$ –2.5) in the outer halo came from. However, one possible solution is that these stars may have their origin due to the accretion of objects similar to the very low mass dwarf galaxies which have been discovered recently from SDSS. Those galaxies would have been expected to have very inhomogeneous ISM, enriched by only a few SNe II.

- It is plausible, by comparing with models of stellar halo formation from Font et

al. (2006a, 2006b), that some fraction of the low -α stars with low metallicity ([Fe/H] < -2.0) might have once been members of low mass dwarf galaxies like the ones we see at present. However, it is not likely that metal-rich ([Fe/H] $>$ -1.8) outer halo stars could have been accreted from low mass dwarf galaxies, because their α-abundance, on average, are much higher than that of the typical stars in dSphs. They might have been accreted from massive systems at during early epochs of halo formation. It seems unlikely that a large fraction of halo stars have been accreted from low mass dwarf galaxies like those around the Milky at present.

- Assuming all low-α stars ([α/Fe] < 0.15) were captured from other small systems, and excluding them in the averaging the α-abundance in each bin of metallicity, there may exist a relation between [α/Fe] and [Fe/H] (Figure 5.13) as found by Stephens & Boesgaard (2002). A slope of -0.093 is derived by a linear fit to the mean values of [α/Fe].

- The mean value of [α/Fe] for stars on prograde orbits is slightly higher than that of the counter-rotating stars at a given $R_{\rm apo}$ distance, providing evidence for the extra-galactic origin for the counter-rotating stars. The discrepancy becomes larger as the metallicity decreases and $R_{\rm apo}$ increases.

- For metallicities above [Fe/H] = -2.25, the accreted stars display lower α values, on average, for all rotation velocity cuts (Figure 5.11). Below [Fe/H] = -2.25, although not many stars are involved, the dissipative component exhibits lower (or at the same level) α-enhancement, on average. The discrepancy in the mean α values becomes larger with lower V_ϕ, providing more supporting evidence for the accretion of these stars from very low mass dwarf galaxies.

From these findings, we can conclude that there is no significant fraction of halo stars that may have been accreted, especially at very late time, from small systems

like the low mass dSphs we observe today around the Milky Way. There exists the possibility for early accretion from massive satellites, which are responsible for intermediate metallicity, low-α halo stars. The ultra low luminous dwarf galaxies discovered recently may be possible sources for the very low metallicity, very high-α halo stars.

The next extension of SDSS, known as SDSS-III, includes a program to continue the SEGUE effort, known as SEGUE-2. This will result, over the course of the next year, with about another 200,000 stars with medium-resolution spectra. The techniques we have developed will naturally be applied to these stars. In addition, we can also expect large numbers of additional calibration stars to be observed during the course of other surveys that are part of SDSS-III. The much larger samples will enable more detailed studies of the α patterns in the different stellar populations of the Milky Way. Equally necessary is the development of new numerical Galactic chemical evolution models, with which these large data sets can be compared in the future.

APPENDICES

Appendix A: Line List for Line index Calculations

Table A.1: Line Band and Sideband Widths and Output Format

Column	Format	Description	Central (Å)	Width (Å)	Red (Å)	Width (Å)	Blue (Å)	Width (Å)
1	A22	spSpec name	...	...	...	...	...	...
2	F8.3	H8 (3)	3889.0	3.0	3912.0	8.0	3866.0	8.0
3	F8.3	H8 (12)	3889.1	12.0	4010.0	20.0	3862.0	20.0
4	F8.3	H8 (24)	3889.1	24.0	4010.0	20.0	3862.0	20.0
5	F8.3	H8 (48)	3889.1	48.0	4010.0	20.0	3862.0	20.0
6	F8.3	Ca II K12 (12)	3933.7	12.0	4010.0	20.0	3913.0	20.0
7	F8.3	Ca II K18 (18)	3933.7	18.0	4010.0	20.0	3913.0	20.0
8	F8.3	Ca II K6 (6)	3933.7	6.0	4010.0	20.0	3913.0	20.0
9	F8.3	Ca II K30 (30)	3933.6	30.0	4010.0	5.0	3910.0	5.0
10	F8.3	Ca II H & K (75)	3962.0	75.0	4010.0	5.0	3910.0	5.0
11	F8.3	Hϵ (50)	3970.0	50.0	4010.0	5.0	3910.0	5.0
12	F8.3	Ca II K16 (16)	3933.7	16.0	4018.0	20.0	3913.0	10.0
13	F8.3	Sr II (8)	4077.0	8.0	4090.0	6.0	4070.0	4.0
14	F8.3	He I (12)	4026.2	12.0	4154.0	20.0	4010.0	20.0
15	F8.3	Hδ (12)	4101.8	12.0	4154.0	20.0	4010.0	20.0
16	F8.3	Hδ (24)	4101.8	24.0	4154.0	20.0	4010.0	20.0

Table A.1: Line Band and Sideband Widths and Output Format (continued)

Column	Format	Description	Central (Å)	Width (Å)	Red (Å)	Width (Å)	Blue (Å)	Width (Å)
17	F8.3	Hδ (48)	4101.8	48.0	4154.0	20.0	4010.0	20.0
18	F8.3	Hδ (64)	4102.0	64.0	4154.0	20.0	4010.0	20.0
19	F8.3	Ca I (4)	4226.0	4.0	4232.0	4.0	4211.0	6.0
20	F8.3	Ca I (12)	4226.7	12.0	4257.0	20.0	4154.0	20.0
21	F8.3	Ca I (24)	4226.7	24.0	4257.0	20.0	4154.0	20.0
22	F8.3	Ca I (6)	4226.7	6.0	4257.0	20.0	4154.0	20.0
23	F8.3	G-band (15)	4305.0	15.0	4367.0	10.0	4257.0	20.0
24	F8.3	Hγ (12)	4340.5	12.0	4425.0	20.0	4257.0	20.0
25	F8.3	Hγ (24)	4340.5	24.0	4425.0	20.0	4257.0	20.0
26	F8.3	Hγ (48)	4340.5	48.0	4425.0	20.0	4257.0	20.0
27	F8.3	Hγ (54)	4340.5	54.0	4425.0	20.0	4257.0	20.0
28	F8.3	He I (12)	4471.7	12.0	4500.0	20.0	4425.0	20.0
29	F8.3	G-blue (26)	4305.0	26.0	4507.0	14.0	4090.0	12.0
30	F8.3	G-whole (28)	4321.0	28.0	4507.0	14.0	4096.0	12.0
31	F8.3	Ba II (6)	4554.0	6.0	4560.0	4.0	4538.0	4.0
32	F8.3	$^{12}C^{13}C$ (36)	4737.0	36.0	4770.0	20.0	4423.0	10.0
33	F8.3	^{12}C (256)	4618.0	256.0	4780.0	5.0	4460.0	10.0
34	F8.3	Metal-1 (442)	4584.0	442.0	4805.8	5.0	4363.0	5.0
35	F8.3	Hβ (12)	4862.3	12.0	4905.0	20.0	4790.0	20.0
36	F8.3	Hβ (24)	4862.3	24.0	4905.0	20.0	4790.0	20.0
37	F8.3	Hβ (48)	4862.3	48.0	4905.0	20.0	4790.0	20.0
38	F8.3	Hβ (60)	4862.3	60.0	4905.0	20.0	4790.0	20.0
39	F8.3	C_2 (204)	5052.0	204.0	5230.0	20.0	4935.0	10.0
40	F8.3	C_2+Mg I (238)	5069.0	238.0	5230.0	20.0	4935.0	10.0
41	F8.3	MgH+Mg I+C_2 (270)	5085.0	270.0	5230.0	20.0	4935.0	10.0

Table A.1: Line Band and Sideband Widths and Output Format (continued)

Column	Format	Description	Central (Å)	Width (Å)	Red (Å)	Width (Å)	Blue (Å)	Width (Å)
42	F8.3	MgH+Mg I (44)	5198.0	44.0	5230.0	20.0	4935.0	10.0
43	F8.3	MgH (20)	5210.0	20.0	5230.0	20.0	4935.0	10.0
44	F8.3	Cr I (12)	5206.0	12.0	5239.0	8.0	5197.5	5.0
45	F8.3	Mg I + Fe II(20)	5175.0	20.0	5240.0	10.0	4915.0	10.0
46	F8.3	Mg I (2)	5183.0	2.0	5240.0	10.0	4915.0	10.0
47	F8.3	Mg I (12)	5170.5	12.0	5285.0	20.0	5110.0	20.0
48	F8.3	Mg I (24)	5176.5	24.0	5285.0	20.0	5110.0	20.0
49	F8.3	Mg I (12)	5183.5	12.0	5285.0	20.0	5110.0	20.0
50	F8.3	Na I (20)	5890.0	20.0	5918.0	6.0	5865.0	10.0
51	F8.3	Na I (12)	5892.9	12.0	5970.0	20.0	5852.0	20.0
52	F8.3	Na I (24)	5892.9	24.0	5970.0	20.0	5852.0	20.0
53	F8.3	Hα (12)	6562.8	12.0	6725.0	50.0	6425.0	50.0
54	F8.3	Hα (24)	6562.8	24.0	6725.0	50.0	6425.0	50.0
55	F8.3	Hα (48)	6562.8	48.0	6725.0	50.0	6425.0	50.0
56	F8.3	Hα (70)	6562.8	70.0	6725.0	50.0	6425.0	50.0
57	F8.3	CaH (505)	6788.0	505.0	7434.0	10.0	6532.0	5.0
58	F8.3	TiO (333)	7209.0	333.0	7434.0	10.0	6532.0	5.0
59	F8.3	CN (26)	6890.0	26.0	7795.0	10.0	6870.0	10.0
60	F8.3	O I tri (30)	7775.0	30.0	7805.0	10.0	7728.0	10.0
61	F8.3	K I (34)	7687.0	34.0	8080.0	10.0	7510.0	10.0
62	F8.3	K I (95)	7688.0	95.0	8132.0	5.0	7492.0	5.0
63	F8.3	Na I (15)	8187.5	15.0	8190.0	55.0	8150.0	10.0
64	F8.3	Na I-red (33)	8190.2	33.0	8248.6	5.0	8140.0	5.0
65	F8.3	Ca II tri (26)	8498.0	26.0	8520.0	10.0	8467.5	25.0
66	F8.3	Paschen (13)	8467.5	13.0	8570.0	14.0	8457.0	10.0

Table A.1: Line Band and Sideband Widths and Output Format (continued)

Column	Format	Description	Central (Å)	Width (Å)	Red (Å)	Width (Å)	Blue (Å)	Width (Å)
67	F8.3	Ca II tri (29)	8498.5	29.0	8570.0	14.0	8479.0	10.0
68	F8.3	Ca II tri (40)	8542.0	40.0	8570.0	14.0	8479.0	10.0
69	F8.3	Ca II tri (16)	8542.0	16.0	8600.0	60.0	8520.0	20.0
70	F8.3	Paschen (42)	8598.0	42.0	8630.5	23.0	8570.0	14.0
71	F8.3	Ca II tri (16)	8662.1	16.0	8694.0	12.0	8600.0	60.0
72	F8.3	Ca II tri (40)	8662.0	40.0	8712.5	25.0	8630.5	23.0
73	F8.3	Paschen (42)	8751.0	42.0	8784.0	16.0	8712.5	25.0
74	F7.3	TiO1 (5)	6720.5	5.0	6720.5	5.0	6705.5	5.0
75	F7.3	TiO2 (5)	7059.5	5.0	7059.5	5.0	7044.5	5.0
76	F7.3	TiO3 (5)	7094.5	5.0	7094.5	5.0	7081.5	5.0
77	F7.3	TiO4 (5)	7132.5	5.0	7132.5	5.0	7117.5	5.0
78	F7.3	TiO5 (9)	7130.5	9.0	7130.5	9.0	7044.0	4.0
79	F7.3	CaH1 (10)	6385.0	10.0	6415.0	10.0	6350.0	10.0
80	F7.3	CaH2 (32)	6830.0	32.0	6830.0	32.0	7044.0	4.0
81	F7.3	CaH3 (30)	6975.0	30.0	6975.0	30.0	7044.0	4.0
82	F7.3	CaOH (10)	6235.0	10.0	6235.0	10.0	6349.5	9.0
83	F7.3	Hα (6)	6563.0	6.0	6563.0	6.0	6550.0	10.0

APPENDIX B: OUTPUT FORMAT OF THE SSPP

Table B.1: Key to Each Column and Format of SSPP Parameter File

Column	Format	Description
1	A10	Running number
2	A16	SPEC NAME - MJD-Plate-Fiber
3	A3	Initial target type - BHB (Blue Horizontal Branch), CVR (Star Caty Var), WD (White Dwarf), KD (Brown Dwarf), FTO (Serendipity Blue), MD (Serendipity Red), AGB (Serendipity Distant), SER (Serendipity First), HOT (Hot Std), ROS (ROSAT_D), KG (Star Carbon), GD (Star Red Dwarf), LOW (Star Sub Dwarf), RED (Reddening Standard), PHO (Spectrophotometric Standard), QA (Quality Assurance), GAL (Galaxy), QSO (QSO), SKY (SKY), SER (Serendipity Manual)
4	A3	Spectral Type based on HAMMER program. NA-Not Applicable
5	A3	Spectral Type based on ELODIE templates
6	A5	Flag raised for a variety of reasons. Combination of four letters. - First letter : indicates several things n = all appears well D = likely white dwarf selected by $D_{0.2}$ and Rc d = sdO or sdB selected by $D_{0.2}$ and Rc

Table B.1: Key to Each Column and Format of SSPP Parameter File (continued)

Column	Format	Description
		H = too hot for abundance determinations
		h = Helium line detected
		l = late-type star with solar abundance
		E = emission lines noted (usually more than one)
		S = Sky spectrum, ignore
		V = Radial velocity missing
		N = spectrum quite noisy
		- Second letter : color flag
		n = $g - r$ color is OK, compared with predicted color
		C = $g - r$ color could be wrong
		- Third letter : Balmer flag, disagreement between Hα and Hδ
		= n if normal
		= B if not
		- Fourth letter : G-band flag
		= n if normal
		= G if likely G-band strong relative to expectation
		= g if mildly G-band strong relative to expectation
		- Fifth letter : parameter flag
		= n if normal
		= P if $5.0 \leq S/N < 10.0$
		= N if no parameters estimated
7	F8.3	Adopted [Fe/H]
8	I3	Number of estimators used
9	F8.3	Error in the adopted [Fe/H]
10	F8.3	[Fe/H] estimate from `NGS2`
11	I3	Indicator variable

Table B.1: Key to Each Column and Format of SSPP Parameter File (continued)

Column	Format	Description
12	F8.3	Error in [Fe/H] estimate from NGS2
13	F8.3	[Fe/H] estimate from NGS1
14	I3	Indicator variable
15	F8.3	Error in [Fe/H] estimate from NGS1
16	F8.3	[Fe/H] estimate from ANNSR method
17	I3	Indicator variable
18	F8.3	Error in [Fe/H] estimate from ANNSR
19	F8.3	[Fe/H] estimate from ANNRR
20	I3	Indicator variable
21	F8.3	Error in [Fe/H] estimate from ANNRR
22	F8.3	[Fe/H] estimate from CaIIK1
23	I3	Indicator variable
24	F8.3	Error in [Fe/H] estiimate from CaIIK1
25	F8.3	[Fe/H] estimate from CaIIK2
26	I3	Indicator variable
27	F8.3	Error in [Fe/H] estimate from CaIIK2
28	F8.3	[Fe/H] from estimate CaIIK3
29	I3	Indicator variable
30	F8.3	Error in [Fe/H] estimate from CaIIK3
31	F8.3	[Fe/H] estimate from ACF
32	I3	Indicator variable
33	F8.3	Error in [Fe/H] estimate from ACF
34	F8.3	[Fe/H] estimate from CaIIT
35	I3	Indicator variable
36	F8.3	Error in [Fe/H] estimate from CaIIT
37	F8.3	[Fe/H] estimate from WBG

Table B.1: Key to Each Column and Format of SSPP Parameter File (continued)

Column	Format	Description
38	I3	Indicator variable
39	F8.3	Error in [Fe/H] estimate from WBG
40	F8.3	[Fe/H] estimate from k24
41	I3	Indicator variable
42	F8.3	Error in [Fe/H] estimate from k24
43	F8.3	[Fe/H] estimate from ki13
44	I3	Indicator variable
45	F8.3	Error in [Fe/H] estimate from ki13
46	I6	Adopted $T_{\rm eff}$
47	I3	Number of temperature estimators used
48	I6	Error in the adopted temperature
49	I6	$T_{\rm eff}$ estimate from HA24
50	I3	Indicator variable
51	I6	Error in $T_{\rm eff}$ estimate from HA24
52	I6	$T_{\rm eff}$ estimate from HD24
53	I3	Indicator variable
54	I6	Error in $T_{\rm eff}$ estimate from HD24
55	I6	$T_{\rm eff}$ estimate from T_K
56	I3	Indicator variable
57	I6	Error in $T_{\rm eff}$ estimate from T_K
58	I6	$T_{\rm eff}$ estimate from T_G
59	I3	Indicator variable
60	I6	Error in $T_{\rm eff}$ estimate from T_G
61	I6	$T_{\rm eff}$ estimate from T_I
62	I3	Indicator variable
63	I6	Error in $T_{\rm eff}$ estimate from T_{IK}

Table B.1: Key to Each Column and Format of SSPP Parameter File (continued)

Column	Format	Description
64	I6	$T_{\rm eff}$ estimate from NGS1
65	I3	Indicator variable
66	I6	Error in $T_{\rm eff}$ estimate from NGS1
67	I6	$T_{\rm eff}$ estimate from ANNSR
68	I3	Indicator variable
69	I6	Error in $T_{\rm eff}$ estimate from ANNSR
70	I6	$T_{\rm eff}$ estimate from ANNRR
71	I3	Indicator variable
72	I6	Error in $T_{\rm eff}$ estimate from ANNRR
73	I6	$T_{\rm eff}$ estimate from WBG
74	I3	Indicator variable
75	I6	Error in $T_{\rm eff}$ estimate from WBG
76	I6	$T_{\rm eff}$ estimate from k24
77	I3	Indicator variable
78	I6	Error in $T_{\rm eff}$ estimate from k24
79	I6	$T_{\rm eff}$ estimate from ki13
80	I3	Indicator variable
81	I6	Error in $T_{\rm eff}$ estimate from ki13
82	F8.3	Adopted log g
83	I3	Number of log g estimators used
84	F8.3	Error in the adopted log g
85	F8.3	log g estimate from NGS2
86	I3	Indicator variable
87	F8.3	Error in log g estimate from NGS2
88	F8.3	log g estimate from NGS1
89	I3	Indicator variable

Table B.1: Key to Each Column and Format of SSPP Parameter File (continued)

Column	Format	Description
90	F8.3	Error in log g estimate from NGS1
91	F8.3	log g estimate from ANNSR
92	I3	Indicator variable
93	F8.3	Error in log g estimate from ANNSR
94	F8.3	log g estimate from ANNRR
95	I3	Indicator variable
96	F8.3	Error in log g estimate from ANNRR
97	F8.3	log g estimate from CaI1
98	I3	Indicator variable
99	F8.3	Error in log g estimate from CaI1
100	F8.3	log g estimate from CaI2
101	I3	Indicator variable
102	F8.3	Error in log g estimate from CaI2
103	F8.3	log g estimate from MgH
104	I3	Indicator variable
105	F8.3	Error in log g estimate from MgH
106	F8.3	log g estimate from WBG
107	I3	Indicator variable
108	F8.3	Error in log g estimate from WBG
109	F8.3	log g estimate from k24
110	I3	Indicator variable
111	F8.3	Error in log g estimate from k24
112	F8.3	log g estimate from ki13
113	I3	Indicator variable
114	F8.3	Error in log g estimate from ki13
115	F8.3	[α/Fe] estimate from NGS2

Table B.1: Key to Each Column and Format of SSPP Parameter File (continued)

Column	Format	Description
116	I3	Indicator variable
117	F8.3	Error in [α/Fe] estimate from NGS2
118	F9.3	Dwarf distance in kpc from Beers et al. (2000)
119	F9.3	Turnoff distance in kpc from Beers et al. (2000)
120	F9.3	Giant distance in kpc from Beers et al. (2000)
121	F9.3	AGB distance in kpc from Beers et al. (2000)
122	F9.3	FHB distance in kpc from Beers et al. (2000)
123	F9.3	Distance in kpc from Allende Prieto et al. (2006)
124	F9.3	Distance (z) from the Galactic plane
125	A10	Radial velocity flag
126	F8.1	Adopted heliocentric radial velocity
127	F8.1	Error in the adopted heliocentric radial velocity
128	F8.1	Calculated radial velocity, based on IDL code
129	F8.1	Error in the calculated radial velocity
130	F8.1	Radial velocity estimate (RVBS) from SDSS templates
131	F8.1	Error in SDSS template radial velocity determination
132	F8.1	Radial velocity estimate (RBEL) from ELODIE template
133	F8.1	Error in ELODIE template radial velocity
134	F8.1	Radial velocity; set to -9999.9
135	F8.1	Error in Radial velocity; set to -9999.9
136	F8.1	Galactocentric radial velocity based on adopted velocity
137	F8.3	g magnitude
138	F8.3	V magnitude from $V = g - 0.561(g - r) - 0.004$
139	F8.3	$g - r$ color
140	F8.3	Adopted $g - r$ color prediction
141	F8.3	$g - r$ color prediction from $0.818 - 0.092 \cdot HA24$

Table B.1: Key to Each Column and Format of SSPP Parameter File (continued)

Column	Format	Description
142	F8.3	$g-r$ color prediction from 0.469 - 0.058·$HD24$
143	F8.3	$g-r$ color prediction from half power point (HHP)
144	F8.3	$B-V$ color from $B-V = 0.916(g-r) + 0.187$
145	F8.3	$B-V$ color predicted color from Balmer lines
146	F8.3	$u-g$ color
147	F8.3	$r-i$ color
148	F8.3	$i-z$ color
149	F8.3	Error in u mag in PSF
150	F8.3	Error in g mag in PSF
151	F8.3	Error in r mag in PSF
152	F8.3	Error in i mag in PSF
153	F8.3	Error in z mag in PSF
154	F8.3	$E(B-V)$ from Schlegel et al. (1998)
155	F7.1	Average S/N per pixel over 4000 − 8000 Å
156	I3	Quality check on spectrum. 1 for $S/N > 30$, 2 for $20 < S/N \leq 30$, 3 for $15 < S/N \leq 20$, 4 for $10 < S/N \leq 15$, 5 for $5 < S/N \leq 10$, 6 for $S/N \leq 5$
157	F12.7	RA in decimal degrees
158	F12.7	DEC in decimal degrees
159	F12.7	Galactic longitude (l) in decimal degrees
160	F12.7	Galactic latitude (b) in decimal degrees
161	F6.4	Correlation coefficient over 3850−4250 Å region
162	F7.4	Correlation coefficient over 4500−5500 Å region

Appendix C: Properties of Selected Cluster Members

Table C.1: SSPP-Derieved Properties for Selected Member Stars of M 13[m]

spSpec name	α (2000.0) (degrees)	δ (2000.0) (degrees)	RV (km/s)	σ(RV) (km/s)	$T_{\rm eff}$ (K)	$\sigma(T_{\rm eff})$ (K)	log g	σ(log$g$) (dex)	[Fe/H]	σ([Fe/H]) (dex)	u	g	r	i	z	S/N
53521−2174−054	250.8113861	36.380367	−238.4	5.2	5617	28	2.80	0.22	−1.67	0.04	19.00	17.83	17.39	17.23	17.17	21.2
53521−2174−082	250.6566925	36.292824	−241.1	1.8	5183	23	2.18	0.21	−1.55	0.03	16.88	15.43	14.85	14.63	14.50	55.0
53521−2174−087	250.5986176	36.141987	−231.8	3.5	5544	5	2.95	0.16	−1.51	0.04	18.42	17.26	16.79	16.62	16.54	29.3
53521−2174−093	250.6486664	36.331833	−242.5	1.9	5088	34	2.04	0.18	−1.71	0.04	16.77	15.30	14.64	14.38	14.24	57.3
53521−2174−094	250.6187286	36.193378	−234.7	3.6	5514	36	2.96	0.19	−1.51	0.05	18.42	17.25	16.78	16.56	16.47	30.3
53521−2174−098	250.6272430	36.330879	−250.5	1.6	5127	22	2.11	0.18	−1.80	0.03	16.99	15.60	14.99	14.73	14.60	54.8
53521−2174−121	250.5334473	36.323925	−249.2	1.9	5326	20	2.46	0.15	−1.52	0.01	17.56	16.23	15.70	15.49	15.39	48.1
53521−2174−126	250.4946899	36.287205	−232.9	3.9	5400	64	2.83	0.12	−1.62	0.02	18.25	17.01	16.54	16.34	16.28	33.2
53521−2174−128	250.4741516	36.309807	−252.8	4.0	5421	76	3.23	0.16	−1.64	0.04	18.65	17.48	17.02	16.82	16.75	24.8
53521−2174−131	250.4893646	36.332115	−242.8	2.0	5113	39	2.09	0.14	−1.65	0.07	16.69	15.20	14.58	14.84	14.16	58.3
53521−2174−133	250.5125122	36.321091	−242.4	3.5	5425	40	2.70	0.18	−1.52	0.01	18.10	16.88	16.38	16.18	16.09	37.9
53521−2174−134	250.5464020	36.344273	−242.3	3.2	5559	46	3.09	0.13	−1.55	0.05	18.45	17.28	16.83	16.62	16.52	30.1
53521−2174−136	250.4905701	36.363522	−242.3	1.9	9177	279	3.34	0.15	−1.64	0.08	16.34	15.22	15.49	15.68	15.79	54.4
53521−2174−137	250.5240936	36.376110	−252.0	1.6	5248	29	2.25	0.18	−1.47	0.07	17.06	15.62	15.05	14.84	14.70	55.7
53521−2174−145	250.4505157	36.393330	−246.2	1.6	5084	36	1.93	0.17	−1.56	0.03	16.61	15.02	14.35	14.62	13.94	60.2

Table C.1: SSPP-Derieved Properties for Selected Member Stars of M 13 (continued)

spSpec name	α (2000.0) (degrees)	δ (2000.0) (degrees)	RV (km/s)	σ(RV) (km/s)	$T_{\rm eff}$ (K)	$\sigma(T_{\rm eff})$ (K)	log g	σ(log$g$) (dex)	[Fe/H]	σ([Fe/H]) (dex)	u	g	r	i	z	S/N
53521−2174−146	250.3612061	36.200855	−248.1	4.5	5634	42	2.84	0.27	−1.51	0.05	18.84	17.68	17.25	17.06	17.04	23.5
53521−2174−149	250.3400269	36.200890	−243.5	4.9	5642	39	3.25	0.14	−1.64	0.06	18.93	17.78	17.36	17.17	17.13	21.1
53521−2174−152	250.3966980	36.394932	−246.5	1.8	8343	20	3.14	0.19	−1.77	0.08	16.18	14.95	15.17	15.33	15.42	56.0
53521−2174−153	250.4664001	36.409313	−247.5	1.8	8243	106	3.28	0.12	−1.84	0.09	16.22	14.98	15.10	15.24	15.32	56.6
53521−2174−154	250.4661713	36.326332	−249.6	1.6	5099	23	1.89	0.17	−1.59	0.02	16.70	15.11	14.49	14.72	14.07	59.2
53521−2174−155	250.3851166	36.147091	−240.0	2.4	5362	28	2.56	0.15	−1.70	0.04	17.76	16.52	16.01	15.81	15.70	42.0
53521−2174−156	250.3521576	36.409504	−239.4	1.7	5167	27	2.08	0.20	−1.71	0.04	17.15	15.72	15.11	14.87	14.76	53.7
53521−2174−158	250.4085236	36.303894	−243.6	1.7	5281	37	2.22	0.17	−1.44	0.07	17.05	15.62	15.09	14.84	14.69	54.2
53521−2174−159	250.3711243	36.398438	−237.1	1.4	5119	29	1.80	0.15	−1.60	0.07	16.66	15.08	14.45	14.72	14.05	59.0
53521−2174−160	250.3690338	36.363808	−255.1	1.7	5162	39	1.77	0.17	−1.56	0.04	16.90	15.41	14.81	15.02	14.42	56.9
53521−2174−166	250.2722931	36.365372	−236.8	1.9	5190	35	2.47	0.20	−1.68	0.06	17.04	15.69	15.09	14.84	14.71	54.2
53521−2174−167	250.2756042	36.422920	−246.3	1.4	5066	32	1.69	0.14	−1.59	0.06	16.50	14.88	14.24	14.52	13.81	60.1
53521−2174−168	250.2608337	36.437668	−243.7	1.4	5158	16	1.91	0.15	−1.57	0.04	16.85	15.31	14.72	14.98	14.30	57.4
53521−2174−171	250.3128967	36.398254	−246.8	1.6	5033	38	1.93	0.16	−1.70	0.06	16.56	15.02	14.34	14.60	13.93	60.3
53521−2174−172	250.3078461	36.417362	−247.5	1.5	5123	34	1.99	0.17	−1.60	0.03	16.83	15.36	14.74	14.95	14.34	57.7

Table C.1: SSPP-Derieved Properties for Selected Member Stars of M 13 (continued)

spSpec name	α (2000.0) (degrees)	δ (2000.0) (degrees)	RV (km/s)	σ(RV) (km/s)	$T_{\rm eff}$ (K)	$\sigma(T_{\rm eff})$ (K)	log g	$\sigma(\log g)$ (dex)	[Fe/H]	σ([Fe/H]) (dex)	u	g	r	i	z	S/N
53521−2174−174	250.1682281	36.190548	−253.4	7.6	5539	121	3.14	0.30	−1.80	0.06	18.85	17.90	17.48	17.35	17.28	18.8
53521−2174−175	250.3200226	36.326923	−235.5	1.7	8507	168	3.18	0.12	−1.44	0.11	16.15	14.93	15.11	15.26	15.33	53.5
53521−2174−176	250.3260651	36.347130	−240.8	1.8	5230	29	2.30	0.18	−1.63	0.03	17.20	15.79	15.21	14.96	14.84	53.6
53521−2174−215	250.0930939	36.313175	−242.1	1.8	5244	25	2.23	0.17	−1.60	0.03	16.76	15.34	14.78	14.56	14.42	56.9
53521−2174−217	250.0905457	36.281464	−231.7	6.6	5910	104	2.96	0.32	−1.52	0.04	19.01	17.99	17.68	17.52	17.46	17.6
53521−2174−368	250.1569672	36.596581	−253.4	3.5	5473	52	2.95	0.09	−1.55	0.02	18.64	17.51	17.04	16.87	16.78	27.0
53521−2174−376	250.1804047	36.558369	−250.0	1.8	5230	25	2.19	0.22	−1.66	0.03	17.10	15.78	15.21	14.99	14.93	47.1
53521−2174−402	250.2494965	36.627911	−252.5	4.0	5552	86	3.13	0.12	−1.59	0.03	18.90	17.81	17.40	17.22	17.09	23.4
53521−2174−403	250.2917633	36.632149	−258.2	5.3	5811	62	3.60	0.10	−1.47	0.05	18.95	17.98	17.61	17.44	17.38	22.0
53521−2174−406	250.2974548	36.656551	−249.7	4.5	5533	84	3.01	0.17	−1.64	0.05	18.97	17.89	17.49	17.31	17.25	24.1
53521−2174−407	250.2983246	36.606567	−250.4	1.9	5340	36	2.69	0.17	−1.54	0.03	17.81	16.61	16.09	15.89	15.77	44.7
53521−2174−412	250.2389069	36.587105	−242.5	3.7	5462	45	2.58	0.15	−1.59	0.02	18.61	17.47	16.96	16.80	16.74	28.8
53521−2174−413	250.3145905	36.517387	−237.3	1.6	5177	31	1.93	0.15	−1.52	0.09	17.08	15.61	15.02	14.76	14.63	57.1
53521−2174−414	250.2673035	36.586380	−241.6	3.5	5404	59	2.45	0.22	−1.56	0.01	18.60	17.46	16.91	16.79	16.71	31.1
53521−2174−418	250.2429047	36.708576	−246.4	1.9	5386	38	2.51	0.13	−1.52	0.01	17.65	16.36	15.86	15.64	15.56	47.3

Table C.1: SSPP-Derieved Properties for Selected Member Stars of M 13 (continued)

spSpec name	α (2000.0) (degrees)	δ (2000.0) (degrees)	RV (km/s)	σ(RV) (km/s)	$T_{\rm eff}$ (K)	$\sigma(T_{\rm eff})$ (K)	log g	$\sigma(\log g)$ (dex)	[Fe/H]	σ([Fe/H]) (dex)	u	g	r	i	z	S/N
53521−2174−442	250.3338928	36.614479	−248.7	1.6	8379	124	3.15	0.14	−1.61	0.10	16.17	14.95	15.09	15.25	15.30	57.9
53521−2174−443	250.3404846	36.465477	−257.6	1.4	5177	34	2.05	0.19	−1.65	0.09	16.91	15.40	14.80	15.00	14.41	58.7
53521−2174−444	250.3637085	36.539543	−243.3	1.3	5153	33	2.04	0.17	−1.57	0.06	16.72	15.18	14.56	14.25	14.13	60.1
53521−2174−445	250.3153534	36.581833	−247.3	4.5	5705	43	3.06	0.09	−1.61	0.02	18.97	17.89	17.49	17.32	17.26	23.4
53521−2174−446	250.3713074	36.493649	−237.2	1.5	5138	33	1.91	0.16	−1.64	0.07	16.71	15.14	14.53	14.63	14.13	60.5
53521−2174−447	250.3488159	36.637089	−245.9	3.8	5615	21	2.83	0.25	−1.57	0.02	18.74	17.68	17.24	17.05	17.01	27.4
53521−2174−449	250.3311310	36.507713	−243.0	1.5	5152	29	2.07	0.18	−1.61	0.02	16.92	15.42	14.82	15.06	14.39	58.5
53521−2174−451	250.4059753	36.421410	−245.0	1.9	8368	166	3.14	0.19	−1.75	0.08	16.25	15.05	15.21	15.41	15.49	58.2
53521−2174−452	250.2902679	36.445755	−256.4	1.6	5088	39	2.18	0.16	−1.63	0.03	16.65	15.18	14.55	14.82	14.13	60.0
53521−2174−453	250.3791046	36.437355	−238.0	1.6	5173	36	2.19	0.19	−1.56	0.02	16.83	15.35	14.72	15.00	14.38	59.1
53521−2174−455	250.3236237	36.436779	−250.8	1.3	5146	36	2.30	0.17	−1.57	0.06	16.93	15.44	14.83	15.14	14.44	58.7
53521−2174−456	250.3559265	36.608372	−247.5	2.9	5492	32	2.82	0.16	−1.65	0.04	18.54	17.37	16.91	16.72	16.64	32.2
53521−2174−457	250.3617706	36.424606	−243.5	1.4	5159	35	2.02	0.17	−1.58	0.02	16.78	15.24	14.61	14.85	14.21	60.0
53521−2174−458	250.3153839	36.463863	−248.9	1.4	5140	32	2.04	0.18	−1.56	0.08	16.73	15.14	14.51	14.74	14.10	60.5
53521−2174−459	250.3159637	36.554893	−244.7	1.4	5126	55	2.11	0.19	−1.54	0.04	16.82	15.31	14.65	14.93	14.26	59.7

Table C.1: SSPP-Derieved Properties for Selected Member Stars of M 13 (continued)

spSpec name	α (2000.0) (degrees)	δ (2000.0) (degrees)	RV (km/s)	σ(RV) (km/s)	$T_{\rm eff}$ (K)	$\sigma(T_{\rm eff})$ (K)	log g	$\sigma(\log g)$ (dex)	[Fe/H]	σ([Fe/H]) (dex)	u	g	r	i	z	S/N
53521−2174−460	250.3238525	36.491585	−236.9	1.6	5080	36	1.76	0.14	−1.50	0.05	16.56	14.90	14.26	14.51	13.79	61.8
53521−2174−461	250.4161987	36.592712	−244.9	3.0	5563	29	3.15	0.16	−1.59	0.04	18.45	17.36	16.89	16.70	16.61	30.1
53521−2174−462	250.3755035	36.591190	−245.2	1.6	5092	30	2.13	0.14	−1.63	0.03	16.67	15.20	14.57	14.27	14.14	59.8
53521−2174−463	250.4506531	36.594818	−245.7	1.5	5178	25	2.19	0.21	−1.56	0.08	17.12	15.71	15.11	14.84	14.73	55.7
53521−2174−464	250.3977661	36.604618	−238.4	1.7	8482	166	3.19	0.12	−1.51	0.10	16.22	14.97	15.15	15.26	15.34	58.1
53521−2174−466	250.4609070	36.555065	−241.6	1.7	7709	133	3.23	0.15	−1.37	0.05	16.12	14.87	14.91	14.95	14.98	59.3
53521−2174−470	250.3885956	36.541203	−243.8	1.2	5068	36	1.93	0.16	−1.58	0.07	16.52	14.92	14.28	13.97	13.83	61.7
53521−2174−471	250.4050598	36.680744	−248.5	2.0	5288	27	2.58	0.16	−1.63	0.01	17.52	16.28	15.74	15.53	15.42	48.7
53521−2174−472	250.4392548	36.430611	−242.9	1.6	7605	99	3.27	0.13	−1.35	0.01	16.12	14.86	14.86	14.90	14.95	59.5
53521−2174−473	250.3910980	36.507465	−238.1	1.4	5122	29	1.97	0.20	−1.53	0.06	16.67	15.11	14.51	14.23	14.09	60.5
53521−2174−474	250.4210815	36.630798	−239.2	3.7	5495	45	3.07	0.20	−1.71	0.03	18.78	17.61	17.15	16.97	16.90	27.6
53521−2174−475	250.4187622	36.526752	−238.0	1.4	5119	38	2.18	0.16	−1.49	0.09	16.52	14.98	14.59	14.06	13.92	61.2
53521−2174−476	250.4537811	36.534679	−251.7	1.6	5245	24	2.23	0.17	−1.58	0.02	17.28	15.80	15.24	14.97	14.85	53.8
53521−2174−478	250.4082642	36.497627	−236.0	1.4	5195	24	2.11	0.16	−1.55	0.02	16.94	15.49	14.89	14.67	14.52	58.2
53521−2174−480	250.3775940	36.560562	−244.1	2.5	5405	42	2.69	0.15	−1.59	0.05	18.09	16.90	16.41	16.19	16.10	39.5

Table C.1: SSPP-Derieved Properties for Selected Member Stars of M 13 (continued)

spSpec name	α (2000.0) (degrees)	δ (2000.0) (degrees)	RV (km/s)	σ(RV) (km/s)	$T_{\rm eff}$ (K)	$\sigma(T_{\rm eff})$ (K)	log g	$\sigma(\log g)$ (dex)	[Fe/H]	σ([Fe/H]) (dex)	u	g	r	i	z	S/N
53521−2174−481	250.4867401	36.625168	−247.1	5.6	5710	28	3.26	0.19	−1.64	0.03	18.91	17.87	17.46	19.47	17.23	20.7
53521−2174−483	250.5531464	36.489174	−254.2	1.4	5149	23	2.05	0.18	−1.55	0.02	16.71	15.21	14.58	14.30	14.18	59.8
53521−2174−484	250.5136871	36.465294	−255.0	1.3	5119	31	2.05	0.17	−1.61	0.06	16.74	15.25	14.60	14.33	14.20	59.9
53521−2174−485	250.5274811	36.482922	−253.0	1.4	5211	25	2.24	0.06	−1.47	0.10	17.00	15.55	14.99	14.72	14.61	57.0
53521−2174−488	250.5207062	36.526783	−245.9	1.6	5182	24	2.25	0.21	−1.63	0.02	17.17	15.79	15.20	14.94	14.81	55.5
53521−2174−489	250.5569153	36.554108	−248.6	1.4	5171	46	2.15	0.21	−1.55	0.09	17.09	15.65	15.02	14.77	14.63	56.8
53521−2174−493	250.4687042	36.450375	−251.0	1.4	5190	42	2.29	0.18	−1.62	0.05	16.67	15.15	14.53	14.24	14.10	60.5
53521−2174−494	250.4691467	36.473980	−237.0	1.3	5134	48	2.06	0.07	−1.50	0.02	16.73	15.21	14.57	14.30	14.16	60.0
53521−2174−495	250.5358582	36.516228	−250.2	1.6	5219	23	2.30	0.19	−1.66	0.02	17.40	16.07	15.47	15.23	15.11	52.8
53521−2174−497	250.5392151	36.566429	−243.3	1.4	5123	47	1.99	0.17	−1.58	0.06	16.98	15.48	14.83	14.58	14.42	58.1
53521−2174−498	250.5455017	36.409168	−240.5	1.5	5112	26	2.03	0.19	−1.75	0.06	16.66	15.18	14.57	14.28	14.16	60.0
53521−2174−499	250.5073700	36.389557	−244.6	1.4	5153	33	1.95	0.18	−1.48	0.09	16.68	15.15	14.52	14.24	14.11	60.2
53521−2174−500	250.4441376	36.501335	−249.3	1.4	5129	30	2.12	0.20	−1.62	0.01	16.79	15.37	14.75	14.48	14.36	58.9
53521−2174−522	250.5714569	36.525883	−247.5	1.4	5197	31	2.16	0.20	−1.51	0.06	17.05	15.57	14.97	14.70	14.58	57.6
53521−2174−529	250.6122742	36.650723	−245.2	2.0	5368	29	2.76	0.12	−1.63	0.01	17.70	16.49	15.96	15.75	15.66	46.8

Table C.1: SSPP-Derieved Properties for Selected Member Stars of M 13 (continued)

spSpec name	α (2000.0) (degrees)	δ (2000.0) (degrees)	RV (km/s)	σ(RV) (km/s)	$T_{\rm eff}$ (K)	$\sigma(T_{\rm eff})$ (K)	log g	σ(log$g$) (dex)	[Fe/H]	σ([Fe/H]) (dex)	u	g	r	i	z	S/N
53521−2174−530	250.5795441	36.617588	−245.5	1.5	5112	43	2.01	0.17	−1.63	0.05	16.91	15.36	14.72	14.45	14.29	59.0
53521−2174−531	250.6083527	36.451302	−243.7	1.6	5076	27	2.14	0.15	−1.63	0.01	16.72	15.30	14.66	14.39	14.26	59.5
53521−2174−532	250.5847015	36.450947	−245.5	1.6	8533	169	3.16	0.13	−1.43	0.13	16.24	15.04	15.22	15.36	15.45	57.9
53521−2174−533	250.5825653	36.416344	−249.1	4.5	5508	63	2.62	0.18	−1.79	0.03	18.85	17.80	17.36	17.17	17.12	24.5
53521−2174−537	250.6071167	36.431816	−251.6	1.6	5291	34	2.44	0.16	−1.58	0.03	17.28	15.97	15.43	15.19	15.08	53.5
53521−2174−538	250.5686798	36.437107	−252.0	1.2	5094	49	2.01	0.17	−1.61	0.08	16.63	15.11	14.46	14.18	14.05	61.0
53521−2174−539	250.6033020	36.480679	−251.5	3.3	5423	56	2.91	0.20	−1.58	0.02	18.76	17.66	17.18	16.98	16.88	28.4
53521−2174−542	250.4867096	36.697521	−247.6	1.3	5145	33	2.33	0.17	−1.63	0.07	16.80	15.28	14.66	14.41	14.26	58.8
53521−2174−554	250.4524536	36.731075	−247.4	1.6	5252	21	2.23	0.19	−1.59	0.03	17.22	15.84	15.28	15.04	14.93	54.2
53521−2174−560	250.4494934	36.746979	−247.1	3.5	5393	31	2.62	0.20	−1.61	0.04	18.72	17.55	17.02	16.86	16.75	30.3
53521−2174−563	250.7275696	36.537083	−245.0	2.0	5325	38	2.61	0.18	−1.71	0.02	17.66	16.42	15.90	15.69	15.58	44.2
53521−2174−565	250.6674805	36.541718	−248.5	4.6	5633	74	2.77	0.23	−1.78	0.02	18.94	17.92	17.49	17.34	17.26	23.8
53521−2174−573	250.7793579	36.401161	−245.8	5.6	5692	68	3.16	0.19	−1.53	0.04	19.09	17.98	17.59	17.45	17.38	23.3
53521−2174−576	250.6557617	36.483734	−241.0	3.7	5581	40	3.01	0.20	−1.55	0.02	18.89	17.67	17.22	17.02	16.94	28.7
53521−2174−577	250.6542358	36.559769	−250.7	4.0	5557	65	2.84	0.11	−1.53	0.01	18.99	17.90	17.48	17.31	17.24	24.7

Table C.1: SSPP-Derieved Properties for Selected Member Stars of M 13 (continued)

spSpec name	α (2000.0) (degrees)	δ (2000.0) (degrees)	RV (km/s)	σ(RV) (km/s)	$T_{\rm eff}$ (K)	$\sigma(T_{\rm eff})$ (K)	log g	σ(log$g$) (dex)	[Fe/H]	σ([Fe/H]) (dex)	u	g	r	i	z	S/N
53532−2185−106	250.6608429	36.252338	−246.5	8.1	6150	198	3.97	0.08	−1.55	0.06	20.55	19.70	19.42	19.28	19.37	13.2
53532−2185−111	250.6518555	36.315819	−247.2	4.9	6339	99	3.33	0.30	−1.67	0.02	19.47	18.58	18.34	18.32	18.37	25.7
53532−2185−113	250.6327362	36.302673	−260.0	11.7	6031	210	3.85	0.41	−1.33	0.07	20.66	19.82	19.49	19.39	19.36	11.2
53532−2185−116	250.6650848	36.212494	−254.8	8.0	6126	143	3.56	0.27	−1.72	0.04	20.33	19.38	19.12	19.02	18.98	17.0
53532−2185−120	250.6814728	36.301613	−232.5	6.3	6363	28	4.18	0.10	−1.38	0.07	20.02	19.20	18.92	18.81	18.68	18.9
53532−2185−141	250.5120239	36.217281	−240.0	3.8	6375	91	3.15	0.33	−1.66	0.03	19.28	18.39	18.17	18.10	18.08	31.9
53532−2185−143	250.5701752	36.201962	−233.6	5.0	6342	55	3.58	0.11	−1.61	0.03	19.45	18.52	18.27	18.21	18.20	28.4
53532−2185−146	250.5652161	36.224529	−236.3	10.9	6059	28	2.00	0.75	−1.40	0.15	20.84	19.75	19.46	19.35	19.37	11.6
53532−2185−148	250.6033325	36.234558	−245.3	5.4	6357	96	3.32	0.21	−1.70	0.04	19.86	19.00	18.75	18.66	18.69	22.1
53532−2185−150	250.6054077	36.200813	−242.1	5.5	6327	67	3.38	0.20	−1.61	0.03	19.79	18.78	18.54	18.48	18.44	25.1
53532−2185−151	250.5511475	36.331841	−226.8	7.0	6150	84	3.82	0.29	−1.75	0.02	20.40	19.42	19.14	19.07	19.06	16.6
53532−2185−152	250.6186066	36.331161	−235.7	5.6	6465	69	3.52	0.19	−1.62	0.05	19.72	18.80	18.58	18.49	18.46	25.1
53532−2185−153	250.5179138	36.306831	−244.3	2.8	5862	34	3.27	0.20	−1.75	0.02	19.08	18.10	17.72	17.59	17.51	41.1
53532−2185−154	250.5811462	36.316139	−234.2	9.4	6167	142	3.36	0.29	−1.78	0.03	20.63	19.69	19.42	19.29	19.34	14.1
53532−2185−156	250.5538483	36.304375	−242.3	7.2	6377	39	3.76	0.19	−1.60	0.05	19.89	19.05	18.79	18.70	18.68	21.7

Table C.1: SSPP-Derieved Properties for Selected Member Stars of M 13 (continued)

spSpec name	α (2000.0) (degrees)	δ (2000.0) (degrees)	RV (km/s)	σ(RV) (km/s)	$T_{\rm eff}$ (K)	$\sigma(T_{\rm eff})$ (K)	log g	σ(log$g$) (dex)	[Fe/H]	σ([Fe/H]) (dex)	u	g	r	i	z	S/N
53532−2185−158	250.5086365	36.321423	−243.8	5.9	6326	55	3.77	0.25	−1.63	0.02	19.91	18.93	18.68	18.61	18.56	23.6
53532−2185−160	250.5746155	36.340302	−239.5	6.6	6335	85	4.00	0.10	−1.53	0.08	20.03	19.20	18.96	18.88	18.84	18.9
53532−2185−161	250.4026489	36.216274	−239.0	8.7	6147	276	3.75	0.09	−1.62	0.02	20.53	19.65	19.39	19.34	19.20	13.5
53532−2185−167	250.3744202	36.210903	−249.6	4.5	6332	80	3.30	0.19	−1.65	0.02	19.73	18.74	18.52	18.42	18.41	26.9
53532−2185−169	250.3382111	36.202835	−237.4	6.0	6289	68	2.90	0.35	−1.55	0.04	20.00	19.01	18.76	18.66	18.68	22.4
53532−2185−172	250.4851227	36.205223	−248.2	5.2	6424	38	3.73	0.15	−1.43	0.03	19.67	18.77	18.53	18.46	18.41	25.6
53532−2185−175	250.4423218	36.258049	−253.7	5.4	6527	114	3.92	0.26	−1.32	0.07	19.75	18.80	18.62	18.50	18.52	21.4
53532−2185−176	250.4879761	36.319519	−237.7	4.9	6379	107	3.55	0.12	−1.53	0.01	19.78	18.81	18.57	18.47	18.41	25.6
53532−2185−177	250.4530029	36.298698	−249.3	5.4	6448	94	3.76	0.11	−1.64	0.05	19.74	18.86	18.64	18.52	18.58	24.5
53532−2185−178	250.4822845	36.300014	−245.6	5.9	6237	86	3.62	0.16	−1.69	0.04	19.95	19.08	18.83	18.75	18.73	22.0
53532−2185−179	250.4799957	36.221458	−242.5	4.1	6346	93	3.21	0.28	−1.60	0.05	19.26	18.44	18.21	18.12	18.14	31.7
53532−2185−181	250.2265778	36.218925	−247.7	5.3	6432	84	3.38	0.31	−1.77	0.04	19.59	18.74	18.51	18.44	18.37	25.8
53532−2185−195	250.1907959	36.271461	−243.2	10.5	6071	63	3.16	0.81	−1.67	0.03	21.16	19.96	19.64	19.47	19.52	11.6
53532−2185−196	250.1731720	36.201431	−247.7	6.4	6346	50	3.99	0.17	−1.52	0.06	19.83	19.02	18.76	18.69	18.73	21.3
53532−2185−197	250.1752930	36.316170	−242.2	7.3	6314	75	3.17	0.27	−1.50	0.14	20.09	19.11	18.85	18.80	18.82	18.8

Table C.1: SSPP-Derieved Properties for Selected Member Stars of M 13 (continued)

spSpec name	α (2000.0) (degrees)	δ (2000.0) (degrees)	RV (km/s)	σ(RV) (km/s)	$T_{\rm eff}$ (K)	$\sigma(T_{\rm eff})$ (K)	log g	σ(log$g$) (dex)	[Fe/H]	σ([Fe/H]) (dex)	u	g	r	i	z	S/N
53532−2185−198	250.2095490	36.280247	−244.2	5.4	6340	50	4.03	0.23	−1.65	0.03	19.57	18.89	18.62	18.52	18.52	24.9
53532−2185−200	250.1689453	36.354950	−247.4	8.7	6139	214	3.63	0.42	−1.32	0.14	20.62	19.76	19.47	19.36	19.23	12.7
53532−2185−237	250.1001129	36.310001	−239.2	3.2	5985	116	3.26	0.15	−1.75	0.04	19.04	18.06	17.78	17.64	17.61	39.9
53532−2185−388	250.0598145	36.565910	−250.6	3.5	6366	85	3.72	0.09	−1.55	0.01	19.18	18.28	18.04	17.94	17.89	34.5
53532−2185−390	250.0875244	36.539959	−249.5	8.0	6248	197	4.27	0.21	−1.56	0.03	20.21	19.37	19.11	19.02	19.00	14.1
53532−2185−393	250.0617828	36.626545	−254.8	8.9	6062	158	3.87	0.26	−1.64	0.16	20.75	19.91	19.54	19.45	19.49	11.8
53532−2185−423	250.1191559	36.614777	−249.8	5.2	6340	107	3.44	0.23	−1.48	0.03	19.80	18.88	18.63	18.56	18.57	25.2
53532−2185−424	250.1623840	36.546970	−243.6	4.7	6335	73	4.13	0.22	−1.71	0.04	19.95	19.23	18.96	18.80	19.00	26.0
53532−2185−425	250.1024933	36.708916	−250.1	3.3	6254	43	3.54	0.05	−1.65	0.02	19.23	18.31	18.05	17.98	17.94	36.5
53532−2185−426	250.1142273	36.579521	−244.7	2.7	5940	59	3.53	0.13	−1.73	0.01	19.02	18.01	17.67	17.54	17.49	42.0
53532−2185−427	250.1687622	36.572681	−245.7	2.7	5896	46	3.43	0.17	−1.58	0.06	19.01	18.00	17.65	17.52	17.49	42.9
53532−2185−428	250.2005005	36.620838	−246.7	5.8	6221	61	4.14	0.22	−1.65	0.05	20.09	19.19	18.90	18.80	18.85	20.3
53532−2185−430	250.1428375	36.630520	−254.8	8.5	6236	2	3.98	0.64	−1.78	0.07	20.49	19.69	19.39	19.26	19.25	14.3
53532−2185−433	250.0788116	36.418709	−254.9	9.4	5764	205	3.08	0.77	−1.51	0.21	20.56	19.93	19.55	19.43	19.37	12.7
53532−2185−435	250.1384125	36.391571	−239.8	5.7	6385	72	3.90	0.14	−1.54	0.04	19.84	19.03	18.79	18.72	18.74	22.5

Table C.1: SSPP-Derieved Properties for Selected Member Stars of M 13 (continued)

spSpec name	α (2000.0) (degrees)	δ (2000.0) (degrees)	RV (km/s)	σ(RV) (km/s)	$T_{\rm eff}$ (K)	$\sigma(T_{\rm eff})$ (K)	log g	σ(log$g$) (dex)	[Fe/H]	σ([Fe/H]) (dex)	u	g	r	i	z	S/N
53532−2185−439	250.0806732	36.503437	−240.7	2.7	6146	67	3.27	0.11	−1.63	0.02	19.08	18.13	17.86	17.71	17.73	40.5
53532−2185−440	250.1068573	36.427521	−232.1	8.9	6197	95	3.49	0.21	−1.37	0.06	20.63	19.73	19.45	19.34	19.34	13.5
53532−2185−461	250.3284149	36.700005	−241.3	3.6	6330	77	3.64	0.09	−1.52	0.08	19.30	18.37	18.13	18.03	18.07	34.4
53532−2185−462	250.2369232	36.717884	−247.9	2.7	6174	67	3.54	0.12	−1.71	0.02	19.08	18.20	17.93	17.84	17.85	39.0
53532−2185−464	250.2901764	36.685863	−236.6	8.7	6177	65	3.28	0.32	−1.62	0.06	20.45	19.43	19.16	19.13	19.06	17.3
53532−2185−466	250.2878876	36.725266	−245.5	5.2	6448	96	3.80	0.11	−1.42	0.05	19.67	18.80	18.60	18.46	18.53	23.5
53532−2185−469	250.2945404	36.606640	−246.3	5.8	6283	93	3.39	0.26	−1.57	0.04	19.87	18.98	18.75	18.64	18.61	20.5
53532−2185−473	250.2791901	36.576611	−238.4	6.2	6365	62	4.06	0.20	−1.57	0.05	20.23	19.26	18.99	18.92	18.99	20.1
53532−2185−475	250.2398529	36.588871	−249.1	4.1	6298	46	3.48	0.17	−1.63	0.03	19.47	18.59	18.29	18.24	18.30	30.7
53532−2185−476	250.2485657	36.574799	−244.4	5.8	6182	54	3.95	0.11	−1.65	0.07	19.95	19.07	18.74	18.69	18.63	22.6
53532−2185−477	250.2305450	36.610828	−243.8	7.2	6122	52	3.91	0.38	−1.46	0.06	20.60	19.58	19.26	19.18	19.35	15.6
53532−2185−478	250.2751617	36.618698	−243.7	5.3	6260	40	3.97	0.15	−1.58	0.08	19.86	19.01	18.70	18.60	18.59	24.4
53532−2185−479	250.2099609	36.532490	−251.3	6.9	6128	36	4.13	0.09	−1.81	0.09	20.31	19.45	19.12	19.06	18.99	17.4
53532−2185−480	250.2232056	36.626942	−242.8	7.3	6129	148	4.00	0.39	−1.59	0.07	20.52	19.68	19.38	19.25	19.43	14.3
53532−2185−481	250.3259277	36.655441	−244.5	3.1	6231	49	3.47	0.17	−1.57	0.03	19.16	18.19	17.92	17.80	17.75	37.2

Table C.1: SSPP-Derieved Properties for Selected Member Stars of M 13 (continued)

spSpec name	α (2000.0) (degrees)	δ (2000.0) (degrees)	RV (km/s)	σ(RV) (km/s)	$T_{\rm eff}$ (K)	$\sigma(T_{\rm eff})$ (K)	log g	σ(log$g$) (dex)	[Fe/H]	σ([Fe/H]) (dex)	u	g	r	i	z	S/N
53532−2185−482	250.4379120	36.601913	−233.6	3.0	6054	46	3.31	0.16	−1.57	0.06	19.08	18.10	17.79	17.66	17.62	40.8
53532−2185−483	250.4119263	36.610191	−252.2	5.5	6351	44	3.71	0.11	−1.41	0.02	20.05	19.13	18.86	18.79	18.74	21.1
53532−2185−485	250.3427429	36.637764	−248.3	3.9	6414	80	3.90	0.17	−1.68	0.04	19.27	18.45	18.22	18.07	18.10	32.4
53532−2185−486	250.3913116	36.619122	−259.4	6.2	6288	133	4.38	0.13	−1.67	0.02	20.19	19.40	19.17	19.06	19.00	17.7
53532−2185−487	250.3905029	36.591457	−242.2	3.5	6361	92	3.74	0.10	−1.57	0.00	19.23	18.32	18.05	17.98	17.95	35.0
53532−2185−489	250.3863983	36.711922	−244.8	5.4	6336	97	4.02	0.10	−1.61	0.03	19.92	19.03	18.81	18.69	18.59	23.0
53532−2185−490	250.4195862	36.592098	−240.9	6.7	6225	81	4.07	0.18	−1.57	0.05	20.22	19.34	19.07	18.98	19.00	18.2
53532−2185−492	250.3582611	36.607357	−240.5	3.0	6155	77	3.54	0.17	−1.76	0.04	19.04	18.17	17.88	17.77	17.79	39.4
53532−2185−493	250.3370056	36.581230	−238.0	3.4	6393	81	3.91	0.19	−1.45	0.09	19.31	18.35	18.13	18.02	18.04	35.5
53532−2185−494	250.4333649	36.619698	−243.7	7.4	6169	35	3.41	0.14	−1.66	0.06	20.17	19.21	18.92	18.86	18.89	20.5
53532−2185−495	250.3131714	36.642708	−242.4	4.7	6391	67	3.73	0.16	−1.64	0.03	19.45	18.66	18.43	18.32	18.31	29.0
53532−2185−497	250.3796539	36.606239	−237.5	9.2	6085	59	4.09	0.26	−1.53	0.06	20.53	19.58	19.27	19.17	19.10	15.5
53532−2185−498	250.4183960	36.693439	−235.0	4.5	6324	40	3.62	0.16	−1.65	0.05	19.45	18.69	18.42	18.33	18.35	28.6
53532−2185−499	250.3423157	36.618721	−230.4	4.9	6358	85	3.83	0.20	−1.56	0.04	19.55	18.73	18.50	18.39	18.39	27.8
53532−2185−500	250.3634491	36.578873	−245.7	2.9	6464	93	4.24	0.08	−1.61	0.02	19.90	19.11	18.91	18.77	18.75	41.2

Table C.1: SSPP-Derieved Properties for Selected Member Stars of M 13 (continued)

spSpec name	α (2000.0) (degrees)	δ (2000.0) (degrees)	RV (km/s)	σ(RV) (km/s)	$T_{\rm eff}$ (K)	$\sigma(T_{\rm eff})$ (K)	log g	$\sigma(\log g)$ (dex)	[Fe/H]	σ([Fe/H]) (dex)	u	g	r	i	z	S/N
53532−2185−504	250.5587463	36.680569	−250.3	4.4	6381	80	4.09	0.14	−1.80	0.03	19.55	18.74	18.51	18.41	18.44	28.2
53532−2185−506	250.5240936	36.660801	−245.7	2.4	5898	45	3.33	0.11	−1.70	0.02	19.01	18.04	17.66	17.52	17.47	45.1
53532−2185−507	250.4723969	36.677731	−243.3	5.5	6173	32	3.22	0.20	−1.55	0.08	20.07	19.17	18.86	18.79	18.75	21.4
53532−2185−508	250.4435272	36.712978	−248.8	4.5	6422	129	3.77	0.22	−1.66	0.06	19.96	19.00	18.83	18.66	18.64	24.1
53532−2185−511	250.5202179	36.342960	−246.3	7.1	6149	66	3.92	0.24	−1.51	0.06	20.69	19.86	19.56	19.39	19.31	16.8
53532−2185−512	250.5370789	36.365250	−250.4	3.4	6336	59	3.65	0.06	−1.62	0.00	19.19	18.26	18.00	17.89	17.89	38.3
53532−2185−513	250.5628357	36.372688	−246.2	4.8	6264	51	3.32	0.27	−1.61	0.01	19.77	18.92	18.65	18.59	18.58	26.1
53532−2185−514	250.5161896	36.359978	−237.7	5.1	6266	41	3.74	0.28	−1.45	0.09	20.30	19.25	18.98	18.93	18.94	21.6
53532−2185−515	250.5661469	36.400230	−246.3	5.2	6408	74	3.61	0.19	−1.62	0.03	19.79	18.94	18.70	18.62	18.66	25.0
53532−2185−516	250.4558868	36.613400	−239.4	9.6	6090	190	3.98	0.17	−1.70	0.04	20.76	19.87	19.57	19.41	19.35	13.1
53532−2185−519	250.5725555	36.425186	−246.2	5.0	6366	74	4.15	0.08	−1.55	0.08	19.81	18.97	18.74	18.62	18.63	26.1
53532−2185−520	250.5612183	36.355461	−250.0	3.3	6293	81	2.88	0.31	−1.72	0.06	19.38	18.40	18.14	18.07	18.04	35.3
53532−2185−534	250.3009644	36.802814	−252.7	4.3	6338	30	3.64	0.16	−1.70	0.06	19.46	18.61	18.32	18.26	18.24	30.4
53532−2185−537	250.4304962	36.822891	−241.5	4.9	6323	30	3.66	0.18	−1.63	0.02	19.59	18.78	18.52	18.46	18.42	27.5
53532−2185−539	250.3805847	36.807693	−250.6	6.8	6157	72	3.85	0.16	−1.62	0.10	20.42	19.52	19.23	19.11	19.14	16.5

Table C.1: SSPP-Derieved Properties for Selected Member Stars of M 13 (continued)

spSpec name	α (2000.0) (degrees)	δ (2000.0) (degrees)	RV (km/s)	σ(RV) (km/s)	$T_{\rm eff}$ (K)	$\sigma(T_{\rm eff})$ (K)	log g	σ(log$g$) (dex)	[Fe/H]	σ([Fe/H]) (dex)	u	g	r	i	z	S/N
53532−2185−540	250.3366394	36.751308	−232.9	6.8	6434	55	4.51	0.17	−1.72	0.07	19.98	19.21	18.96	18.85	18.92	19.7
53532−2185−541	250.6444855	36.637691	−226.8	11.4	5968	185	4.11	0.05	−1.66	0.06	20.76	19.88	19.55	19.40	19.42	12.6
53532−2185−542	250.6344757	36.460258	−237.3	6.8	6128	55	3.67	0.28	−1.68	0.07	20.38	19.43	19.12	19.00	19.03	18.0
53532−2185−543	250.6009674	36.613602	−252.5	3.4	6243	57	3.36	0.20	−1.67	0.03	19.21	18.28	18.02	17.92	17.88	37.2
53532−2185−544	250.6094360	36.447392	−248.0	5.2	6317	76	3.15	0.21	−1.45	0.05	19.89	18.85	18.60	18.52	18.52	24.1
53532−2185−545	250.6271667	36.714451	−242.3	5.6	6382	65	4.26	0.14	−1.66	0.07	19.95	19.07	18.78	18.70	18.70	21.5
53532−2185−546	250.6421814	36.477982	−254.9	8.8	5958	340	4.39	0.40	−1.58	0.11	20.69	19.92	19.60	19.41	19.52	13.6
53532−2185−547	250.6228180	36.621357	−256.8	8.6	5992	21	3.90	0.45	−1.83	0.11	20.71	19.92	19.56	19.45	19.48	12.9
53532−2185−548	250.6524048	36.419621	−253.1	9.7	5987	0	4.14	0.08	−1.60	0.16	20.86	19.96	19.60	19.51	19.69	11.8
53532−2185−549	250.5913239	36.461399	−235.8	6.0	5923	11	4.45	0.18	−1.49	0.05	20.36	19.51	19.12	18.98	19.02	16.5
53532−2185−550	250.6149445	36.501305	−235.9	8.3	6101	241	4.39	0.37	−1.76	0.07	20.54	19.74	19.45	19.30	19.27	14.7
53532−2185−551	250.5914764	36.413662	−233.3	10.1	5876	422	3.79	0.28	−1.68	0.14	20.80	19.91	19.60	19.43	19.46	12.6
53532−2185−552	250.6224670	36.431900	−257.1	5.7	6376	44	4.00	0.11	−1.84	0.06	19.71	18.90	18.65	18.58	18.59	23.2
53532−2185−553	250.6461029	36.350220	−246.2	3.0	5916	67	3.71	0.10	−1.61	0.03	18.99	18.07	17.73	17.57	17.55	42.8
53532−2185−554	250.6182556	36.410843	−246.6	3.7	6232	61	4.00	0.13	−1.81	0.06	19.21	18.35	18.08	17.98	17.94	35.4

Table C.1: SSPP-Derieved Properties for Selected Member Stars of M 13 (continued)

spSpec name	α (2000.0) (degrees)	δ (2000.0) (degrees)	RV (km/s)	σ(RV) (km/s)	$T_{\rm eff}$ (K)	$\sigma(T_{\rm eff})$ (K)	log g	σ(log$g$) (dex)	[Fe/H]	σ([Fe/H]) (dex)	u	g	r	i	z	S/N
53532−2185−555	250.6027374	36.400173	−244.9	7.1	6208	27	3.82	0.08	−1.74	0.05	20.21	19.34	19.04	18.93	18.87	19.0
53532−2185−556	250.6363068	36.383652	−246.3	7.1	6218	49	4.05	0.17	−1.73	0.05	20.24	19.38	19.09	19.00	18.99	18.4
53532−2185−557	250.6013031	36.364738	−244.7	4.7	6394	47	3.45	0.19	−1.68	0.04	19.59	18.69	18.42	18.34	18.37	28.4
53532−2185−558	250.5827942	36.475479	−250.0	3.9	6307	39	3.79	0.10	−1.52	0.05	19.44	18.58	18.31	18.21	18.24	30.9
53532−2185−559	250.6181030	36.472069	−244.1	4.6	6384	34	3.94	0.13	−1.47	0.03	19.83	18.92	18.66	18.55	18.57	24.8
53532−2185−560	250.5843353	36.379768	−239.9	3.6	6358	37	3.48	0.14	−1.68	0.03	19.27	18.42	18.16	18.08	18.07	34.2
53532−2185−575	250.6388245	36.796120	−234.8	9.8	6002	92	3.64	0.37	−1.35	0.06	20.67	19.78	19.42	19.33	19.19	14.0
53532−2185−577	250.5796356	36.790611	−257.9	5.1	6260	46	3.64	0.19	−1.58	0.05	20.02	19.17	18.91	18.81	18.85	21.2
53532−2185−580	250.5894928	36.770725	−245.7	10.2	5959	96	4.23	0.52	−1.46	0.03	20.73	20.19	19.83	19.77	19.74	10.1
53532−2185−581	250.7305756	36.608727	−244.1	5.3	6254	29	4.10	0.20	−1.47	0.01	20.18	19.31	19.01	18.92	18.87	19.6
53532−2185−583	250.6839142	36.503529	−243.5	6.3	6157	70	3.56	0.13	−1.83	0.06	20.25	19.33	19.04	18.98	18.97	18.7
53532−2185−585	250.6607666	36.504436	−234.6	5.8	6159	52	3.61	0.25	−1.82	0.05	20.13	19.14	18.85	18.77	18.75	21.5
53532−2185−587	250.7492065	36.463837	−241.5	10.1	6051	247	3.98	0.02	−1.36	0.17	20.73	19.81	19.51	19.38	19.33	13.5
53532−2185−589	250.7702637	36.421120	−243.7	5.7	6327	74	3.22	0.28	−1.38	0.10	19.93	18.97	18.73	18.64	18.61	23.2
53532−2185−591	250.6871948	36.405094	−251.8	4.8	6427	56	3.49	0.23	−1.60	0.06	19.68	18.77	18.55	18.45	18.40	26.9

Table C.1: SSPP-Derieved Properties for Selected Member Stars of M 13 (continued)

spSpec name	α (2000.0) (degrees)	δ (2000.0) (degrees)	RV (km/s)	σ(RV) (km/s)	$T_{\rm eff}$ (K)	$\sigma(T_{\rm eff})$ (K)	log g	$\sigma(\log g)$ (dex)	[Fe/H]	σ([Fe/H]) (dex)	u	g	r	i	z	S/N
53532−2185−592	250.7585297	36.405731	−238.7	7.2	6202	105	2.89	0.44	−1.52	0.04	20.43	19.45	19.21	19.06	19.10	16.6
53532−2185−593	250.6662598	36.387859	−243.3	4.9	6448	63	3.96	0.18	−1.39	0.05	19.74	18.89	18.66	18.59	18.60	24.7
53532−2185−594	250.6430359	36.701591	−233.5	7.7	6210	42	3.90	0.06	−1.47	0.10	20.31	19.53	19.24	19.16	19.16	16.0
53532−2185−596	250.6537323	36.525860	−238.2	8.4	5943	62	3.77	0.25	−1.54	0.11	20.79	19.88	19.52	19.40	19.45	13.0
53532−2185−599	250.6560211	36.458805	−245.9	6.3	6318	57	4.06	0.16	−1.47	0.08	20.25	19.39	19.13	19.02	19.04	17.5
53532−2185−600	250.7173309	36.396912	−237.8	8.5	6090	239	4.22	0.23	−1.35	0.03	20.70	19.84	19.54	19.41	19.32	12.8
53565−2255−103	250.6466827	36.307610	−246.6	5.4	5869	41	3.25	0.20	−1.44	0.06	19.01	17.99	17.60	17.48	17.40	22.2
53565−2255−112	250.6735535	36.331844	−238.6	4.1	5056	42	2.21	0.15	−1.34	0.10	16.67	15.23	14.59	14.34	14.21	20.7
53565−2255−113	250.6521149	36.330883	−250.4	4.9	5295	98	2.32	0.24	−1.52	0.07	16.89	15.52	14.94	14.69	14.57	17.2
53565−2255−114	250.5359039	36.338322	−241.6	3.0	5439	29	2.70	0.16	−1.56	0.03	18.30	17.08	16.56	16.40	16.30	37.3
53565−2255−115	250.6161957	36.345905	−241.7	4.7	5795	36	3.15	0.14	−1.52	0.02	19.00	17.93	17.54	17.37	17.32	24.6
53565−2255−116	250.5545197	36.267830	−248.0	1.8	5355	33	2.62	0.12	−1.53	0.02	17.54	16.29	15.75	15.53	15.42	52.2
53565−2255−118	250.5711975	36.306198	−246.0	3.7	5129	72	1.89	0.19	−1.32	0.04	15.06	15.06	14.38	13.98	13.98	24.9
53565−2255−120	250.6273346	36.330883	−250.7	1.7	5201	20	2.20	0.19	−1.71	0.04	16.89	15.52	14.94	14.69	14.57	61.8
53565−2255−143	250.5123444	36.306122	−228.4	3.1	5286	28	2.34	0.10	−1.54	0.06	17.32	15.96	15.41	15.19	15.08	57.5

Table C.1: SSPP-Derieved Properties for Selected Member Stars of M 13 (continued)

spSpec name	α (2000.0) (degrees)	δ (2000.0) (degrees)	RV (km/s)	σ(RV) (km/s)	$T_{\rm eff}$ (K)	$\sigma(T_{\rm eff})$ (K)	log g	σ(log$g$) (dex)	[Fe/H]	σ([Fe/H]) (dex)	u	g	r	i	z	S/N
53565−2255−144	250.4085236	36.303902	−245.5	1.7	5243	37	2.16	0.18	−1.49	0.05	15.60	15.60	15.06	14.66	14.66	60.4
53565−2255−148	250.4909821	36.308311	−240.4	1.7	5234	20	2.15	0.18	−1.58	0.01	17.22	15.82	15.26	15.02	14.93	58.9
53565−2255−153	250.4041443	36.351501	−247.7	1.6	5226	34	2.18	0.19	−1.61	0.03	15.71	15.71	15.17	14.77	14.77	60.0
53565−2255−159	250.4909515	36.326302	−250.6	3.9	5112	42	1.97	0.21	−1.40	0.11	15.06	15.06	14.40	14.00	14.00	23.6
53565−2255−160	250.5141449	36.332100	−248.3	3.7	5178	95	1.89	0.18	−1.60	0.04	15.18	15.18	14.52	14.12	14.12	21.9
53565−2255−171	250.3690338	36.363800	−253.9	1.5	5165	43	1.84	0.15	−1.55	0.09	15.33	15.33	14.73	14.33	14.33	63.7
53565−2255−172	250.3862305	36.390400	−247.4	3.9	5311	97	2.00	0.19	−1.51	0.12	15.10	15.10	14.46	14.06	14.06	25.8
53565−2255−173	250.3810425	36.249397	−234.9	4.0	5474	91	3.48	0.11	−1.63	0.04	18.74	17.64	17.18	16.99	16.91	28.4
53565−2255−175	250.3260651	36.347099	−241.2	1.7	5230	28	2.29	0.20	−1.51	0.02	15.77	15.77	15.20	14.80	14.80	57.4
53565−2255−192	250.1939392	36.281242	−238.2	1.7	8794	184	3.30	0.12	−1.87	0.08	16.20	15.09	15.31	15.47	15.58	61.0
53565−2255−423	250.1767273	36.542747	−249.2	1.9	8785	162	3.39	0.13	−1.68	0.11	16.18	15.11	15.31	15.53	15.65	60.5
53565−2255−424	250.3054199	36.463902	−251.0	4.7	5669	68	3.19	0.20	−1.52	0.06	17.12	17.12	16.62	16.42	16.42	21.4
53565−2255−425	250.2703552	36.638271	−256.4	4.7	5801	25	3.31	0.13	−1.45	0.04	18.97	17.92	17.52	17.34	17.27	23.8
53565−2255−430	250.3401794	36.463902	−250.5	3.9	5443	119	2.48	0.19	−1.51	0.12	15.06	15.06	14.44	14.04	14.04	30.2
53565−2255−436	250.3326111	36.417400	−238.4	3.9	5274	81	2.18	0.29	−1.43	0.07	15.25	15.25	14.67	14.27	14.27	22.6

Table C.1: SSPP-Derieved Properties for Selected Member Stars of M 13 (continued)

spSpec name	α (2000.0) (degrees)	δ (2000.0) (degrees)	RV (km/s)	σ(RV) (km/s)	$T_{\rm eff}$ (K)	$\sigma(T_{\rm eff})$ (K)	log g	$\sigma(\log g)$ (dex)	[Fe/H]	σ([Fe/H]) (dex)	u	g	r	i	z	S/N
53565−2255−437	250.2912445	36.512798	−253.3	3.8	5546	62	2.68	0.30	−1.37	0.15	16.77	16.77	16.27	16.07	16.07	29.0
53565−2255−443	250.2730255	36.837120	−254.6	1.9	8918	192	3.32	0.08	−1.50	0.12	16.21	15.05	15.28	15.43	15.55	61.0
53565−2255−463	250.4259186	36.438000	−243.4	1.6	5714	44	2.78	0.24	−1.46	0.03	14.43	14.43	13.83	13.43	13.43	59.7
53565−2255−466	250.8296051	36.382706	−257.6	4.5	5694	56	2.78	0.24	−1.74	0.06	18.92	17.87	17.48	17.28	17.19	24.5
53565−2255−471	250.4281769	36.491299	−237.0	2.2	5447	34	2.40	0.27	−1.52	0.08	14.32	14.32	13.60	13.20	13.20	45.4
53565−2255−476	250.5411072	36.356194	−243.6	2.9	5563	26	2.78	0.26	−1.55	0.01	18.36	17.17	16.70	16.50	16.40	36.3
53565−2255−481	250.3587036	36.614510	−241.0	6.9	8407	239	3.07	0.09	−1.81	0.01	16.07	14.87	15.04	15.20	15.27	19.3
53565−2255−482	250.3339233	36.614510	−249.8	1.7	8470	148	3.21	0.08	−1.35	0.10	16.07	14.87	15.04	15.20	15.27	63.9
53565−2255−483	250.3755646	36.591225	−252.5	1.4	5207	55	2.30	0.18	−1.54	0.03	16.56	15.13	14.51	14.23	14.11	65.2
53565−2255−484	250.4003448	36.591225	−244.8	4.0	5053	31	1.83	0.23	−1.75	0.13	16.56	15.13	14.51	14.23	14.11	21.9
53565−2255−485	250.3701477	36.529301	−255.1	1.3	5345	26	2.25	0.14	−1.42	0.02	15.62	15.62	15.09	14.69	14.69	60.3
53565−2255−486	250.3407440	36.554901	−243.3	4.6	5306	100	2.13	0.23	−1.41	0.07	15.24	15.24	14.64	14.24	14.24	21.4
53565−2255−488	250.4460602	36.480400	−247.6	1.6	5535	50	2.29	0.27	−1.45	0.08	14.17	14.17	13.37	12.97	12.97	57.7
53565−2255−490	250.3626251	36.566055	−244.6	1.9	5491	54	2.71	0.16	−1.44	0.02	17.56	16.28	15.76	15.53	15.44	50.9
53565−2255−492	250.4226074	36.604641	−235.1	7.8	8584	261	3.25	0.17	−1.61	0.11	16.11	14.89	15.09	15.22	15.31	19.1

Table C.1: SSPP-Derieved Properties for Selected Member Stars of M 13 (continued)

spSpec name	α (2000.0) (degrees)	δ (2000.0) (degrees)	RV (km/s)	σ(RV) (km/s)	$T_{\rm eff}$ (K)	$\sigma(T_{\rm eff})$ (K)	log g	σ(log$g$) (dex)	[Fe/H]	σ([Fe/H]) (dex)	u	g	r	i	z	S/N
53565−2255−493	250.4668274	36.454601	−248.4	2.2	5651	31	2.66	0.33	−1.44	0.11	14.35	14.35	13.61	13.21	13.21	46.3
53565−2255−496	250.4133911	36.541199	−248.8	3.3	5171	88	2.02	0.24	−1.43	0.11	14.88	14.88	14.24	13.84	13.84	29.5
53565−2255−499	250.4612732	36.390900	−241.4	2.2	5235	38	1.92	0.26	−1.30	0.08	14.07	14.07	13.31	12.91	12.91	42.9
53565−2255−500	250.3884888	36.539501	−240.3	3.7	5071	54	1.85	0.17	−1.52	0.03	15.13	15.13	14.53	14.13	14.13	24.9
53565−2255−505	250.4429932	36.553799	−246.7	1.9	8738	204	2.85	0.59	−1.85	0.10	15.21	15.21	15.42	15.02	15.02	59.9
53565−2255−506	250.4873199	36.565201	−252.9	1.7	8537	166	2.68	0.49	−1.65	0.25	14.94	14.94	15.11	14.71	14.71	63.1
53565−2255−507	250.4755554	36.594837	−245.5	5.7	5097	62	2.30	0.22	−1.69	0.04	17.02	15.63	15.05	14.80	14.70	15.6
53565−2255−508	250.5657043	36.373901	−254.4	3.0	5245	27	1.88	0.19	−1.59	0.05	14.40	14.40	13.87	13.47	13.47	34.5
53565−2255−509	250.5384674	36.465302	−251.3	3.5	6537	56	2.84	0.38	−1.36	0.15	15.22	15.22	14.65	14.25	14.25	31.6
53565−2255−510	250.4507599	36.594837	−248.2	1.6	5309	48	2.24	0.16	−1.42	0.04	17.02	15.63	15.05	14.80	14.70	59.7
53565−2255−511	250.5200195	36.485901	−237.4	3.1	5435	102	2.49	0.21	−1.63	0.10	14.95	14.95	14.35	13.95	13.95	31.9
53565−2255−518	250.5189362	36.462898	−236.1	3.2	5172	46	2.04	0.20	−1.69	0.07	14.85	14.85	14.21	13.81	13.81	28.0
53565−2255−519	250.5262451	36.423500	−243.8	2.9	5231	57	2.03	0.17	−1.31	0.08	14.64	14.64	14.00	13.60	13.60	31.6
53565−2255−544	250.5659027	36.495499	−249.6	4.5	5109	71	2.00	0.10	−1.77	0.07	15.16	15.16	14.52	14.12	14.12	23.5
53565−2255−546	250.6332245	36.451298	−237.2	4.3	5105	44	1.99	0.25	−1.51	0.02	16.62	15.23	14.61	14.35	14.23	22.8

Table C.1: SSPP-Derieved Properties for Selected Member Stars of M 13 (continued)

spSpec name	α (2000.0) (degrees)	δ (2000.0) (degrees)	RV (km/s)	σ(RV) (km/s)	$T_{\rm eff}$ (K)	$\sigma(T_{\rm eff})$ (K)	log g	σ(log$g$) (dex)	[Fe/H]	σ([Fe/H]) (dex)	u	g	r	i	z	S/N
53565−2255−547	250.6033783	36.504299	−249.3	3.8	5020	117	1.81	0.16	−1.79	0.05	15.18	15.18	14.56	14.16	14.16	23.5
53565−2255−549	250.5353241	36.542400	−249.3	4.5	5227	72	2.25	0.20	−1.68	0.11	15.11	15.11	14.49	14.09	14.09	23.7
53565−2255−550	250.5207062	36.526798	−246.5	1.6	5361	69	2.39	0.21	−1.50	0.03	15.75	15.75	15.17	14.77	14.77	59.5
53565−2255−551	250.6084442	36.451298	−243.3	1.4	5227	73	2.34	0.19	−1.53	0.02	16.62	15.23	14.61	14.35	14.23	65.3
53565−2255−553	250.5565186	36.476799	−239.5	1.5	5314	56	2.19	0.17	−1.38	0.01	15.38	15.38	14.80	14.40	14.40	64.2
53565−2255−556	250.5987854	36.482475	−247.2	2.9	5597	34	3.00	0.10	−1.45	0.04	18.41	17.25	16.79	16.59	16.51	36.9
53565−2255−586	250.6133118	36.564800	−237.4	3.1	5303	46	1.82	0.10	−1.68	0.09	14.56	14.56	13.98	13.58	13.58	32.3
53565−2255−597	250.6601868	36.517498	−252.9	1.9	5464	37	2.73	0.12	−1.40	0.03	17.69	16.41	15.89	15.66	15.56	49.3

[m]The column labeled spSpec name is constructed from the Modified Julian Date (5 digits), the spectroscopic plug-plate number (four digits), and the fiber used (three digits). The error in the listed RV is computed from ELODIE template matching. The atmospheric parameter estimates ($T_{\rm eff}$, log g, and [Fe/H]) are the adopted values from the SSPP; the quoted internal error is also listed. The photometric errors in each band are not listed because most errors are less than 0.02. In the last column, S/N is the average signal-to-noise per pixel of the spectra, calculated over the range 4000−8000 Å.

Table C.2: SSPP-Derived Properties for Selected Member Stars of M 15

spSpec name	α (2000.0) (degrees)	δ (2000.0) (degrees)	RV (km/s)	σ(RV) (km/s)	$T_{\rm eff}$ (K)	$\sigma(T_{\rm eff})$ (K)	log g	σ(log$g$) (dex)	[Fe/H]	σ([Fe/H]) (dex)	u	g	r	i	z	S/N
53289−1960−401	322.4521790	12.338844	−108.1	2.6	5369	41	2.23	0.18	−2.18	0.02	17.23	16.08	15.59	15.37	15.27	56.1
53289−1960−402	322.4679565	12.327691	−106.9	2.4	5209	25	1.92	0.21	−2.33	0.05	16.72	15.39	14.84	14.58	14.47	62.3
53289−1960−406	322.4168396	12.266688	−101.2	2.3	5205	33	1.85	0.21	−2.34	0.03	16.69	15.39	14.84	14.59	14.49	65.2
53289−1960−411	322.4046326	12.227963	−112.6	4.0	5450	69	2.35	0.29	−2.48	0.04	17.48	16.41	15.94	15.74	15.61	48.9
53289−1960−413	322.4143066	12.305798	−103.6	3.0	5305	42	1.90	0.19	−2.31	0.02	16.89	15.69	15.18	14.95	14.84	57.7
53289−1960−419	322.4579773	12.303373	−110.8	2.1	5238	47	2.13	0.25	−2.34	0.02	16.71	15.43	14.89	14.65	14.54	65.2
53289−1960−420	322.6591187	12.145007	−91.5	13.9	5986	66	3.65	0.32	−1.97	0.01	19.24	18.41	18.07	17.99	17.96	15.3
53289−1960−441	322.5975342	12.257596	−114.8	6.1	5562	99	2.61	0.33	−2.08	0.02	18.50	17.58	17.18	17.03	16.96	23.7
53289−1960−442	322.5028076	12.375646	−122.4	3.9	5330	57	2.33	0.14	−2.27	0.02	17.46	16.34	15.85	15.66	15.56	46.8
53289−1960−457	322.5315247	12.312680	−113.1	9.2	5608	114	2.42	0.46	−2.04	0.03	18.87	17.91	17.54	17.36	17.27	20.6
53289−1960−459	322.7053528	12.125361	−105.3	1.9	5361	21	1.76	0.09	−2.34	0.04	16.25	15.07	14.57	14.35	14.25	68.2
53289−1960−460	322.7267761	12.119604	−101.0	3.4	5475	50	2.48	0.22	−2.22	0.03	17.46	16.42	15.97	15.79	15.68	47.9
53289−1960−500	322.4296570	12.004886	−106.8	5.2	5572	49	2.52	0.19	−2.17	0.02	18.17	17.18	16.74	16.55	16.51	35.7
53289−1960−501	322.5649414	11.992488	−84.0	10.6	5723	79	2.81	0.29	−2.17	0.05	19.25	18.29	17.91	17.74	17.67	16.6
53289−1960−506	322.5260010	11.946434	−103.6	2.8	5296	30	1.93	0.22	−2.20	0.04	17.00	15.74	15.20	14.94	14.83	58.4

Table C.2: SSPP-Derived Properties for Selected Member Stars of M 15 (continued)

spSpec name	α (2000.0) (degrees)	δ (2000.0) (degrees)	RV (km/s)	σ(RV) (km/s)	$T_{\rm eff}$ (K)	$\sigma(T_{\rm eff})$ (K)	log g	σ(log$g$) (dex)	[Fe/H]	σ([Fe/H]) (dex)	u	g	r	i	z	S/N
53289−1960−511	322.5564575	12.010468	−112.0	4.0	5394	38	2.15	0.18	−2.22	0.00	17.73	16.58	16.08	15.89	15.79	43.7
53289−1960−522	322.6466675	12.302749	−110.0	5.0	5456	93	1.78	0.27	−2.35	0.04	17.94	16.91	16.50	16.31	16.23	33.8
53289−1960−529	322.5634155	12.329430	−102.9	2.4	5259	44	1.77	0.16	−2.22	0.01	16.78	15.51	14.99	14.75	14.65	63.9
53289−1960−530	322.5755615	12.443088	−112.6	4.9	5529	65	2.40	0.21	−2.28	0.03	18.47	17.49	17.04	16.86	16.78	29.6
53321−1962−323	322.3222656	12.281335	−100.7	6.9	6095	104	2.87	0.33	−1.90	0.04	19.27	18.40	18.13	18.01	17.97	23.3
53321−1962−328	322.3479919	12.310190	−103.7	9.3	6520	110	4.22	0.22	−2.03	0.09	19.53	18.66	18.45	18.39	18.37	18.0
53321−1962−329	322.4080811	12.358446	−102.9	6.7	6222	70	3.38	0.11	−1.91	0.03	19.41	18.52	18.25	18.16	18.17	20.5
53321−1962−335	322.3918152	12.275231	−124.5	7.4	5958	81	3.04	0.10	−2.20	0.06	19.36	18.41	18.11	18.01	17.93	23.3
53321−1962−364	322.4689941	12.278071	−108.5	3.3	5565	78	2.54	0.21	−2.29	0.03	18.66	17.58	17.19	17.02	16.94	40.7
53321−1962−368	322.5046692	12.286249	−105.7	8.2	6264	114	3.02	0.34	−1.93	0.04	19.44	18.55	18.33	18.26	18.21	21.1
53321−1962−369	322.4819946	12.320425	−119.6	7.2	6235	171	2.91	0.48	−1.85	0.08	19.43	18.59	18.35	18.25	18.21	18.9
53321−1962−370	322.4340820	12.294349	−118.5	7.1	6200	60	3.55	0.23	−2.29	0.09	19.33	18.45	18.17	18.08	18.06	22.4
53321−1962−371	322.4648743	12.303191	−131.9	6.8	6031	13	3.27	0.30	−2.06	0.04	19.45	18.51	18.25	18.14	18.08	21.1
53321−1962−372	322.4102173	12.272476	−123.3	7.2	5988	110	2.98	0.27	−2.17	0.04	19.30	18.37	18.09	17.96	17.93	24.3
53321−1962−374	322.4890747	12.276496	−94.7	7.1	5941	75	3.02	0.36	−2.55	0.10	19.37	18.42	18.11	18.00	17.91	23.9

Table C.2: SSPP-Derived Properties for Selected Member Stars of M 15 (continued)

spSpec name	α (2000.0) (degrees)	δ (2000.0) (degrees)	RV (km/s)	σ(RV) (km/s)	$T_{\rm eff}$ (K)	$\sigma(T_{\rm eff})$ (K)	log g	σ(log$g$) (dex)	[Fe/H]	σ([Fe/H]) (dex)	u	g	r	i	z	S/N
53321−1962−375	322.4530640	12.260857	−106.5	4.2	5605	72	2.58	0.40	−2.15	0.05	18.81	17.76	17.37	17.21	17.15	31.7
53321−1962−376	322.4066772	12.290338	−108.2	3.4	5639	68	3.04	0.31	−2.15	0.00	18.52	17.51	17.12	16.94	16.86	41.6
53321−1962−378	322.4337463	12.256533	−123.6	12.9	6688	97	3.67	0.17	−1.96	0.14	19.95	19.05	18.86	18.80	18.83	14.3
53321−1962−399	322.2647400	12.088030	−128.7	9.4	6695	121	3.67	0.26	−2.51	0.18	19.68	18.82	18.64	18.65	18.57	17.2
53321−1962−402	322.5315247	12.312680	−103.6	3.9	5640	92	3.13	0.05	−2.26	0.05	18.87	17.91	17.54	17.36	17.27	33.8
53321−1962−403	322.5715332	12.283740	−114.8	4.5	5689	60	2.90	0.19	−2.03	0.02	18.91	17.89	17.50	17.34	17.28	32.3
53321−1962−406	322.5553284	12.353999	−104.2	4.7	5687	72	2.91	0.21	−2.14	0.03	18.93	17.94	17.56	17.41	17.34	32.6
53321−1962−407	322.5682373	12.340600	−105.0	7.8	6314	99	3.39	0.25	−1.99	0.06	19.34	18.44	18.22	18.12	18.11	20.9
53321−1962−409	322.5322266	12.338534	−113.6	14.1	6884	185	3.71	0.28	−1.96	0.16	20.07	19.15	18.99	19.00	18.86	11.9
53321−1962−412	322.5373535	12.294172	−114.9	10.7	6678	339	3.62	0.17	−1.87	0.11	19.79	18.87	18.70	18.64	18.59	14.8
53321−1962−413	322.4278564	12.366820	−110.1	3.2	5551	101	2.42	0.25	−2.17	0.06	18.65	17.56	17.17	16.96	16.90	40.9
53321−1962−414	322.5430603	12.254919	−88.1	6.5	6096	89	2.80	0.33	−1.89	0.04	19.34	18.47	18.20	18.08	18.05	22.2
53321−1962−415	322.4989014	12.316244	−106.0	3.5	5639	68	2.90	0.19	−2.12	0.03	18.44	17.42	17.03	16.88	16.79	43.1
53321−1962−416	322.5141602	12.304797	−119.6	11.2	6511	410	3.58	0.29	−2.04	0.21	19.99	19.08	18.92	18.87	18.80	13.5
53321−1962−421	322.3530884	12.238419	−117.8	5.1	5811	87	3.01	0.25	−2.22	0.01	19.27	18.37	18.03	17.89	17.85	25.1

Table C.2: SSPP-Derived Properties for Selected Member Stars of M 15 (continued)

spSpec name	α (2000.0) (degrees)	δ (2000.0) (degrees)	RV (km/s)	σ(RV) (km/s)	$T_{\rm eff}$ (K)	$\sigma(T_{\rm eff})$ (K)	log g	σ(log$g$) (dex)	[Fe/H]	σ([Fe/H]) (dex)	u	g	r	i	z	S/N
53321−1962−423	322.3211060	12.217339	−114.6	5.1	5712	104	2.91	0.21	−2.10	0.04	19.18	18.20	17.85	17.69	17.61	27.3
53321−1962−424	322.2882080	12.088967	−117.3	7.9	6575	16	3.78	0.48	−2.23	0.03	19.59	18.94	18.79	18.79	18.86	14.4
53321−1962−427	322.3056030	12.249682	−112.0	3.9	5545	121	2.64	0.29	−2.22	0.05	18.63	17.64	17.25	17.09	17.00	38.8
53321−1962−430	322.3014832	12.204044	−96.0	9.5	6457	41	2.99	0.46	−2.24	0.06	20.20	19.21	19.01	18.91	18.85	12.9
53321−1962−438	322.3101501	12.185511	−111.9	3.2	5493	72	2.54	0.24	−2.38	0.02	18.56	17.55	17.13	16.90	16.82	42.5
53321−1962−441	322.6382141	12.257859	−133.8	6.2	6264	140	3.46	0.49	−2.38	0.06	19.26	18.56	18.33	18.28	18.24	19.6
53321−1962−442	322.6037598	12.366948	−103.8	8.4	6448	166	3.40	0.35	−2.06	0.06	19.55	18.73	18.55	18.48	18.49	17.6
53321−1962−449	322.6358032	12.290989	−131.2	13.9	6511	16	3.61	0.51	−2.08	0.05	20.18	19.37	19.18	19.17	19.16	10.8
53321−1962−454	322.5975342	12.257596	−116.2	4.0	5513	108	2.27	0.31	−2.19	0.03	18.50	17.58	17.18	17.03	16.96	38.2
53321−1962−460	322.6270447	12.246479	−115.9	14.6	6616	52	4.09	0.28	−2.05	0.27	20.19	19.36	19.14	19.06	19.13	11.8
53321−1962−465	322.3361511	12.095001	−132.2	9.5	6621	104	3.96	0.19	−2.24	0.12	19.61	18.94	18.80	18.76	18.70	16.2
53321−1962−466	322.3733521	12.240548	−115.5	3.5	5518	84	2.88	0.20	−2.24	0.03	18.51	17.52	17.11	16.94	16.87	45.6
53321−1962−468	322.3805237	12.261485	−134.1	7.2	5677	127	2.64	0.28	−2.30	0.03	19.29	18.33	17.99	17.87	17.79	25.9
53321−1962−469	322.4008179	12.225221	−132.3	8.2	6396	131	3.22	0.27	−2.15	0.04	19.39	18.63	18.45	18.40	18.38	21.5
53321−1962−470	322.3207092	12.106877	−119.1	6.2	6543	78	3.50	0.25	−2.06	0.04	19.34	18.62	18.40	18.34	18.34	22.8

Table C.2: SSPP-Derived Properties for Selected Member Stars of M 15 (continued)

spSpec name	α (2000.0) (degrees)	δ (2000.0) (degrees)	RV (km/s)	σ(RV) (km/s)	$T_{\rm eff}$ (K)	$\sigma(T_{\rm eff})$ (K)	log g	σ(log$g$) (dex)	[Fe/H]	σ([Fe/H]) (dex)	u	g	r	i	z	S/N
53321−1962−471	322.4016724	12.009658	−102.8	8.0	6532	148	3.54	0.32	−1.95	0.02	19.57	18.83	18.68	18.60	18.63	19.1
53321−1962−472	322.3984680	11.973695	−98.4	11.5	6571	76	4.14	0.27	−1.85	0.08	20.48	19.63	19.39	19.31	19.22	11.5
53321−1962−474	322.3290100	12.039521	−111.9	3.2	5554	117	2.76	0.31	−2.38	0.05	18.36	17.44	17.06	16.91	16.84	44.9
53321−1962−478	322.3526611	12.008277	−126.3	12.8	6377	9	3.33	0.32	−2.43	0.18	20.68	19.72	19.50	19.37	19.30	10.7
53321−1962−480	322.3417664	12.023521	−113.4	8.4	6356	150	3.38	0.33	−1.93	0.09	19.79	18.99	18.79	18.71	18.82	17.8
53321−1962−482	322.5291748	12.030179	−115.0	7.8	6584	122	3.38	0.32	−1.88	0.12	19.64	18.86	18.71	18.62	18.69	18.5
53321−1962−483	322.4589844	11.991854	−84.9	12.0	6699	206	4.07	0.33	−2.06	0.09	20.04	19.22	19.03	18.98	18.96	13.0
53321−1962−484	322.5236511	12.006750	−101.0	9.2	6617	95	3.84	0.26	−2.11	0.07	19.99	19.20	19.00	18.95	18.85	15.2
53321−1962−487	322.5066223	11.983128	−117.6	7.8	6131	56	2.98	0.36	−2.15	0.06	19.61	18.79	18.44	18.30	18.28	20.4
53321−1962−488	322.4795532	12.013686	−101.2	7.9	6345	97	3.72	0.12	−2.31	0.13	19.52	18.65	18.38	18.36	18.37	18.7
53321−1962−490	322.4822083	11.986870	−111.6	8.7	6536	57	3.95	0.27	−2.14	0.03	19.69	18.90	18.65	18.55	18.58	17.4
53321−1962−493	322.5000610	11.843804	−106.9	5.6	5822	73	3.13	0.27	−2.37	0.04	19.19	18.32	17.98	17.82	17.78	28.4
53321−1962−495	322.4521179	11.955274	−95.2	7.6	6425	111	3.57	0.39	−2.46	0.06	19.60	18.80	18.55	18.46	18.48	19.7
53321−1962−496	322.4375000	11.972004	−83.7	7.7	6522	93	4.05	0.23	−2.06	0.07	19.52	18.78	18.56	18.48	18.53	19.7
53321−1962−497	322.4447021	12.011971	−114.9	8.5	6557	115	3.73	0.21	−2.13	0.06	19.67	18.77	18.59	18.54	18.55	18.7

Table C.2: SSPP-Derived Properties for Selected Member Stars of M 15 (continued)

spSpec name	α (2000.0) (degrees)	δ (2000.0) (degrees)	RV (km/s)	σ(RV) (km/s)	$T_{\rm eff}$ (K)	$\sigma(T_{\rm eff})$ (K)	log g	$\sigma(\log g)$ (dex)	[Fe/H]	σ([Fe/H]) (dex)	u	g	r	i	z	S/N
53321−1962−498	322.4617920	12.019878	−92.8	9.9	6656	94	3.58	0.18	−2.13	0.06	20.06	19.13	18.90	18.96	18.82	14.3
53321−1962−500	322.4923096	11.963464	−111.2	6.2	6376	80	4.10	0.10	−2.28	0.04	19.23	18.41	18.16	18.07	18.08	26.6
53321−1962−503	322.6179810	11.996145	−96.8	8.2	6678	104	4.19	0.18	−2.22	0.06	19.76	18.97	18.78	18.74	18.78	17.0
53321−1962−505	322.6524048	12.082651	−106.5	14.1	6767	203	3.65	0.23	−2.34	0.10	20.40	19.49	19.33	19.29	19.32	11.5
53321−1962−506	322.6019592	12.044020	−99.7	2.9	5526	71	2.68	0.10	−2.07	0.07	18.40	17.38	16.96	16.76	16.67	46.6
53321−1962−509	322.6124878	12.028808	−104.3	10.2	6753	64	4.04	0.31	−2.21	0.13	19.97	19.27	19.03	18.99	18.96	13.5
53321−1962−510	322.6307373	12.017861	−91.2	6.4	6175	72	3.22	0.21	−2.14	0.01	19.53	18.54	18.26	18.16	18.12	23.9
53321−1962−512	322.5454712	12.024155	−93.1	14.9	6415	125	3.65	0.56	−2.14	0.03	20.34	19.52	19.28	19.26	19.23	11.7
53321−1962−515	322.5826111	11.990081	−104.8	2.8	5561	41	2.85	0.18	−2.33	0.01	18.54	17.58	17.15	16.95	16.86	43.3
53321−1962−516	322.5649414	11.992488	−97.6	5.3	5783	38	3.13	0.17	−2.23	0.02	19.25	18.29	17.91	17.74	17.67	28.8
53321−1962−518	322.6694946	12.089317	−94.9	4.8	5838	85	3.56	0.24	−2.44	0.08	19.10	18.25	17.90	17.78	17.74	30.7
53321−1962−519	322.5717163	12.034966	−94.8	8.8	6720	93	3.75	0.23	−2.18	0.07	19.88	19.06	18.90	18.86	18.84	16.3
53321−1962−520	322.5625916	12.011796	−108.6	5.8	6354	87	3.39	0.23	−2.26	0.02	19.50	18.63	18.37	18.28	18.24	23.8
53321−1962−532	322.6614685	12.270009	−113.4	3.4	5612	107	2.57	0.22	−2.22	0.02	18.46	17.48	17.11	16.94	16.84	43.9
53321−1962−533	322.6655579	12.248962	−106.3	7.2	6337	93	3.28	0.32	−2.44	0.09	19.48	18.64	18.37	18.32	18.38	21.6

Table C.2: SSPP-Derived Properties for Selected Member Stars of M 15 (continued)

spSpec name	α (2000.0) (degrees)	δ (2000.0) (degrees)	RV (km/s)	σ(RV) (km/s)	$T_{\rm eff}$ (K)	$\sigma(T_{\rm eff})$ (K)	log g	$\sigma(\log g)$ (dex)	[Fe/H]	σ([Fe/H]) (dex)	u	g	r	i	z	S/N
53321−1962−535	322.6758423	12.262588	−99.8	3.3	5550	33	2.89	0.32	−2.24	0.02	18.79	17.82	17.38	17.21	17.17	38.0
53321−1962−539	322.7539978	12.195694	−89.5	8.8	6695	68	3.82	0.23	−2.13	0.07	19.73	18.81	18.62	18.57	18.51	20.1
53321−1962−540	322.6919556	12.215733	−88.5	11.9	6528	159	3.48	0.11	−2.14	0.09	20.26	19.39	19.20	19.17	19.17	12.9
53321−1962−543	322.6426392	12.200052	−103.3	9.1	6331	91	3.38	0.41	−2.45	0.11	19.77	18.91	18.64	18.61	18.71	17.0
53321−1962−549	322.6310120	12.212295	−119.3	5.6	5980	86	3.06	0.28	−2.45	0.05	19.24	18.33	18.03	17.88	17.78	24.1
53321−1962−550	322.6591187	12.145007	−105.5	6.3	5940	46	3.27	0.17	−2.26	0.05	19.24	18.41	18.07	17.99	17.96	24.8
53321−1962−554	322.7246094	12.159374	−102.0	11.8	6784	150	3.51	0.42	−2.19	0.04	20.16	19.37	19.22	19.16	19.10	12.3
53321−1962−558	322.6465759	12.128071	−108.9	5.7	6021	97	3.74	0.16	−2.10	0.03	19.25	18.34	18.05	17.92	17.91	25.8

Table C.3: SSPP-Derived Properties for Selected Member Stars of M 2

spSpec name	α (2000.0) (degrees)	δ (2000.0) (degrees)	RV (km/s)	σ(RV) (km/s)	$T_{\rm eff}$ (K)	$\sigma(T_{\rm eff})$ (K)	log g	σ(log$g$) (dex)	[Fe/H]	σ([Fe/H]) (dex)	u	g	r	i	z	S/N
53299−1961−124	323.2988892	−0.926583	−9.2	1.5	5154	38	2.31	0.12	−1.54	0.03	17.53	16.09	15.49	15.22	15.10	52.0
53299−1961−125	323.3046265	−0.900651	−1.7	1.6	5162	31	2.24	0.07	−1.38	0.07	17.54	16.00	15.40	15.16	15.04	52.7
53299−1961−131	323.4663696	−0.819519	6.3	1.9	5245	17	2.24	0.14	−1.55	0.02	18.04	16.68	16.13	15.91	15.80	43.8
53299−1961−134	323.4247131	−0.804700	−2.5	1.1	4996	46	1.72	0.17	−1.34	0.05	16.96	15.10	14.40	14.10	13.93	60.9
53299−1961−136	323.2869568	−0.885027	7.7	2.4	5271	51	2.51	0.12	−1.62	0.03	18.22	16.91	16.39	16.18	16.06	39.3
53299−1961−137	323.3279114	−0.839687	−9.9	1.4	5183	33	1.91	0.18	−1.44	0.06	17.27	15.62	15.02	14.77	14.61	56.4
53299−1961−140	323.3161316	−0.936875	−5.1	2.9	5448	50	2.67	0.10	−1.45	0.04	18.55	17.28	16.80	16.57	16.52	34.3
53299−1961−144	323.4824524	−0.780800	6.5	2.7	5393	60	2.48	0.22	−1.55	0.03	18.30	16.94	16.47	16.23	16.15	37.7
53299−1961−152	323.5119629	−0.501376	3.1	2.0	5233	19	2.10	0.17	−1.68	0.01	17.99	16.62	16.05	15.84	15.72	44.3
53299−1961−159	323.5318298	−0.781852	2.8	2.4	5345	59	2.41	0.17	−1.58	0.05	18.21	16.87	16.37	16.15	16.07	39.7
53299−1961−194	323.1741943	−0.712977	−7.0	2.4	8784	203	3.17	0.16	−1.13	0.24	17.14	15.91	16.13	16.33	16.41	46.1
53299−1961−202	323.2455750	−0.889511	2.3	2.3	8924	266	3.15	0.16	−1.45	0.15	17.06	15.86	16.11	16.28	16.38	49.0
53299−1961−213	323.2510986	−0.805550	−6.6	3.3	5311	97	2.00	0.25	−1.84	0.02	18.55	17.18	16.71	16.50	16.43	33.4
53299−1961−215	323.2557068	−0.864036	3.3	2.0	5166	52	2.14	0.10	−1.65	0.04	17.78	16.35	15.77	15.54	15.41	48.4
54331−1963−043	323.5525513	−0.890733	8.7	5.8	5644	93	2.69	0.15	−1.43	0.02	19.86	18.76	18.38	18.20	18.09	20.0

Table C.3: SSPP-Derived Properties for Selected Member Stars of M 2 (continued)

spSpec name	α (2000.0) (degrees)	δ (2000.0) (degrees)	RV (km/s)	σ(RV) (km/s)	$T_{\rm eff}$ (K)	$\sigma(T_{\rm eff})$ (K)	log g	σ(log$g$) (dex)	[Fe/H]	σ([Fe/H]) (dex)	u	g	r	i	z	S/N
54331−1963−057	323.5624695	−0.853803	12.9	13.5	6299	191	3.55	0.50	−1.77	0.07	20.50	19.64	19.39	19.32	19.24	10.2
54331−1963−082	323.5061035	−0.865724	−21.3	15.5	6291	72	3.20	0.47	−1.38	0.04	20.45	19.54	19.27	19.25	19.20	11.1
54331−1963−083	323.5080261	−0.824424	−9.2	8.6	5818	104	2.74	0.41	−1.47	0.12	19.97	18.91	18.57	18.46	18.38	17.4
54331−1963−085	323.4545288	−0.802932	−12.4	11.7	6614	354	4.14	0.21	−1.48	0.06	20.44	19.53	19.31	19.23	19.18	10.1
54331−1963−087	323.3307495	−0.906959	−6.3	14.6	6413	72	3.67	0.31	−1.39	0.06	20.57	19.61	19.37	19.35	19.28	10.2
54331−1963−090	323.4566040	−0.765115	−9.0	5.9	5816	84	3.49	0.18	−1.56	0.04	19.94	18.87	18.51	18.36	18.32	19.0
54331−1963−091	323.4995117	−0.948989	9.6	4.1	5457	33	3.22	0.14	−1.59	0.05	19.57	18.51	18.03	17.86	17.83	23.9
54331−1963−092	323.3335266	−0.957192	11.4	14.1	6242	197	3.91	0.22	−1.60	0.03	20.57	19.66	19.40	19.31	19.36	10.2
54331−1963−096	323.4652710	−0.816831	−6.9	6.8	5986	63	3.33	0.26	−1.53	0.01	19.96	18.95	18.63	18.53	18.47	16.9
54331−1963−098	323.4837952	−0.832883	−5.1	2.6	5376	54	2.42	0.23	−1.73	0.03	18.82	17.56	17.08	16.88	16.80	40.8
54331−1963−100	323.4888306	−0.866385	−9.6	6.8	6027	29	3.65	0.17	−1.53	0.05	19.94	18.93	18.59	18.49	18.38	17.0
54331−1963−102	323.5220337	−0.778994	−11.3	9.5	6254	11	3.43	0.16	−1.34	0.11	19.89	18.95	18.66	18.57	18.51	15.8
54331−1963−107	323.5381165	−0.751534	10.2	9.4	6139	76	3.79	0.22	−1.84	0.03	19.85	19.00	18.70	18.67	18.59	16.2
54331−1963−114	323.5265503	−0.677912	1.8	9.2	6409	169	4.18	0.21	−1.75	0.05	20.02	19.25	19.00	18.93	18.95	13.4
54331−1963−121	323.2814026	−0.907666	0.4	2.5	5440	36	2.79	0.10	−1.48	0.01	18.79	17.54	17.05	16.86	16.75	40.6

Table C.3: SSPP-Derived Properties for Selected Member Stars of M 2 (continued)

spSpec name	α (2000.0) (degrees)	δ (2000.0) (degrees)	RV (km/s)	σ(RV) (km/s)	$T_{\rm eff}$ (K)	$\sigma(T_{\rm eff})$ (K)	log g	σ(log$g$) (dex)	[Fe/H]	σ([Fe/H]) (dex)	u	g	r	i	z	S/N
54331−1963−123	323.3062134	−0.993524	2.1	5.2	5539	76	2.89	0.21	−1.24	0.16	19.87	18.69	18.28	18.11	18.03	20.8
54331−1963−124	323.2615051	−0.910594	−4.4	9.0	6129	129	3.01	0.45	−1.67	0.04	20.00	19.07	18.81	18.74	18.81	15.3
54331−1963−126	323.3119507	−0.933239	−1.9	3.8	5475	57	2.98	0.19	−1.29	0.10	19.41	18.29	17.84	17.64	17.58	27.4
54331−1963−128	323.2590942	−0.836635	−8.3	3.6	5568	76	3.25	0.11	−1.34	0.05	19.43	18.22	17.80	17.61	17.54	28.0
54331−1963−131	323.3119507	−0.911349	−1.8	3.7	5422	73	2.67	0.09	−1.61	0.06	19.36	18.21	17.75	17.57	17.49	28.5
54331−1963−134	323.2798462	−0.847540	−0.6	6.2	5807	111	2.60	0.53	−1.72	0.02	19.87	18.89	18.54	18.41	18.30	18.2
54331−1963−137	323.3194885	−0.976572	−2.3	3.0	5490	37	3.10	0.07	−1.66	0.07	19.07	17.90	17.42	17.24	17.18	33.7
54331−1963−139	323.2646790	−0.864309	−5.7	3.2	5471	31	2.92	0.23	−1.49	0.04	19.06	17.92	17.44	17.25	17.16	34.0
54331−1963−143	323.4908142	−0.783230	2.5	6.1	5878	74	3.66	0.31	−1.37	0.02	19.89	18.81	18.46	18.30	18.27	19.4
54331−1963−144	323.4483032	−0.729351	−0.4	2.3	5459	41	2.91	0.11	−1.51	0.03	18.89	17.66	17.19	17.01	16.88	39.0
54331−1963−145	323.4632263	−0.724424	0.9	6.3	5920	55	4.23	0.13	−1.35	0.07	19.87	18.91	18.54	18.39	18.28	17.9
54331−1963−146	323.4815979	−0.809713	5.6	10.3	6380	63	3.69	0.42	−1.62	0.01	20.23	19.19	18.96	18.88	18.85	13.5
54331−1963−147	323.4628601	−0.750568	−24.5	10.1	6339	316	4.14	0.31	−1.30	0.22	20.11	19.25	19.04	18.99	18.93	13.6
54331−1963−148	323.4973755	−0.808784	−8.2	7.4	5774	68	3.47	0.13	−1.62	0.05	19.89	18.90	18.51	18.37	18.35	18.2
54331−1963−150	323.4602051	−0.679670	−6.4	7.7	6073	78	4.08	0.09	−1.51	0.04	19.88	18.98	18.68	18.57	18.49	17.2

Table C.3: SSPP-Derived Properties for Selected Member Stars of M 2 (continued)

spSpec name	α (2000.0) (degrees)	δ (2000.0) (degrees)	RV (km/s)	σ(RV) (km/s)	$T_{\rm eff}$ (K)	$\sigma(T_{\rm eff})$ (K)	log g	σ(log$g$) (dex)	[Fe/H]	σ([Fe/H]) (dex)	u	g	r	i	z	S/N
54331−1963−154	323.4409485	−0.625550	9.7	10.8	6359	17	3.45	0.35	−1.43	0.10	20.49	19.59	19.36	19.32	19.31	10.9
54331−1963−156	323.4447327	−0.651404	−3.6	9.8	6443	243	3.24	0.34	−1.34	0.11	20.47	19.44	19.23	19.19	19.22	11.9
54331−1963−162	323.2671814	−0.670811	3.7	12.3	6310	310	3.44	0.16	−1.87	0.26	20.55	19.58	19.38	19.29	19.25	11.0
54331−1963−163	323.4221802	−0.748114	−4.4	10.2	6400	49	3.75	0.32	−1.52	0.06	20.51	19.65	19.40	19.33	19.37	11.1
54331−1963−164	323.4361267	−0.765563	2.0	3.7	5451	83	2.78	0.18	−1.52	0.09	19.62	18.43	18.00	17.84	17.74	27.1
54331−1963−170	323.4298401	−0.733806	−10.4	10.8	6193	327	3.69	0.34	−1.57	0.06	20.43	19.48	19.32	19.24	19.26	12.0
54331−1963−178	323.4222717	−0.635959	−8.8	4.0	5522	84	3.00	0.17	−1.56	0.01	19.59	18.48	18.05	17.89	17.84	25.3
54331−1963−179	323.2658691	−0.708226	11.1	9.2	6402	113	3.68	0.62	−1.58	0.00	20.04	19.22	18.98	18.92	18.93	14.3
54331−1963−180	323.4226990	−0.714586	−1.8	4.8	5597	80	3.34	0.12	−1.57	0.07	19.79	18.72	18.31	18.18	18.02	22.4
54331−1963−181	323.2662964	−0.726436	0.1	8.5	6364	153	3.54	0.21	−1.33	0.05	20.11	19.17	18.97	18.88	18.87	15.1
54331−1963−184	323.2333374	−0.738061	−4.8	4.4	5643	50	3.51	0.09	−1.57	0.05	19.72	18.64	18.23	18.05	17.98	22.7
54331−1963−185	323.2148438	−0.726361	−3.7	11.6	6433	176	3.80	0.24	−1.62	0.07	20.31	19.51	19.30	19.24	19.22	11.2
54331−1963−186	323.2448730	−0.776209	−23.4	13.9	6369	207	3.46	0.11	−1.63	0.10	20.56	19.65	19.47	19.37	19.38	10.6
54331−1963−188	323.2501831	−0.697996	−13.4	12.2	6464	93	3.58	0.15	−1.48	0.09	20.23	19.33	19.13	19.06	19.15	12.7
54331−1963−189	323.2506104	−0.651933	10.6	9.2	6381	222	3.71	0.19	−1.25	0.09	20.21	19.27	19.06	19.00	19.12	12.8

Table C.3: SSPP-Derived Properties for Selected Member Stars of M 2 (continued)

spSpec name	α (2000.0) (degrees)	δ (2000.0) (degrees)	RV (km/s)	σ(RV) (km/s)	$T_{\rm eff}$ (K)	$\sigma(T_{\rm eff})$ (K)	log g	$\sigma(\log g)$ (dex)	[Fe/H]	σ([Fe/H]) (dex)	u	g	r	i	z	S/N
54331−1963−193	323.2621460	−0.802807	8.6	4.7	5737	88	3.54	0.10	−1.25	0.04	19.90	18.73	18.33	18.15	18.13	21.3
54331−1963−194	323.2321777	−0.758979	−4.0	8.7	6289	15	3.79	0.17	−1.63	0.15	20.09	19.22	18.94	18.88	18.85	14.7
54331−1963−196	323.2610779	−0.770765	−2.4	9.8	6398	145	3.92	0.26	−1.36	0.16	20.13	19.25	19.09	18.96	18.88	13.7
54331−1963−197	323.1915894	−0.710805	−14.9	10.6	6499	311	4.12	0.27	−1.58	0.15	20.38	19.58	19.38	19.28	19.32	11.0
54331−1963−200	323.2678223	−0.754401	−10.6	12.9	6461	51	3.41	0.28	−1.75	0.12	20.54	19.56	19.34	19.27	19.24	11.2
54331−1963−201	323.2361145	−0.796597	−17.2	5.1	5655	83	2.99	0.19	−1.38	0.10	19.82	18.66	18.27	18.12	18.00	22.6
54331−1963−204	323.2236633	−0.962825	−0.8	2.7	5467	34	2.90	0.04	−1.54	0.06	19.14	17.95	17.46	17.28	17.19	34.5
54331−1963−207	323.2109985	−0.851545	14.2	11.8	6547	145	3.92	0.16	−1.85	0.10	20.44	19.50	19.27	19.18	19.15	11.1
54331−1963−208	323.2533569	−0.887787	−5.2	2.8	5459	52	2.77	0.14	−1.77	0.00	18.96	17.82	17.35	17.15	17.05	36.8
54331−1963−209	323.2061462	−0.803604	5.1	4.0	5605	59	3.27	0.12	−1.53	0.02	19.46	18.34	17.93	17.71	17.68	28.1
54331−1963−211	323.2515259	−0.853978	−11.8	4.1	5505	36	3.10	0.13	−1.38	0.04	19.51	18.35	17.88	17.71	17.60	28.0
54331−1963−212	323.1940918	−0.849611	7.2	5.0	5631	62	3.32	0.17	−1.60	0.00	19.72	18.64	18.21	18.05	17.95	22.5
54331−1963−217	323.2306213	−0.819139	−1.3	3.2	5517	36	3.06	0.10	−1.46	0.02	19.09	17.82	17.36	17.14	17.08	33.5
54331−1963−218	323.2166138	−0.902027	−8.4	3.1	5530	46	3.16	0.13	−1.48	0.04	19.20	17.96	17.51	17.35	17.27	33.6
54331−1963−223	323.1011353	−0.693063	5.4	11.3	6322	7	3.71	0.12	−1.38	0.05	20.15	19.27	19.01	18.92	18.93	13.6

Table C.3: SSPP-Derived Properties for Selected Member Stars of M 2 (continued)

spSpec name	α (2000.0) (degrees)	δ (2000.0) (degrees)	RV (km/s)	σ(RV) (km/s)	$T_{\rm eff}$ (K)	$\sigma(T_{\rm eff})$ (K)	log g	$\sigma(\log g)$ (dex)	[Fe/H]	σ([Fe/H]) (dex)	u	g	r	i	z	S/N
54331−1963−254	323.1844177	−0.806918	−2.3	8.1	6550	139	3.54	0.37	−1.66	0.05	20.22	19.27	19.04	18.98	19.00	13.6

Table C.4: SSPP-Derived Properties for Selected Member Stars of NGC 2420

spSpec name	α (2000.0) (degrees)	δ (2000.0) (degrees)	RV (km/s)	σ(RV) (km/s)	$T_{\rm eff}$ (K)	$\sigma(T_{\rm eff})$ (K)	log g	σ(log$g$) (dex)	[Fe/H]	σ([Fe/H]) (dex)	u	g	r	i	z	S/N
53378−2078−071	114.8806229	21.542664	86.0	2.5	5176	129	4.31	0.14	−0.44	0.07	19.79	18.22	17.66	17.44	17.35	20.2
53378−2078−111	114.7337723	21.533043	77.5	1.8	5918	30	4.30	0.07	−0.40	0.03	18.28	17.06	16.66	16.55	16.50	34.3
53378−2078−114	114.7632294	21.450647	76.5	1.8	6080	52	4.05	0.08	−0.47	0.01	17.89	16.72	16.38	16.28	16.28	41.5
53378−2078−116	114.7709503	21.494595	79.7	3.1	5117	60	4.43	0.09	−0.41	0.04	19.95	18.34	17.71	17.52	17.37	18.3
53378−2078−118	114.7212982	21.550411	75.7	2.7	5353	51	4.60	0.02	−0.41	0.03	19.60	18.03	17.47	17.30	17.19	22.0
53378−2078−142	114.6714630	21.474438	73.9	2.0	5846	42	4.27	0.05	−0.30	0.04	18.48	17.19	16.78	16.65	16.62	32.8
53378−2078−149	114.6430588	21.448729	74.3	1.2	6769	84	3.68	0.08	−0.37	0.02	16.07	15.00	14.82	14.80	14.83	63.0
53378−2078−150	114.6955032	21.390019	76.9	1.9	5927	20	4.28	0.06	−0.56	0.04	18.11	16.95	16.57	16.44	16.37	37.1
53378−2078−151	114.6724091	21.539541	77.2	1.8	6144	35	4.25	0.03	−0.49	0.05	17.82	16.67	16.33	16.24	16.24	41.9
53378−2078−152	114.6924210	21.552748	76.6	2.0	5265	34	4.37	0.10	−0.39	0.02	19.67	18.09	17.46	17.24	17.12	23.3
53378−2078−154	114.6604004	21.508270	74.0	2.2	5538	54	4.53	0.04	−0.34	0.03	19.40	17.90	17.37	17.20	17.10	24.7
53378−2078−155	114.7134628	21.373636	70.7	1.9	5515	42	4.41	0.06	−0.48	0.07	19.02	17.62	17.11	16.93	16.88	28.5
53378−2078−156	114.7031097	21.515936	78.1	1.9	6094	53	4.26	0.02	−0.43	0.02	17.88	16.75	16.40	16.29	16.28	41.1
53378−2078−157	114.6541367	21.529306	74.1	1.8	5884	34	4.28	0.06	−0.49	0.02	18.17	17.08	16.66	16.54	16.55	35.8
53378−2078−158	114.6927338	21.469568	78.4	2.4	5303	25	4.57	0.03	−0.53	0.03	19.48	17.96	17.35	17.13	17.04	24.2

Table C.4: SSPP-Derived Properties for Selected Member Stars of NGC 2420 (continued)

spSpec name	α (2000.0) (degrees)	δ (2000.0) (degrees)	RV (km/s)	σ(RV) (km/s)	$T_{\rm eff}$ (K)	$\sigma(T_{\rm eff})$ (K)	log g	$\sigma(\log g)$ (dex)	[Fe/H]	σ([Fe/H]) (dex)	u	g	r	i	z	S/N
53378−2078−159	114.6708221	21.450685	73.1	1.2	6795	73	3.76	0.10	−0.35	0.02	16.29	15.23	15.05	15.02	15.05	61.0
53378−2078−161	114.5712433	21.543400	79.0	1.2	6792	82	3.63	0.14	−0.36	0.04	16.02	14.95	14.78	14.76	14.80	63.2
53378−2078−165	114.6024323	21.426910	76.5	2.9	5205	53	4.46	0.08	−0.43	0.03	19.86	18.23	17.65	17.45	17.39	20.0
53378−2078−166	114.5820389	21.519642	73.9	1.4	6580	60	4.10	0.05	−0.35	0.02	16.69	15.64	15.42	15.38	15.40	56.3
53378−2078−167	114.6017532	21.449791	73.6	1.6	5948	52	4.29	0.03	−0.45	0.03	18.12	16.95	16.58	16.46	16.45	37.5
53378−2078−168	114.6115570	21.318134	74.0	1.4	6488	84	3.99	0.07	−0.48	0.02	16.79	15.75	15.51	15.47	15.51	55.0
53378−2078−169	114.5819626	21.280655	78.8	1.1	6795	90	3.69	0.11	−0.40	0.04	15.54	14.49	14.28	14.26	14.33	66.8
53378−2078−170	114.6131287	21.505037	74.7	2.4	4985	91	4.28	0.13	−0.44	0.12	20.24	18.49	17.82	17.60	17.50	17.4
53378−2078−171	114.6197968	21.561134	75.3	2.0	5700	29	4.31	0.07	−0.51	0.03	18.79	17.46	17.00	16.85	16.81	30.7
53378−2078−172	114.5688705	21.504910	74.2	1.7	5759	31	4.26	0.09	−0.27	0.04	18.59	17.34	16.90	16.76	16.73	31.8
53378−2078−173	114.6417999	21.560446	80.0	2.9	5170	53	4.41	0.11	−0.32	0.06	20.03	18.36	17.71	17.50	17.42	18.4
53378−2078−174	114.6007996	21.527756	75.5	2.1	5538	51	4.53	0.05	−0.35	0.04	19.37	17.89	17.35	17.19	17.11	21.4
53378−2078−175	114.6295471	21.542133	78.5	2.6	5384	11	4.40	0.08	−0.35	0.05	19.48	17.93	17.38	17.21	17.14	20.6
53378−2078−176	114.6416779	21.603819	75.0	1.2	6747	64	3.89	0.14	−0.51	0.04	15.99	14.93	14.74	14.71	14.77	63.5
53378−2078−177	114.6228180	21.586617	77.0	2.1	5505	51	4.54	0.02	−0.48	0.01	19.20	17.76	17.26	17.11	17.05	26.1

Table C.4: SSPP-Derived Properties for Selected Member Stars of NGC 2420 (continued)

spSpec name	α (2000.0) (degrees)	δ (2000.0) (degrees)	RV (km/s)	σ(RV) (km/s)	$T_{\rm eff}$ (K)	$\sigma(T_{\rm eff})$ (K)	log g	σ(log$g$) (dex)	[Fe/H]	σ([Fe/H]) (dex)	u	g	r	i	z	S/N
53378–2078–178	114.6506577	21.588242	78.9	2.4	5225	8	4.49	0.07	−0.49	0.06	19.72	18.15	17.55	17.36	17.29	21.3
53378–2078–179	114.5720901	21.569319	71.7	1.2	6820	69	3.88	0.10	−0.38	0.02	16.24	15.18	15.00	14.97	15.02	61.6
53378–2078–182	114.5458374	21.481653	75.3	1.2	6885	96	4.05	0.04	−0.47	0.03	15.87	14.81	14.64	14.62	14.67	63.5
53378–2078–186	114.5329285	21.496721	73.4	1.3	6860	90	4.01	0.06	−0.34	0.03	16.16	15.13	14.96	14.93	14.98	61.5
53378–2078–192	114.5202713	21.508390	74.1	1.8	5946	31	4.34	0.04	−0.31	0.02	18.30	17.10	16.70	16.59	16.58	34.8
53378–2078–194	114.4920883	21.528856	77.5	2.6	5553	59	4.37	0.04	−0.35	0.06	19.02	17.65	17.16	16.99	16.94	27.1
53378–2078–195	114.5080185	21.480667	73.2	1.3	6739	66	3.96	0.07	−0.34	0.04	16.43	15.40	15.20	15.16	15.22	58.2
53378–2078–197	114.5511093	21.571732	75.1	2.0	5954	53	4.39	0.08	−0.29	0.01	18.30	17.12	16.71	16.59	16.56	33.4
53378–2078–199	114.5634613	21.418985	75.2	1.6	6426	73	3.95	0.13	−0.38	0.02	16.99	15.90	15.66	15.59	15.60	53.3
53378–2078–200	114.5384979	21.543732	75.6	2.2	5338	21	4.38	0.08	−0.45	0.02	19.45	17.99	17.42	17.22	17.13	23.0
53378–2078–223	114.3904495	21.523254	71.6	1.5	6452	37	4.01	0.08	−0.50	0.01	16.95	15.90	15.63	15.58	15.59	53.4
53378–2078–224	114.4638596	21.543934	78.3	1.2	6796	64	3.80	0.13	−0.43	0.03	15.78	14.73	14.54	14.52	14.56	65.4
53378–2078–227	114.4512711	21.468901	74.9	1.7	6019	27	4.27	0.04	−0.31	0.02	18.05	16.90	16.53	16.44	16.43	37.5
53378–2078–232	114.4003372	21.434925	76.4	1.3	6793	75	3.80	0.11	−0.30	0.04	16.21	15.17	15.01	14.96	15.01	61.4
53378–2078–233	114.3611526	21.547220	78.8	1.8	6065	55	4.19	0.04	−0.30	0.03	17.86	16.73	16.38	16.28	16.25	41.7

Table C.4: SSPP-Derived Properties for Selected Member Stars of NGC 2420 (continued)

spSpec name	α (2000.0) (degrees)	δ (2000.0) (degrees)	RV (km/s)	σ(RV) (km/s)	$T_{\rm eff}$ (K)	$\sigma(T_{\rm eff})$ (K)	log g	σ(log$g$) (dex)	[Fe/H]	σ([Fe/H]) (dex)	u	g	r	i	z	S/N
53378−2078−235	114.4902191	21.548447	78.1	1.7	5751	44	4.13	0.09	−0.37	0.03	18.47	17.24	16.80	16.67	16.61	33.4
53378−2078−273	114.3406677	21.562317	76.1	3.1	6089	52	4.32	0.11	−0.25	0.04	17.85	16.81	16.45	16.37	16.25	18.3
53378−2078−422	114.4277878	21.642904	72.6	1.7	5608	60	4.38	0.06	−0.14	0.05	19.20	17.74	17.27	17.08	17.03	27.3
53378−2078−427	114.4302673	21.777519	74.2	1.6	6017	35	4.26	0.02	−0.14	0.04	18.17	16.98	16.60	16.46	16.49	38.8
53378−2078−431	114.4749222	21.663054	71.8	1.1	6737	79	3.88	0.05	−0.36	0.04	15.73	14.64	14.47	14.45	14.45	67.1
53378−2078−435	114.4620132	21.588032	74.3	1.7	5560	40	4.37	0.07	−0.15	0.04	19.14	17.74	17.24	17.08	17.02	28.2
53378−2078−440	114.4428024	21.680481	73.7	1.6	5871	47	4.44	0.05	−0.15	0.02	18.73	17.47	17.03	16.88	16.84	32.6
53378−2078−462	114.5509872	21.740852	71.4	1.4	6368	47	4.25	0.04	−0.41	0.01	17.38	16.30	16.01	15.91	15.91	50.3
53378−2078−463	114.5498276	21.721819	72.7	1.1	6673	62	4.00	0.10	−0.33	0.04	16.52	15.46	15.25	15.21	15.22	60.7
53378−2078−464	114.5740967	21.872315	73.7	1.4	5843	128	4.00	0.13	−0.49	0.00	18.04	16.89	16.50	16.38	16.37	40.7
53378−2078−465	114.5717773	21.840559	74.6	1.6	5745	46	4.46	0.09	−0.28	0.03	18.87	17.52	17.05	16.87	16.83	31.0
53378−2078−466	114.5513763	21.821871	72.3	1.2	6797	84	4.00	0.10	−0.41	0.02	16.20	15.11	14.92	14.88	14.90	62.2
53378−2078−468	114.5113068	21.658003	74.5	1.6	5811	20	4.38	0.11	−0.34	0.02	18.75	17.47	17.01	16.88	16.82	32.0
53378−2078−469	114.5523911	21.648226	75.1	1.0	6626	73	3.59	0.10	−0.35	0.05	15.55	14.45	14.23	14.20	14.22	67.0
53378−2078−470	114.5214005	21.710367	74.1	1.5	5879	38	4.38	0.05	−0.33	0.03	18.51	17.22	16.80	16.67	16.62	36.2

Table C.4: SSPP-Derived Properties for Selected Member Stars of NGC 2420 (continued)

spSpec name	α (2000.0) (degrees)	δ (2000.0) (degrees)	RV (km/s)	σ(RV) (km/s)	$T_{\rm eff}$ (K)	$\sigma(T_{\rm eff})$ (K)	log g	$\sigma(\log g)$ (dex)	[Fe/H]	σ([Fe/H]) (dex)	u	g	r	i	z	S/N
53378−2078−471	114.5303192	21.614901	76.5	1.3	6362	36	4.23	0.02	−0.34	0.02	17.39	16.33	16.04	15.97	15.98	49.5
53378−2078−472	114.5822067	21.598427	75.1	1.1	6801	62	3.86	0.07	−0.38	0.03	15.68	14.62	14.44	14.42	14.45	67.3
53378−2078−473	114.5220795	21.600906	73.1	1.4	6283	27	4.27	0.03	−0.37	0.02	17.62	16.52	16.20	16.13	16.12	46.4
53378−2078−475	114.4970779	21.644300	72.5	1.9	5277	33	4.46	0.07	−0.33	0.03	19.85	18.22	17.61	17.41	17.29	22.8
53378−2078−476	114.5061035	21.610609	75.8	1.6	5589	49	4.44	0.07	−0.25	0.01	19.35	17.91	17.38	17.23	17.12	26.6
53378−2078−477	114.5529404	21.628851	76.9	1.4	5982	48	4.38	0.09	−0.30	0.04	18.35	17.13	16.71	16.60	16.55	37.9
53378−2078−478	114.5313034	21.647833	80.3	1.5	5772	51	4.48	0.06	−0.22	0.03	19.05	17.64	17.16	17.01	16.94	30.3
53378−2078−480	114.5518036	21.664013	75.1	1.4	5908	16	4.38	0.06	−0.26	0.04	18.50	17.26	16.84	16.71	16.67	35.7
53378−2078−481	114.5914230	21.674248	70.0	1.8	6439	46	4.15	0.04	−0.28	0.01	17.21	16.13	15.84	15.77	15.79	51.4
53378−2078−485	114.6053772	21.694122	79.3	1.3	6008	31	4.38	0.06	−0.36	0.02	17.97	16.80	16.42	16.31	16.28	41.7
53378−2078−491	114.6300507	21.615072	75.4	1.1	6738	60	3.98	0.08	−0.39	0.03	15.91	14.85	14.64	14.59	14.62	64.9
53378−2078−492	114.6291809	21.672440	74.8	1.4	6085	37	4.23	0.06	−0.30	0.03	18.04	16.88	16.50	16.40	16.37	40.5
53378−2078−493	114.5901718	21.628422	77.3	1.7	5604	34	4.51	0.08	−0.36	0.03	19.25	17.78	17.26	17.11	17.03	27.9
53378−2078−496	114.6028900	21.614571	73.3	1.5	6111	39	4.41	0.06	−0.31	0.03	18.09	16.90	16.52	16.41	16.37	39.6
53378−2078−499	114.5844727	21.697393	76.7	1.5	5922	35	4.28	0.07	−0.33	0.07	18.40	17.18	16.77	16.65	16.62	35.8

Table C.4: SSPP-Derived Properties for Selected Member Stars of NGC 2420 (continued)

spSpec name	α (2000.0) (degrees)	δ (2000.0) (degrees)	RV (km/s)	σ(RV) (km/s)	$T_{\rm eff}$ (K)	$\sigma(T_{\rm eff})$ (K)	log g	σ(log$g$) (dex)	[Fe/H]	σ([Fe/H]) (dex)	u	g	r	i	z	S/N
53378−2078−503	114.6588974	21.779421	72.2	1.1	6778	99	3.88	0.10	−0.34	0.03	15.72	14.63	14.45	14.42	14.47	67.0
53378−2078−510	114.7120285	21.617662	64.4	1.5	5896	19	4.29	0.07	−0.56	0.06	18.15	16.96	16.54	16.40	16.37	40.3
53378−2078−511	114.6601486	21.613201	73.8	1.3	6850	97	4.10	0.04	−0.34	0.02	16.25	15.20	15.01	14.99	15.03	62.4
53378−2078−512	114.6719818	21.630064	72.7	1.2	6637	54	3.99	0.07	−0.34	0.03	16.66	15.61	15.39	15.35	15.36	58.2
53378−2078−513	114.6427383	21.634518	75.7	1.3	6241	51	4.47	0.07	−0.25	0.03	17.65	16.56	16.23	16.14	16.13	47.3
53378−2078−514	114.7189484	21.580208	73.5	1.4	6099	31	4.31	0.05	−0.36	0.03	17.97	16.83	16.47	16.38	16.33	40.7
53378−2078−515	114.7006531	21.605631	73.7	1.4	6244	39	4.32	0.09	−0.40	0.01	17.69	16.60	16.26	16.19	16.18	45.2
53378−2078−516	114.6420288	21.651564	72.4	1.3	6387	42	4.23	0.03	−0.29	0.03	17.28	16.21	15.93	15.87	15.88	51.2
53378−2078−517	114.6432877	21.728846	76.8	1.4	5716	18	4.41	0.06	−0.21	0.03	18.80	17.50	17.02	16.89	16.85	32.2
53378−2078−518	114.6788712	21.703911	67.6	1.2	6601	84	4.03	0.06	−0.42	0.02	16.68	15.65	15.43	15.39	15.42	57.6
53378−2078−519	114.7201385	21.600649	74.6	1.4	5851	54	4.31	0.11	−0.35	0.03	18.41	17.19	16.74	16.60	16.55	37.0
53378−2078−520	114.6900711	21.580940	74.8	1.3	6270	19	4.31	0.05	−0.38	0.02	17.60	16.52	16.18	16.09	16.11	46.8
53378−2078−548	114.7715225	21.684803	74.3	1.2	6883	94	3.97	0.08	−0.39	0.03	15.87	14.80	14.64	14.60	14.67	64.4
53378−2078−552	114.7907104	21.658455	81.7	2.4	5202	58	4.05	0.21	−0.24	0.05	20.13	18.39	17.76	17.55	17.48	17.5
53378−2078−553	114.7563171	21.637693	79.8	1.8	5309	20	4.53	0.08	−0.43	0.02	19.65	18.02	17.45	17.28	17.21	23.7

Table C.4: SSPP-Derived Properties for Selected Member Stars of NGC 2420 (continued)

spSpec name	α (2000.0) (degrees)	δ (2000.0) (degrees)	RV (km/s)	σ(RV) (km/s)	$T_{\rm eff}$ (K)	$\sigma(T_{\rm eff})$ (K)	log g	$\sigma(\log g)$ (dex)	[Fe/H]	σ([Fe/H]) (dex)	u	g	r	i	z	S/N
53378−2078−554	114.7373505	21.682465	71.8	1.2	6901	83	4.01	0.06	−0.33	0.04	15.89	14.85	14.67	14.65	14.70	64.7
53378−2078−557	114.7612228	21.602289	74.1	1.3	6501	38	4.12	0.05	−0.22	0.03	17.04	15.96	15.70	15.65	15.66	52.8
53378−2078−560	114.7902832	21.615337	77.0	1.6	5910	32	4.34	0.05	−0.20	0.04	18.42	17.18	16.77	16.66	16.63	34.9
53379−2079−071	114.8473511	21.432501	79.5	1.6	4936	53	4.31	0.09	−0.40	0.03	20.50	18.74	18.02	17.80	17.69	26.9
53379−2079−076	114.8654022	21.591274	77.8	1.4	4948	60	4.32	0.11	−0.49	0.06	20.29	18.57	17.86	17.65	17.58	28.8
53379−2079−101	114.7611084	21.490309	74.1	2.6	4496	95	4.61	0.19	−0.40	0.08	21.72	19.59	18.65	18.28	18.16	17.6
53379−2079−102	114.7788467	21.400061	79.9	2.1	4484	96	4.43	0.23	−0.44	0.08	21.78	19.54	18.56	18.26	18.14	19.0
53379−2079−108	114.7754898	21.503532	78.3	2.9	4279	78	4.25	0.16	−0.47	0.11	22.22	20.01	18.92	18.51	18.40	14.4
53379−2079−113	114.7522812	21.451731	83.1	3.2	4313	74	4.32	0.06	−0.54	0.07	22.00	20.11	19.05	18.62	18.41	13.1
53379−2079−114	114.8108063	21.427294	62.3	2.1	4778	100	4.82	0.30	−0.33	0.04	21.34	19.36	18.54	18.24	18.08	18.4
53379−2079−119	114.7431717	21.578207	74.3	3.0	4401	75	4.35	0.07	−0.50	0.19	22.16	19.84	18.83	18.42	18.28	15.7
53379−2079−141	114.7252884	21.498737	75.7	1.9	4753	88	4.76	0.30	−0.49	0.01	21.75	19.25	18.42	18.13	17.94	20.8
53379−2079−148	114.6623688	21.491985	75.2	2.0	4696	73	4.53	0.03	−0.32	0.12	21.56	19.20	18.39	18.07	17.95	22.1
53379−2079−149	114.7246323	21.518278	76.7	1.7	4826	55	4.23	0.14	−0.44	0.07	20.82	18.89	18.14	17.92	17.76	24.9
53379−2079−152	114.7128296	21.469206	76.8	2.2	4720	139	4.47	0.07	−0.57	0.14	21.25	19.23	18.38	18.10	17.95	21.1

Table C.4: SSPP-Derived Properties for Selected Member Stars of NGC 2420 (continued)

spSpec name	α (2000.0) (degrees)	δ (2000.0) (degrees)	RV (km/s)	σ(RV) (km/s)	$T_{\rm eff}$ (K)	$\sigma(T_{\rm eff})$ (K)	log g	$\sigma(\log g)$ (dex)	[Fe/H]	σ([Fe/H]) (dex)	u	g	r	i	z	S/N
53379−2079−153	114.6333389	21.580303	69.3	2.5	4463	75	4.44	0.06	−0.46	0.12	22.15	19.71	18.72	18.36	18.16	16.7
53379−2079−157	114.6400223	21.563114	74.6	2.0	4495	93	4.41	0.23	−0.38	0.09	21.76	19.59	18.62	18.31	18.14	18.4
53379−2079−158	114.6514664	21.519800	77.2	2.0	4585	81	4.62	0.30	−0.27	0.06	21.79	19.43	18.57	18.26	18.09	19.1
53379−2079−159	114.6842728	21.541288	80.3	1.9	4648	117	4.72	0.30	−0.40	0.09	21.29	19.36	18.47	18.16	18.02	20.5
53379−2079−160	114.6688385	21.578449	75.6	1.7	4807	132	4.32	0.35	−0.37	0.10	21.19	19.13	18.32	18.03	17.89	22.9
53379−2079−161	114.6037903	21.466938	75.1	2.9	4464	93	4.34	0.07	−0.34	0.11	21.88	19.77	18.81	18.44	18.20	13.2
53379−2079−162	114.6411285	21.466083	77.0	1.4	4995	63	4.44	0.10	−0.34	0.04	20.60	18.68	17.96	17.75	17.69	28.5
53379−2079−164	114.5535889	21.543980	79.1	1.9	4830	122	4.54	0.04	−0.30	0.03	21.08	18.99	18.19	17.92	17.78	23.1
53379−2079−165	114.5703201	21.534151	73.6	2.3	4454	80	4.52	0.20	−0.42	0.05	22.15	19.70	18.73	18.31	18.20	16.8
53379−2079−166	114.5640030	21.557892	75.9	1.4	4950	53	4.04	0.26	−0.39	0.03	20.55	18.68	17.98	17.73	17.61	28.1
53379−2079−167	114.6235504	21.455992	78.5	3.4	4264	79	4.32	0.04	−0.46	0.09	22.38	20.20	19.09	18.65	18.47	12.8
53379−2079−168	114.6708298	21.438009	76.3	2.5	4437	97	4.48	0.36	−0.16	0.03	21.61	19.75	18.75	18.39	18.24	15.0
53379−2079−169	114.5825729	21.549602	76.3	1.7	4972	73	4.35	0.19	−0.45	0.03	20.87	18.81	18.09	17.84	17.71	23.7
53379−2079−178	114.5719376	21.445641	75.5	1.6	5026	115	4.51	0.11	−0.34	0.06	20.63	18.70	17.98	17.75	17.63	26.2
53379−2079−181	114.5458374	21.481653	72.6	0.9	6887	84	3.79	0.07	−0.45	0.03	15.87	14.81	14.64	14.62	14.68	79.6

Table C.4: SSPP-Derived Properties for Selected Member Stars of NGC 2420 (continued)

spSpec name	α (2000.0) (degrees)	δ (2000.0) (degrees)	RV (km/s)	σ(RV) (km/s)	$T_{\rm eff}$ (K)	$\sigma(T_{\rm eff})$ (K)	log g	$\sigma(\log g)$ (dex)	[Fe/H]	σ([Fe/H]) (dex)	u	g	r	i	z	S/N
53379−2079−182	114.5021820	21.350065	79.0	2.0	4641	212	4.96	0.30	−0.38	0.07	21.08	19.15	18.34	18.05	17.87	19.7
53379−2079−185	114.5404129	21.421194	67.0	3.1	4201	109	4.17	0.28	−0.53	0.36	22.42	20.28	19.09	18.65	18.40	12.1
53379−2079−191	114.5309906	21.548798	81.3	2.2	4809	48	4.66	0.30	−0.23	0.06	21.04	19.14	18.31	18.05	17.89	20.3
53379−2079−192	114.5139694	21.403902	76.4	1.6	4971	53	4.35	0.10	−0.38	0.06	20.58	18.72	18.01	17.79	17.68	26.5
53379−2079−194	114.5345688	21.444080	76.5	1.4	5122	50	4.44	0.08	−0.40	0.04	20.26	18.53	17.86	17.65	17.52	30.0
53379−2079−195	114.5383835	21.459230	77.8	1.7	4830	60	4.30	0.12	−0.38	0.07	20.86	18.89	18.15	17.90	17.76	24.0
53379−2079−196	114.4932785	21.577396	74.9	2.4	4496	86	4.47	0.29	−0.21	0.02	22.24	19.63	18.68	18.35	18.17	16.6
53379−2079−198	114.5100632	21.580110	77.6	1.7	5041	55	4.30	0.13	−0.36	0.06	20.27	18.60	17.92	17.69	17.57	29.6
53379−2079−199	114.5401535	21.574060	77.1	2.4	4412	55	4.38	0.06	−0.46	0.09	22.05	19.75	18.76	18.42	18.17	16.3
53379−2079−200	114.5501785	21.515902	78.4	1.9	4786	44	4.26	0.18	−0.36	0.07	21.04	19.05	18.25	17.98	17.89	22.2
53379−2079−237	114.3715134	21.576729	75.1	1.8	4745	106	4.44	0.07	−0.35	0.09	21.43	19.21	18.36	18.08	17.92	21.4
53379−2079−238	114.4818726	21.496136	74.8	1.7	4887	79	4.43	0.10	−0.32	0.07	20.68	18.80	18.09	17.83	17.73	25.1
53379−2079−270	114.3305511	21.473141	79.2	1.6	4761	62	4.22	0.14	−0.38	0.05	20.74	18.86	18.08	17.78	17.65	24.2
53379−2079−429	114.4196396	21.693394	79.4	3.7	4238	88	4.28	0.10	−0.57	0.16	21.69	20.34	19.18	18.69	18.40	11.6
53379−2079−431	114.3533020	21.674223	72.7	1.3	4813	66	4.36	0.14	−0.35	0.07	20.62	18.85	18.07	17.79	17.71	26.6

Table C.4: SSPP-Derived Properties for Selected Member Stars of NGC 2420 (continued)

spSpec name	α (2000.0) (degrees)	δ (2000.0) (degrees)	RV (km/s)	σ(RV) (km/s)	$T_{\rm eff}$ (K)	$\sigma(T_{\rm eff})$ (K)	log g	σ(log$g$) (dex)	[Fe/H]	σ([Fe/H]) (dex)	u	g	r	i	z	S/N
53379−2079−434	114.3718185	21.656651	87.0	1.6	4754	54	4.25	0.10	−0.58	0.05	20.94	18.93	18.15	17.82	17.72	25.4
53379−2079−440	114.3739700	21.682238	78.6	2.1	4534	73	4.38	0.04	−0.32	0.04	22.06	19.50	18.57	18.22	18.09	17.9
53379−2079−463	114.4646530	21.774120	80.8	3.1	4263	104	4.30	0.09	−0.47	0.07	23.34	20.23	19.10	18.69	18.44	12.5
53379−2079−466	114.4835968	21.728159	77.5	2.0	4548	84	4.59	0.23	−0.50	0.01	21.98	19.50	18.59	18.29	18.16	18.5
53379−2079−467	114.5359192	21.782801	78.3	1.5	4844	72	4.36	0.15	−0.38	0.03	21.10	18.95	18.18	17.87	17.73	24.4
53379−2079−474	114.4939804	21.612207	76.7	2.3	4457	87	4.39	0.06	−0.41	0.03	21.68	19.68	18.69	18.31	18.05	18.9
53379−2079−476	114.4833527	21.630688	74.0	2.4	4465	98	4.37	0.08	−0.21	0.00	21.93	19.77	18.80	18.44	18.29	15.6
53379−2079−477	114.5016327	21.681393	75.7	1.5	4839	72	4.22	0.17	−0.40	0.04	21.10	18.94	18.17	17.94	17.79	25.3
53379−2079−480	114.5439606	21.591728	72.3	1.5	4759	108	4.70	0.30	−0.46	0.02	21.21	19.08	18.27	17.97	17.82	24.3
53379−2079−482	114.6128006	21.662743	76.9	2.1	4515	104	4.39	0.39	−0.48	0.10	21.37	19.43	18.50	18.12	17.91	19.5
53379−2079−483	114.5822067	21.598427	68.3	1.0	6793	66	3.84	0.08	−0.33	0.04	15.68	14.62	14.44	14.42	14.46	82.4
53379−2079−484	114.6317978	21.675659	72.8	3.3	4296	82	4.33	0.10	−0.58	0.17	22.70	20.04	18.96	18.55	18.36	13.9
53379−2079−487	114.6304016	21.655710	78.7	2.0	4579	134	4.35	0.09	−0.37	0.16	21.61	19.44	18.51	18.21	18.05	19.9
53379−2079−490	114.5893326	21.713299	79.7	2.2	4458	88	4.62	0.18	−0.53	0.14	22.38	19.76	18.75	18.43	18.24	17.2
53379−2079−493	114.5601196	21.648806	76.5	2.7	4329	68	4.34	0.11	−0.40	0.09	22.12	19.97	18.92	18.55	18.33	14.5

Table C.4: SSPP-Derived Properties for Selected Member Stars of NGC 2420 (continued)

spSpec name	α (2000.0) (degrees)	δ (2000.0) (degrees)	RV (km/s)	σ(RV) (km/s)	$T_{\rm eff}$ (K)	$\sigma(T_{\rm eff})$ (K)	log g	σ(log$g$) (dex)	[Fe/H]	σ([Fe/H]) (dex)	u	g	r	i	z	S/N
53379−2079−495	114.5839233	21.631277	78.5	1.6	4831	49	4.37	0.08	−0.32	0.03	20.98	18.91	18.18	17.93	17.81	24.7
53379−2079−496	114.6000900	21.607351	78.6	1.3	4945	81	4.31	0.10	−0.41	0.04	20.46	18.67	17.94	17.75	17.65	29.9
53379−2079−498	114.6408386	21.609079	79.4	1.6	4795	54	4.30	0.19	−0.44	0.06	20.89	18.98	18.22	17.96	17.80	24.4
53379−2079−500	114.5563812	21.802401	78.4	1.9	4755	84	4.98	0.30	−0.38	0.12	21.37	19.21	18.39	18.11	17.93	21.5
53379−2079−502	114.6971817	21.661120	76.2	1.8	4798	130	4.79	0.30	−0.48	0.09	21.18	19.10	18.30	18.02	17.87	22.3
53379−2079−507	114.7510529	21.611731	81.5	1.9	4513	98	4.48	0.26	−0.37	0.07	21.39	19.37	18.51	18.17	18.08	20.1
53379−2079−510	114.7320633	21.659275	82.7	3.3	4211	140	4.25	0.18	−0.61	0.12	23.09	20.38	19.19	18.80	18.56	11.8
53379−2079−511	114.7137070	21.664612	76.7	1.7	4793	22	4.28	0.10	−0.48	0.03	20.82	18.98	18.21	17.93	17.83	24.0
53379−2079−512	114.6809235	21.718416	74.6	1.3	5122	55	4.40	0.09	−0.25	0.05	20.16	18.51	17.85	17.63	17.53	30.9
53379−2079−516	114.6617126	21.614836	75.0	1.4	4886	70	4.39	0.10	−0.33	0.04	20.72	18.76	18.04	17.76	17.70	27.4
53379−2079−519	114.6623764	21.765589	79.2	1.7	4718	132	4.55	0.30	−0.31	0.02	21.19	19.20	18.38	18.08	17.93	21.6
53379−2079−552	114.8454590	21.609291	62.1	2.0	4559	95	4.55	0.24	−0.56	0.01	21.37	19.42	18.51	18.23	18.10	19.9
53379−2079−558	114.7901764	21.681410	76.2	1.5	4978	85	4.18	0.19	−0.26	0.03	20.25	18.57	17.88	17.67	17.59	29.2

Table C.5: SSPP-Derived Properties for Selected Member Stars of M 67

spSpec name	α (2000.0) (degrees)	δ (2000.0) (degrees)	RV (km/s)	σ(RV) (km/s)	$T_{\rm eff}$ (K)	$\sigma(T_{\rm eff})$ (K)	log g	σ(log$g$) (dex)	[Fe/H]	σ([Fe/H]) (dex)	u	g	r	i	z	¡S/N¿
54142−2667−361	132.6933289	11.871265	36.3	0.8	5525	23	4.52	0.06	−0.10	0.00	16.83	15.22	14.66	14.44	14.36	60.9
54142−2667−372	132.6952972	11.897903	33.6	0.9	5465	37	4.59	0.05	−0.17	0.03	17.16	15.55	14.96	14.80	14.76	57.6
54142−2667−378	132.6899872	11.926571	37.8	0.8	5046	91	4.57	0.12	−0.07	0.04	18.07	16.11	15.40	15.18	15.09	51.0
54142−2667−404	132.7532043	11.886464	34.7	0.8	5791	26	4.42	0.06	−0.06	0.02	16.40	14.96	14.48	14.36	14.31	61.2
54142−2667−406	132.7005005	11.913181	34.8	0.9	6132	35	4.31	0.03	−0.07	0.02	15.43	14.20	13.82	13.72	13.73	63.7
54142−2667−407	132.7347107	11.858081	36.1	0.9	6144	26	4.25	0.03	−0.08	0.02	15.46	14.22	13.85	13.75	13.75	63.9
54142−2667−408	132.7437439	11.994214	34.3	0.9	6043	28	4.31	0.05	−0.08	0.01	15.64	14.36	13.97	13.85	13.81	63.3
54142−2667−409	132.7742462	11.886261	35.7	0.8	5642	30	4.53	0.07	−0.11	0.02	16.77	15.25	14.73	14.59	14.53	59.7
54142−2667−410	132.7377930	11.947349	32.8	0.9	5686	26	4.49	0.07	−0.09	0.02	16.60	15.15	14.64	14.49	14.46	60.1
54142−2667−411	132.8010254	11.787528	28.4	0.9	5591	32	4.53	0.06	−0.11	0.03	16.85	15.33	14.79	14.62	14.54	60.0
54142−2667−412	132.7361145	11.831808	34.6	0.9	5850	30	4.39	0.06	−0.07	0.01	16.18	14.80	14.36	14.23	14.20	62.3
54142−2667−413	132.7688141	11.862833	24.8	0.8	5981	40	4.38	0.04	−0.09	0.01	15.49	14.18	13.75	13.63	13.59	64.1
54142−2667−415	132.7000732	11.828167	35.4	0.8	5900	21	4.38	0.05	−0.06	0.02	16.04	14.69	14.24	14.12	14.08	62.6
54142−2667−417	132.7567139	11.937789	34.5	0.8	5663	19	4.54	0.07	−0.06	0.03	16.64	15.12	14.61	14.46	14.41	60.9
54142−2667−418	132.7534637	11.814725	36.5	0.9	5884	22	4.40	0.05	−0.07	0.02	16.11	14.77	14.32	14.21	14.18	62.4

Table C.5: SSPP-Derived Properties for Selected Member Stars of M 67 (continued)

spSpec name	α (2000.0) (degrees)	δ (2000.0) (degrees)	RV (km/s)	σ(RV) (km/s)	$T_{\rm eff}$ (K)	$\sigma(T_{\rm eff})$ (K)	log g	σ(log$g$) (dex)	[Fe/H]	σ([Fe/H]) (dex)	u	g	r	i	z	¡S/N¿
54142−2667−419	132.7431183	11.970697	32.5	1.0	5958	22	4.36	0.03	−0.12	0.02	15.95	14.64	14.22	14.09	14.08	62.5
54142−2667−420	132.7914276	11.771442	34.5	0.9	5898	24	4.37	0.05	−0.07	0.01	16.02	14.70	14.27	14.13	14.09	62.5
54142−2667−441	132.8041229	11.950172	35.9	0.9	5965	16	4.35	0.04	−0.04	0.02	15.89	14.58	14.17	14.03	14.02	62.0
54142−2667−444	132.8395844	11.984572	31.2	1.0	6159	24	4.27	0.05	−0.00	0.02	15.49	14.23	13.85	13.74	13.76	63.3
54142−2667−445	132.7831726	11.981397	34.3	0.8	5815	24	4.40	0.06	−0.08	0.02	16.34	14.92	14.45	14.31	14.28	60.8
54142−2667−451	132.8012543	11.906319	35.4	0.9	6048	20	4.22	0.06	−0.05	0.02	15.56	14.28	13.88	13.78	13.78	63.5
54142−2667−452	132.7928009	12.025431	37.5	0.9	4967	77	4.59	0.12	−0.10	0.01	18.39	16.39	15.68	15.45	15.33	50.6
54142−2667−453	132.8423767	11.807839	23.3	0.8	5136	51	4.52	0.08	−0.16	0.00	17.86	16.00	15.31	15.07	14.95	55.3
54142−2667−454	132.8407745	11.861747	36.2	1.0	6003	31	4.33	0.03	−0.09	0.01	15.46	14.19	13.77	13.64	13.62	63.8
54142−2667−455	132.9283295	11.991872	33.3	1.0	6114	4	4.21	0.08	−0.08	0.02	15.37	14.15	13.77	13.66	13.66	63.6
54142−2667−457	132.9065857	11.945644	36.0	0.9	5946	13	4.36	0.05	−0.08	0.03	15.88	14.55	14.13	14.03	14.01	62.5
54142−2667−459	132.8128357	11.822606	34.0	0.9	6121	31	4.30	0.04	−0.09	0.01	15.47	14.24	13.87	13.77	13.78	63.5
54142−2667−460	132.7881317	11.950017	35.6	0.9	5918	20	4.38	0.04	−0.07	0.02	16.02	14.69	14.26	14.14	14.13	61.9
54142−2667−466	132.6327057	11.502099	36.4	0.8	5211	44	4.58	0.08	−0.10	0.02	17.71	15.90	15.23	15.04	14.97	56.5
54142−2667−477	132.7222900	11.727772	35.8	0.9	5803	28	4.39	0.06	−0.09	0.01	15.95	14.58	14.12	13.95	13.92	63.5

Table C.5: SSPP-Derived Properties for Selected Member Stars of M 67 (continued)

spSpec name	α (2000.0) (degrees)	δ (2000.0) (degrees)	RV (km/s)	σ(RV) (km/s)	$T_{\rm eff}$ (K)	$\sigma(T_{\rm eff})$ (K)	log g	σ(log$g$) (dex)	[Fe/H]	σ([Fe/H]) (dex)	u	g	r	i	z	¡S/N¿
54142−2667−478	132.6963654	11.715228	33.9	0.9	6090	32	4.32	0.04	−0.06	0.01	15.55	14.28	13.90	13.78	13.81	63.8
54142−2667−479	132.7179260	11.750975	35.4	0.8	5874	22	4.42	0.05	−0.09	0.02	16.14	14.79	14.36	14.22	14.21	62.6
54142−2667−481	132.7949219	11.664139	39.5	0.9	5845	24	4.40	0.06	−0.09	0.02	16.20	14.83	14.39	14.24	14.21	62.1
54142−2667−485	132.7586517	11.755369	31.8	0.8	5680	30	4.49	0.08	−0.06	0.02	16.66	15.18	14.67	14.51	14.49	60.6
54142−2667−486	132.7528229	11.678155	36.8	0.8	5391	24	4.59	0.07	−0.09	0.02	17.25	15.62	15.03	14.85	14.79	58.6
54142−2667−487	132.7740936	11.729775	41.8	0.9	5825	21	4.47	0.04	−0.14	0.02	15.58	14.22	13.76	13.62	13.60	64.2
54142−2667−505	132.8408203	11.734822	37.4	0.9	5923	13	4.25	0.04	−0.05	0.02	15.65	14.35	13.91	13.76	13.74	61.7
54142−2667−507	132.8529358	11.718478	36.0	0.8	5653	32	4.51	0.08	−0.14	0.02	16.37	14.93	14.42	14.23	14.15	61.5
54142−2667−508	132.8550415	11.637817	33.9	0.8	5533	24	4.57	0.06	−0.07	0.02	17.06	15.47	14.92	14.75	14.69	58.8
54142−2667−522	133.0017548	11.935228	38.5	1.1	5957	14	4.33	0.05	−0.02	0.02	15.81	14.49	14.07	13.95	13.95	63.2
54142−2667−531	132.9857483	11.790237	36.3	0.9	5977	8	4.33	0.05	−0.09	0.01	15.81	14.53	14.12	14.01	14.00	63.4
54142−2667−533	132.9949951	11.804089	34.3	0.9	5257	39	4.60	0.09	−0.09	0.02	17.65	15.85	15.21	15.01	14.93	57.7
54142−2667−537	132.9948730	11.833992	33.5	0.9	5948	30	4.35	0.04	−0.14	0.02	15.75	14.48	14.05	13.90	13.87	63.5
54142−2667−538	132.9619751	11.869030	34.4	0.8	5023	86	4.44	0.14	−0.13	0.03	18.11	16.18	15.46	15.24	15.14	53.9
54142−2667−539	133.0189972	11.980183	37.1	1.0	5172	46	4.59	0.09	−0.15	0.02	17.84	15.99	15.33	15.11	15.00	55.9

Table C.5: SSPP-Derived Properties for Selected Member Stars of M 67 (continued)

spSpec name	α (2000.0) (degrees)	δ (2000.0) (degrees)	RV (km/s)	σ(RV) (km/s)	$T_{\rm eff}$ (K)	$\sigma(T_{\rm eff})$ (K)	log g	$\sigma(\log g)$ (dex)	[Fe/H]	σ([Fe/H]) (dex)	u	g	r	i	z	¡S/N¿
54142−2667−540	132.9941711	11.870869	32.9	0.8	5481	29	4.55	0.06	−0.08	0.02	17.16	15.52	14.94	14.77	14.70	58.9
54142−2667−546	133.0400848	11.779472	35.7	1.0	6145	6	4.18	0.08	−0.08	0.02	15.38	14.16	13.79	13.69	13.70	63.7
54142−2667−551	132.9911041	11.762748	38.3	0.8	5058	41	4.45	0.09	−0.17	0.02	17.62	15.81	15.11	14.83	14.66	57.4
54142−2667−552	133.0268097	11.670785	33.7	0.8	5381	54	4.66	0.07	−0.21	0.02	17.16	15.50	14.92	14.72	14.62	58.7
54142−2667−575	133.0644226	11.883697	34.4	0.9	5951	34	4.38	0.05	−0.07	0.02	15.93	14.64	14.22	14.10	14.09	62.6
54142−2667−576	133.0925751	11.817458	38.7	1.0	5659	27	4.47	0.05	−0.13	0.03	16.59	15.12	14.60	14.42	14.35	60.7
54142−2667−579	133.0659180	11.775536	35.4	0.8	5689	27	4.48	0.05	−0.10	0.02	16.69	15.21	14.70	14.53	14.49	61.1

REFERENCES

REFERENCES

Abadi, M., Navarro, J., Steinmetz, M., & Eke, V. 2003, ApJ, 597, 21

Abazajian, K., et al. 2003, AJ, 126, 2081

Abazajian, K., et al. 2004, AJ, 128, 502

Abazajian, K., et al. 2005, AJ, 129, 1755

Adelman-McCarthy, J. K., et al. 2006, ApJS, 162, 38

Adelman-McCarthy, J. K., et al. 2007, ApJS, 172, 634

Adelman-McCarthy, J. K., et al. 2008, ApJS, 175, 297

Allen, L. E., & Strom, K. M. 1995, AJ, 109, 1379

Allende Prieto, Barklem, P. S., Lambert, D. L., & Cunha, K. 2004 A&A, 420, 183

Allende Prieto, C., Beers, T. C., Wilhelm, R., et al. 2006, ApJ, 636, 804

Allende Prieto, C., et al. 2008, AJ, in press (Paper III)

Alvares, R., & Plez, B. 1998, A&A, 330, 1109

An, D., et al. 2008, ApJS, in press

Anthony-Twarog, B. J., et al. 2006, AJ, 131, 461

Argast, D., et al. 2000, A&A, 356, 873

Arnone, E., et al. 2005, A&A, 388, 842

Audouze, J., & Silk, J. 1995, ApJ, 451, L49

Asplund, M., Grevesse, N., & Sauval, A. J. 2005, EAS Pub. Ser., 17, 21

Bagnulo, S., et al. 2003, The Messenger, 114, 10

Barklem, P. S., & O'Mara, B. J. 1998, MNRAS, 300, 863

Beers, T. C., Preston, G. W., & Shectman, S. A. 1985, AJ, 90, 2089

Beers, T. C., Flynn, K., & Gebhardt, C. 1990, AJ, 100, 32

Beers, T. C., Preston, G. W., & Shectman, S. A. 1992, AJ, 103, 1987

Beers, T. C., et al. 1999, ApJ, 506, 892

Beers, T. C., et al. 2000, AJ, 119, 2866

Beers, T. C., et al. 2007, AAS, 211, 1427

Belokurov, B., et al. 2007, ApJ, 654, 897

Belokurov, B., et al. 2006, ApJ, 647, L111

Bensby, T., Feltzing, S., & Lundstrom, I. 2004, A&A, 415, 155

Bensby, T., et al. 2005, A&A, 433, 185

Carney, B. W., et al. 1997, AJ, 114, 363

Carollo, D., et al. 2007, Nature, 450, 1020

Castelli, F., & Kurucz, R. L. 2003, IAU Symposium, 210, A20

Castelli, F., Gratton, R. G., & Kurucz, R. L. 1997, A&A, 318, 841

Cayrel, R. 1988, IAUS, 132, 345C

Cayrel de Strobel, G., Soubiran, C., & Ralite, N. 2001, A&A, 373, 159

Cenarro, A. J., et al. 2001a, MNRAS, 326, 959

Cenarro, A. J., et al. 2001b, MNRAS, 326, 981

Chen, L., Hou, J. L., & Wang, J. J. 2003, AJ, 125, 1397

Chiba, M., & Beers, T. .C. 2000, AJ, 119, 2843

Christlieb, N. 2003, Rev. Mod. Astron., 16, 191

Cohen, J. G., Briley, M. M., & Stetson, P. B. 2005, AJ, 130, 1177

Cohen, J. G., & Meléndez, J. 2005, AJ, 129, 303

Covey, K. R., et al. 2007, AJ, 134, 2398

Cudworth, K. M. 1976, AJ, 81, 519

Cudworth, K. M., & Monet, D. G. 1979, AJ, 84, 774

Cudworth, K. M., & Rauscher, B. 1987, AJ, 93, 856

Dias, W. S., Alessi, B. S., Moitinho, A., & Lepine, J. R. D. 2002, A&A, 389, 871

Eggen, O. J., Lynden-Bell, D., & Sandage, A. R. 1962, ApJ, 136, 748

Fan, X., et al. 1996, AJ, 112, 628

Feltzing, S., Bensby, T., & Lundstrom, I. 2003, A&A, 397, L1

Ferreras, I., Wyse, R. F. G., & Silk, J. 2003, MNRAS, 345, 1381

Font, A., et al. 2006a, ApJ, 638, 585

Font, A., et al. 2006b, ApJ, 638, 585

Friel, E. D., Liu, T., & Janes, K. 1989, PASP, 101, 1105

Friel, E. D., & Boesgaard, A. M. 1992, ApJ, 387, 170

Friel, E. D. 1993, PASP, 101, 244

Friel, E. D., & Janes, K. A. 1993, A&A, 267, 75

Friel, E. D., Janes, K. A., Tavarez, M., Scott, J., et al. 2002, AJ, 124, 2693

Frieman, J. A., et al. 2008, AJ, 135, 338

Fuhrmann, K. 1998, A&A, 338, 161

Fuhrmann, K. 2004, AN, 325, 3

Fukugita, M., et al. 1996, AJ, 111, 1748

Fulbright, J. P. 2002, AJ, 123, 404

Geisler, D., et al. 2005, AJ, 129, 1428

Geisler, D., et al. 2007, PASP, 119, 939

Gilmore, G., & Reid, I. N. 1983, MNRAS, 202, 1025

Gilmore, G., Wyse, R. F. G., & Norris, J. E. 2002, ApJ, 574, L39

Gilmore, G., & Wyse, R. F. G. 1998, AJ, 116, 748

Girard, T. M., et al. 1989, AJ, 98,227

Girardi, L., Grebel, E. K., Odenkirchen, M., & Chiosi, C. 2004, A&A, 422, 205

Gratton, R. 2000, ASP Conf. Ser. 198, 225

Gratton, R. G., et al. 2003, A&A, 404, 187

Gray, R. O., & Corbally, C. J. 1994, AJ, 107, 742

Grevesse, N., & Sauval, A. J. 1998, SSRv, 85, 161G

Grillmair, C. J., Freeman, K. C., Irwin, M., & Quinn, P. J. 1995, AJ, 109, 2553

Gunn, J. E., et al. 1998, AJ, 116, 3040

Gunn, J. E., et al. 2006, AJ, 131, 2332

Harris, W. E. 1996, AJ, 112, 1487

Hawley, S. L., et al. 2002, AJ, 123, 3409

Hogg, D. W., Finkbeiner, D. P., Schlegel, D. J., & Gunn, J. E. 2001, AJ, 122, 2129

Ibata, R. A., Gilmore, G., & Irwin, M. J. 1994, Nature, 370, 194

Ishimaru, Y., & Wanajo, S. 1999, ApJ, 511L, 331

Ivezić, Z., et al. 2004, Astron. Nach., 325, 583

Ivezić, Z., et al. 2008, ApJ, in press

Johnston, K. V., et al. 2008, arXiv:0807.3911

Johnston, K. V., Hernquist, L., & Bolte, M. 1996, ApJ, 465, 278

Kerr, F. J., & Lynden-Bell, D. 1986, MNRAS, 221, 1023

King, J. R. 1997, AJ, 113, 2302

Kirby, E. N., Guhathakurta, P., & Sneden, C. 2008, ApJ, in press

Kirby, E., et al. 2008, 2008arXiv0807.1925

Koesterke, L., Allende Prieto, C., & Lambert, D. L. 2008, ApJ, in press

Kraft, R. P., & Ivans, I. I. 2003, PASP, 115, 143

Kupka, F., et al. 1999, A&AS, 138, 119

Kurucz, R. L. 1993, Kurucz CD-ROM 13, ATLAS9 Stellar Atmosphere Programs and 2 km/s grid (Camgridge: SAO)

Le Borgne, J. -F., et al. 2003, A&A, 402, 433

Lee, Y. S., Beers, T. C., Sivarani, T., et al. 2008a, AJ, in press (Paper I)

Lee, Y. S., Beers, T. C., Sivarani, T., et al. 2008b, AJ, in press (Paper II)

Lupton, R., et al. 2001, in ASP Conf. Ser. 238, 269

Mathieu, R. D., Latham, D. W., Griffin, R. F., & Gunn, J. E. 1986, AJ, 92, 1100

Matteucci, F., & Recchi, S. 2001, ApJ, 558, 351

Matteucci, F., & Greggio, L. 1986, A&A, 154, 279

McWilliam, A. 1998, AJ, 115, 1640

Mihalas, D., & Binney, J. 1981, Galactic Astronomy (San Francisco: Freeman)

Morrison, H. L., Norris, J., Mateo, M., et al. 2003, AJ, 125, 2502

Morrison, H. L., Flynn, C., & Freeman, K. C. 1990, AJ, 100, 1191

Moultaka, J., Ilovaisky, S. A., Prugniel, P., & Soubiran, C. 2004, PASP, 116, 693

Munn, J., et al. 2004, AJ, 127, 3034

Navarro, J. F., Frenk, C. S., & White, S. D. M. 1997, ApJ, 490, 493

Nelder, J., & Mead, R. 1965, Comput. J., 7, 308

Nissen, P. E., & Schuster, W. J. 1997, A&A, 326, 751

Nomoto, K., Thielemann, F. -K., & Wheeler, C. J. 1984, ApJ, 279, L23

Norris, J. 1986, ApJS, 61, 667

Otsuki, K., Honda, S., Aoki, W., Kajino, T., & Mathews, G. 2006, ApJ, 641L, 117

Pier, J.R., et al. 2003, AJ, 125, 1559

Plez, B., & Cohen, J. G. 2005, A&A, 434, 1117

Pritzl, B. J., Venn, K. A., & Irwin, M. 2005, AJ, 130, 2140

Prochaska, J. X., et al. 2000, AJ, 120, 2513

Prugniel, Ph., & Soubiran, C. 2001, A&A, 369,1048

Randich, S., Sestito, P., Primas, F., et al. 2006, A&A, 450, 557

Rastorguev, A. S., et al. 1999, Astron. Letters, 25, 689

Recchi, S., et al. 2008, arXiv:0808.0118

Re Fiorentin, P., Bailer-Jones, C. A. L., Lee, Y. S., et al. 2007, A&A, 467, 1373

Reimers, D., & Wisotzki, L. 1997, Msngr, 88, 14

Robertson, B., et al. 2005, ApJ, 632, 872

Ryan, S. G., Norris, J. E., & Beers, T. C. 1996, ApJ, 471, 254

Sadler, E., Rich, R. M., & Terndrup, D. 1996, AJ, 112, 171

Sánchez-Blázquez, P., et al. 2006, MNRAS, 371, 703

Sanders, W. L. 1989, Rev., Mex. Astron. Astro. 17, 31

Schlegel, D. J., Finkbeiner, D. P., & Davis, M. 1998, ApJ, 500, 525

Scott, J. E., Friel, E. D., & Janes, K. A. 1995, AJ, 109, 1706

Searle, L., & Zinn, R. 1978, ApJ, 225,357

Shetrone, M. D., & Sandquist, E. L. 2000, AJ, 120, 1913

Shetron, M., et al. 2003, AJ, 125, 684

Shetron, M., Cote, P., & Sargent, W. L. W. 2001, ApJ, 548, 592

Simon, J. D., & Geha, M. 2007, ApJ, 670, 313

Smecker-Hane, T., & Wyse, R. F. G. 1992, AJ, 103, 1621

Smith, G. H., & Briley, M. M. 2006, PASP, 118, 740

Smith, G. H., & Mateo, M. 1990, ApJ, 353, 533

Smith, J. A., et al. 2002, AJ, 123, 2121

Sneden, C., Kraft, R. P., Shetrone, M. D., Smith, G. H., et al. 1997, AJ, 114, 1964

Sneden, C., et al. 2004, AJ, 127, 2162

Sneden, C., Pilachowski, C. A., & Kraft, R. P. 2000, AJ, 120, 1351

Soubiran, C., Bienayme, O., & Siebert, A. 2003, A&A, 398, 141

Stephens, A., & Boesgaard, A. M. 2002, AJ, 123, 1647

Stetson, P. B. 1987, PASP, 99, 191

Stetson, P. B. 1990, PASP, 102, 932

Stetson, P. B. 1994, PASP, 106, 250

Stoughton, C., et al. 2002, AJ, 123, 485

Strauss, M., & Gunn, J. E. 2001, SDSS Data Release 3, Technical Note (Baltimore: STScI), http://www.wdss.org/dr3/instruments/imager/index.html

Timmes, F., Woosley, S. E., & Weaver, T. A. 1995, ApJS, 98, 617

Tinsley, B. M. 1979 ApJ, 229, 1046

Tolstoy, E., et al. 2003, AJ, 125, 707

Tsujimoto, T., Shigeyama, T., & Yoshii, Y. 1999, ApJ, 519, L63

Twarog, B. A., Ashman, K. M., & Anthony-Twarog, B. J. 1997, AJ, 114, 2556

Tucker, D., et al. 2006, AN, 327, 821

Unavane, M., Wyse, R. F. G., & Gilmore, G. 1996, MNRAS, 278, 727

Valdes, F., Gupta, R., Rose, J. A., Singh, H. P., & Bell, D. J. 2004, ApJS, 152, 251

Venn, K. A., et al. 2004, AJ, 128, 1177

White, S. D. M., & Rees, M. J. 1978, MNRAS, 183, 341

Wilhelm, R., Beers, T., & Gray, R. 1999, AJ, 117, 2308 (WBG99)

Willemsen, P. G., et al. 2005, A&A, 436, 379

Wisotzki, L., Christlieb, N., Bade, N., et al. 2000, A&A, 358, 77

Yong, D., Carney, B. W., & Teixera de Almeida, M. L. 2005, AJ, 130, 597

Woolf, V. M., & Wallerstein, G. W. 2006, PASP, 118, 218

Wyse, R. F. G. & Gilmore, G. 1986, AJ, 91, 855

York, D. G., et al. 2000, AJ, 120, 1579

Zhao, C., & Newberg, H. J. 2006, astro-ph/0612034

Zinn, R. 1993, in ASP Conf. Ser. 48, 38

Zucker, D., et al. 2006, ApJ, 643, L103

MICHIGAN STATE UNIVERSITY LIBRARIES
3 1293 02956 7942